

Lighting the Path of Phagocytosis: Exploring Signaling Resolution and Rheological Parameters with Optical Tweezers

Von der Universität Bayreuth
zur Erlangung des Grades eines
Doktors der Naturwissenschaften (Dr. rer. nat.)
genehmigte Abhandlung

von
Manuel Konrad Eisentraut
aus Erlangen

1. Gutachter: Prof. Dr. Holger Kress
2. Gutachter: Prof. Dr. Oliver Bäumchen

Tag der Einreichung: 26. Januar 2024

Tag des Kolloquiums: 29. April 2024

PhD Thesis

**Lighting the Path of Phagocytosis:
Exploring Signaling Resolution and Rheological
Parameters with Optical Tweezers**

Manuel Konrad Eisentraut
born Feb., 9th, 1992 in Erlangen

1st Reviewer: Prof. Dr. Holger Kress

2nd Reviewer: Prof. Dr. Oliver Bäumchen

Day of Submission: January 26th, 2024

Day of Colloquium: April 29th, 2024

Experimental Physics VI

University of Bayreuth

Universitätsstr. 30

95447 Bayreuth

Abstract

Phagocytosis, the cellular process by which specialized immune cells engulf and eliminate foreign particles, is a fundamental mechanism in host defense and tissue homeostasis. This thesis addresses the intricate interplay of signaling pathways and mechanical forces that govern phagocytosis and sheds light on the nature of this dynamic cellular event.

When antibody-opsionized bacteria come into contact with Fc receptors on macrophages, they initiate signaling pathways that orchestrate the process of phagocytosis. These pathways end in actin polymerization, which pushes the cell membrane around the bacterium until it is completely engulfed. While considerable progress has been made in identifying the key proteins involved in the formation of the phagocytic cup, there still is a gap in our knowledge concerning the distance to which the initial stimulus triggered by the bacterium-cell contact propagates within the cell. Our hypothesis is that this propagation distance is related to the spatial resolution limit of phagocytosis, which represents the shortest distance at which two stimuli can be distinguished. To explore this resolution limit, we used holographic optical tweezers to attach pairs of Immunoglobulin G-coated polystyrene microparticles (serving as a model system for opsonized bacteria) to murine macrophages at different distances from zero to a few micrometers.

Our studies showed that particles with 1 – 3 μm diameter were often internalized simultaneously into a single phagosome when attached to the cell in close proximity. Conversely, when attached at larger distances from each other, they were engulfed individually. To elucidate this phenomenon, we developed a computational model predicting the separate uptake probabilities as a function of particle size and distance, incorporating cellular parameters such as the mean receptor distance. By comparing the predictions of the model based on data for 2 μm -sized particles with experimental separate uptake probabilities for particles with a diameter of 1 μm and 3 μm and for cells with reduced Fc γ receptors, the validity of the model was confirmed. Remarkably, our model suggests an effective phagocytic signaling range of approximately 500 nm, which matches with the lower size threshold of phagocytosis.

The formation of the phagocytic cup requires significant rearrangements in the cytoskeleton, guided by the signaling cascades that regulate phagocytic uptake. To measure the cytoskeletal dynamics during phagocytosis, we used fluorescence microscopy to monitor the density of filamentous actin, and simultaneously used blinking optical tweezers to measure the cell's viscoelastic properties in a time-resolved manner. This combined approach provided a unique overview on the timing of the individual steps of phagocytosis and the mechanical properties of the cell during the individual phases. We found that phagocytosis resulted in a transient, around 15 s long increase in the actin density at the beads location, which was found in roughly on third of the experiments. Within 15 – 20 s after this actin flash, the rheological properties of the bead's surroundings changed rapidly, indicating that the bead passed through the actin cortex and entered the more viscous environment inside the cytoplasm. The observed temporary decrease of the bead's mobility, followed by an increase can be mapped to the phagosome passing through the stiff actin cortex and finally decoupling from it. This mechanic has not been documented in this manner before, marking an exciting breakthrough.

In summary, our research provides a unique quantitative analysis of phagocytosis. We measured the spatial parameters that influence the dynamics of cellular signaling during phagocytosis, as well as the kinematics of particle binding and the uptake process. This unique overview of phagocytosis covers both biochemical signaling and mechanical processes, contributing to a more comprehensive understanding of phagocytosis.

Zusammenfassung

Phagozytose, der zelluläre Prozess, bei dem spezialisierte Immunzellen fremde Partikel aufnehmen und eliminieren, ist ein grundlegender Mechanismus der Wirtsabwehr und der Gewebemöostase. Diese Arbeit befasst sich mit dem komplexen Zusammenspiel von Signalwegen und mechanischen Kräften, die die Phagozytose steuern, und bringt uns die Natur dieses dynamischen zellulären Vorgangs näher.

Wenn Bakterien, die mit Antikörpern opsonisiert sind, mit Fc-Rezeptoren auf Makrophagen in Kontakt kommen, werden Signalwege aktiviert, die den Prozess der Phagozytose steuern. Diese Signalwege führen über mehrere Schritte zur Aktinpolymerisation, die die Zellmembran um die Bakterien drückt, bis diese vollständig umschlossen ist. Obwohl bei der Identifizierung der Schlüsselproteine, die an der Bildung der phagozytischen Schale beteiligt sind, beträchtliche Fortschritte erzielt wurden, besteht weiterhin eine Wissenslücke hinsichtlich des Ausbreitung des anfänglichen Stimulus, der durch den Kontakt zwischen Bakterium und Zelle ausgelöst wird. Unsere Hypothese besagt, dass diese Ausbreitungsdistanz mit der räumlichen Auflösungsgrenze der Phagozytose zusammenhängt, die die kürzeste Distanz darstellt, bei der zwei Reize unterschieden werden können. Um diese Auflösungsgrenze zu erforschen, haben wir holographische optische Pinzetten verwendet, um Paare von mit Immunglobulin G beschichteten Polystyrol-Mikropartikeln (Modellsystem für opsonierte Bakterien) in verschiedenen Abständen null bis zu einigen Mikrometern an Mäuse-Makrophagen anzuheften.

Unsere Untersuchungen ergaben, dass Partikel mit einem Durchmesser im Bereich von 1 – 3 μm oft gleichzeitig in ein einziges Phagosom internalisiert wurden, wenn sie sich auf der Zelle in unmittelbarer Nähe zueinander befanden. Umgekehrt wurden sie einzeln aufgenommen, wenn sie in größerem Abstand zueinander angehaft wurden. Zur Klärung dieses Phänomens haben wir ein Rechenmodell entwickelt, das die Wahrscheinlichkeiten für eine getrennte Aufnahme in Abhängigkeit der Partikelgrößen und -abstände vorhersagt und dabei zelluläre Parameter wie den mittleren Rezeptorabstand berücksichtigt. Durch den Vergleich der Vorhersagen des Modells, die auf den Daten für Partikel der Größe 2 μm basieren, mit experimentellen separaten Aufnahmewahrscheinlichkeiten für Partikel mit einem Durchmesser von 1 μm und 3 μm sowie für Zellen mit reduzierter Zahl Fc γ -Rezeptoren, wurde die Aussagekraft des Modells bestätigt. Bemerkenswert ist, dass unser Modell eine effektive phagozytische Signalreichweite von etwa 500 nm vorschlägt, was mit der unteren Größenschwelle der Phagozytose übereinstimmt.

Die Bildung der phagozytischen Tasse erfordert eine Umstrukturierung des Zytoskeletts, die von den Signalkaskaden gesteuert wird, die die phagozytische Aufnahme regulieren. Um die Dynamik des Zytoskeletts während der Phagozytose zu messen, nutzten wir die Fluoreszenzmikroskopie, um die Dichte des filamentösen Aktins zu überwachen, und verwendeten gleichzeitig blinkende optische Pinzetten, um die viskoelastischen Eigenschaften der Zelle zeitaufgelöst zu messen. Dieser kombinierte Ansatz ermöglichte einen einzigartigen Überblick über den zeitlichen Ablauf der einzelnen Schritte der Phagozytose und die mechanischen Eigenschaften der Zelle während der einzelnen Phasen. Wir fanden heraus, dass die Phagozytose zu einem vorübergehenden, etwa 15 s langen Anstieg der Aktindichte an der Stelle der Partikel führt, der in etwa einem Drittel der Experimente festgestellt wurde. Innerhalb von 15 – 20 s nach diesem Aktin-Blitz änderten sich die rheologischen Eigenschaften der Umgebung des Partikels plötzlich, was darauf hindeutet, dass das Partikel den Aktin-Kortex durchquert hat und in die zähflüssigere Umgebung im Zytoplasma eingetreten ist. Die beobachtete vorübergehende Abnahme der Beweglichkeit des Partikels, gefolgt von einer

Zunahme, lässt sich darauf zurückführen, dass das Phagosom in dieser Zeit den starren Aktin-Kortex durchquert und sich schließlich von ihm abkoppelt. Dieser Mechanismus in dieser Art bisher nicht dokumentiert, was einen spannenden Durchbruch darstellt.

Zusammenfassend lässt sich sagen, dass unsere Forschung eine einzigartige quantitative Analyse der Phagozytose ermöglicht. Wir haben die räumlichen Parameter gemessen, die die Dynamik der zellulären Signalübertragung während der Phagozytose beeinflussen, sowie die Kinematik der Partikelbindung und des Aufnahmeprozesses. Dieser einzigartige Überblick über die Phagozytose deckt sowohl die biochemische Signalübertragung als auch mechanische Prozesse ab und trägt so zu einem umfassenderen Verständnis der Phagozytose bei.

Contents

1	Introduction	1
1.1	Preface	1
1.2	Biology of eukaryotic cells	2
1.2.1	Basic structure of a eukaryotic animal cell	2
1.2.2	The cell membrane	2
1.2.3	The cytoskeleton and actin dynamics	5
1.2.4	Cellular Adhesion	6
1.2.5	Receptors	7
1.3	Phagocytosis	8
1.3.1	Definition of phagocytosis	8
1.3.2	Relevance of phagocytosis for the immune response in mammals	8
1.3.3	Initiation of phagocytosis	9
1.4	Thesis roadmap	10
2	Measuring the spatial resolution limit of phagocytosis	13
2.1	Motivation	13
2.2	Methods and Materials	17
2.2.1	Cell culture	17
2.2.2	RNA interference and Western Blotting	18
2.2.3	Preparation of the microparticles	20
2.2.4	Sample mounting	21
2.2.5	Light microscopy	22
2.2.5.1	Microscopy setup	22
2.2.5.2	Pixel size in images	24
2.2.5.3	Widefield microscopy contrast techniques	26
2.2.5.4	Fluorescence microscopy	27
2.2.6	Optical tweezers	28
2.2.6.1	History of optical tweezers	28
2.2.6.2	Theory of optical tweezers	29
2.2.6.3	Holographic optical tweezers	31
2.2.7	Implementation of holographic optical tweezers	32
2.2.7.1	Trapping laser beam path	32
2.2.7.2	Hologram generation	35
2.2.7.3	Ray transfer matrix analysis	36
2.2.7.4	Characterization of the hologram efficiency	41
2.2.7.5	Multi-trap holograms	43
2.2.7.6	The Gerchberg-Saxton algorithm	46
2.2.8	Experimental procedure	47
2.2.9	Radial symmetry center tracking	50
2.2.10	Trajectory classification	58

2.3	Results	65
2.3.1	Separate uptake probability	65
2.3.2	Actin activity during uptake	66
2.3.3	Signaling model	66
2.3.4	Fit results	70
2.3.5	siRNA knockdown	74
2.4	Discussion	77
2.4.1	Trajectory classification and spatial resolution model	77
2.4.2	Actin dynamics and receptor mobility	80
2.4.3	Phagocytic efficiency	81
2.5	Summary	83
3	Cell rheology using optical tweezers and mechanical aspects of phagocytosis	85
3.1	Introduction	85
3.1.1	Mechanical aspects of phagocytosis	85
3.1.2	Available microrheological methods	87
3.1.3	Microrheology during phagocytosis using blinking optical tweezers	90
3.2	Methods	92
3.2.1	Live tracking and feedback	92
3.2.1.1	Cross correlation tracker	92
3.2.1.2	Performance comparison of radial and cross correlation tracker	93
3.2.1.3	3D tracking	96
3.2.1.4	Piezo stage testing	97
3.2.2	Force calibration	98
3.2.3	Experimental procedure	100
3.2.4	Viscoelasticity and power-law rheology	104
3.2.4.1	Constitutive models of viscoelasticity	104
3.2.4.2	The power law rheological model	106
3.2.4.3	Application to blinking optical tweezers	107
3.2.4.4	Simulated blinking events	110
3.2.5	Rheological evaluation of experimental data	112
3.2.5.1	Radial tracking and calculation of the optical force	112
3.2.5.2	Camera synchronization	113
3.2.5.3	Calculation of the bead's position relative to the trap	114
3.2.5.4	Example blinking measurement	116
3.2.5.5	Blinking event breakdown	118
3.2.5.6	Blinking event fitting	119
3.3	Results	121
3.3.1	Overview of the performed experiments	121
3.3.2	LifeAct flash analysis	121
3.3.3	Piezo stage overshoot	128
3.3.4	Results of the rheological measurements	129
3.3.4.1	Binding phase	129
3.3.4.2	Phagocytic uptake	132
3.4	Discussion	140
3.4.1	Uptake efficiency	140
3.4.2	LifeAct flashes	141

3.4.3	Binding phase	142
3.4.4	Actin oscillations	143
3.4.5	Rheology around the moment of uptake	144
3.4.6	Piezo stage overshoot	146
3.4.7	Thoughts on future methodical improvements	147
3.5	Conclusion	150
4	Synopsis	153
5	Appendix	155
6	Bibliography	159
7	List of Figures	177
8	List of Tables	179
9	Acknowledgments	181
10	List of Publications	183
11	Eidesstattliche Versicherung	185

1 Introduction

This chapter provides a summary of biological background knowledge and the current state of research. This is done by firstly giving a short description on the composition of eukaryotic cells. Here, more detail is provided to specific subjects relevant to phagocytosis, especially the cellular membrane and specific membrane molecules, and the cytoskeleton. The second part focuses on phagocytosis and explains its relevance to our immune system. Finally, the process of phagocytosis is covered in great detail, with a special focus on the mechanical aspects of phagocytosis and the molecular cascades responsible for the signaling prior and during phagocytosis.

1.1 Preface

A human adult contains around $3 \cdot 10^{13}$ human cells^[1]. To put that number into perspective: If every cell was inflated to the size of a grain of rice, the resulting human would roughly be the size of the whole earth. In reality, around 80% of this cell count is made up by erythrocytes, which are so tiny that all of them combined only contribute around 4% of our body mass^[1].

Because mammalian erythrocytes lack a nucleus and some other organelles, they hold more oxygen compared to their size, at the cost of being unable to reproduce by themselves. In combination with the inviscid blood plasma this enables a circulatory system capable of supplying even the largest mammals. With this many cells present, around 200 to 300 billion cells die each day within our bodies^[2], even in a healthy human. A large part of these is made up by red blood cells, which have a limited lifespan of around 120 days^[3]. At the end of their lifetime, erythrocytes are filtered out in the liver, the spleen, or the marrow, where they are taken up by macrophages^[4] in a process called phagocytosis. However, phagocytosis is more than a routine garbage collection, it emerges as a vital component of the innate immune system, safeguarding our health against potential threats. This thesis seeks not only to contribute to the growing body of knowledge surrounding phagocytosis but also to inspire a deeper appreciation for the elegance inherent in the cellular mechanisms that sustain life.

The concepts of cell biology relevant to this thesis will be covered briefly in chapter 1.2, after which the process of phagocytosis will be described in more detail in chapter 1.3. Finally, in chapter 1.4, the thesis will outline the key questions it seeks to address and provide insights into how these questions will be addressed in following chapters.

1.2 Biology of eukaryotic cells

1.2.1 Basic structure of a eukaryotic animal cell

Eukaryotic cells are complex, membrane-bound structures that make up the fundamental units of most multicellular organisms, including plants, animals, and fungi. They possess several organelles, each with distinct functions and structures. Figure 1.1 shows a thin cross-section through a eukaryotic animal cell and provides a non-exhaustive list organelles.

The nucleus, directs protein synthesis through the transcription of genetic information into mRNA. Ribosomes, responsible for translation, are either scattered in the cytoplasm or attached to the rough endoplasmic reticulum (ER)^[5]. The ER aids protein folding and lipid metabolism^[6], while the Golgi apparatus processes and packages various biomolecules^[7]. Mitochondria generate ATP, and peroxisomes control oxygen metabolites^[8]. The centrosome organizes microtubules during cell division^[9]. Finally, lysosomes (yellow) contain enzymes that are especially relevant to phagocytosis. Because those enzymes that can break down waste materials, cellular debris, and pathogens, they have to be contained inside the lysosomes to prevent those enzymes from attaching the organelles of the cell itself. When a foreign particle is taken up, the lysosomes fuse with the phagosome, transferring those enzymes to the phagosome and decreasing the pH inside the phagosome^[10]. While lysosomes are usually thought of as small, spherical vesicles, new evidence reveals that they can exist as a complex tubular network^[11].

All these organelles are submerged in cytosol, a liquid containing water, ions, small molecules and larger water-soluble molecules like proteins^[12]. The cell's structure is supported by the cytoskeleton, a complex network of protein filaments, including microtubules, microfilaments, and intermediate filaments. These filaments are crucial to phagocytosis, as their dynamic rearrangement creates the forces necessary to engulf the target particle^[13], as described in more detail in chapter 1.2.3.

The cell membrane is a lipid bilayer, wrapping around the whole cell and controlling the passage of substances in and out of the cell. It contains many proteins embedded into the membrane, for example receptors (yellow) which can react to specific molecules in the cells surrounding^[14]. Since this thesis focuses on phagocytosis, a process in which the membrane is wrapped around an external particle with the goal to engulf it, the cell membrane and its properties are especially relevant and will be discussed thoroughly in the following chapter.

1.2.2 The cell membrane

The cell membrane, seemingly a simple shell around the cell, is in fact a dynamic structure with diverse functions found in all kinds of cells – animal, plant, bacterial, and fungal. The first, most obvious function is to serve as a barrier that separates the cell's internal components from the external environment, regulating the exchange of molecules between the cell and its environment. However, acting as a hull around the cell is only one of the many functions of the membrane.

It also is essential to cell migration^[15], adhesion^[16], and to signaling, for example during intercellular interaction^[17]. Moreover it allows selective metabolism via Exo- and Endocytosis, which is essential for maintaining cellular homeostasis. Even the process of photosynthesis, which is essential to life on earth, relies on photosystems embedded within thylakoid membranes inside the chloroplasts^[18].

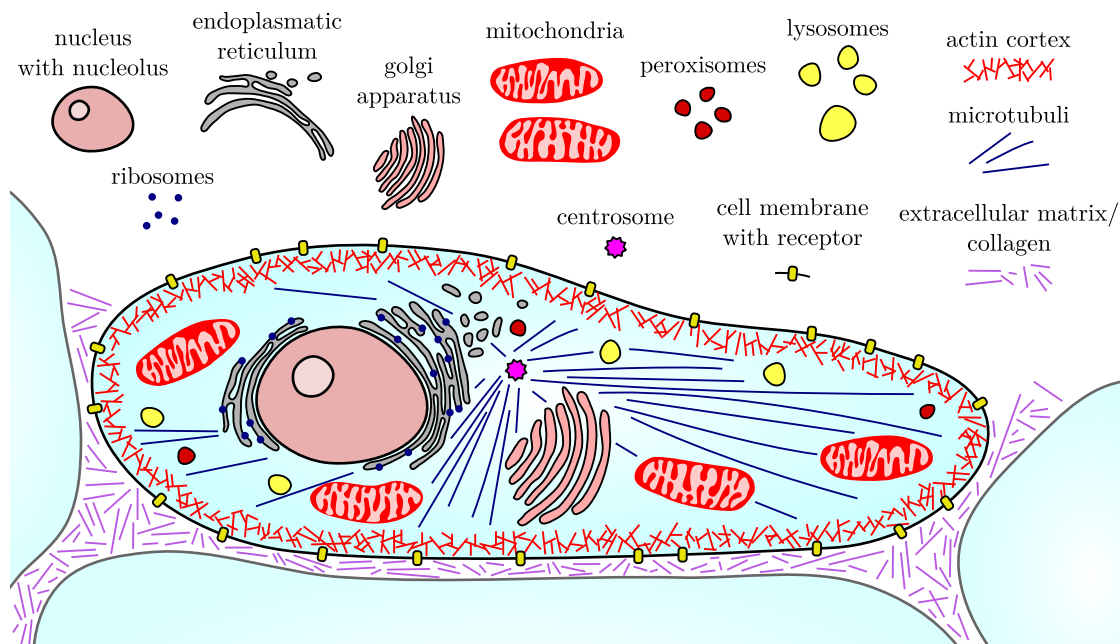


Figure 1.1: Schematic of a section through an eukaryotic animal cell. The different organelles shown are not to scale.

Compositionally, the cell membrane is made out of a lipid bilayer, which consists of two layers of phospholipid molecules. Phospholipid molecules are amphipathic, meaning they have a hydrophilic (water-loving) head and a hydrophobic (water-fearing) tail. In aqueous environment, the hydrophilic heads face outward, while the hydrophobic tails face inward, forming a stable bilayer that acts as a flexible barrier, preventing the free movement of most molecules in and out of the cell. While the membrane is structurally stable, the lipid bilayer is a fluid and dynamic structure can stretch, bend, and deform. This way the membrane can change shape and respond to external forces. The flexibility of the membrane is influenced by the presence of cholesterol, which can increase or decrease the membrane's rigidity depending on its concentration^[19].

In addition to the phospholipids forming the bulk of the lipid bilayer, the cell membrane also contains various proteins^[14]. These proteins fulfill various functions and can for example transport molecules through the membrane, or have other purposes regarding to cell signaling or adhesion. The exact combination of proteins present in the cell membrane depends on the cell type. Membrane proteins can be classified into integral membrane proteins, which are at least partially embedded into the membrane, and peripheral membrane proteins, which are not part of the membrane but can temporally adhere to it or to other integral membrane proteins. Both of these protein families can affect the mechanical properties of the membrane. For example, integral membrane proteins such as ion channels and transporters can generate forces that influence the membrane's shape and stability. Similarly, peripheral membrane proteins such as the actin-binding proteins spectrin or actinin can interact with the cytoskeleton to regulate the mechanical properties of the cell membrane^[20,21]. Overall, the elastic properties of the cell membrane are crucial for maintaining cell shape, cell motility^[18], and allowing cells to respond to their environment. A better understanding of these properties is essential for understanding various cellular processes, including phagocytosis.

1 Introduction

Over the years, the knowledge about biological membranes has grown and newer models have been developed to better understand the role of the membrane in biological processes^[22]. The fact that the membrane only consist of a only two molecule thick layer of lipid molecules has first been suggested in 1924^[23]. This idea was later refined by Danielli and Davson in 1935^[24], who suggested that the lipid bilayer is sandwiched between two protein layers to explain their observations on the surface tension of cell membranes.

However, because the available experimental data at the time was limited, it took many years for the lipid bilayer model to be accepted. A large contributor was the progress made in electron microscopy in the 1950s, making it possible to directly image the cell membrane. In 1972, the bilayer structure of the membrane was widely accepted and formulated as the fluid mosaic model^[25]. The model describes membranes as a fluid phospholipid bilayer with embedded proteins. As the membrane acts like a two-dimensional liquid, the proteins are not fixed inside the membrane but move and shift around constantly. The lipids are arranged so that their polar ends face towards the aqueous surrounding of the membrane, while the hydrophobic tails face inwards, forming a non-polar barrier which blocks the free movement of most molecules through the membrane. The hydrophobic region inside the membrane can interact with the embedded proteins and anchors them tightly into the membrane. The fluid mosaic model can be verified by multiple, modern experimental techniques. For example, the lateral movement of various integral membrane proteins has been measured by methods like single particle tracking, fluorescence correlation spectroscopy or Förster resonance energy transfer^[26].

Since its proposal, the fluid mosaic model has been refined several times to account for new discoveries. In the 1990s, the idea of lipid rafts emerged, which are small patches of the membrane that show a different composition of molecules compared to the rest of the membrane. Early evidence on the existence of lipid rafts came from studies on insoluble membrane fragments found in membranes treated with non-ionic detergents such as Triton-X-100^[27,28]. These fragments contained high amounts of sphingolipids and cholesterol, which lead to the conclusion that the membrane contains microdomains which differ in composition from the rest of the membrane. These microdomains are 50 – 100 nm large and, in the case of immune cells, cover approximately 40% of the cell's membrane^[29]. The membrane structure seems to have a higher order of organization inside the lipid rafts, which is referred to as the liquid ordered phase to distinguish it from the liquid disordered phase which can be observed in membranes with more unsaturated lipids^[30]. The different membrane domains can be detected by wide angle x-ray scattering^[30].

Lipid rafts are thought to fulfill specialized functions^[27]. For example, lipid rafts seem to be entangled with signal transduction and can even change their size and composition in response to external or internal stimuli^[31]. Considering the membrane's multitude of functions, it makes sense that some level of organization inside the membrane is necessary. The lipid rafts seem more ordered and less fluid than the surrounding membrane, and may serve as platforms for membrane organization, signaling and trafficking^[32]. The exact mechanisms contributing to the formation and function of lipid rafts are still subject to active research^[33]. Despite the strong evidence, there is some criticism that the concept of lipid rafts relies on indirect methods, and direct proof of their existence is still lacking^[34].

More recent observations indicate that the membrane is compartmentalized^[35], meaning that the movement of single molecules seems to be more restricted to small areas of the membrane. Tools like single-particle tracking, fluorescence correlation spectroscopy and super-resolution imaging have revealed that molecules inside biological membranes do not

diffuse freely over the whole membrane but are usually confined to specific regions^[36]. It has been suggested that membrane compartmentalization is caused by transmembrane proteins which are fixed to the actin cortex of the cell^[37,38]. This suggestion is labeled the “picket-fence model”, as the actin cortex acts as a rigid structure (fence), which is attached to the membrane using transmembrane proteins as anchors (pickets).

1.2.3 The cytoskeleton and actin dynamics

The cytoskeleton is a complex network of protein filaments that are present in the cytoplasm of cells. The cytoskeleton provides structural support and helps the cell to maintain its form. Moreover, it offers functional organization and play a key role in various cellular processes, including intracellular transport, cell division, and cell motility^[39]. The components of the cytoskeleton can be divided into three major components, namely actin filaments, intermediate filaments and microtubules, all of which can quickly polymerize or disassemble as needed. While the whole cytoskeleton undergoes drastic changes during phagocytosis, this thesis focuses on the dynamics of actin.

Actin filaments, also known as microfilaments, are the smallest, with a diameter of only 6 – 10 nm^[40]. They are composed of actin monomers, which can polymerize into long, thin filaments. These filaments are dynamic structures that can undergo rapid assembly and disassembly, a process known as actin dynamics. Actin dynamics are essential for many cellular processes, including cell migration, cytokinesis, and endocytosis. In eukaryotic cells, a large portion of the cell’s actin lies just beneath the plasma membrane, forming the actin cortex. It is a thin, dynamic network of actin fibers that plays a critical role in cell shape, mechanical stability, and cell motility^[41,42]. Actin filaments are polar, meaning they possess a fast polymerizing (+)-end, and a slower polymerizing (-)-end. In the actin cortex, the actin filaments are oriented with their fast polymerizing plus ends facing the plasma membrane. The actin cortex is highly dynamic and constantly remodeling, allowing cells to rapidly change shape and move. It can also generate contractile forces that help the cell to exert mechanical stresses on its environment, which is important for processes such as cell division and tissue morphogenesis.

The actin cortex is attached to the plasma membrane through a complex of proteins that link the actin filaments to transmembrane proteins, such as integrins, which connect the cell to the extracellular matrix. The specific proteins involved in this linkage can vary depending on the cell type and the specific functions of the actin cortex in that cell. These linkers are often adaptor proteins that bind both actin filaments and transmembrane proteins, and they can also interact with other cytoskeletal components, such as microtubules. Some examples of proteins that have been implicated in linking the actin cortex to the cell membrane include talin, ankyrin, and spectrin^[43,44,38]. Actin is also essential for the formation of specialized structures such as filopodia and lamellipodia^[45], which are involved in cell motility. Overall, the actin cortex is a critical component of eukaryotic cells, playing a vital role in cell shape, mechanical stability, and motility, as well as in cell signaling and membrane trafficking.

The regulation of actin dynamics is a complex process that involves multiple signaling pathways and actin-binding proteins^[46]. One of the most critical actin-binding proteins is the Arp2/3 complex, which can nucleate new actin filaments and promote their branching^[47]. The Arp2/3 complex is activated by a family of proteins called WASP (Wiskott-Aldrich syndrome proteins). One of these proteins is known as WAVE (WASP-family verprolin-homologous protein, also known as SCAR)^[48]. The protein got its two names, WAVE and SCAR, because

two separate research articles independently described and named it [49,50]. SCAR/WAVE forms a larger regulatory complex together with four other proteins [51,52]. This complex is called the WAVE (or SCAR) regulatory complex and can bind to the Arp2/3 complex, initiating actin polymerization [53].

Another important family of actin-binding proteins is the formins, which promote actin filament assembly and elongation. Formins can bind to the growing end of an actin filament and promote the addition of new actin monomers [54]. The dynamic behavior of actin filaments is also regulated by various signaling pathways, including Rho family GTPases. Rho GTPases are small signaling molecules that can activate multiple downstream effectors, including actin-binding proteins. The Rho family includes three main members, RhoA, Rac1, and Cdc42, which have distinct roles in actin dynamics. RhoA is involved in actin stress fiber formation and cell contractility, Rac1 promotes lamellipodia and membrane ruffling, and Cdc42 regulates filopodia formation [55,56].

Lamellipodia are flat, sheet-like protrusions of the plasma membrane that are rich in actin filaments. They are involved in cell migration and are essential for the extension of the leading edge of the cell during migration. [57,58] Lamellipodia contain actin-binding proteins, including Arp2/3 and cofilin, which regulate actin dynamics and promote the extension of the protrusion. Filopodia, on the other hand, are thin, finger-like protrusions of the plasma membrane that also are rich in actin filaments. They are involved in multiple functions, including cell adhesion, signaling, and sensing. [59] Filopodia contain various actin-binding proteins, including fascin and formin. While formin promotes actin polymerization, fascin promotes actin bundling, contributing to the characteristic shape of filopodia [60]. In the context of phagocytosis, cells can use filopodia to bind to target particles and pull them towards the cell, where they then are engulfed [61,62].

Actin dynamics also play a critical role for endocytosis, the process in which cells internalize extracellular material. Especially during the phagocytic uptake, the actin network is the main force-generator driving the membrane around the target. This is facilitated by actin-binding motor proteins such as myosin [63]. This way, the phagocytic cup is completed, and actin-binding proteins such as dynamin can promote the vesicle scission [64]. Since the actin dynamics are such a critical part of many cellular processes, many signaling molecules can influence the actin cytoskeleton. The individual steps of phagocytosis are covered in chapter 1.3. More information on how the different signaling molecules interact during phagocytosis is provided in chapter 2.1.

1.2.4 Cellular Adhesion

Cellular adhesion enables cells to stick to each other or to the extracellular matrix surrounding them. It is a fundamental process that is important for a wide range of cellular functions, including tissue development, wound healing, immune response, and cancer metastasis [65]. Cellular adhesion involves various types of molecular interactions, including non-specific electrostatic forces, hydrophobic interactions, and specific protein-protein interactions. The specific protein-protein interactions involved in cellular adhesion are often mediated by adhesion molecules, which are proteins that are expressed on the surface of cells and interact with corresponding adhesion molecules on other cells or in the extracellular matrix.

Adhesion molecules can be classified into several families based on their structure and function. One of the most well-known families of adhesion molecules is the integrin family, which are transmembrane receptors that mediate the attachment of cells to the extracellular

matrix^[66]. Integrins can also interact with other signaling molecules, such as growth factors, to regulate various cellular processes. Another family of adhesion molecules is the cadherin family^[67], which are calcium-dependent transmembrane proteins that mediate the attachment of cells to other cells. Cadherins are important for maintaining tissue integrity and mediating cell-cell communication during tissue development homeostasis. In addition to integrins and cadherins, there are many other molecules that contribute to cellular adhesion, including selectins, proteoglycans, and members of the immunoglobulin superfamily^[68]. One specific member of the immunoglobulin superfamily proteins, the Fc receptors, will be covered in great detail in this thesis, as they play a key role in the signaling cascade which initiates phagocytosis.

Adhesion molecules, especially integrins, can cluster and form focal adhesions^[43]. Integrins can bind to specific molecules like collagen or glycoproteins such as fibronectin, vitronectin or laminin in the extracellular matrix using their extracellular domain. The cytoplasmic sides of the integrins are linked to the actin cortex via adaptor proteins like talin, actinin, filamin or vinculin^[43]. The focal adhesions anchor the cell inside it's surrounding, giving it stability and allowing for the transmission of mechanical signals and forces between the cell and its extracellular environment. In cells growing on glass coverslips coated with fibronectin, the cell membrane focal adhesions onto the coverslip can easily be studied by super-resolution microscopy or total internal reflections fluorescence microscopy (TIRF)^[69].

1.2.5 Receptors

One special family of adhesion proteins embedded in the lipid bilayer are receptors, which enable cells to probe their environment. Receptor proteins, together with many other special membrane proteins like ion channels, proton pumps or glycoproteins, can make up around half of the membrane's mass^[70]. Membrane receptors are proteins capable of binding to very specific molecules in the cell's surroundings, such as hormones, inflammatory markers or antibodies. Using receptors, the cell can sense a change in these molecules' concentrations and react accordingly. A famous example for a receptor-mediated process is the chemotaxis of *E. Coli* bacteria, which are constantly swimming around and use a feedback loop to guide themselves towards areas with higher food concentration^[71]. Although this mechanism is relatively simple, it already involves a whole family of membrane receptors, known as the methyl-accepting chemotaxis proteins.

In eukaryotic cells, the number of different membrane receptors is multitudinous. A well-known class of receptors is the Fc γ receptors, which are found on many immune cells, such as macrophages, neutrophils or large granular lymphocytes. Because these receptors bind specifically to the Fc region of IgG antibodies outside the cell, they play a crucial role in the immune system's ability to recognize and eliminate pathogens. There are multiple subclasses of Fc γ receptors, differing in the number of binding sites and the affinity to bind to different subclasses of IgG antibodies. Also, the exact number of different receptors present depends on the species, for example murine cells only contain five subclasses of receptors while human cells contain seven different types^[72,73].

When Fc γ receptors are engaged, for example by an encounter with a particle covered with IgG antibodies, phagocytosis can be triggered and the particle will be engulfed by the cell^[74]. This process and the signaling involved will be the main topic of this thesis. A further introduction to the process follows in chapter 1.3.3.

1.3 Phagocytosis

1.3.1 Definition of phagocytosis

Multiple mechanisms which enable cells to take up liquid or particles out of their surrounding via engulfment of the plasma membrane are consolidated under the name endocytosis^[70]. In this thesis we will focus on phagocytosis, which is defined as the uptake of particles larger than 500 nm^[75,76,77]. This lower size limit seems to originate from early observations which revealed that polystyrene particles smaller than 500 nm will not directly be taken up by phagocytosis, but rather cluster on the cell surface and later be taken up together in larger phagosomes^[78]. Based on this definition, phagocytosis plays an important role in the degradation of pathogens, which are typically a few micrometers in size. The process of phagocytosis is depicted in Figure 1.2. After the target particle has firmly bound a cell, the receptors on the cell's surface get activated. A signal is then passed down into the cell and a complex cascade of signaling molecules causes the cell membrane to be pushed around the particle until it is completely engulfed into the cell.

1.3.2 Relevance of phagocytosis for the immune response in mammals

The mammalian immune system is a complex network of specialized cells, tissues, and organs that work together to protect the body from foreign invaders, such as bacteria, viruses, and other pathogens. There are two main branches of the immune system: the innate immune system and the adaptive immune system. Phagocytosis is relevant to both of those branches^[79,80].

The innate immune consists of physical barriers, such as the skin and mucous membranes, as well as specialized cells, including macrophages, dendritic cells, natural killer cells, and granulocytes. These cells are capable of recognizing and responding to a wide range of pathogen-associated molecular patterns through specialized receptors, such as Toll-like receptors, scavenger receptors or Fc γ -receptors^[81,79]. When a pathogen is detected, innate immune cells like macrophages release inflammatory mediators and chemokines that recruit additional immune cells to the site of infection^[82]. These cell then can engulf and destroy the pathogens via phagocytosis. Inside the macrophage, after phagocytosis, the pathogen will get broken down and some antigens originating from this specific pathogen can be presented on the macrophage's surface via MHC complexes^[83]. These antigens than get recognized by B or T cells, initiating the adaptive immune system. While T cells can differentiate into different subsets with specialized functions, B cells will produce antibodies adopted to the specific pathogen.

During a infection, B lymphocytes inside our blood start secreting antibodies specific to the pathogenic virus or bacteria only days after the infection. The most abundant antibody class are immunoglobulin G (IgG) antibodies, making up up to 20% of the total protein in human blood serum^[84]. Each IgG antibody can specifically bind to a certain pathogenic antigen using its two antigen binding sites in its Fab-region. The antibodies counteract infections by covering the pathogen's surface or by causing agglutination. In this process, pathogens and antibodies form immune complexes, binding free pathogenic material and preparing it to be removed by specialized immune cells^[85].

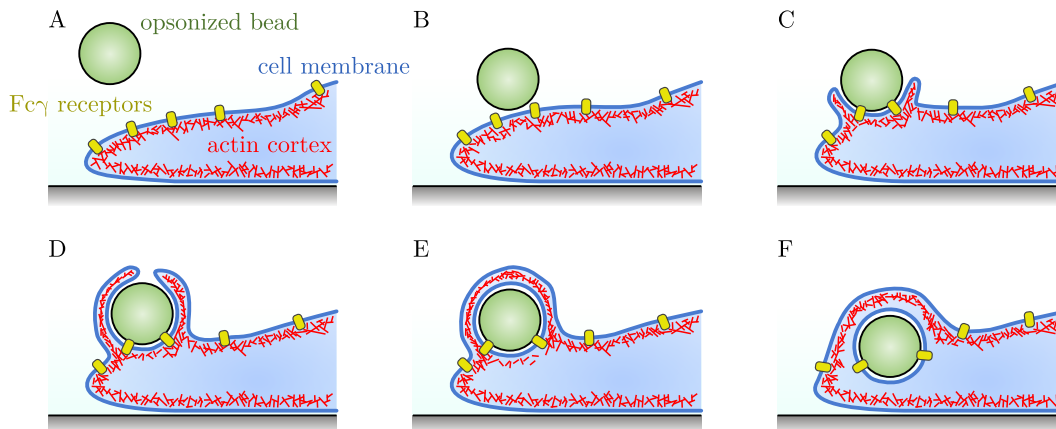


Figure 1.2: Steps during the phagocytic cup formation. As an opsonized bead binds to a macrophage (panels A and B), the antibodies on the bead come into contact with $Fc\gamma$ receptors in the cell membrane. Those initiate the process of phagocytosis via a complex signaling cascade, resulting in the formation of the phagocytic cup (panels C and D). When the particle is completely engulfed, the membrane of the phagosome separates from the cell membrane, passes the actin cortex and forms a phagosome (panel E and D).

1.3.3 Initiation of phagocytosis

Upon interaction with an opsonized particle, a series of events unfolds within the cell. To begin with, numerous receptors bind to the antibodies coating the target particle. The most well studied receptors are the $Fc\gamma$ receptors, which will be studied in great detail in this thesis. The binding to these receptors triggers a complex signaling cascade that leads to the formation of a cup-shaped membrane structure called the phagocytic cup.

Several signaling pathways can contribute to the initiation of phagocytosis. The most relevant is the Fc receptor signaling pathway, in which Fc receptors bind to the Fc region of antibodies and can hand over the signal to various intracellular signaling pathways, via signal transducer enzymes such as phosphoinositide 3-kinases (PI3K) and small GTPases. However, PI3K can also be activated via the activation of Toll-like receptors, which also recognize pathogen-associated molecular patterns (PAMPs)^[86]. In phagocytes, the initial stimulus can lead to the activation of the spleen tyrosine kinase (Syk) pathway, which is important for receptor-mediated phagocytosis as it triggers downstream signaling events that lead to actin polymerization, membrane rearrangement, and the formation of the phagocytic cup. The activation of these signaling pathways leads to the formation of actin-rich membrane protrusions and the recruitment of intracellular effectors that facilitate the engulfment and processing of the particle by the phagocyte. Myosin motor proteins are recruited to the site of particle binding, where they contribute to create the necessary forces^[63].

The engulfment process involves the coordinated action of several signaling pathways, including those mediated by Rho family GTPases, phosphoinositide 3-kinase (PI3K), and protein kinase C (PKC), which regulate actin polymerization, membrane dynamics, and vesicle trafficking. For example, small GTPases such as Rac and Cdc42 are important regulators of actin polymerization and cytoskeletal rearrangements during phagocytosis^[87].

Several key proteins are involved in the formation of the phagocytic cup, including the transmembrane $Fc\gamma$ receptors, which recognize IgG-coated particles and activate downstream

signaling cascades. These signaling cascades include the tyrosine kinase Syk, the adaptor protein Grb2, which links receptor signaling to downstream Rho GTPase activation, and the Wiskott-Aldrich syndrome protein (WASp), which is an important regulator of actin polymerization during phagocytosis^[88,48,89].

The formation of the phagocytic cup is also influenced by mechanical factors, such as the physical properties of the particle and the mechanical properties of the cell membrane. For example, the stiffness of the particle can affect the kinetics of phagocytosis, with more rigid particles requiring more force to be engulfed. Additionally, the mechanical properties of the cell membrane, such as its elasticity and tension, can also influence phagocytosis by affecting the curvature of the phagocytic cup and the stability of the phagosome^[90].

After the formation of the phagocytic cup, the cup must constrict and eventually close around the particle to form the phagosome. This process is aided by myosin motors moving along the actin filaments and generating contractile forces, which contribute to the cup's constriction^[91]. The process of separating the phagosome from the cell membrane is facilitated by a protein called Dynamin^[92]. Cup constriction and closure involves the coordinated actions of actin, myosin, and other cytoskeletal proteins.

Once the phagosome has formed, it is transported along microtubules to the perinuclear region for degradation^[93]. The phagosome's maturation involves a series of fusion events with different intracellular compartments, such as lysosomes, which contribute to the degradation of the ingested particle^[10].

1.4 Thesis roadmap

While a lot is already known about the molecular components involved in phagocytosis, the knowledge about the localization and the mechanical principles involved were studied to a far lesser extend. Often, the signaling cascades are described like linear paths, that once engaged follow a precise pattern to activate phagocytosis. However, it is already known that the process of phagocytosis can be influenced by mechanical aspects, such as the target's size, shape^[94,95] or their surface charge or chemical composition^[96]. It is still unknown how exactly these circumstances can interact with the signaling cascades and influence the outcome of phagocytosis. It is very likely that signals involved in phagocytosis are not purely biochemical, as signals can also be conducted via mechanical stimuli such as stress, pressure or membrane curvature. This thesis aims to explore the signaling pathways involved in phagocytosis, especially the Fc γ pathway, its spatial organization, and how it interfaces with the mechanical machinery of phagocytosis.

To provide a full picture, this thesis approaches the process of phagocytosis from two directions. The first project, described in chapter 2, aimed to characterize the spatial resolution of the signaling cascade controlling Fc γ -mediated phagocytosis. For this chapter, experiments with two opsonized beads, brought into contact with a macrophage simultaneously, were performed for varying bead sizes and attachment distances. Section 2.1 outlines the motivation behind these experiments. Briefly speaking, the outcome of the experiments depends on different biophysical parameters, such as particle attachment distance, particle size or receptor density, which is why a lot could be learned from this experiments. In the extensive methodical section 2.2, the holographical optical tweezers setup, on which most experiment during this thesis were performed, is introduced, as well as the methodical basics of cell culture, RNA interference, optical trapping, hologram generation, and particle tracking.

After that, the results of the dual-bead experiments are presented in section 2.3. The experiments were classified as joint and separate uptake depending on the evaluation of the particle distance after the uptake. A mathematical model was developed, describing the connection between biological parameter like the mean receptor distance or the length scale of phagocytic signaling and the experimental separate uptake probability. This model was fitted on experimental data, and verified using additional measurements. In section 2.4, the implications of our results and the phagocytic uptake model are discussed with regards to already established knowledge on phagocytosis. Finally, section 2.5 provides a summary of the findings of the dual-bead project.

In the subsequent chapter 3, the focus shifts towards the mechanical aspect of phagocytosis. Using blinking optical tweezers, a periodic optical force was created on the target particle. Analyzing the cell's viscoelastic response to this force allows provides insights on the cup formation and the mechanical properties of the cell during phagocytosis. Simultaneously, the distribution of filamentous actin inside the cell was recorded using fluorescence microscopy. Even though the same optical setup was used, section 3.2 provides additional methodical knowledge required only for this chapter. This includes the calibration of the optical tweezers, the theory of microrheology, and a comprehensive explanation on the experimental details of the rheological measurements. This section also introduces the viscoelastic model used to model the stress-strain relationship of the macrophages, and provides a simulation of the expected particle trajectories during the rheological measurements. The results of this chapter are shown in section 3.3. Here, an localized increase in the concentration of filamentous actin around the particle is described, which marks the moment of the phagocytic uptake. This chapter also explains how the rheological evaluation was carried out, providing insight into the binding kinematics of the cell-particle interaction. The measurements also revealed that the observed actin flashes are often accompanied by an increase in the bead's mobility. Those results are elaborated further in section 3.4, where it is shown that this increased mobility can be explained by the detachment of the phagosome from the actin cortex once the bead has been fully engulfed. Section 3.5 provides a summary of the chapter.

Finally, chapter 4 reflects on the thesis, consolidating the results and contemplating potential future projects.

2 Measuring the spatial resolution limit of phagocytosis

This chapter focuses on experiments in which two opsonized beads were attached to macrophages in order to gain information on the underlying signaling cascades. Partly, the results and the methods used during this project were already published as a research article in the Biophysical Journal^[97]. This chapter recapitulates the key findings of this paper. It also grants deeper insight into the spatial resolution limit of phagocytosis and the underlying measurement techniques by showing additional data not published previously.

2.1 Motivation

Humans acquire information about their environment through diverse sensory organs, the largest of which is the skin^[98]. To fulfill its sensory functions, the skin is packed with various sensory cells, each with a specific role to play in our perception of the world around us^[99]. Particularly important for tactile sensation are the pressure-sensitive Merkel cells, which can reach densities of around $10,000 \text{ cm}^{-2}$ in the fingertips. The signals originating from these cells are processed and relayed by the nervous system, particularly the slowly adapting type I fibers. In the fingertips, about 70 such fibers can be found per square centimeter^[99]. It is this density of neural connections that limits the spatial resolution of haptic stimuli sensed by the skin. When stimuli are positioned closer than 5 millimeters at the fingertips, the discrimination of two separate stimuli becomes challenging, often leading to misjudgment as a single stimulus. In regions with less densely packed innervation, this threshold is substantially larger, stretching to around 10 millimeters for the palm or even beyond for the forearm.

Physicians test the skin's capability to differentiate between two distinct yet closely positioned tactile stimuli during a neurological examination^[100], which provides useful information on how finely innervated the skin is and how dense the sensory cells are spaced at the probed location. While it was recently suggested that letting patients discriminate between differently oriented patterns may be a superior diagnostic method^[101], two-point discrimination remains a reliable tool, providing information on how finely innervated the skin is and how dense the sensory cells are spaced at the probed location.

Similar to the skin^[102], the cell membrane fulfills a multitude of functions. It serves as a physical divider between the inside and outside of the cell, and as a regulator for the exchange of substances and information, enabling the cell to engage with its surroundings^[22]. To do so, the cell membrane houses a multitude of different membrane receptors. These receptors empower the cell to perceive a range of stimuli, such as the concentrations of various molecules in its environment.

Presently, more than a thousand different types of membrane receptors are known^[103,14], all playing a crucial role in sensing biochemical or physical cues. A well-examined instance of such a receptor is the $\text{Fc}\gamma$ receptor^[104]. This membrane-bound receptor is found on professional phagocytes such as macrophages, where its activation occurs upon contact with

an opsonized particle that exposes immunoglobulin G (IgG) to the cell surface^[105,106]. IgG antibodies possess two antigen-binding sites, called Fab regions, which bind to antigens specific to pathogens like bacteria, fungi, or viruses. Meanwhile, the single Fc region of IgG binds to the Fc γ receptors on the cell, setting off a signaling cascade through the cell membrane. This renders the Fc γ receptor vital for the ability of immune cells to recognize and engulf pathogens and debris.

Activated Fc γ receptors tend to form clusters at the stimulus site, bringing the intracellular domains of the receptors into close proximity^[107]. Most Fc γ receptors possess an immunoreceptor tyrosine-based activation motif (ITAM)^[82] on their cytoplasmic side, as depicted in Figure 2.1. When multiple ITAMs come into close contact, SRC-family kinases like Hck, Lyn, or Fgr^[108,87,109] become activated and phosphorylate the tyrosine residue within the ITAMs. Further, tyrosine kinases like Syk or ZAP-70 attach to these phosphorylated ITAMs via their SH2 domains, triggering the phosphorylation of additional ITAMs surrounding the receptor cluster^[110,111]. Once phosphorylated, different adaptor proteins connect with the receptors and transmit the signal to lipid-modifying enzymes and small GTPases. The lipid-modifying enzymes like phosphoinositide 3-kinases^[112] directly impact the properties of the cell membrane, while GTPases engage nucleation-promoting factors like SCAR/WAVE or WASP, prompting the assembly of filamentous actin by activating the Arp2/3-complex^[48]. A schematic of this signaling process can be found in Figure 2.1. Finally, the actin polymerization propels the membrane around the target particle, which leads to the particle's engulfment^[113,114,115]. The phagosome is subsequently pinched off from the plasma membrane, an action controlled by the GTPase dynamin^[64], which marks the end of the uptake process.

As the signal progresses through this cascade, the involved signaling molecules can diffuse, propagating the signal spatially inside the cell. The range to which the signal spreads is important, as it may influence in which area the actin polymerization is triggered, or where lipid-modifying enzymes and small GTPases are activated. Thus, the signaling range plays a major role during the formation of the phagosome. While extensive efforts have been invested in uncovering the molecular constituents of this signaling network^[116,117,75], the quantitative spatial and temporal parameters of the signaling remain relatively unexplored. Crucially, the extent to which this phagocytic signal spreads within the cell remains unknown. This spatial propagation likely correlates with the spatial resolution limit of phagocytosis, determining the conditions under which a macrophage perceives two bacteria as distinct entities. Understanding this cellular resolution limit holds the potential to foster a more comprehensive and quantitative grasp of cellular information processing.

Here, we probed the resolution limit of phagocytosis by simultaneously bringing two IgG-coated particles into contact with the cell and observing whether both beads will be taken up in one joint phagosome or not. To ensure a precisely defined gap between the particles, holographic optical tweezers^[118,119,120] were used during the attachment process. Following this, the cell could internalize the particles either into a single unified phagosome or into distinct phagosomes (panels A-B in Figure 2.2). It also was possible that the cell did not take up one or both phagosomes during the observation period (panels C-D in Figure 2.2). Our hypothesis stated that the likelihood of the joint uptake scenario depends on the particle distance and the length scale of cellular signaling. If the particle distance is small compared to the signaling length scale, joint uptake will be likely. Additionally, we assume that receptor density on the membrane and particle size factor into this equation. For example, a low receptor density might make the single uptake and no uptake scenarios more

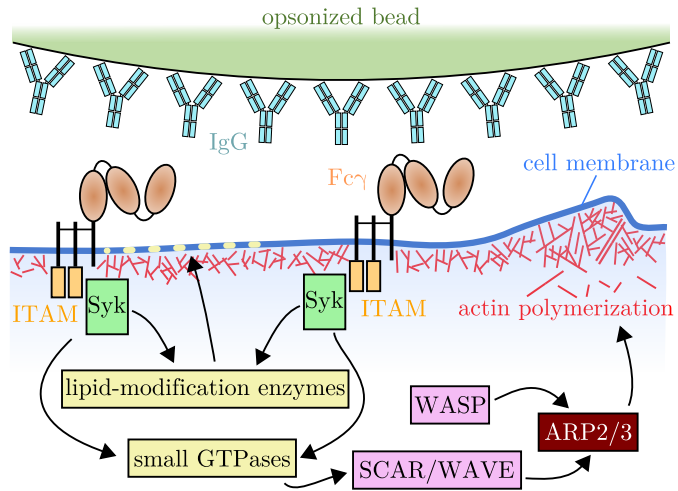


Figure 2.1: Schematic of the phagocytic signaling process and the involved key proteins. After the ligand IgG binds to a $Fc\gamma$ receptor, the immunoreceptor tyrosine-based activation motif (ITAM) on the cytoplasmic side of the receptor phosphorylates. As a result, tyrosine kinases like Syk inside the cell bind to the receptor and activate enzymes further down the signaling cascade (yellow) like lipid-modification enzymes and small GTPases (for example Rac). This leads to an increase in nucleation-promoting factors (purple) which activate the ARP2/3 complex. This finally enhances actin polymerization and thus the formation of the phagocytic cup.

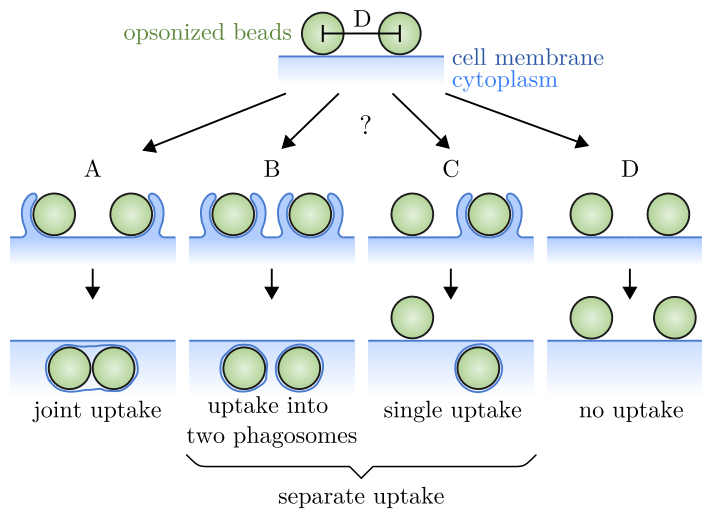


Figure 2.2: Different uptake scenarios after attachment of a bead pair. After two beads are attached to a macrophage at a certain distance D , four different uptake scenarios are possible. The beads can be taken up into a joint phagosome (A) or into two separate phagosomes (B). Another scenario entails the uptake of a single bead by the cell, while the second bead remains on the cell surface, referred to as single uptake (C). The other outcome is the absence of bead uptake altogether, termed no uptake (D). Both scenario B and C are considered separate uptake during this thesis. We hypothesize that the probability of each event depends on the length scale of the cellular signaling, the receptor density, the particle distance D and the size of the particles.

2 Measuring the spatial resolution limit of phagocytosis

likely. Systematically varying particle distance, particle size, and employing cells with reduced $Fc\gamma$ receptor expression enabled us to test these assumptions rigorously. This methodical approach empowered us to quantify the length scale characterizing phagocytic signaling and thus the resolution limit of receptor-mediated phagocytosis.

2.2 Methods and Materials

2.2.1 Cell culture

All cells used during this research were J774A.1 mouse macrophages. These cells originate from a reticulum cell sarcoma of a female BALB/cN laboratory mouse in the year 1968^[121]. This cell line has been chosen because, as a macrophage, it actively engages antibody-mediated phagocytosis and thus is perfectly suited as a model organism for phagocytosis in general. The cells were bought from the Leibniz Institute DSMZ located in Braunschweig, Germany in 2016. Upon receiving the cells, cell culture was immediately started to multiply the number of cells, then the cells were collected, aliquoted and stored cryogenically.

To begin a new cell culture, a single aliquot can be thawed and then be used to seed a new cell culture flask. In line with the datasheet^[122], the J774A.1 mouse macrophages were cultured in a medium consisting of 90% Dulbeccos's Minimal Eagle's Medium (DMEM, Gibco, Carlsbad, USA) with phenol red and 10% of fetal bovine serum (Gibco, Carlsbad, USA) in vented polystyrene cell culture flasks with a surface area of 25 cm² (BioLite, Thermo Fisher Scientific, Darmstadt, Germany). We noticed that when splitting the cells only two times a week, as recommended in the datasheet, the cell culture will exceed 100% confluence and a lot of the cells will detach from the culture flask due to limited space. As splitting should be done prior to reaching confluence, we choose to split our cells three times a week, usually on Monday, Wednesday and Friday. For splitting, the cell culture medium from the flask was removed and substituted with 5 ml of fresh medium at 37 °C. The removed medium can be frozen and used later to test the culture for infection with mycoplasma, which was done regularly. The cells then were detached from the bottom of the culture flask using a plastic cell scraper. To obtain the optimal splitting ratio, we used a haemocytometer to determine the cell concentration in the resulting suspension, which usually was around 10⁶ cells/ml. A new culture flask was labeled and prepared by adding 10 ml of fresh, warm medium. Then, depending on the result of the cell counting, 0.2 – 2 ml of the cell suspension in the old flask was transferred to the new culture, so that the new culture flask contained $5 \cdot 10^5$ cells. Since the flask have a total surface area of 25 cm², this resulted in an initial cell density of 200 cells/mm², which is in line with the suggestion in the datasheet to seed the cells at a density of 125 – 250 cells/mm². Usually a splitting ratio of 1:5 to 1:10 was necessary to achieve this density. After that, the new culture flask was stored in an incubator at standard conditions (5% CO₂, 100% humidity). The cell suspension in the old flask was used to prepare samples as required.

The doubling time of the cells is specified as 35 hours in the datasheet. If the cells would multiply a constant rate, this should result in a 28-fold increase in cell number per week. Following this, the number of cells should be kept constant by splitting the cells three times per week in the ratio of only 1:3, which in our case was not enough to keep the cell count constant. It is plausible that the doubling time in optimal conditions is much smaller than 35 h, but the effect is counteracted by the cells growing slower in the hours after splitting the cell culture. Additionally, if the cells are allowed to reach confluence or the cells are seeded at very low densities, the doubling time can also increase. To keep our cells at optimal health, we avoided both scenarios and kept them at medium densities where the growth rate is optimal. When the passage number approached 30, a new batch of cells was thawed and cultured parallel until for approximately one week. At this point, the new culture usually has established a stable population and the old culture can be discarded.

A line of stably LifeAct-GFP-transfected J774 macrophages was provided by Alexander Rohrbach and Rebecca Michiels^[123] (University of Freiburg, Germany). These cells were cultured parallel in a second cell culture flask in the same way as the regular J774A.1 mouse macrophages. Since a puromycin resistance gene was used as a selection marker during the transfection, it would be possible to apply evolutionary pressure by adding puromycin to the cell culture medium. Since the LifeAct cells imaged during this thesis showed a clear fluorescent signal without adding puromycin, the addition has been omitted. These cells express the relatively small fusion protein LifeAct-GFP, which is a combination of the F-actin binding peptide LifeAct^[124] and the fluorescent protein GFP. Because of the F-actin binding capacity of the LifeAct peptide, the GFP colocalizes with the filamentous actin and allows imaging of actin dynamics by fluorescence microscopy (see chapter 2.2.5.4) in living cells. In comparison with other established methods of visualizing actin, such as staining the sample using labeled phalloidin, this method enables imaging in living cells because of its relatively low toxicity^[125]. While the original authors did not find any interference of the small protein LifeAct-GFP with cellular processes such as neuronal polarization, lamellopodial flow or leukocyte chemotaxis^[124], it has been observed more recently that high concentration of LifeAct can influence the formation of actin filaments^[125]. In our experiments the LifeAct transfected cells showed a slightly more rounded up shape in the cell culture flask compared to the traditional J774A.1 in culture. When transferred to glass coverslips, the LifeAct-GFP transfected cells spread out over the course of 24 – 48 hours and then match the phenotype of the non transfected J774A.1 macrophages.

2.2.2 RNA interference and Western Blotting

In this chapter, experiments were done on J774A.1 mouse macrophages to investigate the signal processing during phagocytosis. It is highly beneficial repeat these experiments on cells with a different densities of phagocytic receptors, as the results may provide a deeper insight on how the receptor density influences the spatial resolution of the phagocytic receptor network.

To achieve this, a mechanism known as RNA interference was used. RNA interference is a natural process occurring in all eucaryotic life forms^[126], in which small, RNA molecules inhibit the expression of specific genes. Central to this process are microRNA and small interfering RNA (siRNA), which both are formed as longer strands of double-stranded RNA is cut into short segments by ribonuclease enzymes such as Dicer or Drosha^[127]. These RNA strands can bind to specific target mRNA molecules. Once bound, they can inhibit their translation and promote their degradation^[127]. Due to the lower number of this specific mRNA in the cytosol, the corresponding protein can only be produced in a reduced number or not at all. Today, siRNAs targeting a multitude of different genes are available commercially, which can be used to downregulate the expression of specific genes. Recently, even the first commercial pharmaceuticals based on siRNA became available^[128]. In this thesis, the RNA interference was used to reduce the number of Fc receptors in J774A.1 mouse macrophages. For this application, siRNA targeting the FcγR1 gene, encoding the murine FcγR1 receptor, was purchased (sense sequence `GGAAUAAUGUUUCGUUGAtt`, Ambion SilencerSelect FcγR1, #4390771, Thermo Fisher Scientific). This receptor is also known as the CD64 antigen. Additionally, a negative control siRNA was acquired (Invitrogen Silencer Select Negative Control No. 2, #4390846, Thermo Fisher Scientific).

To prepare samples, cells were seeded onto round 18 mm coverslips inside a 12-well plate

three days prior to the experiments. On the next day, the medium inside the wells was replaced with 1 ml of fresh cell culture medium per well. The siRNA was then brought into the cells via transfection, which was achieved using the commercial lipid-based transfection reagent Lipofectamine RNAiMAX (Invitrogen, Thermo Fisher Scientific). Following the manufacturer's recommendations, 3 μ l of transfection reagent (Lipofectamine RNAiMAX, Thermo Fisher Scientific) was diluted in 100 μ l of Opti-MEM medium (Gibco, Carlsbad, California) for each well. After that, the siRNA for each well was diluted in 100 μ l of Opti-MEM. During the dual-bead experiments, 10 pmol of siRNA was used per well, either targeting CD64 or non-targeting. The two solutions were mixed and incubated for 5 min at room temperature to form siRNA-lipid complexes. Then, 200 μ l of the solution was added to each well and the cells were placed back in the incubator. After 48 hours, the cells were washed and prepared for the cell experiments as described in chapter 2.2.4.

The effectiveness of the RNA interference was verified by Western Blotting. This method can directly verify that the amount of Fc γ R1 receptors decreases after the treatment with siRNA, proving that the production rate of new Fc γ R1 proteins drops drastically after the transfection. For that, three distinct samples of transfected cells were prepared. These cells were seeded directly into a 12-well plate with 1 ml cell culture medium. After one day, the medium was replaced, and the first sample was treated with 10 pmol siRNA targeting Fc γ RI as described above. The second sample was subjected to the same procedure, but using only 5 pmol of siRNA. For the final treatment, 10 pmol of non-targeting siRNA (Ambion SilencerSelect Negative Control #2, Thermo Fisher Scientific) was used. 48 hours after the transfection, the medium was replaced with 100 μ l of homogenization buffer and the cells were gently scraped from the well's bottom while being kept on ice. They were then homogenized by sonicating them 3 \times for 10 s on ice. Subsequently, 20 μ l of 6 \times Laemmli buffer (375 mM Tris-HCl pH 6.8, 12% w/v sodium dodecyl sulfate, 60% v/v glycerol, 15% v/v 2-mercaptoethanol, 0.075% w/v bromophenol blue, in water) was added, the lysate was heated to 60 $^{\circ}$ C for 10 minutes, and finally stored it at -20 $^{\circ}$ C. The homogenization buffer was freshly prepared before use. This involved dissolving 4.9 mg of dithiothreitol (DTT) in 30 μ l of motility assay buffer (MAB). The MAB consisted of 10 mM piperazine-N,N'-bis(2-ethanesulfonic acid), also known as PIPES, 50 mM K-Acetate, 4 mM MgCl₂, 1 mM egtazic acid (EGTA), and 1% Triton-X dissolved in water (pH 7.0). Additionally, 30 μ l of a 1 mM solution of adenosine triphosphate (ATP) in MAB was prepared. Next, 30 μ l of protease inhibitor solution (1 mM phenylmethylsulfonyl fluoride, 105 μ M leupeptin, 0.75 μ M pepstatin-A, 26.4 μ M N-p-Tosyl-L-arginine methyl ester, in MAB) was mixed. Similarly, a sucrose solution was created adding MAB to 42 g of sucrose until a total volume of 50 ml was reached. The homogenization buffer was then created by mixing 2.6 ml of MAB, 0.3 ml of sucrose solution, 30 μ l of ATP solution, 30 μ l of DTT solution and 30 μ l of protease inhibitor solution in this order. Throughout this process, all liquids were kept cool on ice to prevent premature degradation.

For the blotting process, the lysates were thawed and briefly heated to 95 $^{\circ}$ C. A precast SDS-PAGE gel (10% Mini-PROTEAN[®] TGX[™] Precast Protein Gels, BioRad Laboratories Inc., Hercules, California) was placed into the electrophoresis cell (Mini-PROTEAN Tetra cell, BioRad Laboratories Inc.) and filled with buffer (0.29% w/v Tris, 1.44% w/v Glycine, 0.1% SDS w/v in Milli-Q water). The lysates underwent centrifugation at $17 \cdot 10^3$ g for 30 s to remove debris. For each lysate, two pockets of the gel were filled, one with 25 μ l and another with only 5 μ l of lysate on opposing sides of the blotting gel. An extra pocket in the middle was filled with 5 μ l of a protein ladder (Page Ruler Plus Prestained Protein

Ladder #26619, Thermo Fisher Scientific). The electrophoresis was initiated with 80 V for 15 minutes, followed by 120 V for about one hour until the protein ladder was spread out over the whole gel. Subsequently, a nitrocellulose membrane (0.45 μm Amersham Protran Nitrocellulose Blotting Membrane, GE Healthcare Life Science, Chicago, Illinois), filter paper, and sponges were soaked in transfer buffer (0.29% w/v Tris, 1.45% w/v Glycine, 20% v/v methanol in Milli-Q water). The blot was assembled and immersed in the electrophoresis cell filled with transfer buffer. The blot ran at 100 mA overnight at room temperature.

After blotting, the membrane was washed in PBS and stained using a Ponceau S solution (0.25% Ponceau S in 40 ml methanol, 15 ml acetic acid, 45 ml water) to confirm the successful transfer of the protein to the membrane. The dye was then removed by washing with Milli-Q water. To prevent non-specific binding, the membrane was incubated in PBS-T (PBS with 0.1% Tween-20) with 5% w/v non-fat milk powder for an hour.

The membrane was cut in half at the marker, resulting in two sections, each containing three lanes with the distinct treatments and part of the marker lane. Each half was individually incubated for an hour with different primary antibodies. These antibodies, specifically CD64 Recombinant Rabbit Monoclonal Antibody (Invitrogen MA5-29706, Thermo Fisher Scientific) and α -Tubulin DM1A mouse mAb (#3873S, Cell Signaling Technology, Danvers, Massachusetts), were used diluted 1:1000 in PBS-T with 5% w/v milk powder. The part of the membrane incubated with the CD64 antibody corresponded to the half of the gel to which 25 μl of lysate was added while the half to which only 5 μl of lysate was added was incubated with the tubulin antibody. This was done because the concentration of CD64 in the lysate is expected to be much lower than the concentration of tubulin. The membrane was then washed three times for 15 minutes each in PBS-T. Corresponding secondary antibodies, Goat Anti-Rabbit IgG (H+L)-HRP conjugate #1706515 and Immun-Star Goat Anti-Mouse (GAM)-HRP Conjugate #1705047 (BioRad Laboratories Inc.), were diluted 1:3000 in PBS-T with 5% w/v milk powder, and they were incubated with the respective membrane pieces for an hour at room temperature. Finally, the membrane pieces were washed thrice in PBS-T and thrice in PBS. The membrane was then transferred to a transparent plastic bag. 400 μl of chemiluminescence substrate (Clarity ECL Western Blot Substrate, BioRad Laboratories Inc.) was prepared and evenly applied to the nitrocellulose membrane. The chemiluminescence signal was recorded using a biomolecular imager (ImageQuant LAS 4000, GE Healthcare).

2.2.3 Preparation of the microparticles

Microparticles of the diameters 1 μm , 2 μm and 3 μm were purchased from micromod Partikeltechnologie GmbH, Rostock, Germany. (micromerTM COOH, product numbers #01-02-103, #01-02-203 and #01-02-303). These particles are made of polystyrene and are functionalized to have carboxylated surfaces. To be used in the experiments, the beads were opsonized using a passive adsorption protocol as previously described^[93]. The beads are provided by the manufacturer in a suspension containing 50 mg/ml of beads. To start the opsonization, 100 μl of the bead suspension was transferred into a 1.5 ml Eppendorf tube and filled with 900 μl of MES buffer. The sample tube was vortexed and then centrifuged at 2000 g for 20 minutes. After that, 950 μl of the supernatant was removed and replaced with fresh MES buffer. The washing step consisting of centrifuging and replacing the buffer was then repeated one additional time, but this time only 950 μl of fresh MES buffer was added. The IgG antibody was added in the form of a IgG solution from mouse serum (Merck Millipore, Darmstadt, Germany) with a concentration of 24 mg/ml. The quantity of the solution to add was chosen

to so that the IgG would cover the surface of all polystyrene beads approximately two times. This estimation is based on a molecular weight of $m_{\text{IgG}} = 150 \text{ kDa}$ ^[84] and the stokes radius $r_{\text{IgG}} = 6.4 \text{ nm}$ ^[129]. Using this logic, 4.4 μl , 2.2 μl , and 1.5 μl of 24 mg/ml IgG solution were added for the 1 μm , 2 μm and 3 μm -sized beads, respectively.

The suspension was incubated overnight in darkness while slightly agitated on the roller mixer. After 12 hours, the suspension was centrifuged as before, then 950 μl of the liquid was discarded and replaced by 950 μl of phosphate buffered saline (PBS, Gibco, Carlsbad, USA). The solution was centrifuged again and 950 μl of liquid was replaced with fresh PBS. The mixture was centrifuged one final time, and 950 μl of liquid was discarded. Then, only 930 μl PBS was added and topped of with 20 μl of a previously prepared solution of 50 mg/ml glycine in PBS, which resulted in a final concentration of 1 mg/ml glycine in the bead suspension. The glycine was added to block for any unspecific binding sites on the container's walls to which the IgG could adhere. The final product was transferred to a dark 1.2 ml glass vial and labeled "bead storage solution".

The effectiveness of this opsonization protocol was verified using a fluorescent secondary goat-anti-mouse antibody. This verification was described previously by Berghoff^[130] and Keller^[131]. Briefly, a sample of the opsonized beads was incubated with a secondary fluorescent goat anti-mouse IgG antibody which binds to the primary IgG antibodies. Then a batch of these stained beads was examined using a fluorescence microscope. A negative control using non-opsonized beads stained with the same secondary antibody resulted in a much dimmer fluorescence signal compared to the particles coated with IgG, indicating that the primary IgG adheres well to the microparticles even after several washing steps. It should be noted that W. Groß raised concerns that the opsonization produced by this protocol might not be uniform^[132].

2.2.4 Sample mounting

Microscopic samples were prepared at the time of cell culture by placing round glass coverslips with a diameter of 18 mm and a thickness of 170 μm (grade #1.5) into a 12-well plate. After that, 1 ml of warm (37 °C) cell culture medium was added to each well containing a coverslip. The cells were seeded 24 – 48 hours prior to the experiments. For samples to be used after 24 h, we used $3 \cdot 10^4$ cells/well, if the samples were imaged after 48 h, we only used $2 \cdot 10^4$ cells/well. Since a single well has a surface area of 3.5 cm^2 , this resulted in densities of roughly 55 – 85 cells/ mm^2 , which then increased until the experiments were carried out because the cells continued to grow and divide. We noticed that when seeding the cells only 24 h before the experiments, more cells were rounded up compared to samples which have been incubated 48 h. This was especially true for the LifeAct transfected J774A.1 cells, which made us believe that it should be preferred to seed the cells two days prior to the experiments to give the cells enough time to start growing on the glass coverslips.

To hold the coverslip, a custom aluminum sample holder was used, which features a hole with a diameter of 11 mm and a groove on both side of this hole to fit the 13 mm-sized coverslips. At the day of the experiment, one such coverslip holder was prepared by applying a thin coat of silicon grease (Karasilon paste; Kurt Obermeier, Bad Berleburg, Germany) to the groove around the opening below which the coverslip will sit. A working suspension of microparticles was created by adding 1 μl of the bead storage solution as prepared in chapter 2.2.3 to 1 ml of Image Medium, which is a solution of minimal essential medium (Gibco) supplemented with 5% HEPES (Gibco) as a pH buffer.

The 12-well plate was then taken out of the incubator and one well was visually selected for the experiment using a small phase contrast microscope (Carl Zeiss). The cell culture medium from the selected well was removed and replaced it with image medium. The coverslip then was carefully taken out of the well plate using tweezers and placed directly onto the ring of silicon grease with the cells facing down. The coverslip was pressed down slightly using the tweezers to ensure a good seal, after which the aluminum holder was flipped. Then, 84 μl of the working suspension was pipetted onto the cells and another clean 18 mm coverslip was placed into the second groove of the coverslip holder now on top, where it was held in place by the surface tension of the medium. This created a sealed sample, preventing evaporation or contamination during the experiments.

After that, the bottom of the coverslips on which the cells grow was thoroughly cleaned using lint-free wipes soaked with 70% alcohol to remove cells or other residues which have adhered to the bottom of the coverslip during incubation. The sample than was transferred to the inverted microscope (Nikon Eclipse Ti-E, motorized) at the holographic optical tweezer setup where it was placed on a 60 \times water immersion objective. The top part of the microscope is enclosed in a custom heating chamber which was heated to 37 $^{\circ}\text{C}$ by blowing hot air into it. A overview image of the whole visible area of a coverslip prepared as described here, only without any microparticles, is printed in Figure 2.3. We observed that after 2 – 3 hours, the cells started to round up and showed a increasing number of vacuoles. This could have been caused by multiple reasons, such as metabolites building up or the lack of fetal bovine serum in the imaging medium. The metabolites might also have exhausted the image mediums pH buffering capacity at this point. Because of this, the samples were usually replaced after 1 hour of imaging during the scope of this thesis. If powerful brightfield or fluorescence illumination is used, the cells can be damaged by phototoxicity much earlier. Because of this, the illumination intensity was chosen to be as low as possible while still achieving a good image quality and the illumination shutters were always closed when the light was not needed.

2.2.5 Light microscopy

2.2.5.1 Microscopy setup

The setup used for the experiments in this thesis has been initially set up and described by K. Berghoff^[130]. The central component of the setup was a Nikon Eclipse Ti-E microscope placed on an optical table. The optical table rested on a set of active isolating legs using a pneumatic system to decouple the setup from any external vibrations. The microscope was fully motorized, including the microscope stage (Nikon), the objective revolver, the filter cube revolver, the focus, and the three shutters for brightfield and fluorescence illumination and the trapping laser. A set of four different objectives were available consisting of two dry phase-contrast objectives of 10 \times and 20 \times magnification and two water-immersion objectives featuring 40 \times and 60 \times magnification.

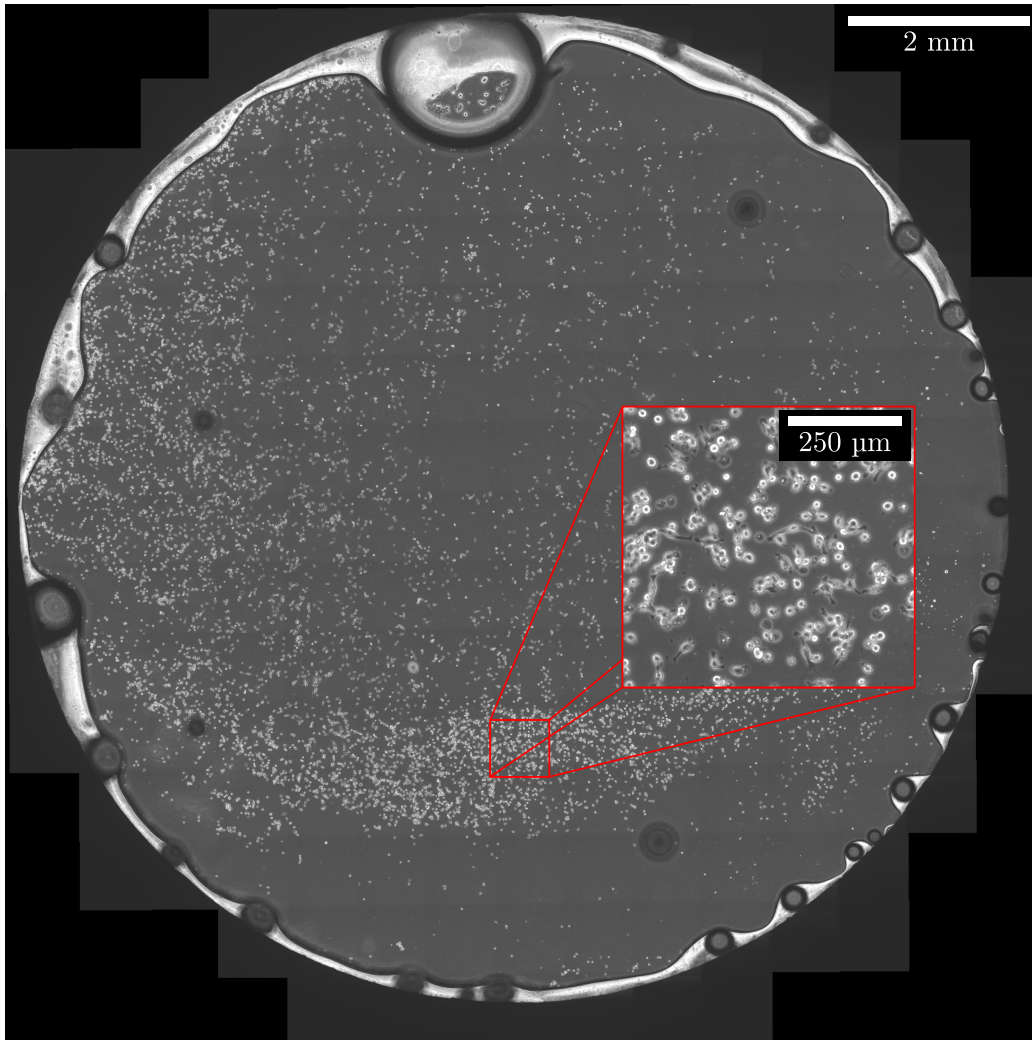


Figure 2.3: Phase contrast image of adherent J774A.1 mouse macrophages. Phase contrast images of the complete visible area of the 18 mm round coverslip mounted in the aluminum holder were acquired with the 10 \times -objective and stitching together automatically. On the edges, the silicon grease used to hold the coverslip in place is visible. The four small circular shadows inside the sample are caused by tiny gas bubbles trapped below the coverslip on top of the sample. The zoom-in shows additional 5 \times magnification.

A list of the objectives' optical properties is provided in Table 2.1. The water immersion objectives have been chosen over oil-immersion objectives despite their lower numerical aperture, because they allow imaging through the cell or tissue chambers used for live cell microscopy. While both the 60 \times - and the 40 \times -objective were suitable for optical trapping, all experiments in this thesis have been done using the 60 \times -objective.

Imaging was done using one of the four cameras provided by the setup. An simplified illustration of the involved light paths is shown in Figure 2.4. On the right camera port, there was the Andor Luca-R, which is a versatile EMCCD camera with a resolution of 1004 \times 1002 pixels. In this thesis, this camera was used to acquire the brightfield and DIC images during the dual-bead experiments. The left camera port was attached to a dual-camera adapter (Andor TuCam type TR-DCIS-CA1-00-I, Oxford Instruments, Belfast, United Kingdom), which split the image into two separate images. A highly sensitive EMCCD-camera (Andor iXon Ultra 897, model DU-897U-CS0-#EX, Oxford Instruments) and a camera capable of very high frame rates (IDT NX4-S2, IDT Vision, Pasadena, United States) were mounted to this adapter. There were two available beam splitters, one of which used a semi-transparent mirror to equally divide the incoming light between both attached cameras. The other beam splitter was a dichroic mirror specifically selected to allow simultaneous acquisition of sensitive fluorescent GFP images and brightfield images with a high frame rate. To achieve this, a longpass filter (RG645, Schott AG, Mainz, Germany) was placed in the brightfield illumination path which blocks all light with wavelengths smaller than 600 nm and transmits more than 90% of light for wavelength larger than 670 nm (see Figure 2.4). In the beam path after the objective, the fluorescence filter cube GFP-L (Nikon, Tokyo, Japan) was placed. This filter cube included an excitation filter transmitting in the range of 460 – 500 nm and a dichroic mirror with a cut-off at 505 nm, which was used to induce the excitation light into the microscope. The brightfield illumination light and the light emitted by the green fluorescence, part of which has wavelengths in the range 510 – 600 nm, were transmitted by the dichroic mirror and by the following barrier filter, which transmits light with wavelengths larger than 510 nm, but filters out any shorter wavelengths to block the excitation light. Later in the dual-camera port, the fluorescence emission and the brightfield light were separated again by another dichroic beam splitter (Chroma zt 605 DCSPXT) which reflected light with wavelengths larger than 605 nm onto the highspeed camera. Any light with shorter wavelengths hit another bandpass filter (Semrock FF01-505/119-25, Semrock, West Henrietta, United States) which only allowed light in the range of 445 – 565 nm to reach the sensor of the iXon Ultra. Light of this wavelength could only originate from the fluorophore. Any light emitted by the fluorophore with wavelengths larger than 605 nm did reach the sensor of the highspeed camera, but will not impact on the brightfield image quality, as the brightfield illumination was usually several magnitudes brighter than any residual light from the fluorescence. In conclusion, the dual-camera port and a combination of beam splitters and filter allowed doing sensitive fluorescence measurements while simultaneously recording a brightfield image with a high frame rate. The fourth camera was a pco.pixelfly usb (PCO imaging, Kelheim, Germany) attached to the eyepiece port of the microscope and was only used during the blinking experiments in chapter 3.

2.2.5.2 Pixel size in images

The length to which a single pixel corresponds to in the microscopic images was measured by recording images of a stage micrometer (10 μ m divisions, R1L3S2P, Thorlabs, Bergkirchen)

name	type	magnification	numerical aperture	working distance (mm)	CS thickness (mm)
CFI Plan Fluor DL 10x	dry	10×	0.3	15.2	1.2
CFI S Plan Fluor ELWD ADM 20xC	dry	20×	0.45	8.2...6.9	0...2
CFI Apo LWD 40x WI λ S	WI	40×	1.15	0.6	0.15-0.19
CFI Plan Apo IR 60xWI	WI	60×	1.27	0.17	0.15-0.19

Table 2.1: List of available objectives. The 10 \times - and 20 \times -objective are dry objectives and both feature an integrated phase ring for phase contrast microscopy. The 40 \times - and 60 \times -objectives both use water immersion and are suitable for DIC-microscopy and optical trapping. While the 10 \times -objective is designed to be used with a fixed coverslip thickness, the other objectives feature a correction collar which adjusting the objective for the used coverslip thickness.

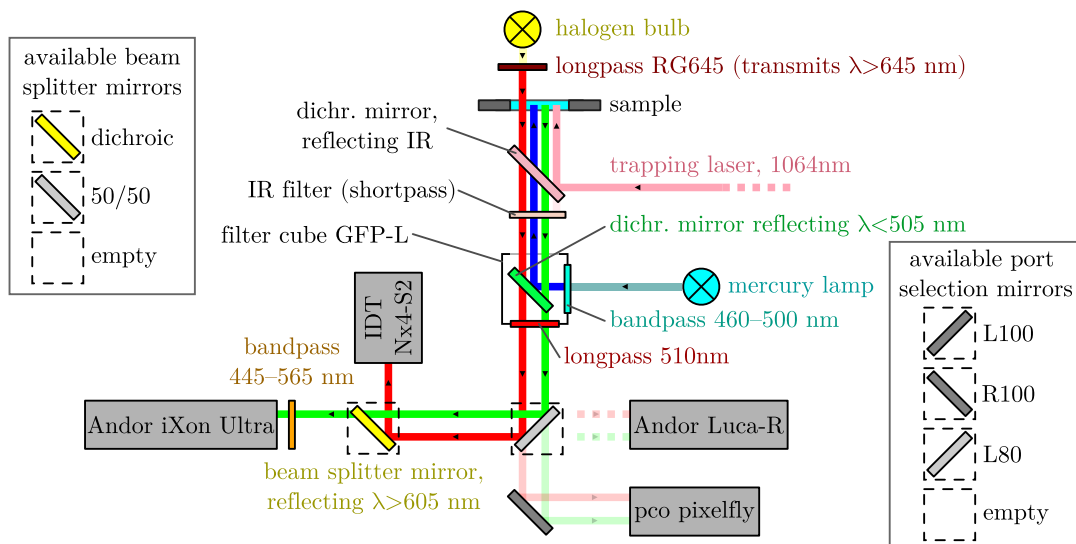


Figure 2.4: Illustration of the light paths for different wavelengths and the filters used in the microscope. To select between cameras, the port selection mirror can be changed (motorized) between four different configurations. Additionally, two beam splitters are available for the dual-camera port on the left, a dichroic one and a 50/50 beam splitter. The configuration shown in this image was used to simultaneously acquire brightfield and fluorescence images during chapter 3. If simultaneous acquisition is not needed, as for the dual-bead experiments described in this chapter, the RG645 filter and the bandpass filter in front of the Andor iXon Ultra can be removed. Here, brightfield and fluorescence images were mostly acquired sequentially using the Andor Luca-R camera and the port selection mirror R100.

using the 60 \times objective. This was done for all cameras. The number of pixels between the micrometer's black vertical lines in the microscopic images was measured. To enhance accuracy, an intensity line-profile was generated perpendicular to the ruler's lines and the locations along the line profile at which the image intensity surpasses the median image intensity were calculated with sub-pixel accuracy. This generated a list of positions along the axis perpendicular to the ruler indicating where each line begins or ends. The distance between adjacent left and right edges of lines was measured for all visible pairs of lines, resulting in a list of distances in pixels that should closely correspond to 10 μm .

Using this data, we obtained the value for the apparent pixel size and its standard deviation for all four cameras, as listed in Table 2.2. For the pco pixelfly and the IDT Nx4-S2, the values in Table 2.2 were divided by 2 respectively 4 to be correct for the binning used when capturing the images of the ruler. The table also provides theoretical pixel pitches values obtained by dividing the hardware pixel sizes taken from the cameras' datasheets by the used magnification. The Andor iXon and the IDT camera were connected to the dual-camera-port (Andor TuCam), which introduced an additional 2 \times magnification for a total magnification of 120 \times . The measured pixel pitches for the Andor Luca-R and the pco pixelfly, both of which were connected directly to the microscope, matched the expected value within 1%. For the cameras mounted to the dual-camera port (IDT Nx4-S2 and Andor iXon DU-897U), the deviations were larger, reaching approximately 6%. This was probably caused by a slightly inaccurate alignment of the dual-camera port. All evaluations in the context of this thesis were done using the experimental values as listed in Table 2.2.

2.2.5.3 Widefield microscopy contrast techniques

The simplest and oldest of all optical microscopy illumination techniques is brightfield microscopy. In this method, the sample is transmitted by light and the image forms because the amount of attenuation in the sample depends on the sample's optical density. Brightfield microscopy has been improved numerous times since it was first developed, for example by introducing the Köhler illumination^[133] or by optimized optical components^[134]. Yet, the basics behind the image formation have remained constant until this day. Even today, brightfield microscopy is still the method of first choice for many tasks in research.

Unfortunately, there is a principle-related disadvantage with brightfield microscopy that is especially prominent when working with biological samples. Most animal cells barely absorb any light, making them almost invisible in brightfield images. To solve this problem, many different contrast enhancing optical methods were developed. One of the most established methods to enhance the contrast is the use of phase-contrast-microscopy, which was developed in the 1930s by Frits Zernike^[135]. Phase contrast microscopy takes advantage of the fact that some of the light in the sample is scattered. To do this, a ring-shaped diaphragm is placed in front of the condenser^[136]. This results in the light always hitting the specimen at a specific range of angles to the optical axis. All light passing the specimen unaffected will hit the objective in the same range of angles, where it will be attenuated by a gray filter ring. This process thus emphasizes image areas in which there is particularly much scattering and thus produces high contrast. In addition, interference also plays a role in image formation. The process is simple and reliable, but a disadvantage is the typical halo effect, where a bright glow becomes visible around larger objects such as individual cells.

In the context of this work, phase contrast microscopy was only used when a quick, low-magnification overview image of the sample was required, which can be helpful to measure

camera	pixel size in image (experimental)	camera pixel size	magn.	pixel size in image (theory)
Andor Luca-R	(134.0 ± 0.2) nm/px	8 μ m	60 \times	133.3 nm/px
Andor iXon DU-897U	(140.4 ± 1.4) nm/px	16 μ m	120 \times	133.3 nm/px
IDT Nx4-S2	(106.7 ± 0.5) nm/px	13.68 μ m	120 \times	114.0 nm/px
pco pixelfly	(108.0 ± 0.4) nm/px	6.45 μ m	60 \times	107.5 nm/px

Table 2.2: Pixel sizes in images acquired by different cameras. Images of a stage micrometer with 10 μ m divisions were taken using the 60 \times -objective and all four available cameras. Then, all distances between the two left or right edges of two adjacent lines were measured in all images and an average and the standard deviation were calculated. From that, the apparent pixel sizes in the cameras' images when using no binning and the 60 \times -objective were calculated as listed here. The table also provides a comparison with theoretical pixel sizes calculated from the cameras' pixel size on their sensors as specified by the manufacturers and the used magnifications.

the cell density accurately. One example of such a image was already shown in Figure 2.3. Also, the microscope used during cell culture to monitor the density and the phenotype of the cells implemented phase contrast.

Another method of enhancing the image contrast is differential interference contrast (DIC) microscopy, which was developed by Georges Nomarski (1919–1997) around the 1950s^[137,138]. DIC microscopy is ideally suited for qualitative examination of biological samples. DIC microscopy relies on small phase differences between different ways through the sample to create a contrast-rich image, even if the observed object is completely translucent. While phase contrast microscopy suffers from halo artifacts, DIC creates sharp images while still fully illuminating the objective's aperture and thus reaching its maximum resolution. Different cell organelles and even the membranes can be imaged without any staining, making method easy to use and completely non-invasive. A nice introduction to the functional principle of DIC was provided by H. Rosenberger^[139] in 1977. During the work presented in this thesis, DIC microscopy was used heavily in the dual bead experiments presented in chapter 2 to provide detailed images of the cell's membrane during the experiments. Unfortunately, the polystyrene particles used in this experiments show such a high difference in the refractive index relative to the medium that the image is over-illuminated in the areas around the beads. This obstructs the direct observation of the phagocytic cup formation around these particles. Still, the method provides an excellent view of the cells morphology.

2.2.5.4 Fluorescence microscopy

Another method to enhance contrast in microscopy is to use fluorescence. This method differs from the previously mentioned methods as it usually requires staining the sample. A fluorescent molecule is brought into the sample and illuminated with light of a wavelength suited to excite this molecule. Before observation, this wavelength is filtered out and the final image is created only from the light emitted by the fluorophore. There are many different stains available which accumulate in different areas of the cell, making it possible to stain specific organelles or proteins. For example, the stain DAPI (4',6-diamidino-2-phenylindole) strongly binds to adenine-rich regions in double-strand DNA^[140].

While most fluorophores are organic small molecules with a molecular weight below 1 kDa, in 1962 a natural biofluorescent protein was first extracted from luminescent jellyfish by Osamu Shimomura^[141]. This molecule is now widely known as “green fluorescent protein” (GFP) and its existence has been an invaluable asset to cellular biology ever since. By inserting the genetic code of the GFP protein into the genome of a target organism at the right location, the relatively small (27 kDa^[142]) GFP protein can be appended to other proteins. This way, no external stains need to be used, as the fluorophore is synthesized by the observed organism itself. In transfected cells, the target protein is expressed with the GFP protein attached to it, which can be used to detect the location of this fusion protein inside the cell with great precision. Usually, the fusion proteins will still be able to maintain their original function. It is however reasonable to assume that the increased size of the protein can impact its natural function or alter the location and movement of the protein in the cell. Still, the ability to monitor individual proteins inside living cells has helped to shine light on the function of thousands of proteins.

In this thesis, LifeAct-GFP transfected J774.A1 macrophages were used to study actin dynamics within cells, with the intention to directly observe the cortical dynamics during phagocytosis.

2.2.6 Optical tweezers

2.2.6.1 History of optical tweezers

Optical tweezers operate based on the fact that small dielectric particles in the focus of a highly focused laser beam feel restoring forces which keep the particle close to the focus point. The optical forces which are exerted in this way are in the magnitude from a few piconewtons up to a nanonewton^[143,144]. While small, these optical forces are enough to keep freely diffusing particles still in their surrounding medium and can be used to counteract and measure other, smaller forces, for example in biological systems.

The first person to trap small particles using the optical forces in the focus of a laser beam, was Arthur Ashkin in the year 1970^[145]. In his work, two opposing laser beams were used to cancel out the scattering forces and create a stable trap potential. Until 1986, Ashkin and his colleagues had achieved trapping a particle with a single laser^[146]. The trick was to use a microscope objective with a large numerical aperture to focus the laser particularly tightly. In the following years, Ashkin’s approach was cited numerous times and saw first uses as a device for micromanipulation^[147,148]. By this means, optical tweezers came to life and are now known as a established method in the field of biophysics^[149]. Optical tweezers allow to exert and measure forces in biological samples with minimal invasion, reaching sub-piconewton precision^[143].

For example, the force required to unfold a strand of DNA was studied using optical tweezers by trapping a probing particle with is attached to the coverslip via a single strand of DNA^[150]. Also, the stall forces and step sizes of single molecular motors and their step sizes were measured using optical tweezers, which revealed the stall forces and step sizes of dynein^[151], myosin^[152] and kinesin^[153,143].

Usually, optical tweezers are created by a collimated laser beam which is focused into the sample by the objective of a microscope. The trap is created in the focal plane of the microscope and trapped objects can be observed directly. Typically, the wavelength of the trapping laser is chosen in the infrared range, because the lower energy compared to

visible light is less harmful to biological samples. Another benefit is that the laser light can easily be filtered out before reaching the camera and the full visible spectrum can still be used for imaging the sample. This has found wide application in biological research, as by moving the beam relative to a microscopic sample, a particle trapped in the beam's focus can be maneuvered inside the sample without direct physical contact. Moreover, if the trap's potential is known, external forces acting on the bead can be calculated by measuring how far they are able to pull the bead out of the trap. Because of this, optical tweezers have found many useful applications in research, especially in research on the mechanics of single molecules.

2.2.6.2 Theory of optical tweezers

Optical tweezers exert forces using light. The simplest approach to calculate the forces exerted on a particle by a focused beam of light is to use ray optics. This is only valid if the diameter of the particle d is much larger than the wavelength λ of the light ($d \gg \lambda$). In this case, the force acting on the particle can be understood as the impulse transferred on the particle by deflected photons. By looking at individual rays of the collimated laser beam hitting the particle, we can qualitatively understand how the optical trapping works^[154]. If the individual rays travel through the center of the sphere like in the left-most panel of Figure 2.5, they enter the bead's surface perpendicular, which means that no forces due to the refraction of the light will arise. However, if the particle is moved away from this position, the incoming beams will be deflected, which creates opposing forces on the particle. In total, the deflection of all incoming beams creates a force which will push the particle back to the equilibrium position, as visible in the other panels of the figure.

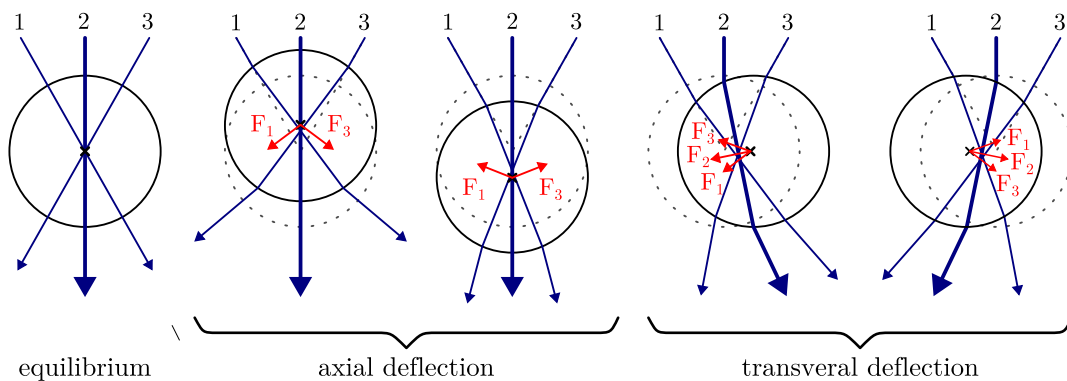


Figure 2.5: Forces created by individual rays of a focused laser beam through a fully transparent dielectric sphere. No matter in which direction the particle is deflected from the equilibrium, the combined force created by the deflection of the individual beams will always be restoring, both for axial and transversal displacements of the sphere. In the figure, only three rays are shown. It should also be noted that the intensity of ray 2 is higher than the intensity of the other rays due to the Gaussian intensity profile of the beam. Also, an additional force will arise because parts of the incoming light will be reflected, absorbed or scattered by the particle. The figure is adapted from Ashkin's 1992 paper^[154].

Not all light hitting the particle passes it. In reality, some light is absorbed or reflected, which creates a net force pushing the particle into the direction of the light's propagation. This force is the radiation pressure force and depends on the amount of light scattered or absorbed by the particle. However, if the beam is focused strongly enough, there is a position at which the restoring force due the refraction of the incoming beams exactly compensates for the additional force created by radiation pressure. So the trap will still work, but the equilibrium position will shift a little bit and look more like the middle panel in Figure 2.5.

A quantitative calculation of the spring constant of an optical trap using ray optics would require modeling the focused laser beam as a field of rays of given direction and intensity and integrating the forces exerted on the particle over all beams. This can be done numerically^[155,156], and the result matches surprisingly well with the exact electromagnetic theory for particles with diameters larger than two wavelengths. For smaller particles, geometrical optics will over- or underestimate the forces. Unfortunately, any attempt to approximate the scattering force using geometrical optics does not deliver satisfactory results. Especially for smaller beads, the scattering force is very sensitive to changes in particles size, as interference effects between light reflected from the front and back size of the sphere strongly influence the particle's reflectivity^[157]. Calculating the forces created by reflected light using the Fresnel equations yields unsatisfactory results, as it ignores interference^[156].

A more direct approach is to calculate the force acting on the particle directly using electromagnetic theory^[156,158,130]. In this case, the particle is usually assumed to be small compared to the wavelength of the light, which means it can be assumed to be a induced electric dipole in the approximately uniform electric field created by the laser. Detailed theory on how to describe a dielectric sphere in a uniform electric field is provided by many textbooks on electromagnetic theory. Following Rocha's paper on the theory of optical tweezers^[159], the induced dipole moment of a dielectric sphere in a uniform electric field can be written as following:

$$\vec{p} = \frac{K - 1}{K + 2} \left(\frac{d}{2}\right)^3 \vec{E}. \quad (2.1)$$

In this equation, \vec{E} is the electric field outside the sphere, d is the spheres diameter and K is defined as the ratio of the electric permittivities of the sphere and the medium:

$$K = \frac{\epsilon_{\text{sphere}}}{\epsilon_{\text{medium}}} \quad (2.2)$$

The electric potential energy of the induced dipole can be calculated as the point product of the induced dipole moment and the electric field:

$$U = \vec{p} \cdot \vec{E} \quad (2.3)$$

The force on the bead is the gradient of this potential energy:

$$\vec{F} = -\vec{\nabla}U = \vec{\nabla}(\vec{p} \cdot \vec{E}) \quad (2.4)$$

Combining equations 2.1 and 2.4 results in the following equation:

$$\vec{F} = \frac{K - 1}{K + 2} \left(\frac{d}{2}\right)^3 \vec{\nabla}E^2 \quad (2.5)$$

This force is proportional to the gradient of the field intensity, which means that it pushes the particle towards the region with the highest intensity, which in the case of optical tweezers is the laser focus, which is why this force is often referred to as the gradient force. If the particle is not perfectly transparent or scatters some light, a additional force in the direction of the light's propagation will occur. This force is generally known as the scattering force. For functional optical tweezers, it is important that the gradient force is higher than the scattering force. This can be ensured by using an objective with a high numerical aperture, which can create a strong focus with a high gradient in the field intensity. Notably, the gradient can also be increased by increasing the overall intensity, meaning the gradient force is also proportional to the laser power. In experiments, the optical force along a single axis, for example the x -axis, is important. It can be calculated as following:

$$F_x = \frac{K - 1}{K + 2} \left(\frac{d}{2}\right)^3 \frac{\partial E^2}{\partial x} \quad (2.6)$$

This equation scales with the cubed bead radius, which means that for bead sizes smaller than the wavelength of the trapping laser, the trapping forces scale with the bead's volume. A easy way to estimate the scattering force was provided by Ashkin himself, as he noted that the scattering force can be calculated from the total power of the light scattered^[146] with the formula $F_{\text{scat}} = n_m P_{\text{scat}}/c$. Here, n_m denotes the refractive index of the medium surrounding the particle. The power of the scattered light can be calculated from its intensity and the refraction indices of the medium and the particle using Reynolds scattering^[146,160]. A easy to understand but detailed description on which approaches can be used to calculate the optical force created by optical tweezers was published by M. Rocha in 2009^[159].

In reality, the diameter of the particles used in experiments are mostly in the range of 0.5 – 10 μm and the used laser wavelength are in the IR regime, meaning the wavelength will be approx. 1 μm . Because the size of the particle and the wavelength are similar, neither the Rayleigh nor the ray optics approach is valid and a more elaborated optical description, for example the Lorenz-Mie theory^[161], is necessary. Fortunately, it is not necessary to calculate the forces as they can be measured experimentally in a calibration experiment. Methods of acquiring the forces on a particle via calibration are described in chapter 3.2.2.

2.2.6.3 Holographic optical tweezers

Many experiments require control over multiple microparticles at once. To achieve that with optical tweezers, multiple traps have to be generated in the sample, which is possible using a few different methods. A very simple method is to use a individual laser beam for each trap. The beams can come from individual laser sources or by dividing one laser into multiple beams. To change the position of each trap inside the sample, the angle in which the corresponding beam enters the objective can be altered slightly. Unfortunately this approach is inflexible as it can only produce a fixed number of traps and can lead to a very complex optical setup, especially aligning multiple beams to enter the objective in very similar angles can become challenging pretty quickly. Because of that, there are approaches to create multiple traps using a single, powerful laser beam. If the trap position can be altered fast, the laser can be switched between the required trap positions with a high frequency. This effectively creates multiple traps, especially if the switching frequency of this time-multiplexing is higher than the frame rate of the observing camera. Optically this can be done by utilizing deflective or refractive optics with a very low response time,

such as galvanometric mirrors or, even faster, acusto-optic modulators^[162]. Finally, a very elegant approach to create multiple traps out of a single beam is to use computer-generated holograms, as firstly described by Eric Dufresne and David Gier in the year 1998^[163]. With a hologram a single beam can be split into multiple traps without any moving parts or relying on multiplexing. Each trap of the holographic optical tweezers can be calibrated the same way as single beam optical tweezers. However, the stiffness of all traps has to be calibrated every time a new hologram is calculated, as changing the hologram may significantly alter the beam shape of each trap. This calibration can be done as described in chapter 3.2.2.

The details on how the holographic optical tweezers are implemented and characterized in our setup was already explained by A. Sabri and K. Berghoff^[164,130] before. A summary on the operational principles will be presented in the next section.

2.2.7 Implementation of holographic optical tweezers

2.2.7.1 Trapping laser beam path

The implementation of the holographic optical tweezers requires multiple optical components set up around the microscope. A schematic of those is shown in Figure 2.6. As the main laser to create the optical traps, a ytterbium fiber laser (PG YLM-5-LP-SC, $\lambda = 1064$ nm, IPG Photonics, Burbach, Germany) was used. While rated for an optical power of 5 W, we only ran the laser at 3 W during our experiments. Directly after the end of the laser fiber, a mechanical shutter (1/2 inch beam shutter, SH05R, Thorlabs) was mounted to allow blocking the laser from entering the setup when it was running, for example while the laser warmed up or while the experimenter searched for a bead to trap inside the sample. After that, a faraday isolator was mounted, which blocked all light from being reflected back into the laser by any component of the setup. Shielding the laser from any backreflection helped keeping the optical resonance stable, minimizing fluctuations in the laser power. After that, the beam passed a beam expander mounted in reverse, which reduced the beam's diameter so that the full beam fit the entrance pupil of the next component, the acusto-optic modulator (AOM, MT110, AA Opto-Electronic, Orsay, France).

The AOM was part of a feedback loop to stabilize the laser output power. It was connected to a commercial laser stabilization controller (NoiseEater, TEM Messtechnik, Hannover). The used AOM is made from a small tellurium dioxide cell which is fixed to a ultrasonic transducer on one end and an acoustic absorber on the other end. The ultrasonic transducer is driven with a high frequency, in our case 110 kHz. The resulting sound wave creates regions of high and low pressure inside the crystal, which resulted in a periodic shift of the medium's refractive index. The periodicity Λ of this modulation in refractive index corresponds to the wavelength of the sound wave. An AOM is usually set up so that the laser entered it almost perpendicular to the propagation of the sound, but tilted by the Bragg angle $\theta_B = \lambda / (2n\Lambda_{\text{Laser}})$. Here, n is the refractive index of the crystal, and λ_{Laser} is the wavelength of the laser. If the modulation of the refractive index is strong enough, most of the incoming beam is reflected on the sound wave and exits the AOM tilted by the angle $2\theta_B$ against the incoming beam. If the sound wave is switched off, the laser passes the AOM unaffected. By changing the intensity of the sound it is possible to control how the intensity of the laser is split into the diffracted and the unaffected beams.

In our setup, the diffracted beam was used, while the other beam was blocked by a beam dump. The AOM had a nominal diffraction efficiency of 90%, meaning that up to 90% of the

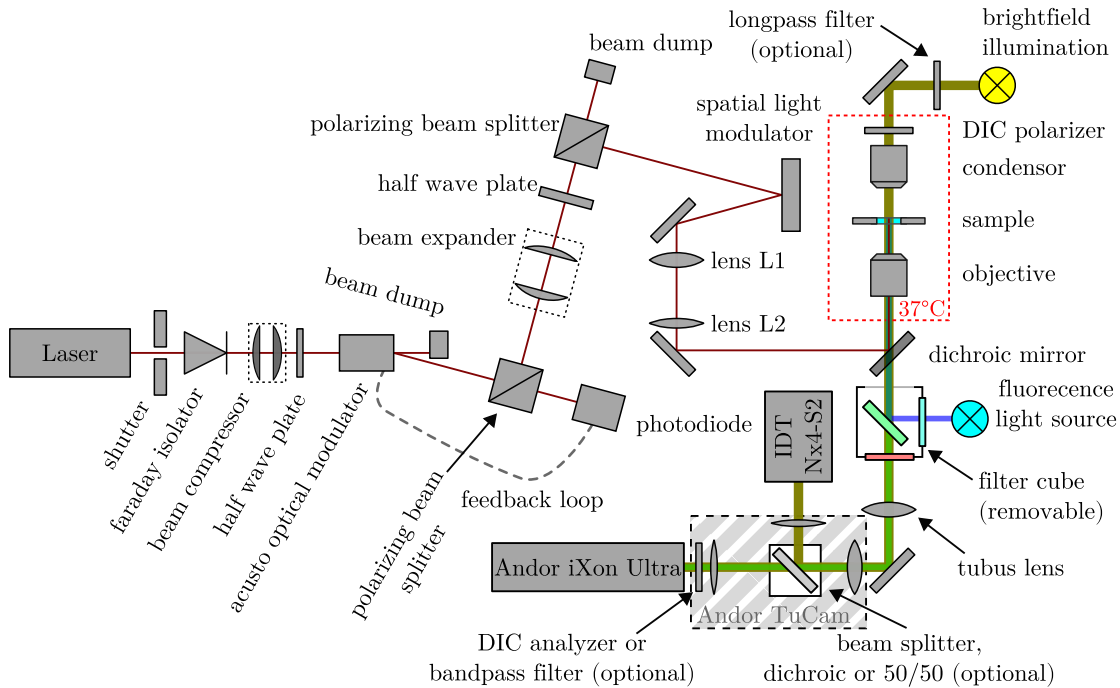


Figure 2.6: Lightpath of the trapping laser in the holographic optical tweezers setup. The beam exiting the fiber laser first passed a mechanical shutter and a faraday isolator. After that, its diameter got reduced and it entered the stabilization feedback loop consisting of an acousto optical modulator to control the passing laser power and an polarizing beam splitter paired with a photodiode to measure the output power. Then, the beam passed a rotatable half wave plate and a polarizing beam splitter used to reduce the laser’s power if necessary. Finally, the beam hit the SLM, passed a pair of lenses and entered the microscope, where it was redirected into the objective by a dichroic mirror.

beams intensity could be redirected into the diffracted beam, while at least 10% of the initial power hit the beam dump. While the signal to create the sound wave was generated by a fixed frequency driver providing a 110 kHz sinusoidal signal, the NoiseEater controlled the optical output power of the AOM by increasing or decreasing the amplitude of this signal. After the AOM, a small amount of light was redirected from the diffracted beam onto a photodiode. This photodiode provided a voltage that increased with the intensity of the diffracted beam.

The feedback from the photodiode allowed the NoiseEater to stabilize the power of the beam diffracted by the AOM: To do this, the photodiode’s voltage was compared with an adjustable reference voltage (setpoint) and the difference was fed into a PID controller. If the intensity of the diffracted beam increased, the controller decreased the voltage of the high frequency wave applied to the transducer of the AOM, reducing the diffracted laser power. Vice versa, if the photodiode voltage was smaller than the setpoint voltage, the amplitude of the RF wave was increased until the two voltages aligned, or – if the setpoint is too high – until the maximum output power was reached. Because of the high speed of sound in the tellurium dioxide (4.2 km/s for longitudinal waves as used by the AOM^[165,166]) and the small size (≈ 1 mm) of the beam passing the AOM, it has a very fast reaction time. The datasheet specifies a rise/fall time of only 160 ns^[165]. During normal operation, the reference voltage

was controlled by a potentiometer (labeled setpoint) on the device. In this mode, the switch labeled “setpoint” was set to “manual”, the regulator switch to “reg”. The setpoint voltage was chosen as high as possible, because the power passing the AOM directly depends on it, but low enough so that the photodiode voltage could reliably reach the setpoint voltage before the AOM has to be driven with its maximum amplitude. The NoiseEater provided an output of the photodiode voltage which could be monitored using an oscilloscope.

It was possible to modulate the NoiseEater’s setpoint voltage using an external signal. This could be used to tweak the PID settings of the controller by applying a square wave voltage created by a function generator which rapidly switches the setpoint between zero and a fixed value. Each time the setpoint voltage changes, the NoiseEater quickly adapted the power applied to the AOM until the photodiode voltage matched the setpoint voltage. The step response of the controller could be monitored on the oscilloscope, and the PID controller settings could be optimized to achieve a fast and stable reaction. Moreover, the external setpoint mode could be useful in the future to rapidly switch the laser power during experiments.

After the feedback loop, the laser beam entered an adjustable beam expander. This component increased the diameter of the beam to roughly 7.5 mm (FWHM), as measured with a beam profiler. This was done so that the beam is large enough to illuminate the whole spatial light modulator (SLM) later. Before hitting the SLM, the beam passed a half-wave plate and a polarizing beam splitter. The sole purpose of this setup was to provide an easy way to lower the laser power by diverting a portion of the beam’s intensity towards a beam dump when needed. After that, the beam hits the SLM which was used to control the creation of the optical traps.

Generally speaking, a SLM is just a liquid crystal display with a highly reflective backlayer displaying a hologram. Our setup used a SLM from Meadowlark Optics, Inc, Frederick, USA (BNS XY Phase Series, model P512-1064). This SLM has an array of 512×512 quadratic pixels with a grid size of $15 \mu\text{m}$. Incoming light passes the cover glass, the transparent liquid crystal layer, reflects on the backlayer, and exits the SLM after passing through the liquid crystal layer a second time. Behind the reflective backlayer is the pixel array. The coverglass of the SLM is conductively coated, which makes it possible to apply a voltage between a specific pixel and the coverglass. The individual pixels serve as electrodes, creating an electric field which twists the nematic molecules above each pixel and increases the optical path length through the SLM by an amount depending on the applied voltage.

In our setup, the phase pattern on the SLM could be changed by sending a 16-bit image to the SLM via its MATLAB interface. By doing this, each pixel was attributed a value between 0 and 65535 which corresponded to phase shifts between 0 and 2π for the wavelength of 1064 nm. The SLM used these values to apply the voltages necessary to achieve this phase shift in every pixel according to a factory-calibrated lookup table. As the SLM was illuminated by a coherent laser beam, the phase of the light exiting each pixel could be chosen arbitrarily for each pixel by setting the applied phase shift to the desired output phase. This allowed a high order of control over the beam shape. By applying certain phase patterns – called holograms – to the SLM, it was possible to create arbitrary intensity distributions in a plane conjugated to the plane of the SLM. The only limitation was that the SLM always has a high reflectiveness and thus cannot change the exiting beam’s total intensity.

After the SLM, the beam was focused by the lens L1 (see Figure 2.6). Depending on the hologram used, this created one or many focal points in the focal plane of the lens. The lens L2 acted as a tubus lens and shared focal planes with the lens L1 and the microscope

objective. The objective and lens L2 formed a telescope configuration, projecting the foci produced by lens L1 into the sample on the microscope stage, creating the optical traps. The beam path from lens L2 to the objective was not straight, but passed a periscope used to raise the beam to the height of the microscope's second filter revolver. In this revolver, a filter cartridge with a dichroic mirror was used to redirect the trapping beam into the objective.

2.2.7.2 Hologram generation

To create functional holographic optical tweezers, an algorithm to calculate the phase pattern displayed on the SLM is needed. There are algorithms like direct binary search^[167] or the Gerchberg-Saxton algorithm^[168] which can calculate holograms corresponding to arbitrary intensity distributions in the sample. An example on how the Gerchberg-Saxton algorithm can be used will be provided later in chapter 2.2.7.6. However, for many applications, such as holographic optical tweezers, arbitrary intensity distributions are not necessary. In this case, it is sufficient to use holograms which can slightly alter the direction with which the laser beam leaves the SLM. Doing this moves the trap in the sample. Additionally, if the beam is slightly defocused by the hologram, it is possible to shift the trap above or below the focal plane of the objective. A schematic illustrating how the deflection or defocusing of the beam influences the trap position is shown in Figure 2.7. To create the beam deflection or focus change, a hologram can be generated using an algorithm based on lenses and gratings^[169,170]. This algorithm allows to place multiple traps freely inside the sample volume. It works in three dimensions, is easy to understand, very reliable, and fast. Because of this, it was used as the primary algorithm during all cell experiments presented in this thesis.

The simplest kind of holograms only change the direction of the beam. By applying a linearly increasing phase shift along one direction across the SLM, the direction of the exiting wavefront can be controlled. Phase shifts larger than 2π can be replaced by equivalent values smaller than 2π . This results in a hologram resembling a blaze grating. This hologram can be described by a grid of phase values Φ_{jk} which describe which phase are applied by each pixel to the beam by the SLM.

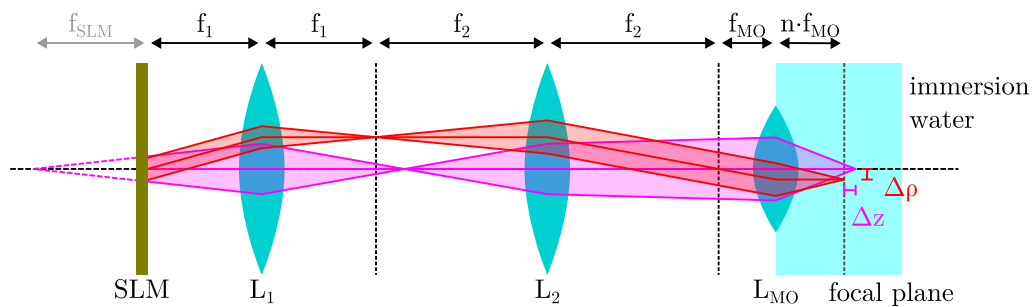


Figure 2.7: Trapping laser propagation after the SLM, as calculated by the ray transfer matrices. The red beam exits the SLM collimated, but at the angle α , which causes it to be focused to the focal plane of the microscope, but slightly shifted from the optical axis by the distance $\Delta\rho$. The purple beam exits the SLM slightly defocused but straight, which causes an axial shift Δz against the focal plane. This defocused beam can be created if the SLM is hit by an collimated beam and acts as a lens with the virtual focal length f_{SLM} .

The angle of the exiting wavefront can be controlled by the periodicity of this grating. A visualization of how this works is depicted in Figure 2.8a. If Λ is the distance on the SLM in which the phase shift increases from 0 to 2π , the angle α between the exiting beam and the optical axis can be calculated via the trigonometric relation $\tan(\alpha) = \lambda_{\text{Laser}}/\Lambda$. A graphical representation of these lengths is shown in Figure 2.8a. Since Λ is usually much larger than the wavelength λ_{Laser} , the following small-angle approximation is valid:

$$\alpha = \lambda_{\text{Laser}}/\Lambda \quad (2.7)$$

Another simple hologram can be used to create a converging wavefront, which makes the SLM act like a curved mirror. To achieve this, the phase shift has to be proportional to the squared distance from the SLM's center. Again, any phase shift larger than 2π can be broken down to a equivalent smaller phase change. This phase pattern acts like a fresnel lens, resulting in a converging wavefront, as visualized in Figure 2.8b.

2.2.7.3 Ray transfer matrix analysis

To calculate on how a slight beam deflection or focus shift at the SLM influences the position of the trap inside the sample, it proved very helpful to use ray transfer matrices. To do this, a transfer matrix was attributed to each optical element (lenses 1 and 2 and the objective) and to each space in which the beam can propagate between those elements. A schematic of the placement of the two lenses L_1 , L_2 and the microscope objective is shown in Figure 2.7. When formulating the transfer matrices, it had to be considered that after passing the microscope objective, the light travels inside the immersion medium, which in our case is water. The image medium surrounding the cells is assumed to have a similar refractive index as PBS, which in turn has a similar refractive index to water^[171]. The transfer matrices of the individual elements are:

$$\begin{array}{l} \text{SLM} \rightarrow \text{L1: } T_1 = \begin{pmatrix} 1 & f_1 \\ 0 & 1 \end{pmatrix} \\ \text{L1: } T_2 = \begin{pmatrix} 1 & 0 \\ -1/f_1 & 1 \end{pmatrix} \\ \text{L1} \rightarrow \text{L2: } T_3 = \begin{pmatrix} 1 & f_1 + f_2 \\ 0 & 1 \end{pmatrix} \\ \text{L2: } T_4 = \begin{pmatrix} 1 & 0 \\ -1/f_2 & 1 \end{pmatrix} \end{array} \quad \left| \quad \begin{array}{l} \text{L2} \rightarrow \text{objective: } T_5 = \begin{pmatrix} 1 & f_2 + f_{\text{MO}} \\ 0 & 1 \end{pmatrix} \\ \text{objective: } T_6 = \begin{pmatrix} 1 & 0 \\ -1/f_{\text{MO}} & 1 \end{pmatrix} \\ \text{transition into water: } T_7 = \begin{pmatrix} 1 & 0 \\ 0 & -1/n \end{pmatrix} \\ \text{objective} \rightarrow \text{sample: } T_8 = \begin{pmatrix} 1 & n \cdot f_{\text{MO}} \\ 0 & 1 \end{pmatrix} \end{array} \right.$$

The focal length f_{MO} of the objective was not provided by the manufacturer. This may be because the objective consists of stack of individual lenses with different focal lengths, which were selected to minimize spherical and chromatic aberrations and to compensate for any error induced by the light passing the glass coverslip. Because the influence of the coverslip is compensated by the objective, it is ignored for the rest of the calculation. The objective's lens stack is modeled as a single, ideal lens with an effective focal length of f_{MO} which sits in the sample-facing principal plane of the lens stack. To match its specified magnification m , the effective focal length of the objective in air has to be $f_{\text{MO}} = 200 \text{ mm}/m$, where 200 mm is the focal length of the tubus lens used with Nikon's infinity corrected objectives. The

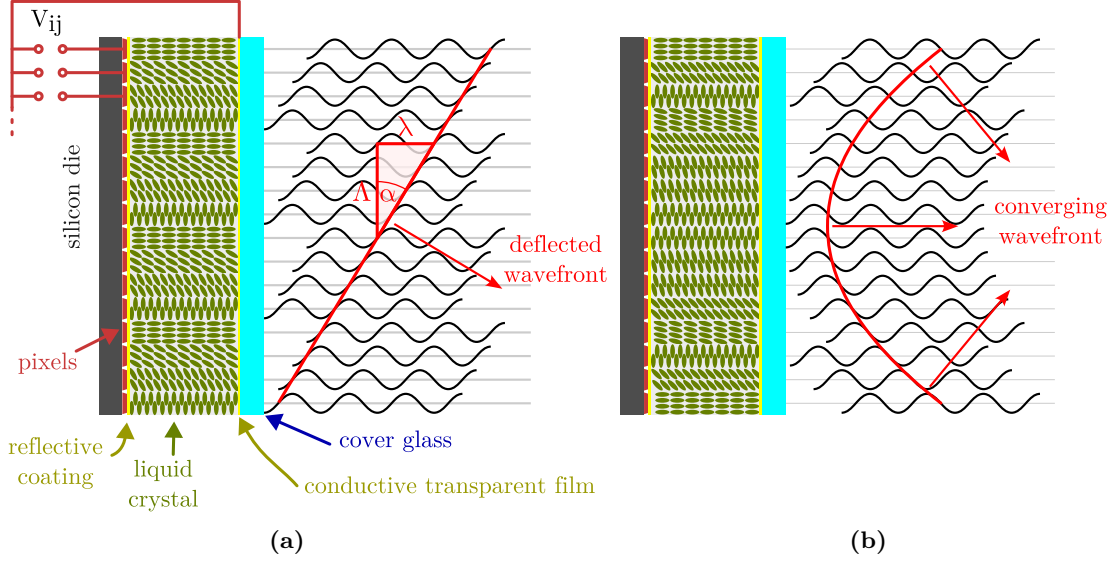


Figure 2.8: The holograms are applied to the SLM in the form of a two-dimensional grid of pixel voltages V_{jk} . The voltages create a shift of the nematic molecules inside the SLM, changing the optical path length the incoming light travels through each pixel. This way, the phase pattern of the reflected light can be controlled, which can be used to create a deflected or defocused wave front after the SLM.

tubus lens is needed to focus the collected light onto the camera sensors, and is not passed by the trapping laser. Because water immersion objectives were used and the imaging is also done in a liquid with a refractive index similar to water, the distance from the objective's sample-facing principal plane to the focal plane will not be the objective's focal length, but $n \cdot f_{MO}$. To obtain a total transfer matrix, all transfer matrices were combined:

$$T = T_8 T_7 T_6 T_5 T_4 T_3 T_2 T_1 = \begin{pmatrix} 0 & -\frac{f_1 \cdot f_{MO}}{f_2} \\ \frac{f_2}{f_1 \cdot f_{MO} \cdot n} & 0 \end{pmatrix} \quad (2.8)$$

Using this matrix, it can be easily calculated at which position and in which angle rays exiting the SLM enter the focal plane. To calculate at by which angle the SLM has to deflect the beam from the optical axis to create a certain displacement in the focal plane, we apply the transfer matrix T to a beam exiting the SLM in the distance r_0 from the SLM's center and tilted by the angle α towards the optical axis:

$$T \cdot \begin{pmatrix} r_0 \\ \alpha \end{pmatrix} = \begin{pmatrix} -\frac{\alpha \cdot f_1 \cdot f_{MO}}{f_2} \\ \frac{f_2 \cdot r_0}{f_1 \cdot f_{MO} \cdot n} \end{pmatrix} \quad (2.9)$$

The top entry of this resulting vector represents the distance to the optical axis in which the beam crosses the focal plane of the microscope. Since this value does not depend on r_0 , all beams leaving the SLM in a specific angle are focused into one spot of the focal plane. The

distance from the optical axis is:

$$\Delta\rho = -\frac{\alpha \cdot f_1 \cdot f_{\text{MO}}}{f_2} \quad (2.10)$$

The tilt angle α can be created by a hologram with a certain periodicity, as described in Equation 2.7. In the next step, it will be calculated what happens when the SLM acts as a lens instead of a grating. In this case, the beams exiting the SLM can be described by the vector obtained when applying the SLM lens to a ray entering the SLM straight and in a distance r_0 from the optical axis:

$$\begin{pmatrix} 1 & 0 \\ -1/f_{\text{SLM}} & 1 \end{pmatrix} \cdot \begin{pmatrix} r_0 \\ 0 \end{pmatrix} = \begin{pmatrix} r_0 \\ -r_0/f_{\text{SLM}} \end{pmatrix} \quad (2.11)$$

This means that when using a lens hologram, the ray r_0 from the optical axis exits the SLM at the angle $-r_0/f_{\text{SLM}}$. To obtain the position and angle in which this ray crosses the focal plane of the microscope, the transfer matrix T is applied:

$$T \cdot \begin{pmatrix} r_0 \\ -r_0/f_{\text{SLM}} \end{pmatrix} = \begin{pmatrix} \frac{f_1 \cdot f_{\text{MO}} \cdot r_0}{f_2 \cdot f_{\text{SLM}}} \\ \frac{f_2 \cdot r_0}{f_1 \cdot f_{\text{MO}} \cdot n} \end{pmatrix} \quad (2.12)$$

Here, the top entry of the vector still depends on r_0 , which means that the rays originating from the SLM do not cross the focal plane in one point. The distance from the focal plane at which the ray described by Equation 2.12 crosses the optical axis can be calculated by dividing the vectors top entry by its bottom entry:

$$\Delta z = \left(\frac{f_1 \cdot f_{\text{MO}} \cdot r_0}{f_2 \cdot f_{\text{SLM}}} \right) / \left(\frac{f_2 \cdot r_0}{f_1 \cdot f_{\text{MO}} \cdot n} \right) = \frac{f_1^2 \cdot (f_{\text{MO}})^2 \cdot n}{f_2^2 \cdot f_{\text{SLM}}} \quad (2.13)$$

An important fact to notice is that Δz does not depend on r_0 . This means that all rays will cross the optical axis exactly in the distance Δz after the focal plane. In our setup, the hologram is displayed on a 512 px \times 512 px large spatial light modulator (SLM). The highly reflective SLM is illuminated by a collimated laser beam at a small angle and is able to shift the phase of the reflected beam individually for each pixel by a value between 0 and 2π . The lenses-and-gratings algorithm is based on the fact, that a lateral displacement of the laser beam can be achieved if the hologram is set to a blazed grating:

$$\varphi_{jk} = \frac{2\pi \cdot d_{\text{Pixel}} \cdot (j \cdot \cos(\theta) + k \cdot \sin(\theta))}{\Lambda(\Delta\rho)} \mod 2\pi \quad (2.14)$$

j and k are the coordinates of the individual pixels on the SLM along the x and the y axis, ranging between 1 and 512. $d_{\text{Pixel}} = 15 \mu\text{m}$ is the spacing of the pixel grid on the SLM. $\Lambda(\Delta\rho)$ is the fringe period of the phase grating which depends on the distance $\Delta\rho$ the trap should be shifted, while $\theta = 0 \dots 2\pi$ denotes the direction in which the trap should be shifted by the hologram. For the periodicity $\Lambda(\Delta\rho)$, the following formula can be derived by inserting

Equation 2.7 into Equation 2.10:

$$\begin{aligned}\Delta\rho &= -\frac{\lambda_{\text{Laser}} \cdot f_1 \cdot f_{\text{MO}}}{\Lambda \cdot f_2} \\ \Rightarrow \Lambda &= -\frac{\lambda_{\text{Laser}} \cdot f_1 \cdot f_{\text{MO}}}{\Delta\rho \cdot f_2}\end{aligned}\quad (2.15)$$

Here, $\lambda_{\text{Laser}} = 1064 \text{ nm}$ is the wavelength of the used laser. By inserting this into Equation 2.14, and introducing the effective focal length $f_{\text{eff}} = f_1 \cdot f_{\text{MO}}/f_2$, we get:

$$\varphi_{jk} = \frac{2\pi \cdot d_{\text{Pixel}} \cdot \Delta\rho}{\lambda_{\text{Laser}} \cdot f_{\text{eff}}} \cdot (j \cdot \cos(\theta) + k \cdot \sin(\theta)) \quad \text{mod } 2\pi \quad (2.16)$$

$\Delta\rho$ denotes the distance of the resulting trap has from the 0th order. The length f_{eff} is the effective focal length of all the optics after the SLM, including the objective. To calculate its theoretical value, we can use $f_{\text{MO}} = 200 \text{ mm}/m$ for the focal length of the objective, with m being the objective's magnification. Because our setup used $f_1 = 500 \text{ mm}$ and $f_2 = 750 \text{ mm}$, the theoretical value for the effective focal length using the 60 \times objective is $f_{\text{eff}} = 2.222 \text{ mm}$. Via calibration, we found the value of f_{eff} to be $f_{\text{eff}} = 2.253 \text{ mm}$ when using the 60 \times objective, which is only 1.4% above to the theoretical value. If another magnification is used, the effective focal length has to be scaled inversely with the magnification. For example, when using the 40 \times water immersion objective, the value needs to be adopted according to $f_{\text{eff},40\times} = 60/40 \cdot f_{\text{eff},60\times}$.

An axial shift of the trap can be produced by setting the hologram to represent a Fresnel lens:. This fresnel lens can be discribed by the following phase pattern:

$$\varphi_{jk} = \frac{\pi}{X} \cdot (d_{\text{Pixel}})^2 \cdot \left((j - j_0)^2 + (k - k_0)^2 \right) \quad \text{mod } 2\pi \quad (2.17)$$

The value of X has the dimension of an area. The relationship between the focal length of the Fresnel phase pattern and the parameter X can be understand in this way: When $j - j_0 = 0$ and $k - k_0 = 0$, the phase φ_{jk} is zero. For $(d_{\text{Pixel}})^2 \cdot (j - j_0)^2 = 2X$ and $k = k_0$, the phase shift applied to incoming light by the SLM is 2π . In simpler terms, moving $\sqrt{2X}$ away from the center of the lens results in a phase shift of 2π . This can be compared to a regular curved mirror (see Figure 2.9). In the case of a curved mirror, for small angles, the phase of the light leaving the mirror experiences a 2π shift relative to the incoming light at a distance of $\sqrt{2\lambda f}$ from the optical axis. Here, f represents the focal length of the mirror, and λ denotes the wavelength of the light used. By comparing this with our phase hologram, we arrive at the equation $\sqrt{2X} = \sqrt{2 \cdot \lambda_{\text{Laser}} \cdot f_{\text{SLM}}}$, or simply $X = \lambda_{\text{Laser}} \cdot f_{\text{SLM}}$.

The focal length f_{SLM} necessary for a certain axial shift Δz can be found using Equation 2.13. For example shifting the focus by $\Delta z = 1 \text{ }\mu\text{m}$ requires a focal length of $f_{\text{SLM}} = 6.5679 \text{ m}$ when using the 60 \times objective. Inserting this into $X = \lambda_{\text{Laser}} \cdot f_{\text{SLM}}$ results in:

$$X = \lambda_{\text{Laser}} \cdot f_{\text{SLM}} = \lambda_{\text{Laser}} \frac{f_1^2 \cdot (f_{\text{MO}})^2 \cdot n}{f_2^2 \cdot \Delta z} \quad (2.18)$$

If we insert the values for $f_1 = 500 \text{ mm}$, $f_2 = 750 \text{ mm}$ and $f_{\text{MO}} = 200 \text{ mm}/m$, and use $n = 1.33$ as the refractive index of the immersion water and the imaging medium, we obtain

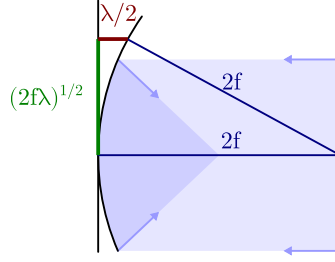


Figure 2.9: Relationship of curvature and focal length of a curved mirror. The focal length of a spherical mirror is half its radius. Assuming a flat wavefront hits the mirror, at some distance away from the optical axis the mirror will have curved in by half a wavelength. At this point, the reflected wave will have a phase shift of 2π against a wave reflected in the mirror's center. Assuming small angles, this distance is equal to $\sqrt{2\lambda f}$, where λ is the used wavelength and f is the focal length of the mirror. This analogy can be used to understand how the focal length of a Fresnel lens phase hologram can be calculated, since there, the distance in which the phase shift reaches 2π is $\sqrt{2X}$, which implies that $X = \lambda_{\text{Laser}} f_{\text{SLM}}$.

the following, calculated relationship:

$$X_{\text{calc}} = 2.5158 \cdot 10^{-8} \text{ m}^2 \cdot \frac{1}{m^2 \cdot \Delta z} \quad (2.19)$$

The coordinates j_0 and k_0 in Equation 2.17 mark the position on the SLM on which the middle of the lens falls. Ideally, this should be exactly the middle of the SLM ($j_0 = 256.5; k_0 = 256.5$). However, we found that the center point had to be moved 20 px in the $+x$ direction and 10 px the $-y$ direction to the position ($j_0 = 276.5; k_0 = 246.5$). This adjustment is necessary, because despite careful alignment, the laser beam seems to hit the SLM slightly off-center by those 20 px, corresponding to 0.3 mm. Without this adjustments, the resulting Fresnel phase pattern will not be aligned with the incoming beam. This would result in the trap not only being shifted axially, but at the same time the lateral position of the trap would move slightly, which is undesired. However, axial and lateral shifts can be created simultaneously by adding the phase values in Equation 2.16 and 2.17.

To test our setup, the values for $X(z)$ have been also been acquired experimentally by measuring the axial shift of the trap for different values of X^{-1} and then fitting a parabolic function to $X^{-1}(\Delta z)$. This was done separately for the 40 \times - and the 60 \times -objective and resulted in the following empirical relationships:

$$\frac{X_{\text{emp}}}{(d_{\text{Pixel}})^2} = \begin{cases} \left(1.4316 \cdot 10^{-5} \cdot \frac{\Delta z}{1 \mu\text{m}} + 4.9475 \cdot 10^{-9} \cdot \frac{\Delta z^2}{(1 \mu\text{m})^2} \right)^{-1} & \text{for 40}\times \text{ objective} \\ \left(3.2035 \cdot 10^{-5} \cdot \frac{\Delta z}{1 \mu\text{m}} + 2.9620 \cdot 10^{-8} \cdot \frac{\Delta z^2}{(1 \mu\text{m})^2} \right)^{-1} & \text{for 60}\times \text{ objective} \end{cases}$$

These exact equations have been used to calculate the phase holograms in the MATLAB code within our lab for many years. The parabolic function was fitted as an empirical approach and enabled to calibrate the setup in z-direction without direct knowledge about the involved optics. It should however correspond to the theoretical value X_{calc} above, which we will test

now. For small Δz less than $5 - 10 \mu\text{m}$, the error from neglecting the quadratic term is small and a linear relationship can be assumed. By doing this and also multiplying the equation by $(d_{\text{Pixel}})^2 = (15 \mu\text{m})^2$, the equation gets much clearer:

$$X_{\text{emp}} = \begin{cases} 1.5717 \cdot 10^{-11} \text{ m}^2 \cdot \frac{1}{\Delta z} & \text{for } 40\times \text{ objective} \\ 7.0236 \cdot 10^{-12} \text{ m}^2 \cdot \frac{1}{\Delta z} & \text{for } 60\times \text{ objective} \end{cases}$$

Furthermore, we know that the factor X should scale with the squared reciprocal of the objective's magnification (see Equation 2.19). We can resolve the need to use different formulas for different objectives by introducing the objective's magnification m into the equation:

$$X_{\text{emp}} = \begin{cases} 2.5147 \cdot 10^{-8} \text{ m}^2 \cdot \frac{1}{m^2 \cdot \Delta z} & \text{for } 40\times \text{ objective} \\ 2.5285 \cdot 10^{-8} \text{ m}^2 \cdot \frac{1}{m^2 \cdot \Delta z} & \text{for } 60\times \text{ objective} \end{cases}$$

Since the two factors are now very similar, we can use the average for our final empirical formula for the value of X :

$$X_{\text{emp}} = 2.5216 \cdot 10^{-8} \text{ m}^2 \cdot \frac{1}{m^2 \cdot \Delta z} \quad (2.20)$$

The factor here is just 0.2% larger than the theoretical value X_{calc} , which impressively shows the power of the paraxial approximation. By using this elegant equation instead of the inverse of the second polynomial above, the code complexity could be further reduced, while still being reasonably accurate for $\Delta z < 10 \mu\text{m}$.

2.2.7.4 Characterization of the hologram efficiency

The trapping beam used to create optical tweezers enters the sample via the objective. While the sample is mostly transparent, a small amount of the infrared trapping beam makes its way back into the objective and onto the imaging sensor by scattering or reflection. Usually, a filter is placed in the observation beam path to avoid this scattered light from interfering with the image, which renders the optical traps invisible in the acquired images. However, most sensors of digital cameras can very well detect infrared light, if no infrared filter is used. One way of checking the intensity distribution inside the sample, is to focus on the interface of the glass coverslip and the water on top of it. Because a part of the trapping laser is reflected by the interface from glass to water, the laser's reflection on the coverslip is directly visible if the infrared filter is removed from the observation beam path. This provides a way of observing the position and the intensity of the deflected main beam when using different gratings on the SLM.

To do this, we moved the trap by $2 \mu\text{m}$, $5 \mu\text{m}$, $10 \mu\text{m}$, $14 \mu\text{m}$, $18 \mu\text{m}$ and $24 \mu\text{m}$ from the 0th order in 16 different directions. In Figure 2.10, the probed trap positions are depicted as colorful circles. For each position, the hologram was generated, applied to the SLM, and after a short time an image was recorded using the pco pixelfly camera. Later, the position of the trap in the image was detected by correlating the acquired image with a image of the reflection of the 0th order without any hologram applied and subsequently detecting the position of the maximum correlation. This position is shown in the Figure as a small cross for

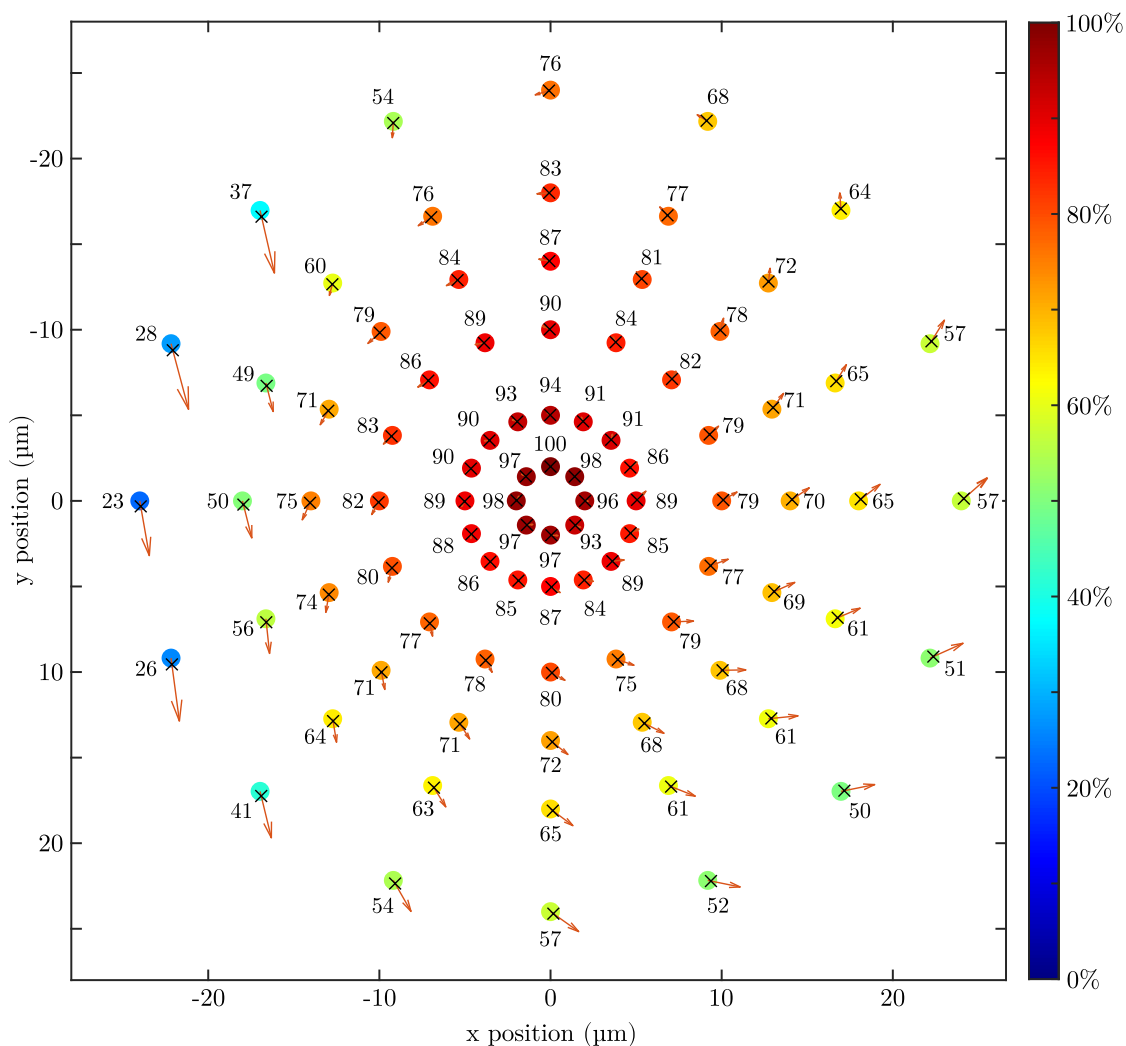


Figure 2.10: Laser deflection and intensity created by different holograms. Shown are the relative intensity and the locations of the laser reflection on the coverslip for different gratings creating different displacements of the trap. The x and y -axis are the displacement on the coverslip using the $60\times$ -objective in micrometers. The colorful circles indicate the expected position of the trap according to the applied deflection. The color of the circles along with the written percentages show the intensity of the observed trap relative to the trap visible without any hologram applied. The small \times -shaped markers on top of the circles represent the observed positions of the traps which – except for a very slight rotation of the camera relative to the SLM – align very well with the predicted positions. To emphasize the deviations, arrows showing the error in the trap placement exaggerated 10-times were added to the measured trap positions. It is visible that the traps are very efficient for displacements smaller than $10\mu\text{m}$, but at larger displacements the grating is not able to efficiently deflect the beam anymore. The asymmetry of the deflection intensity can be explained by the fact that the laser was aligned to hit the SLM at a slight angle, which breaks the symmetry in x -direction.

each trap. Furthermore, the intensity of the reflections was measured by calculating the mean image intensity in a radius of $3\ \mu\text{m}$ around the detected beam position. The mean intensity around the trap's reflection was divided by the mean intensity of the beam reflection when no hologram is applied. This way, a map of the relative trap intensities depending on the trap position could be created, as shown in Figure 2.10. The color of each circle as well as the small number next to each circle indicate the relative intensity of the observed trap's reflection on the coverslip.

When deflecting the beam by $5\ \mu\text{m}$ or less, the beams intensity always stayed above 85% of the beams intensity without any hologram. However, when using deflections of $14\ \mu\text{m}$, the deflected beam's intensity dropped to around 50%...60%. This is because in order to achieve such high deflections, a holographic grating with very fine lines is needed. The high amount of phase jumps from 0 to 2π cannot be displayed perfectly by the SLM, as some transition zone in which the liquid crystals reorient is unavoidable. This reduces the hologram's refraction efficiency. The missing intensity partly gets scattered across the whole sample, another part might not be redirected at all. Because of that, all our experiments were done using small deflections below $10\ \mu\text{m}$.

When comparing the trap's intensity for deflections in $-x$ and $+x$ direction, it is noticeable that the trap does get weaker quicker for large $-x$ deflections than for large deflections in the $+x$ direction. This may be explained by the fact that the laser hits the SLM at a slight angle, which breaks the symmetry in this axis. This off-axis setup is chosen because it separates the incoming light from the light leaving the SLM, which avoids the need for an additional beam splitter, maximizing the usable laser power. Luckily, the asymmetry is insignificant for smaller deflections. Figure 2.10 also shows that the calibration of the lenses-and-gratings algorithm was done correctly, as the crosses highlighting the measured trap positions closely match the intended trap positions marked as circles. To better highlight the differences, small arrows were added to the figure which indicate the error in the trap placement with a 10-fold exaggeration. Except for a very slight rotation of around of the measured trap positions around the origin, no systematic errors in the trap positioning could be identified. The size of this rotation indicates that the pixelfly camera used to measure the traps' positions is rotated by 0.5° relative to the axis of the SLM.

2.2.7.5 Multi-trap holograms

To create multiple traps, multiple gratings used to produce the individual traps have to be combined into a single hologram. This can be done by using complex phase factors to represent the holograms^[169]. The n -th hologram of a set of N holograms can be represented by the complex number array $\hat{\varphi}_{jk}^{(n)} = \exp(i\varphi_{jk})$. This array of complex numbers contains the phase change φ_{jk} applied to the beam at each pixel as a complex argument. The absolute values of the phase factors $|\hat{\varphi}_{jk}^{(n)}|$ represent the attenuation at the position of each pixel and are always exactly one for the individual holograms. This is true because the beam's intensity is not changed by the pure phase-holograms. By summarizing over the complex phase factors of multiple holograms, we obtain the complex representation of the combined hologram:

$$\hat{\varphi}_{jk} = \sum_{n=1}^N e^{i\varphi_{jk}^{(n)}} \quad (2.21)$$

Unfortunately, summarizing over multiple complex numbers which all have the absolute value of 1 can result in complex numbers with totally different absolute values. This means that the hologram represented by $\hat{\varphi}_{jk}$ is no longer a pure phase-hologram. To accurately display the hologram on the SLM the intensity of the beam exiting each pixel would have to be controllable, which is not possible with an SLM. The solution is to simply ignore the necessary intensity modulations and only use the argument of the complex phase factors to calculate the array of phase shifts:

$$\varphi_{jk} = \arg \left(\sum_{n=1}^N e^{i\varphi_{jk}^{(n)}} \right) \quad (2.22)$$

Experience has shown, that the hologram will still create optical traps at the desired locations. As noted by the original authors^[169], ignoring the amplitude of the sum of the phase factors leads to intensity variations between the individual traps. However, the effects of this simplification are hard to predict and were not studied any further by the authors. We noticed that the new hologram can have periodicities which are not present in the holograms for the individual traps, which can lead to additional focus points at unwanted locations, which are typically called ghost traps. These ghost traps are especially prominent when two traps in direct vicinity are to be created. Also, ignoring the amplitude of the complex phase factor can lead to bad performance of the holograms for highly symmetric trap patterns. Despite those drawbacks, the phase factor addition method of combining two holograms performed well during our experiments. However, the unclear consequence of ignoring the amplitude leaves a trace of dissatisfaction.

A superior method of combining multiple holograms into one is to use a random masking algorithm^[172]. To create multiple traps at once, the holograms for each individual trap are calculated by the lenses-and-gratings algorithm as before. Instead of adding the complex phase factor to calculate the necessary phase map, each of the SLM pixels is allocated to a specific trap. Each pixel then displays its value in the hologram of this individual trap. The SLM pixels are not divided by a geometric method, but simply assigned at random to a certain trap, avoiding any periodicity in the pixel allocation, which reduces the amount of ghost traps significantly. A drawback to the random masking approach is its lower efficiency, which limits its use to scenarios in which only a few traps are needed^[172]. This might be caused because holograms generated this way contain regions with rapidly changing phase shifts. A real SLM might struggle to display these abrupt transitions in the hologram due to technical limitations, as the orientation of the liquid crystal molecules needs some transition zone to change between pixels. However, in our tests using only two traps as shown in Figure 2.11, this lower efficiency was not noticeable, it however may have a bigger impact in experiments which require a higher number of traps. The random mask encoding outperforms the phase addition algorithm in all cases. When calibrating the traps generated by a hologram using random mask encoding, we have to keep in mind that due to the random nature of the algorithm the hologram might change when regenerating a the hologram, even when using the exact same trap geometry. It is unclear how strongly the choice of the random mask – meaning which pixel is assigned to which trap – influences the trap stiffnesses. This can be easily avoided by using pseudo-random masks with a fixed seed.

In conclusion, both methods work satisfactory. Due to longer experience with the lenses-and-gratings algorithm and its deterministic nature, it was the primary algorithm used when working with multiple traps during this thesis. In the future it might be sensible to shift

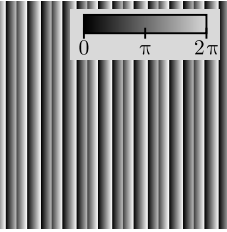
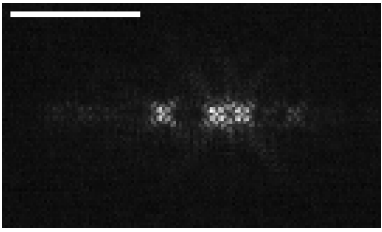
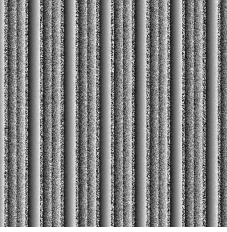
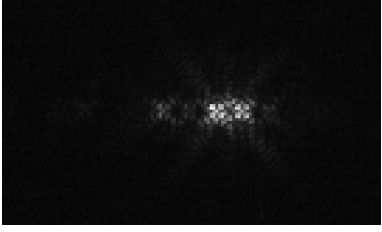
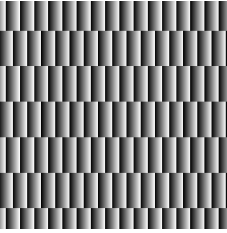
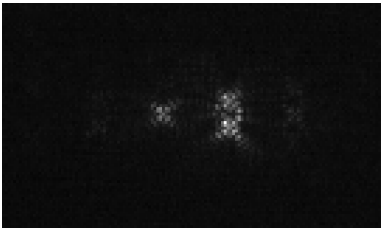
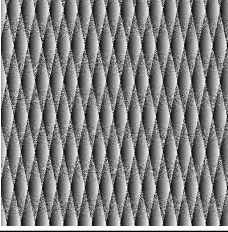
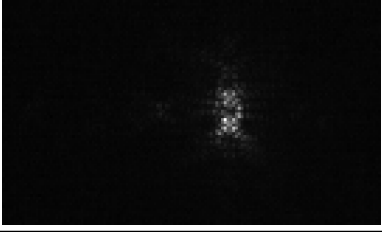
trap positions	algorithm	phase hologram	image of laser reflection
$\begin{pmatrix} 4 \\ 0 \\ 0 \end{pmatrix}; \begin{pmatrix} 6 \\ 0 \\ 0 \end{pmatrix}$	phase addition		
	random mask encoding		
$\begin{pmatrix} 5 \\ 1 \\ 0 \end{pmatrix}; \begin{pmatrix} 5 \\ -1 \\ 0 \end{pmatrix}$	phase addition		
	random mask encoding		

Figure 2.11: Comparison of different methods to combine multiple holograms. Combining two holograms into one was tested and compared using the phase addition (PA) and the random mask encoding (RME) algorithms. While the resulting phase patterns were different, they created similar laser patterns as visible in the images of the laser reflection on the coverslip-water interface. The random mask encoding algorithm seemed to be superior, as the 0th order and possible ghost traps were less visible. The images were recorded using the pco pixelfly camera, the scalebar represents a length of 10 μm.

towards using the random mask encoding algorithm as the primary hologram combination algorithm.

Finally, we noticed that the reflection of the laser on the coverslip showed a strange, four-fold symmetry (see. Figure 2.11). As the beam creating the traps was a perfect Gaussian beam, we would expect the reflections to also show a Gaussian intensity distribution. However, the beam hitting the SLM has a diameter of approx. 7.5 mm as measured with the beam profiler, and the SLM has a square shape with an edge length of 12.8 mm. This means that only about 85% of the incoming intensity are reflected from the SLM, while the rest misses the rectangular mirror of the SLM. Because of that, the reflected beam is cropped, and the profile of the beam exiting the SLM is no longer Gaussian. This might be the cause of said four-fold symmetry. However, over-illuminating the SLM was not done without intend, as a fully illuminated SLM ensures that the maximum spatial resolution in the placement of the optical traps can be achieved. If the incoming laser was much smaller than the SLM, only the few illuminated pixels of the hologram could interact with the reflected light, which would severely limit the resolution of the trap generation. After all, choosing the right beam diameter is a compromise. The fact that the four-fold symmetry of the laser's reflection was perfect and the laser's intensity distribution along any axis through it's symmetry center was symmetric supports the fact that the laser is actually properly aligned. If any astigmatism was present in the system, we would expect the laser's reflection to show different profiles in x - and y -direction.

In theory, the beam shape could be fine-tuned by adding a static corrective hologram to all holograms which create the traps^[173]. Using this approach, any astigmatism in the trapping beam can be corrected without the need to add additional optical elements. This could also further improve the trapping performance for small particles, as for smaller particles deviations in the beam shape have a stronger impact on the trapping stiffness.

2.2.7.6 The Gerchberg-Saxton algorithm

Using the Gerchberg-Saxton algorithm^[168], it is possible to generate pure phase holograms which, when displayed on a spatial light modulator, can create arbitrary two- or three-dimensional intensity distributions^[174,175]. To do that, the sample plane (or volume) is divided into pixels (or voxels) and the desired intensity of each pixel is stored in a matrix. From this data, the algorithm uses an iterative approach relying on the fast Fourier transformation to calculate the necessary hologram. The method provides more versatility than the lenses-and-gratings algorithm, for example it is able to distribute intensity equally into defined volumes. However, this dexterity comes at the cost of complexity. The pixelation of the sample area requires choosing parameters such as pixel size and trap width, and the iterative approach of the hologram calculation requires more processing time. Because of this, and the lack of necessity, the Gerchberg-Saxton algorithm was not used during any cell experiments throughout this work. Instead, the lenses-and-grating algorithm as described above was used. However, the feasibility of this method was demonstrated experimentally. To do this, we created an image representing the desired intensity distribution. This image is shown in Figure 2.12a. Then, a custom MATLAB script implementing the Gerchberg-Saxton algorithm was used to compute a fitting hologram, which is shown in Figure 2.12b. This hologram then was applied to the SLM and the resulting laser pattern was captured by imaging the laser's reflection on the coverslip-medium interface. As visible in Figure 2.12c, the observed intensity pattern closely resembles the reference image in Figure 2.12a, proving that the

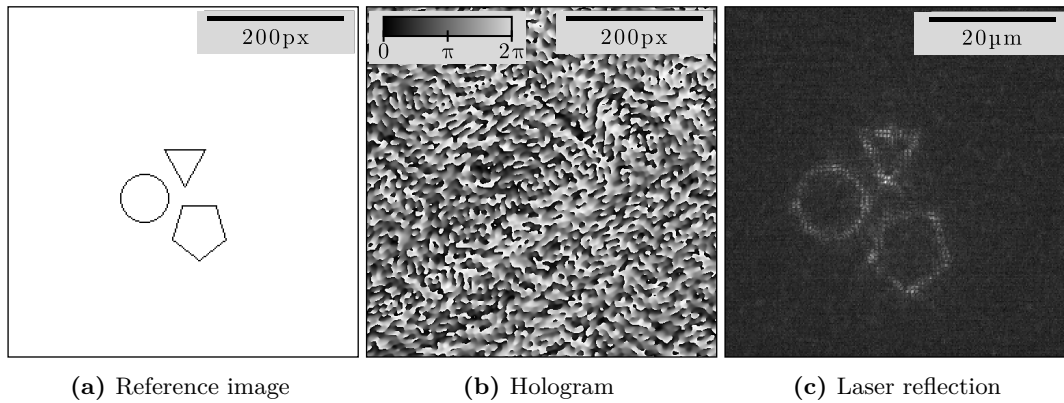


Figure 2.12: Experimental demonstration of the Gerchberg-Saxton algorithm. Using the reference image (a), the hologram in panel (b) was created. The hologram is 512×512 pixels large to fit the SLM exactly. When applied to the SLM, the laser light is directed to create the desired intensity distribution inside the sample. This was observed by focusing onto the coverslip surface, where part of the laser light reflects back into the camera. The observed laser reflection shown in panel (c) fits the provided reference image well, proving that the algorithm works. The reference image (a) is only shown partially, the full image has a size of 512×512 pixels. The position of the 0^{th} order, which the laser would have hit without an active hologram, is still visible as a slight intensity peak at the bottom tip of the triangle.

Gerchberg-Saxton algorithm can be used to find fitting holograms for arbitrary intensity distributions. Because of the non-perfect efficiency of the hologram, the 0^{th} order, i.e. the spot the laser would hit without any hologram, is still visible as a slight intensity peak in the observed intensity distribution in Figure 2.12a as a slight increase in intensity at the bottom tip of the triangle. This proof-of-concept shows that using the used holographic optical tweezers setup is suitable for using the Gerchberg-Saxton algorithm. This might be relevant for future applications that require complex intensity distributions.

2.2.8 Experimental procedure

As a first step, all necessary electronic equipment was powered on and the heating chamber was allowed to reach 37°C , which usually took 45 to 60 minutes. The laser was switched on about 10 minutes before the first experiment and allowed to heat up. Directly before preparing the sample, the laser power after Lens L1 (see Figure 2.6) was measured using a digital handheld power meter (PM100D; Thorlabs, Newton, New Jersey, United States). Then, the measured laser power after lens L1 was adjusted to 500 mW by turning the half-wave plate in front of the polarizing beam splitter, which increases or decreases the amount of light passing the beam splitter. It should be noted that the laser power measured at this point is not the trap laser power in the sample, as further optical components such as the two lenses L1 and L2, the periscope, the dichroic mirror in the microscope and the objective all will introduce some attenuation. For example, the $60\times$ objective transmits only 70% at the wavelength of the trapping laser ($\lambda = 1064\text{ nm}$), according to the manufacturer. It is also possible that the objective is over-illuminated and some light is blocked by the objective's finite entrance pupil.

For each experiment, a sample containing J774A.1 macrophages and opsonized beads suspended in the medium was assembled as described in chapter 2.2.4. For some of the

experiments, the macrophages were previously treated with siRNA. Then the 60 \times objective of the microscope was prepared by putting a drop of immersion water onto the objective. The sample was then transferred to the microscope and the objective was raised until the cells adhering to the coverslip were in focus. Then, the illumination apparatus of the microscope was aligned to achieve Köhler illumination.

After fixing the intensity of the brightfield illumination, the exposure times for all used cameras were set so that the full dynamic range of the camera is used. To avoid problems during tracking, the exposure times were set short enough to prevent any overillumination in the brightfield images. This is not true for the acquisition of differential interference contrast (DIC) images, where some overillumination of the beads can be tolerated to gain higher contrast on the cell's features. Depending on the exact type of measurement, different camera configurations were used. An overview of the used image acquisition configurations can be found in Table 2.3. This table also lists the exact number of experiments performed on the different bead sizes and cell types.

In most dual-bead experiments, brightfield and DIC images were recorded alternately using the Luca-R camera with a frame rate of 0.2 s⁻¹ each. To achieve that, the DIC analyzer was placed in the motorized filter cube revolver where it was automatically inserted and removed from the observation light path between each image. In experiments involving 1 μ m-sized beads, z -Stacks were acquired to make locating the small beads more reliable. In this case, no DIC images were recorded. Instead a stack of four brightfield images, with a focal shift of 1.5 μ m between images, were recorded. This was the maximum amount of images possible while maintaining the frame rate of 0.2 s⁻¹.

Some experiments were performed on LifeAct-transfected cells in order to study the actin polymerization during the phagocytic cup formation. In these cases, an additional fluorescence image had to be recorded. To do that, the microscope was set to switch the filter revolver between the DIC analyzer and the GFP-L filtercube. Both the fluorescence and the brightfield image were recorded with the GFP-L filtercube in the light path. The brightfield and the fluorescence image were taken quickly after each other by briefly opening the corresponding illumination shutter for the exposure time of the image. This way the frame rate could be kept at 0.2 s⁻¹ even when recording the additional GFP image every frame. However, the

cell type	bead size		
	1 μ m	2 μ m	3 μ m
WT	BF stack (78)	2-part BF/DIC (48)	2-part BF/DIC (86)
LifeAct	BF/DIC/GFP (4)	BF/DIC/GFP (21)	BF/DIC/GFP (3+3)
WT + siRNA CD64	BF stack (30)	BF/DIC (30)	BF/DIC (30)
WT + siRNA negCtrl	BF stack (15)	BF/DIC (13)	BF/DIC (15)

Table 2.3: Acquisition modes of dual-bead experiments for different bead sizes and cell treatments. The green numbers in parenthesis indicate the number of experiments performed. In all experiments except for the 2-part experiments, all images in all channels were recorded sequentially using the Luca-R camera with a frame rate of 0.2 s⁻¹. Experiments using 2 μ m and 3 μ m-sized beads on wildtype cells were split into two parts: For the first 5 – 10 min, the brightfield and DIC images were captured simultaneously with a high frame rate using the IDT Nx4-S2 and the Andor iXon Ultra cameras. After that, the Luca-R camera was used as in the other experiments.

additional image recorded each five seconds made it unfeasible to record z -stacks during the experiments using $1\ \mu\text{m}$ performed on LifeAct beads. However, as a test, in three of the six experiments performed on LifeAct-transfected cells using $3\ \mu\text{m}$ -sized particles, a z -stack of images for all three different channels was recorded. This caused the framerate to drop to 0.13 fps. All other experiments on LifeAct-transfected cells were performed as before without acquiring a z -stack.

After the cameras were configured correctly, the function of hologram generation was tested. This was done due to occasional problems with the communication of the acquisition software and the SLM. To do this, the focal plane was set on the interface of the coverslip and the medium in a section without a cell, the infrared filter was removed from the observation light path and the brightfield illumination was turned off. This way, when opening the laser shutter, the reflection of the laser beam becomes visible in the camera image. By switching between different desired trap positions and observing the laser reflection, the correct function of the hologram generation and the communication with the SLM can be checked.

Finally, the infrared filter was put back into the light path and the hologram was set to generate two traps in a distance of roughly $5 - 10\ \mu\text{m}$. The laser shutter was closed. By moving the sample stage, a freely diffusing bead was searched. This bead was placed at the exact location of one of the traps, or slightly below the trap. Then, the laser shutter was opened. When done correctly, the bead should now be captured by the trap. Then, a new bead was searched to fill the second trap. To trap it, it would be possible to switch off the second optical trap independently from the first. However, we found that it was easier to move the sample in a swift movement, so that the bead crosses the trap's location slightly below its equilibrium position. This way, the bead falls into the trap. This has to be done quickly, because otherwise the radiation pressure from the laser pushes the free bead upwards and out of the focal plane. When both traps were occupied by opsonized beads, a vital cell was selected as shown in Figure 2.13.

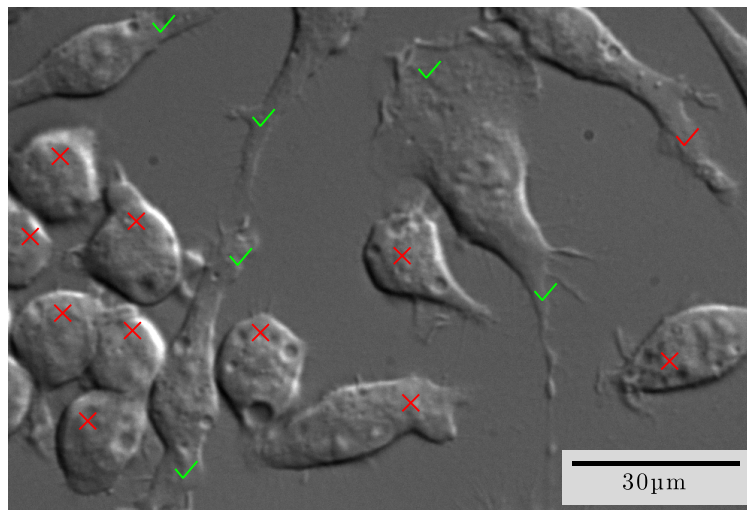


Figure 2.13: DIC image of different cell phenotypes and possible attachment points. Some cells are spread out across the coverslip, showing a various lamellipodia or filopodia. On those cells, attachment points suitable for our dual-bead experiments are highlighted by a green check mark. The red \times -shaped markers indicate cells with a more spherical shape that were usually avoided when selecting an attachment point.

Macrophages that spread out on the coverslip were preferred upon cells with a more spherical shape. This has several reasons: Firstly, J774A.1 macrophages are described as adherent^[121,176]. A strong adhesion force will typically spread out the cell on the coverslip. Another reason to avoid spherical cells, is the fact that cell contractions can indicate the start of mitosis, which is undesired during the course of the experiment. Cellular contraction and volume loss can also be an early sign of apoptosis^[177], a programmed cell death which can be triggered by cellular stress^[178] and can be described as the controlled decomposition of the cell. Because of these reasons, choosing a cell spread out on the coverslip increases the chance for a successful experiment. Additionally, if the cell is flat and extends over a larger area, the intracellular transport of the phagosomes during the experiment is easier to observe.

After a cell was selected, the region of the cell to which the beads will be attached was selected. If membrane ruffling was visible at one side of the cell, but not the other, this can indicate that the cell migrates in this direction. In this case, we choose to attach the beads to the region with active ruffling, as a macrophage migrating in tissue would most likely encounter pathogens with its advancing edge. If ruffling was not obvious, the region furthest away from the nucleus was chosen. The two beads were then brought into the proximity of the attachment point by moving the sample. After that, the beads were moved relative to each other by repeatedly generating new holograms with a slightly different trap geometry. The bead pair was rotated until both beads had the same distance towards the cell's contour on the coverslip and the bead-to-bead distance was gradually decreased until a defined value was reached. The sample was shifted until the beads were hovering a few micrometers above the cell. A diagram of this situation can be found in Figure 2.14. After starting the image acquisition, the sample was slowly moved upwards until the cell touched both beads. Then, the behavior of the cells was observed. As soon as one of the beads has moved out of its trap, the laser shutter was closed and no optical forces were applied to the beads for the rest of the experiment. The uptake and the transport of the beads then was observed for an extended period of time.

This observation period lasted for around 45 min in most experiments. In some experiments, mainly experiments using 2 μm -sized particles on untreated cells, the observation was terminated early if the beads had clearly separated for multiple minutes. While acquiring the data on the 1 μm and 3 μm -sized beads, this course of action was abandoned in favor of a more standardized acquisition period. In those experiments, a fixed amount of frames were recorded, regardless of the beads' movement. Usually, 550 frames at a frame rate of 0.2 fps were recorded, which corresponds to an observation period of around 45 min. Experiments where the beads displayed no discernible movement throughout this entire duration were omitted from the dataset. Moreover, experiments featuring evident signs of cell apoptosis were also excluded. After the experiments, the trajectories of the two beads were determined by using the radial tracker on the captured brightfield images as described in chapter 2.2.9.

2.2.9 Radial symmetry center tracking

To detect the position of beads in images acquired by brightfield microscopy, numerous established methods have been developed. Utilizing a cross correlation tracker is a common and, under ideal circumstances, very accurate method^[179,180]. Cross correlation trackers rely on a reference image of the tracked object to locate it in the captured image.

However, cross-correlation algorithms can introduce errors if the tracked object's appearance changes or if other objects move into the tracking window during the measurement. In this

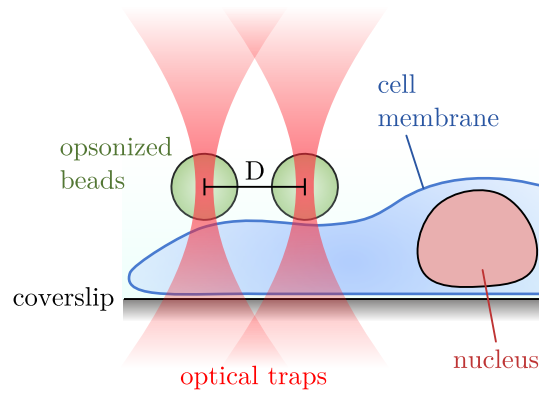


Figure 2.14: Attachment of a bead pair to a cell. To start a dual-bead experiment, two beads were caught in individual optical traps and brought close to each other until the target distance d was reached. Then they were attached to the periphery of a macrophage by placing them above the macrophage and finally lifting the sample until the trapped beads touched the cell membrane.

thesis, these problems emerged because it was difficult to keep both beads in focus when they moved along the optical axis during the measurement, leading to changing bead appearances. Additionally, in the dual-bead experiments discussed in this chapter, two beads in close proximity had to be tracked amid cell organelles. Overlapping beads posed a problem for the accuracy of cross-correlation trackers. A radial symmetry-based tracker and a masking technique that ignores the overlapping second bead inside the tracking window were used to resolve these concerns. This tracker is based on the fact that round objects can be located easily by searching for centers of radial symmetry in the image.

The radial tracker uses an approach adopted from Parthasarathy^[181] to non-iteratively calculate the best fitting radial symmetry center of a given image. It should be mentioned that a very similar algorithm was published by Ma et al. around the same time as Parthasarathy^[182]. The bead position is calculated based on the pixel values in a circular region around the estimated bead position. A detailed description can be found in the original paper^[181]. Pixels which are too close to other tracked objects are excluded from the calculation using a masking method similar as described by Yücel and Okumuşoğlu^[183] which allows precise multi-bead tracking. The operating principle of this algorithm will be the topic of the following paragraphs.

To start with the tracking, the positions of the objects in the first frame have to be provided to initialize the tracking algorithm. These positions can be obtained by different means, the easiest is to manually specify them. Other methods would involve correlating the first image with a reference image of a single bead. If any regions of the first image look similar to this reference bead, a peak will appear in the correlation matrix, which then can be located by using a peak finder algorithm. However, since the bead positions only have to be specified for the first frame of a image series, all software used during this thesis relies on manually specifying them. This image, together with a set of coarse object positions, as illustrated in Figure 2.15a, can then be passed on to the function `snapInUsingRadialTracker.m`. This function, developed by myself, refines the object positions to fit the local radial symmetry center around the specified coarse object positions. In all frames following after the first, the position of the objects in the previous frame is used as a coarse object position around which

2 Measuring the spatial resolution limit of phagocytosis

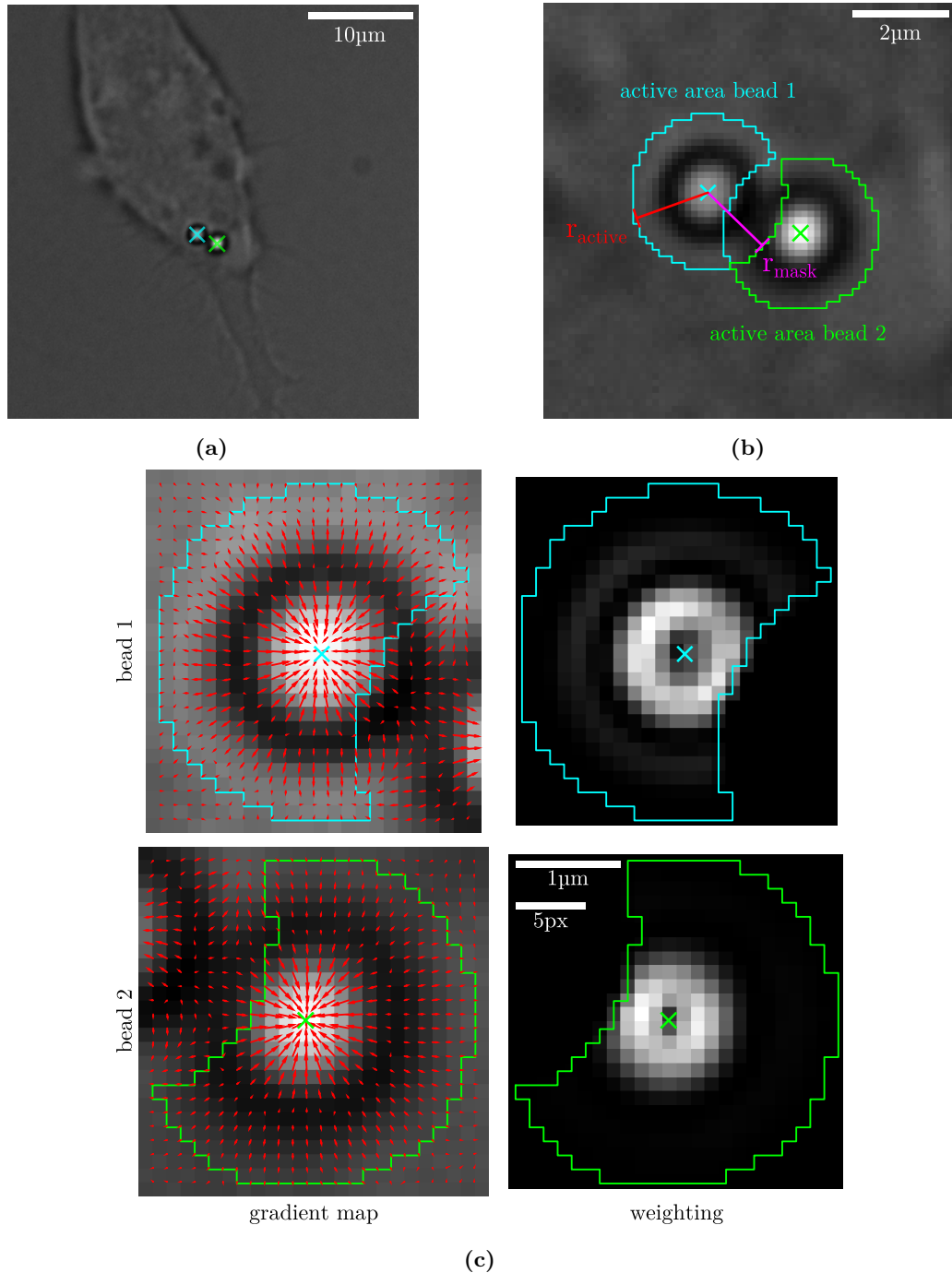


Figure 2.15: Example of the radial tracker's operation. Panel (a) shows an image of two 2 μm-sized beads on a cell captured during the dual bead measurements. The starting positions for the tracker are marked with crosses. In panel (b), the selection of the active area used for calculating the radial symmetry center is shown. Finally, panel (c) shows how the gradients and the weighting factors used in the algorithm are calculated. Note that the weighting map is one pixel smaller in each direction than the cropped image, as the weights apply to the gradients. The finally calculated radial symmetry center of each active area is marked with a cross.

a local radial symmetry center will be search. The algorithm is easy to set up, as it only requires two parameters to be adjusted before the tracking, which are the active radius r_{active} and the masking radius r_{mask} . The active radius depends on the size of the tracked particle, the masking radius is only relevant when tracking more than one particle. The details on how this parameters were chosen will be discussed later.

In the second step, the function `snapInUsingRadialTracker.m` calls the subfunction `portableRadialTrackerGetMasks.m`, which was also written by myself, to define the active areas for all objects. These active areas are a subset of the pixels. For each object, the active area contains all pixels closer than r_{active} to the estimated object position, but at least r_{mask} away from the position of all other objects. An example is provided in Figure 2.15b. These active areas are the areas in which the gradient of the image will be used to determine the radial symmetry center for each object. The idea is that by excluding a region of the radius r_{mask} around each object from influencing the tracking of other objects, the algorithm will get more robust when tracking beads in close contact, as any overlapping regions of adjacent beads will be excluded. In Figure 2.15b, the active and the masking radius were chosen to be identical. This is not necessary, but was done during all tracking in this thesis. The logic is that if r_{active} is the radius of a circle containing the entire bead, the masking should be done with a similar radius to exclude adjacent beads from the active area. However, other settings are possible. A visualization on how the active areas change with the tracker settings and the particle distance is shown in Figure 2.16. If the distance between two particles is smaller than $2r_{\text{active}}$ and $r_{\text{mask}} < r_{\text{active}}$, a single pixel can be part of multiple active areas. If the masking radius is larger than r_{active} , more pixels will be excluded from the active areas, which can further reduce the impact on adjacent objects on the tracking accuracy. However, increasing the masking radius to values larger than r_{active} will also introduce a minimum distance in which objects can be tracked. If the objects are closer than $2(r_{\text{mask}} - r_{\text{active}})$, the active area is empty and tracking becomes impossible. For this another reason why $r_{\text{mask}} = r_{\text{active}}$ is a good choice, as the minimum tracking distance is zero in this case.

After the active areas are set, the image will be cropped for each object individually. The rectangular area to which the image will be cropped is chosen to be as small as possible while still containing the whole active area of the bead plus an additional row or column of pixels in each direction. These cropped images are shown in Figure 2.15c. The cropping is mainly done for speed, as all following operations will only need to be done on a small region around the active area instead of on the whole image. The coarse coordinates for each object in the whole image will be readjusted to fit the new, cropped image. This cropped image, together with a binary mask encoding which pixels of the cropped image are part of the active area for this object, and the coarse image coordinates are passed on to the function `radialcenter_masked.m`, which will calculate the object's position based on this information. While the other functions were developed fully custom for this thesis, the function `radialcenter_masked.m` was adapted from R. Parthasarathy's research paper published in Nature Methods^[181]. The original function was modified to implement the masking algorithm.

If the size of the cropped image handed down to the function `radialcenter_masked.m` is $M \times N$, the function calculates the image's intensity gradients at the edge points at which four pixels meet. This creates an array with the size of $(M - 1) \times (N - 1)$. The gradients are calculated only from the four pixels touching the edge point. After that, the gradient array will be smoothed by a simple 3×3 averaging filter, meaning that each gradient in the array is replaced the average of the 3×3 gradients around its position. This leaves us with

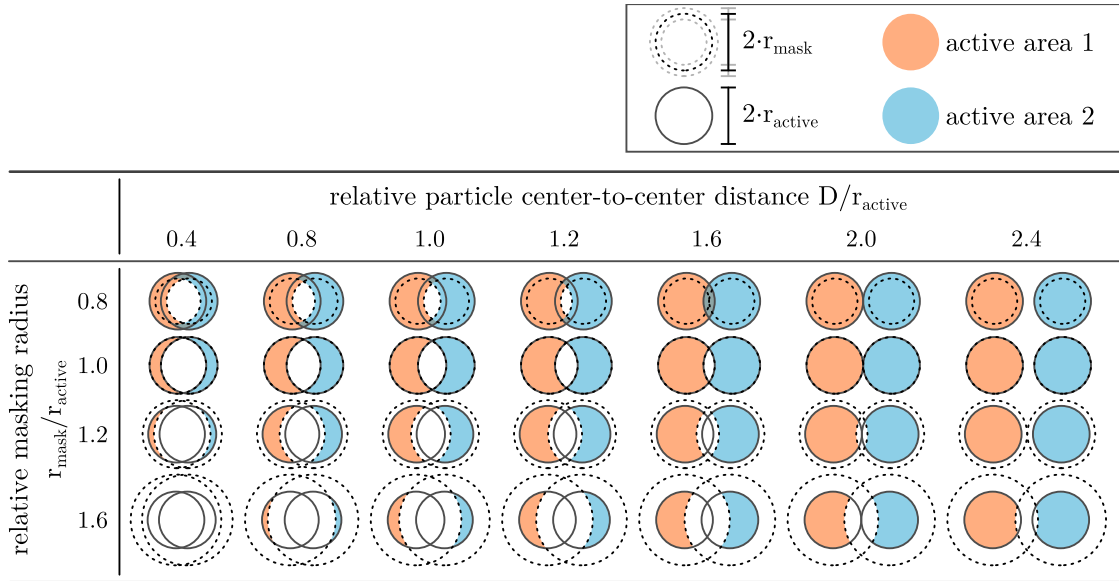


Figure 2.16: Active area shapes depending on the masking radius and the particle distance. For $D \geq (r_{\text{active}} + r_{\text{mask}})$, the active areas are circular. For $D < 2(r_{\text{mask}} - r_{\text{active}})$, as in the bottom left example, no active areas are left, meaning the particles cannot be tracked anymore at this distance. Every time the tracker was applied to experimental data in this thesis, r_{mask} and r_{active} were chosen identical, as shown in the second row in this table.

an array of gradient vectors whose direction and magnitude will be the basis of the radial symmetry center calculation. The gradient vectors are shown as red arrows in Figure 2.15c.

Before the symmetry center can be calculated, each gradient line will be assigned a weighting factor. This factor is calculated by dividing the squared magnitude of the gradient by its distance from the coarse object position. The weight of gradients from pixels outside of the active area will be set to zero. The weighting of gradients which lie directly on the edge of the active area will be reduced depending on how many of the four pixels from which the gradient was calculated lie outside the active area. For each pixel that lies outside the active area, the weighting factor will be reduced by 25%. This is visible when looking at the pixels below the active area border in the weighting maps in Figure 2.15c.

The next step defines the core of the algorithm. While during the calculation of the weighting factor only the magnitude of the gradient mattered, this step is based only on the direction of the gradients. For that lines are drawn through all pixel edge points in the direction of the gradient. The slope and the y-intercept of these gradient lines, defined by the position and direction of the gradient vectors in the image, are calculated and stored. Then, the point in the image, from which the weighted, squared sum of distances to all those gradient lines is minimal, is calculated. The idea behind this is, that for a radially symmetric object, most lines will meet roughly in the same spot in the middle of the object. Because not all lines will meet exactly in one spot, finding the position in the image for which the weighted sum of the squared distances to these lines is minimal, is a great way to find the average meeting point of the lines. An useful illustration of this process is shown in the original paper by Parthasarathy in Figure 1^[181]. Because of the linear nature of this problem and using the previously given information, the coordinates of this point can be calculated directly from

the matrix of gradients and weights. A detailed description on how this calculations work can be found the supplementary information to Parthasarathy’s paper.

While the calculation of the symmetry-centers itself is non-iterative, the active areas for the individual particles were based on estimated bead positions, either specified manually or adopted from the previous frame in an image series. After the radial symmetry centers have been determined for the active areas of all particles, the active areas can be adjusted using the newly calculated particle positions for this frame. Then again, the radial symmetry centers for all areas can be recalculated. This can be repeated multiple times until the symmetry centers do not change anymore. While this algorithm usually converges with only a few iterations, there are situations in which the algorithm gets stuck in a loop, repeatedly adding and removing pixels from an active area and moving the symmetry center periodically by a fraction of a pixel. During the scope of this thesis, this was dealt with by limiting the amount of iterations to 500.

A better solution was identified later, however, it was not put into use during the scope of this thesis. Instead of the binary decision to include a pixel into the active area or not, the pixels close to the edge of the active area can be weight with a factor continuously fading from one to zero in a narrow transition zone, approximately 1 px wide. This tapering of the active areas could greatly improve the convergence of the tracker. A suitable transition function would be the Planck-taper window function^[184], which is infinitely differentiable. This approach aligns with principles in signal processing, where mitigating spectral leakage is crucial for accurate analysis. Spectral leakage is a phenomenon where energy from a signal leaks into neighboring frequency bins due to the finite duration of a signal. This leakage can result in inaccurate frequency representations and distortions in the analysis. Choosing a smooth window function is a common strategy to address this issue^[185]. By analogy, the soft border introduced in the pixel weighting mechanism serves a similar purpose by smoothly transitioning the influence of pixels near the edge of the active area. This transition could mitigate abrupt changes and potential artifacts, contributing to a more robust and accurate tracking algorithm.

Now, that the position of the radial symmetry center in the image is known, we can calculate some scalar values which will be handy for monitoring the tracking process. The first value is called the unroundness of the object. It is a reference value on how good the radial symmetry is in the active area around the new bead position. It is proportional to the sum of the squared distances to the gradient lines, so it is basically the variable which has been minimized during the search for the radial symmetry center. The unroundness value has been normalized to a range of 0 to 1. This can be done by dividing the weighted squared sum of the distances from the symmetry center to all gradient lines by the weighted squared sum of the distance of all pixels in the active area to the symmetry center. An unroundness value of 0 means that all gradient lines meet exactly in the radial symmetry center, which means the object is perfectly radially symmetric. If the gradient lines are oriented randomly, as it is the case in a noise image without any object, the unroundness value reaches 0.5. Examples of patterns with different unroundness values can be found in Figure 2.17. The unroundness can reach 1 if all gradient lines around the symmetry center are aligned tangentially and the weighted squared sum of the lines distances to the symmetry center has reached its theoretical maximum. This case is purely theoretical, as after all the tracker tries to minimize the unroundness value. If the tracker is started at a location with an unroundness value larger than 0.5, it will quickly converge until it has found a spot with a lower unroundness value. Even in image regions with no object, due to random fluctuations the tracker will

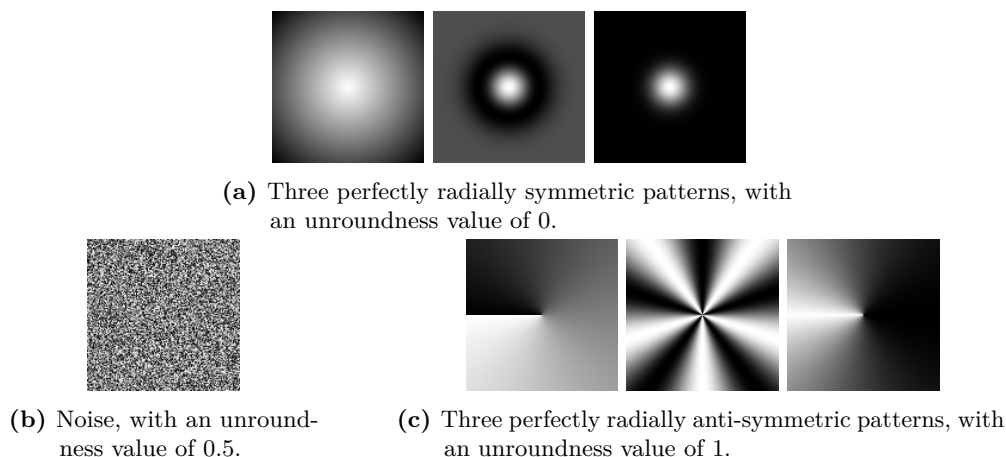


Figure 2.17: Examples for perfectly radially symmetric and perfectly radially anti-symmetric patterns. In the case of the perfectly radially symmetric images (a), all gradient lines meet exactly in the center, which will lead to the radial tracker to detect the center and return an unroundness value of zero. In the case of noise (b), the gradient lines are randomly oriented, which means that there is no special point with minimal distance from all gradient lines. The tracker will then drift around randomly. Unroundness values close to 0.5 occur and usually indicate the loss of the object. In the theoretical case of anti-symmetric patterns (c), all gradient lines are tangential to the center. The tracker will not be able to follow it, as the center is not the point of least weighted squared distance to all gradient lines in the active region. The unroundness value for the middle of those patterns would be 1, however when tracking beads in microscopic images unroundness values larger than 0.5 never occurred.

always find a spot with an unroundness value smaller than 0.5, even if only slightly. Because of this, unroundness values close to 0.5 usually indicate the loss of the object.

To provide easy access to these algorithms, a graphical user interface for this tracker has been developed by myself (`portableRadialTracker.m`). This GUI allows the user to load image files in three different file formats (`*.tif`, `*.avi` and `*.nd2`). After the image file is loaded, the user can specify the location of multiple round objects in the images and refine them using the radial symmetry tracking algorithm. Further, if the user specified the location of the objects in the first frame, it is possible to let the algorithm find the objects in subsequent images by iteratively refining the objects' positions to fit the symmetry centers in the next frame. The software also checks the unroundness value of each bead after each frame, and if it exceeds a customizable threshold (for example 0.4), or if the bead's position changes more than a few micrometers, it is marked as lost. In this case, the user can manually edit the bead positions in problematic frames and continue the automatic tracking from there. When the object positions are set for all frames, a complete trajectory can be exported.

The tracking algorithm can also be used independently from this GUI. Also, there is a module to integrate the functionality of the radial symmetry tracker into the modular software written by Wolfgang Groß, which will be described in chapter 3.2.1. This module makes it possible to use this algorithm for live tracking applications.

In the experiments discussed in this thesis, beads of three different sizes had to be tracked. The active radius was chosen so that it tightly includes the full area the bead occupies in the image. Namely, it was chosen to be $0.94\ \mu\text{m}$ for the $1\ \mu\text{m}$ -sized beads, $1.59\ \mu\text{m}$ for the

2 μm -sized beads and 1.95 μm for the 3 μm -sized beads. The masking radius was chosen to be equal to the active radius. The size of this active area is visible in Figure 2.15. Later in this thesis, the tracker's accuracy was verified by tracking a generated movie and comparing the results to a cross correlation tracker (see chapter 3.2.1.2).

2.2.10 Trajectory classification

All experiments were sorted into two categories depending on whether both particles were taken up into a single joint phagosome or into two separate phagosomes. Joint and separate uptake were discriminated by analyzing the trajectories after the particle uptake. If the distance between the two particles' surfaces remained below 800 nm for no less than 95% of the total experiment duration, the experiment was classified as joint uptake. For the 2 μm -sized particles, this means that the center-to-center distance had to stay below 2.8 μm for 95% of the observation period. Examples of typical joint and separate trajectories are shown in panel A and B of Figure 2.18. The beads' distances from each other are plotted as a function of the time after the attachment in panel C. In situations where the bead distance could exceed the threshold prior to the phagosome formation, beads were only deemed as undergoing separate uptake if the distance threshold was exceeded for more than 5% of the total experiment duration. With the entire experiment spanning 45 minutes, a minimum of 2 minutes of bead separation was necessary for the trajectory to be classified as a separate uptake event.

Additionally to the 69 experiments performed using 2 μm -sized beads and no siRNA, as listed in Table 2.3, 124 similar experiments performed by A. Sabri using 2 μm -sized beads in the scope of his master's thesis^[164] were pooled into the dataset. The trajectories of these experiments were provided by A. Sabri and were newly classified into joint and separate uptake. Figure 2.19 shows all 193 experiments performed with 2 μm -sized beads. In the figure, each individual experiment is represented by a colored time bar, with the horizontal axis representing the time since the beads were attached to the cell. This bar is yellow where the distance threshold has been exceeded and black where the beads were found close to each other. All experiments in which the bar is more than 95% black are classified as joint uptake. As visible, this mainly happened at lower attachment distances. For example, no experiment performed at a center-to-center attachment distance of $D = 5 \mu\text{m}$ was classified as joint uptake. The figure lists the experiments sorted by size and then by the ratio of separate transport. The number of separate or joint uptake events in each distance bin is listed to the left of the time bars. In the figure, experiments performed on LifeAct-transfected cells are mixed with experiment done on wildtype cells. However, cells performed on transfected cells are marked by an asterisk in the experiment tag. In a similar fashion, Figure 2.20 shows the trajectory classification for the 82 experiments with 1 μm -sized and the 92 with 3 μm -sized beads. The classification of all experiments involving siRNA is listed separately in Figure 2.21.

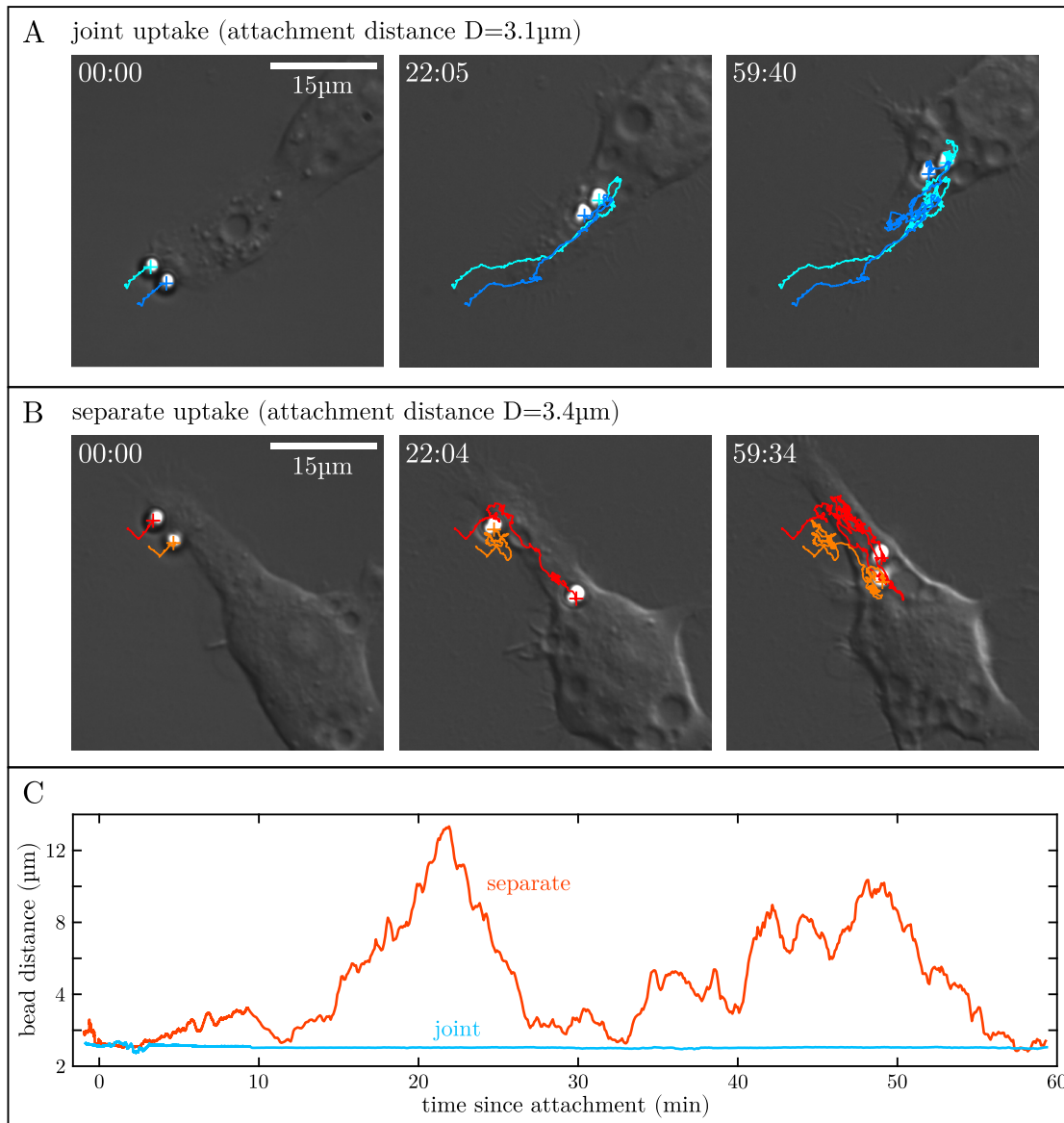


Figure 2.18: Joint and separate uptake trajectory classification examples. Here, two trajectories of experiments classified as joint (panel A) and separate (panel B) uptake are shown. The experiments were performed on $3\mu\text{m}$ -sized particles using different attachment distances. The timestamps in the images indicate the time since the start of the acquisition formatted as minutes and seconds. Panel C shows the temporal development of the center-to-center distance of the beads in those two examples. It is clearly visible that for joint uptake the beads stay very close together at all times, while for the separate uptake the bead distance changes constantly while the beads are independently transported across the cell.

Figure 2.19: Graphical representation of the particle distances for dual-bead experiments performed using $2\ \mu\text{m}$ particles without adding siRNA. Each experiment is represented by a black and yellow bar. Where the bar is black, the beads were closer together than $2.8\ \mu\text{m}$ (center-to-center), where it is yellow, the beads separated further than this threshold. A blue bar indicates that the distance could not be evaluated. The x -direction encodes for the time elapsed after the start of the image acquisition. Next to each bar a label states the date and the number of the experiment's acquisition. Experiments on LifeAct cells are indicated by an asterisk in the experiment label. The experiments are grouped by attachment distance. For each attachment distance, the experiments were sorted by the relative amount of time the bead distance surpassed the threshold. Where applicable, the number of experiments with more or less than 95% joint transport are written next to vertical bars. All experiments with a date up to June 2015 were performed by A. Sabri.



Figure 2.19: (Caption on previous page)

2 Measuring the spatial resolution limit of phagocytosis

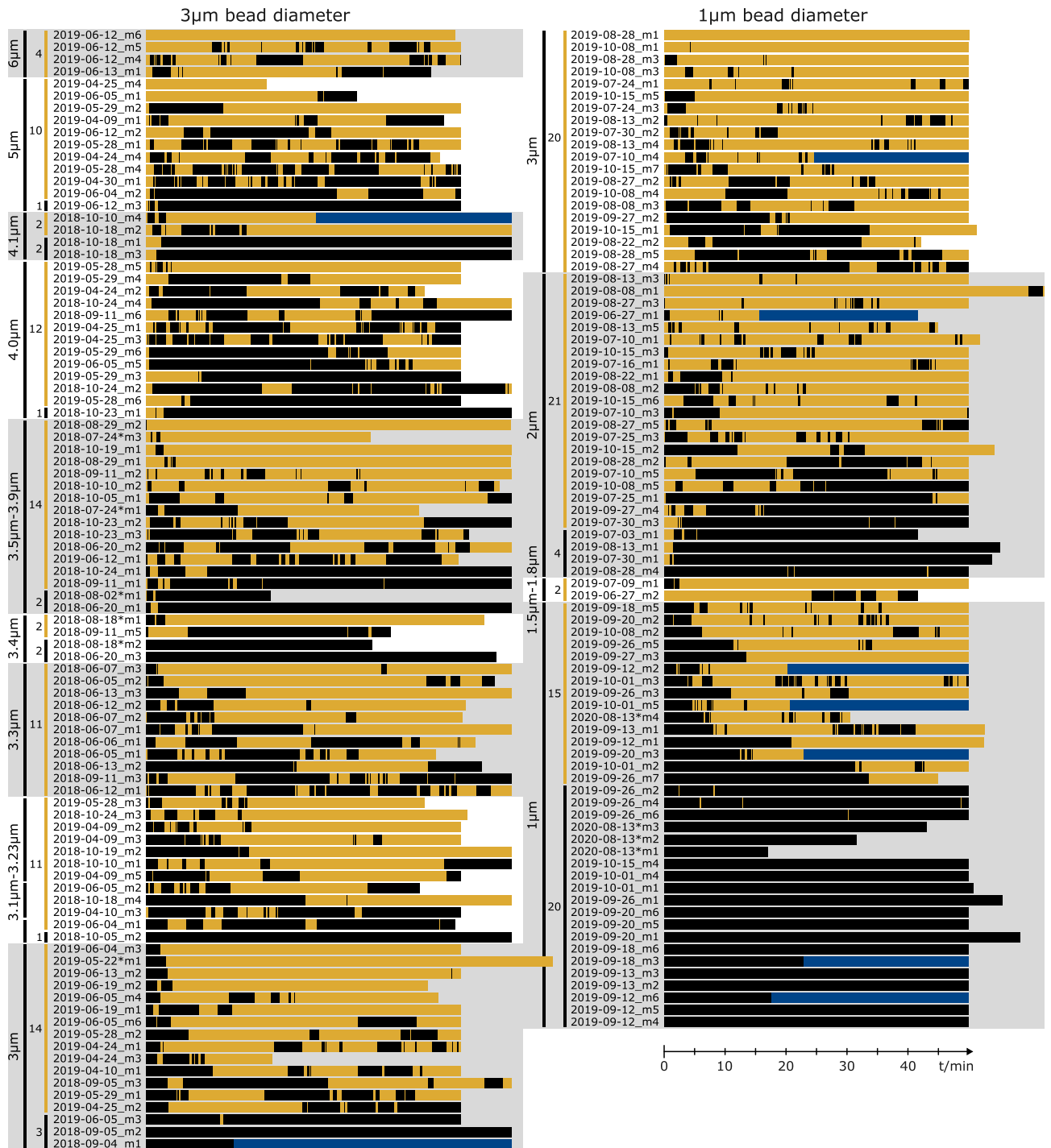


Figure 2.20: Graphical representation of the particle distances for dual-bead experiments performed on 1 μm and 3 μm -sized particles. As before, a yellow bar stands for a bead distance larger than 800 nm surface-to-surface, a black bar indicates a smaller distance, blue areas indicate that the distance could not be evaluated. As in Figure 2.19, the quantities of experiments classified as joint and separate uptake in each bin are written to the left of the bars, and experiments performed on LifeAct cells can be identified by the asterisk in the experiment label.

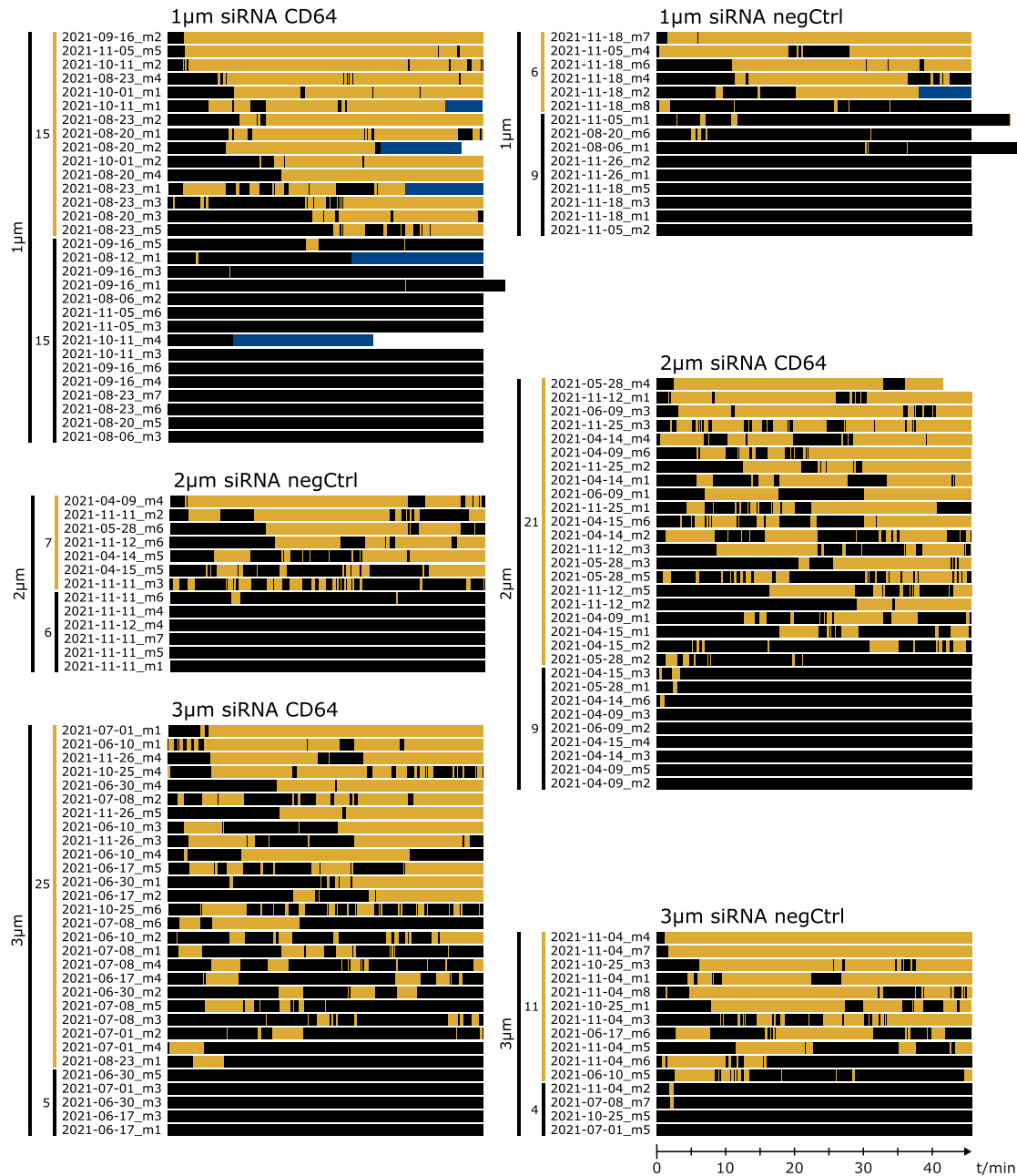


Figure 2.21: Graphical representation of the particle distances for dual-bead experiments performed on cells treated with siRNA (CD64 and negative Control). The experiments were done for three different bead sizes. As in Figure 2.19, a black bar indicates that the beads' surface-to-surface distance is below the threshold of 800 nm, a yellow bar indicates that the threshold was exceeded. A blue bar highlights areas in which the distance could not be evaluated. Here, all experiments were done with an attachment distance equal to the bead diameter, the beads were in direct contact upon attaching them to the cell. Also, no experiments were performed on LifeAct transfected cells. As before, the number of experiments classified as joint and separate uptake is listed to the left of the bars.

2.3 Results

2.3.1 Separate uptake probability

After the beads were attached to the cell, we observed a latency period in which the beads stay attached to the cell’s membrane but are not yet engulfed. This period was described previously^[186,187], and can last from only a few seconds up to 30 minutes.

In many experiments, a rapid displacement of one or both beads towards the interior of the cell, succeeded by a slower and more gradual transit toward the perinuclear region, was observed. This abrupt shift revealed the exact the moment of phagocytosis and took one to three minutes, which fits established values for the duration of phagocytosis^[188]. Notably, in cases classified as separate uptake into two distinct phagosomes, the uptake never happened simultaneous. This implies that the two phagosomes were created independently in these particular experiments.

The classification of the trajectories into joint or separate uptake revealed that for all bead sizes, separate uptake is observed more frequently for larger attachment distances. An overview of the numbers of separate uptake events observed is presented in Table 2.4. The numbers for the 3 μm -sized particles differ slightly from the numbers published before^[97], as four additional experiments performed on LifeAct cells were included in the evaluation. Based on this classification, the percentage of separate uptake or beads with a diameter of 2 μm was calculated for five different attachment distance bins, as listed in Table 2.4. If the 2 μm -beads were attached in direct contact with each other (center-to center bead attachment distance of 2 μm), they separated during the uptake in around 60% of the cases. This separate uptake probability further increased if the beads were attached at a larger distance to each other. If 2 μm -beads were attached with a center-to-center distance larger than 5 μm , no joint uptake could be observed at all. The data for smaller and larger bead diameters shows a similar trend, with higher attachment distances leading to a increasing separate uptake probability.

1 μm bead diameter		2 μm bead diameter		3 μm bead diameter	
d	sep./total	d	sep./total	d	sep./total
1.0 μm	15/35 (43%)	2.0 μm	26/68 (38%)	3.0 – 3.4 μm	38/44 (86%)
1.5 – 2.0 μm	23/27 (85%)	2.2 – 2.9 μm	35/49 (71%)	3.4 – 4.1 μm	28/33 (84%)
3.0 μm	20/20 (100%)	3.0 – 3.4 μm	43/47 (91%)	5.0 μm	10/11 (91%)
		3.5 – 3.6 μm	10/10 (100%)	6.0 μm	4/4 (100%)
		5.0 μm	19/19 (100%)		

Table 2.4: Number of separate uptake events for different bead sizes and attachment distances. This table lists the ratio of separate uptake experiments observed for different bead sizes and different attachment distances d . Experiments performed with similar attachment distance were pooled into bins. For this evaluation, experiments performed on LifeAct cells were pooled together with experiments performed on wildtype cells.

2.3.2 Actin activity during uptake

In total, 31 of all dual-bead experiments were done on LifeAct-transfected macrophages to observe the actin dynamics during the phagocytic cup formation.

Unfortunately, in the majority of the experiments, the polymerization of filamentous actin associated with the phagocytic cup formation^[111,189] could not be observed directly, or only with a poor signal-to-noise ratio. An example of an experiment classified as joint uptake with a particularly clear LifeAct signal is shown in Figure 2.22. This proves that cells will in fact take up phagocytic targets in a single phagosome if the particles are presented to the cell in a compact formation. A more detailed analysis of the actin activity during phagocytosis will be provided in chapter 3, as the experiments in this chapter were performed using a feedback system that keeps the bead perfectly in focus. This made the data collected there much more suitable for a quantitative analysis.

2.3.3 Signaling model

We developed a basic one-dimensional model of the signaling preceding the uptake to describe the experimental data. Although other models for phagocytosis^[187,190,191,192] focus on the mechanical aspects, such as membrane adhesion and stress, our model is based on the receptor-dependent signaling involved. The model uses the given particle size, the set particle distance, the receptor density, the length of the contact line between the cell membrane and the bead, and the length scale of the signaling as input parameters. The output of the model is the probability that a pair of beads is internalized separately. While the particle size and the attachment distance are predetermined by the experiment, the mean receptor density, the contact region size and the length scale of the signaling can be chosen freely and will be determined by a fit onto the experimental data.

Upon binding to the cell, each bead is postulated to establish contact with the cell membrane, thereby activating $\text{Fc}\gamma$ receptors in a defined contact region. This region's width, defined as d_{contact} is assumed to be proportionate to the bead diameter d_{bead} and is represented by the parameter $\alpha = d_{\text{contact}}/d_{\text{bead}}$. This dimensionless parameter reflects the size of the region in which a bead contacts the plasma membrane upon initial binding. Within this contact region, opsonized beads stimulate $\text{Fc}\gamma$ receptors, initiating a signaling pathway that triggers actin branching, actin polymerization, and eventual phagocytosis.

This signaling cascade involves various small signaling molecules, including the tyrosine kinase Syk. To depict the propagation of the signal transmitted by these small signaling molecules originating from the activated $\text{Fc}\gamma$ receptors, we introduced the concept of the phagocytic signaling level $A(x)$. This value can be seen as a composite of different signaling molecule concentrations along the cell membrane. Assuming a freely diffusing signaling molecule is produced at the receptor and its concentration reaches a steady-state quickly, each activated receptor contributes a Gaussian-shaped peak to the cumulative phagocytic signaling level $A(x)$. The activation peak for each receptor is standardized to possess a height of 1 (in arbitrary units) and a Full Width at Half Maximum (FWHM) of L . The width L to which an individual signal extends along the cell membrane is the central fitting parameter in the model.

Figure 2.23 shows the calculated phagocytic signaling level $A(x)$ for ten different, random receptor placements. In the figure, two beads with a diameter of $2\ \mu\text{m}$ in direct contact to each other are contacting the cell. For easy demonstration, the model's parameters in this

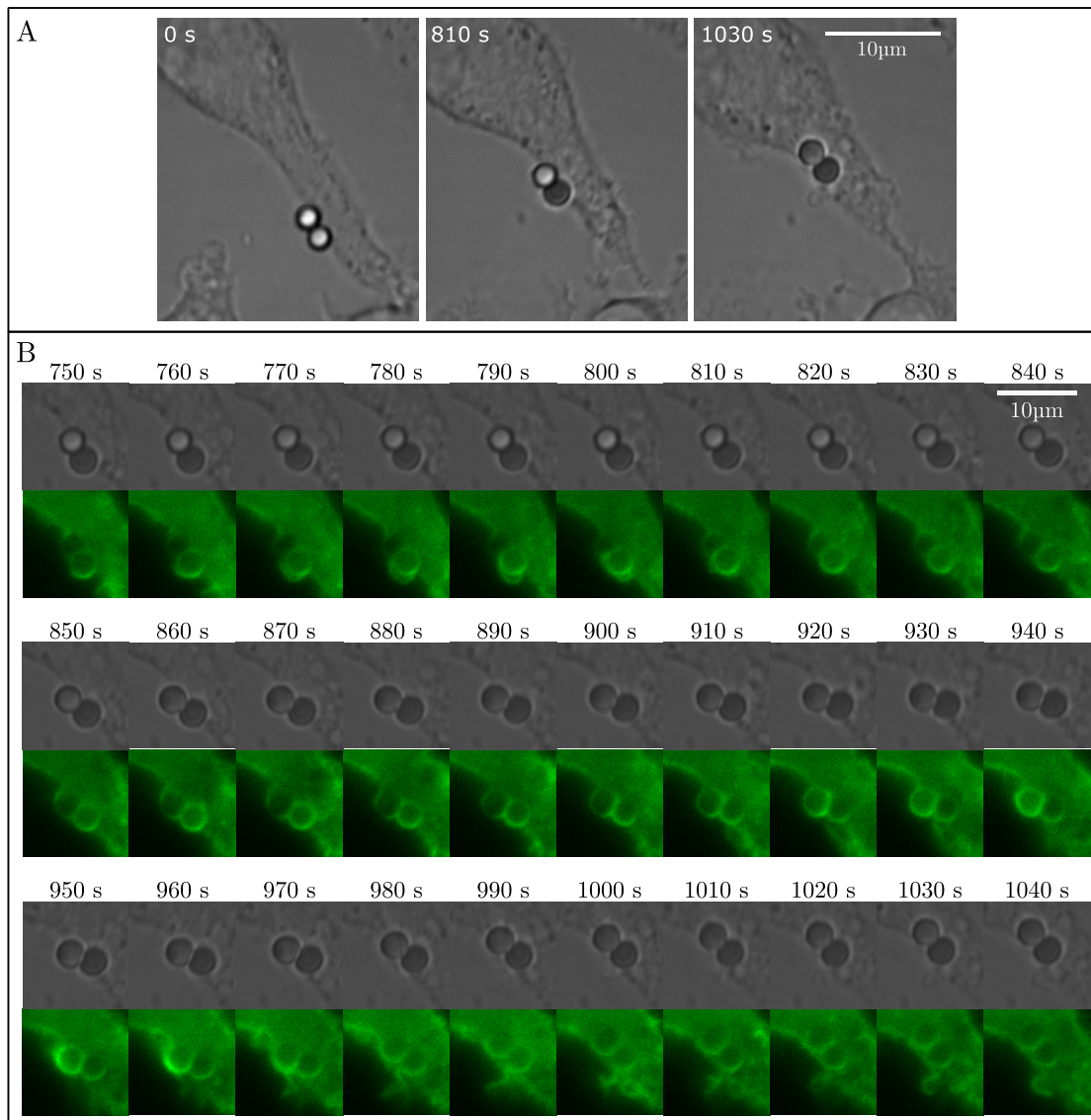


Figure 2.22: Phagocytic cup formation during joint uptake observed by fluorescence microscopy. The three large images in panel A show how the uptake can be observed in the brightfield channel. The two beads quickly move past the cell boundary. The darkening in their appearance indicates a downward motion, affirming that the beads did indeed enter the cell rather than merely resting on its surface. The image sequence in panel B shows the uptake process both in the brightfield and the fluorescence channel. The two beads are taken up in one motion, with the bottom bead being pulled into the cell first. The uptake of the beads is clearly visible as a surge in the fluorescence intensity caused by the polymerization of actin as the membrane pushes around the particle.

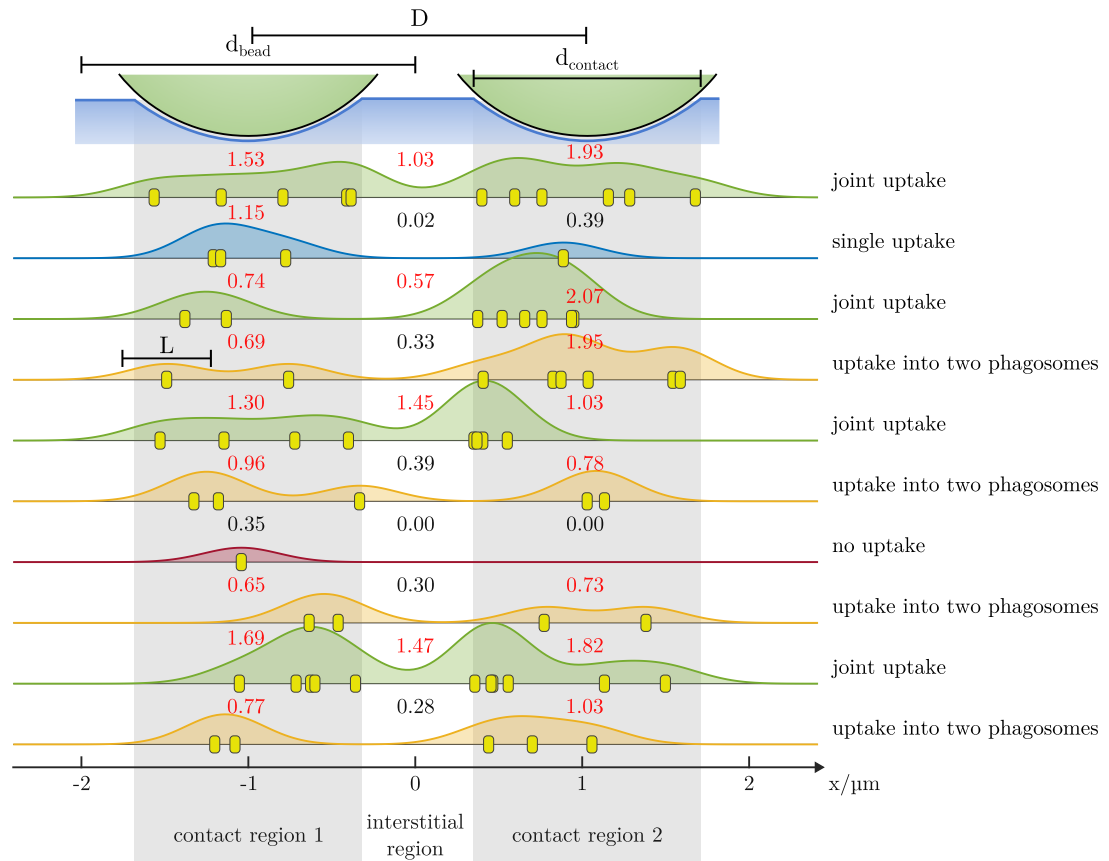


Figure 2.23: Illustration of different receptor placements in the context of the spatial resolution model. $Fc\gamma$ receptors are distributed randomly along a one-dimensional membrane, with an average separation of receptors of δ . Receptors within a contact region, become activated, contributing Gaussian-shaped peaks with a height of 1 and a width of L to the phagocytic signal level $A(x)$. The figure shows the activation level along the cell membrane for ten different receptor distributions inside the contact areas. The small numbers denote the average activation levels for the contact areas and the interstitial area. Mean activation levels exceeding 0.5 are marked red, indicating phagocytic activation in these areas. In the figure, the beads have a diameter of $2\mu\text{m}$ and are directly touching ($D=2\mu\text{m}$). The average receptor density and the relative size of the contact areas are chosen according to the fit results. In this example, the beads are taken up into two phagosomes in only four out of ten cases, with an additional case of single uptake. resulting in a predicted separate uptake probability of 50%.

example were chosen equal to the results obtained by the fit later. In the plot, we can see that the signaling level mainly depends on the number and placement of the receptors inside the contact regions.

From observations in other signaling pathways, it's known that cells can respond abruptly to gradual changes in the concentration of a signaling molecule. This responsiveness can be caused via a positive feedback loop, which, for Fc receptors, is implemented by the Syk kinase, which can phosphorylate the immunoreceptor tyrosine-based activation motifs (ITAMs) on adjacent receptors. To accommodate this binary behavior, a rigid threshold of 0.5 was established for the average signal within the contact region. Setting the threshold to 0.5 was done to ensure that the parameter L signifies the width of the region where the signal generated by an individual active receptor exceeds this threshold. Within the model, each individual bead is handled as taken up if the average activation level within its respective contact region surpasses 0.5. Additionally, it is assumed that adjacent beads cannot be differentiated if the mean signal level within the interstitial region between their contact areas also exceeds 0.5. In Figure 2.23, the average signaling levels are denoted as small red or black numbers. The number was printed in red if it was larger than the threshold 0.5. Generally, two receptors inside a single contact area are enough to exceed the activation level threshold. If receptors are placed close to the interstitial region between the contact area, the activation level in this area will also rise and can exceed the threshold, which can lead to a joint uptake.

This gives the model a total of four potential outcomes, as shown in Figure 2.23. In the first two scenarios, both contact regions display mean activation levels higher than 0.5, indicating the uptake of both beads. If the interstitial region's averaged value exceeds 0.5, the beads are engulfed together in a joint phagosome (green in Figure 2.23). Should the average activation level within the interstitial region fall below 0.5, the beads are taken up individually into two phagosomes (orange). The specific probability of those scenarios depends on receptor spacing, bead dimensions, and the bead distance. In the subsequent pair of scenarios (shown as blue and red in Figure 2.23), either only one contact region demonstrates an activation level above 0.5, resulting in the uptake of one bead while the other remains adhered to the cell surface (blue), or both contact regions yield mean activation levels below 0.5, leading to the none of the beads being taken up (red). To obtain the probabilities for each of the described outcomes, the activation level $A(x)$ was calculated for different patterns of active receptors on the membrane, as done in Figure 2.23. These receptors were placed randomly at different spots x_i on a line representing the cell's membrane, with an average distance δ between them. Since only receptors with direct contact to the opsonized particle can be activated, any receptors outside the contact regions can be ignored.

The total number of randomly placed receptors inside a contact region with a fixed length obeys a Poisson distribution, with the mean number of receptors in one contact region being $\lambda = \frac{d_{\text{bead}} \cdot \alpha}{\delta}$. The total activation level was calculated by adding up the individual activation curves of all receptors in both contact regions:

$$A(x) = \sum_i \exp\left(-\frac{(x_i - x)^2}{L^2}\right) \quad (2.23)$$

The coefficient $4 \ln 2$ in this equation is derived from the fact that the value of the exponential function equals $1/2$ for $x_i - x = L/2$, which is true because L was defined as the full width of the peak at half of its maximum value. The average activation level within the contact

region d_{contact} was computed by integrating $A(x)$ across this region. Because the integration runs over a sum of Gaussian peaks, the result can be expressed as a sum of error functions:

$$\begin{aligned}\bar{A} &= \frac{1}{x_b - x_a} \int_{d_{\text{contact}}} A(x) dx = \\ &= \frac{1}{d_{\text{contact}}} \sum_i \frac{L}{2} \left(1 + \operatorname{erf} \left(\sqrt{\ln 16} \cdot \frac{x - x_i}{L^2} \right) \right)\end{aligned}\quad (2.24)$$

This equation was used to calculate the mean activation levels inside and in between the contact regions. In Figure 2.23, this mean activation levels are printed above each activation level.

Based on the values, the experiment then can be classified as one of the four mentioned uptake scenarios. By doing this multiple times for randomly chosen receptor placements, a probability for each outcome can be computed. For example, in Figure 2.23, four out of ten receptor placements resulted in uptake into two phagosomes and one in single uptake behavior. Since in both of these scenarios, the beads will separate spatially, both are considered separate uptake, leading to a predicted experimental separate uptake probability of 50%. For real applications, 10^6 different receptor placements were considered each time a uptake probability had to be calculated.

In conclusion, the model is able to predict the separate uptake probability based on multiple model parameters, which are the relative contact region size α , the length scale L of phagocytic signaling and the mean receptor distance δ . Additionally, the bead diameter d_{bead} and the attachment distance D influence the probabilities for different uptake scenarios, however, these were varied experimentally and not determined by the fit. Multiplying δ , d_{bead} and D by the same factor does not alter the output probabilities, as the scenarios shown in Figure 2.23 will simply be scaled proportionally. The separate uptake probability is the sum of the probabilities for single uptake and uptake into two phagosomes.

2.3.4 Fit results

The model was fitted to the experimental values of the separate uptake probabilities for the $2\ \mu\text{m}$ -sized beads as shown in panel A of Figure 2.24. The fitting was done using only uptake probabilities observed on $2\ \mu\text{m}$ -sized beads. This was done because of the greater number of conducted experiments and the wide range of attachment distances for this bead size. This approach allows to use the data from the $2\ \mu\text{m}$ -sized beads as a benchmark for other bead sizes. Additionally, it facilitates the verification of the models predictions, as the predictions for $1\ \mu\text{m}$ and $3\ \mu\text{m}$ -sized beads can be compared to experimental results.

To do that, the average bead attachment distance d_i in each bin of experiments as listed in Table 2.4 was calculated. The index i here numbers the different bins. Additionally, the ratio of separate uptake experiments in each bin p_i and the total number of experiments in each bin N_i was calculated. The uncertainty of the experimental separate uptake probability for each attachment distance was calculated using the formula for the standard deviation of a binomial distribution as follows:

$$s_{p_i} = \sqrt{\frac{p_i(1 - p_i)}{N_i}}\quad (2.25)$$

The fit was done using a least-square method. By using MATLAB's `lsqnonlin`-function, the

values of α, δ and L were chosen to minimize the sum of the squared, weighted differences between the measured separate uptake probabilities p_i and the separate uptake probabilities predicted by the model for the attachment distances d_i . Each datapoint was weighted using the number of experiments N_i in this bin. To determine the uncertainty of the fit result values, the fit was redone multiple times on altered input datasets. The value of the experimental separate uptake probability p_i is defined as the ratio of observed separate uptake events n_i and the total number of experiments N_i performed for this datapoint. We altered the value of each datapoint by choosing a new number n'_i of separate uptake events from a binomial distribution centered around the experimental number of separate uptake events $n_i = p_i N_i$. This provided a new set of five separate uptake probabilities $p'_i = n'_i / N_i$, on which the fit was rerun, which resulted in a new set of the fit parameters α, δ and L . This process of data

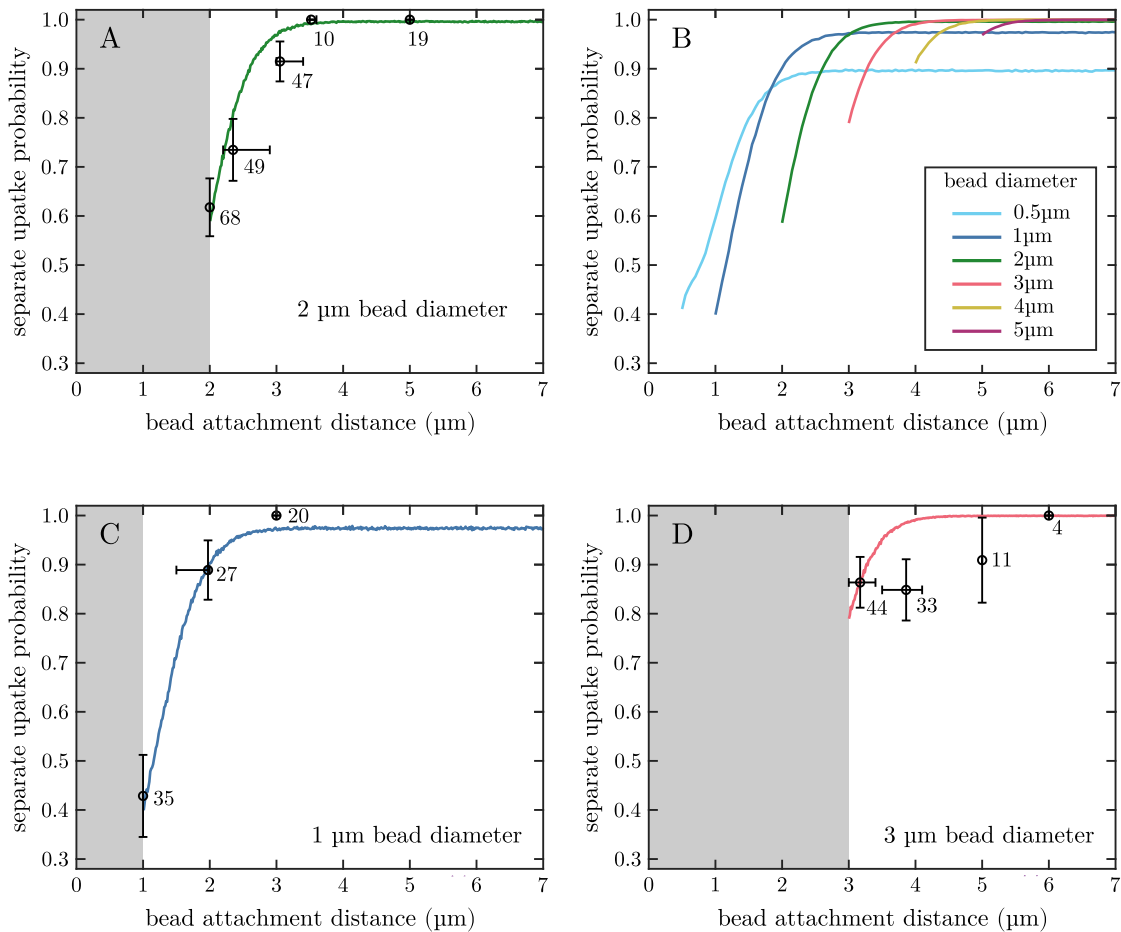


Figure 2.24: Panel A shows the experimental separate uptake probabilities for 2 μm -sized beads. The gray area is experimentally inaccessible because at distances smaller than the bead diameter the beads would intersect. The green line represents the fit using the model as described in chapter 2.3.3. The fit returned the parameter values $\alpha = 0.68 \pm 0.25$, $\delta = (0.30 \pm 0.09) \mu\text{m}$, and $L = (0.53 \pm 0.11) \mu\text{m}$. These parameters can then be used to predict the separate uptake probabilities of arbitrary bead sizes, as visible in panel B. Panels C and D show that this predictions align well with the experimental separate uptake probabilities measured for smaller and larger beads. All error bars in this plot represent the standard deviation and are calculate using Equation 2.25

generation and fitting was repeated a total of 10^5 times. This way, a distribution for each of the three fit parameters was generated. The final error values of α , δ and L are the standard deviation of these distributions. This error estimation method is similar to an approach in earlier work^[193] by W. Groß.

By fitting the model to the experimental separate uptake probabilities of $2\ \mu\text{m}$ -sized beads for different distances, we were able to determine the following parameters:

$$\begin{aligned}\alpha &= 0.68 \pm 0.25 \\ L &= (0.53 \pm 0.11)\ \mu\text{m} \\ \delta &= (0.30 \pm 0.09)\ \mu\text{m}\end{aligned}\tag{2.26}$$

Using these parameters, the predicted separate uptake probability could be calculated for different bead sizes and distances. In panel A of Figure 2.24, the experimental data on $2\ \mu\text{m}$ -sized particles is plotted along with the separate uptake probabilities consistent with the fitted model. The model aligns well with the experimental data. Increasing the bead surface-to-surface distance from zero at direct contact to only a single micrometer increases the amount of separate uptake dramatically from around 60% to about 92%. This is qualitatively consistent with the value for the phagocytic signaling length scale $L = 530\ \text{nm}$, as the localized signaling events will be unlikely to bridge the larger gap between the two particles.

Using the average distance δ between two receptors along a singular dimension it is possible to estimate the two-dimensional receptor surface density. If all receptors were arranged on the membrane in a hexagonal grid with a spacing of δ as the unit length, every receptor would occupy the area of two equilateral triangles, each with side lengths of δ . The area of this region is $A_{\text{receptor}} = \sqrt{3}/4 \cdot \delta^2$ (see Figure 2.25). Consequently, the average count of receptors within an unit membrane area is the reciprocal of this area, yielding

$$n = 1/A_{\text{receptor}} = 2 \cdot 3^{1/2} \cdot \delta^{-2} = (13 \pm 7)\ \mu\text{m}^{-2}.\tag{2.27}$$

Combining the fit parameter values and the model, it becomes possible to predict the phagocytic uptake behavior of the cell for different particle sizes and distances. As illustrated in panel B of Figure 2.24, the model's predictions indicate an increasing likelihood of separate uptake as the attachment distance increases for all bead sizes. As attachment distances become larger, the separate uptake probability converges towards a constant value. This asymptotic value gets closer to one for larger bead sizes and is 95.5% for $3\ \mu\text{m}$ -sized beads, and already 99.2% for $5\ \mu\text{m}$ size beads. For smaller beads and larger attachment distances,

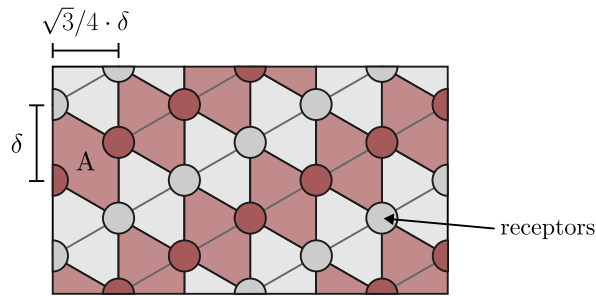


Figure 2.25: Area occupied by a single receptor in a hexagonal grid. With an unit length δ , each receptor inside the grid occupies the area $A_{\text{receptor}} = \sqrt{3}/4 \cdot \delta^2$.

instances where neither bead is taken up become more frequent, thereby the model reports a lower maximum separate uptake probability for large attachment distances. Figure 2.24 shows the separate uptake probability, which includes scenarios where both beads are taken up as individual phagosomes or only one bead is engulfed. A list of the numerical probabilities for the individual scenarios of separate, joint, single and no uptake can be found in the appendix in Table 5.1.

The model's predictions were tested by comparing them to the experimental separate uptake probabilities measured using 1 μm and 3 μm -sized particles. Experimental uptake probabilities were available for three different attachment distances for the 1 μm -sized particles and four different distances for the 3 μm -sized beads (see Table 2.4). The experimental separate uptake probabilities along with the separate uptake probabilities predicted by the model using the parameters listed in Equation 2.27 are plotted in panels C and D of Figure 2.24.

In the experiments involving 1 μm particles, the separate uptake probability stood at 43% for the minimal attachment distance, progressively increasing to nearly 100% for greater attachment distances. This observation is in line with the model's projection. For the larger particles sized at 3 μm , the separate uptake probability exceeded 80% across all attachment distances. The experiments involving 3.4 – 4.1 μm attachment distances displayed slightly less separate uptake than anticipated. However, the model does not account for additional influences, such as variations stemming from cell-to-cell disparities, varying cell passages or differing points in the cell cycle. These influences might have reduced the experimental separate uptake probability, explaining this discrepancy. The experimental data matches with the hypothesis that the likelihood of individual uptake should rise with increasing bead size. Notably, for considerably larger attachment distances of 6 μm center-to-center, all experiments indicated separate uptake. Overall, the model managed to predict the separate uptake probabilities for both 1 μm and 3 μm particle sizes within the uncertainties present in the experimental data.

2.3.5 siRNA knockdown

To validate the model's predictions, we conducted the same dual bead uptake experiments on cells with a reduced number of $Fc\gamma$ receptors. This was achieved using siRNA aimed at the CD64 receptor, also known as $Fc\gamma R1$.

Western blotting results, as depicted in Figure 2.26, demonstrate that the CD64 expression level in the siRNA-transfected cells reached only 14% in comparison to the negative control. The tubulin blot displayed distinct protein bands at the expected molecular weight of 55 kDa. The bands for CD64 were spread across a range of approximately 44 – 65 kDa, which is expected due to variable glycosylation levels of the protein. The quantity of protein in each lane was assessed through densitometry. To do that, areas of equal size were selected around each protein band, both for the CD64 and the tubulin lanes. Then, the average image intensity in these areas was calculated. Additionally, the background image intensity was determined by calculating the median intensity in an area without any visible signal. This background intensity value was subtracted from the average intensities in the areas around the protein bands to obtain a quantitative number for the amount of signal in each protein band. To account for potential differences in protein content of the lysates due to different cell growth rates, the background-corrected intensities of the CD64 bands were then divided through the corresponding tubulin values. The resulting three values for the relative amount of CD64 in the samples indicated that the amount of CD64 was reduced to 51% in the cells treated with 5 pmol of siRNA, and went down to 14% in cells treated with 10 pmol siRNA.

This implies that the average receptor spacing on the membrane underwent an increase by a factor of $0.14^{-1/2} = 2.67$, leading to an increase of the mean receptor distance used in our model from $d = 0.30 \mu\text{m}$ to $d = 0.80 \mu\text{m}$. This extrapolation assumes that the reduction in the expression level of the receptors directly affects the amount of receptors on the cell's surface.

To assess the predictions of the model for an increased mean receptor distance, we performed experiments with bead dimers (i.e., pairs of beads with the minimal possible attachment distance) for beads with a diameter of 1, 2 and 3 μm . For each bead size, 30 experiments were done on cells treated with siRNA targeting CD64. Additionally, 13 to 15 experiments were performed per bead size on cells treated with non-targeting siRNA to serve as a negative control group. The trajectories of the beads were tracked as before and the individual experiments were classified as joint or separate uptake based on the same criteria as before. The process of this classification is shown in Figure 2.21, where as before each experiment is represented by a time bar, indicating at which times the beads were closer than the distance threshold and when they spread further apart.

The number of experiments showing separate uptake in knockdown cells are listed in Table 2.5. In Figure 2.27, all separate uptake probabilities for measured on dimers are printed as a bar plot, together with the dimer separate uptake probabilities predicted for a receptor spacing of $\delta = 0.80 \mu\text{m}$. This figure also includes the separate uptake probabilities for wildtype (non-knockdown) cells at the minimal attachment distances, as presented in Figure 2.24. In these cases, the model's predictions were computed using the unaltered receptor distance of $\delta = 0.30 \mu\text{m}$. The model predicts an increasing separate uptake probability for an increasing bead size for both the untreated cells and the siRNA-treated cells with the increased mean receptor distance. Furthermore, for each bead size, the model predicts a higher uptake probability for the siRNA-treated cells compared to untreated cells. The experimental data shows good agreement with all these predictions.

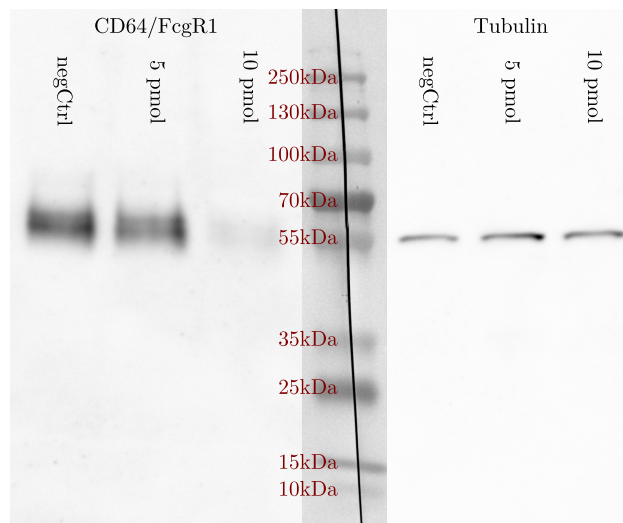


Figure 2.26: Western Blot showing the amount of CD64 and tubulin in three different lysates created from cells treated with 10 pmol of non-targeting siRNA or 5 pmol or 10 pmol of siRNA targeting CD64. The central strip of the image shows the blot in the visible spectrum, as here the bands of the protein ladder can be seen. Those were annotated with the atomic weights of the contained proteins. The left and right sections show the chemoluminescence in those areas. It is visible that the different treatments contain similar amounts of tubulin, while the amount of Fc γ R1 proteins drops drastically when targeting siRNA was used.

		ratio of separate uptake events		
used siRNA	bead size	1 μ m	2 μ m	3 μ m
	neg. control		6/15 (40%)	7/13 (54%)
CD64		15/30 (50%)	21/30 (70%)	25/30 (83%)

Table 2.5: Number of separate uptake events observed on siRNA-treated cells. Listed are the number of separate uptakes observed per number of total experiments, along with the corresponding percentages. All experiments were done using bead dimers, meaning that surface-to-surface distance of the beads was zero at attachment. For all three bead sizes, the relative amount of separate uptake events was higher when treating the cells with CD64-targeting siRNA compared to the non-targeting negative control.

2 Measuring the spatial resolution limit of phagocytosis

As shown in Figure 2.27, the model predicts a rise in the probability of separate uptake as the bead size increases, a trend observed in both untreated cells and siRNA-treated cells. Additionally, the model predicts that the separate uptake probability for a certain bead size is higher for siRNA-treated cells compared to the untreated cells. The experimental results align with all these predictions. Furthermore, the cells treated with non-targeting siRNA show no significant change in the dimer separate uptake probability compared to the untreated wildtype cells, indicating that the siRNA protocol does not have any unwanted side effects.

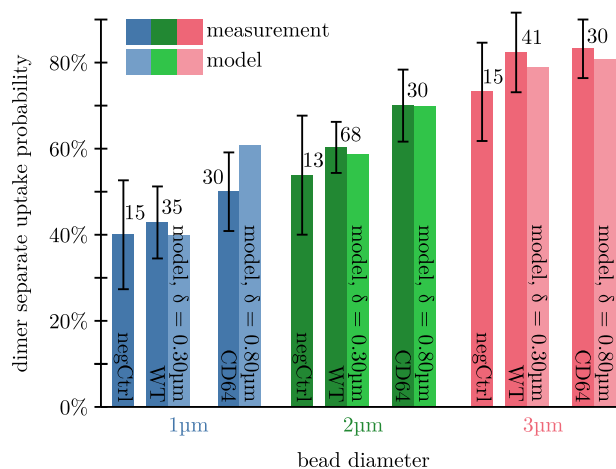


Figure 2.27: Separate uptake probabilities are depicted for dimers (pairs of particles with $0\ \mu\text{m}$ surface-to-surface distance) of varying particle sizes (1, 2 and $3\ \mu\text{m}$). The probabilities are shown across different experimental conditions: cells subjected to CD64-targeting siRNA treatment, cells treated with non-targeting siRNA (negCtrl), and untreated cells (all depicted by the darker-colored bars). Correspondingly, the lighter-colored bars show the model's predictions for those conditions. The model was fitted only to the $2\ \mu\text{m}$ data of the WT cells, making all other model outputs direct predictions of the model. The error bars correspond to the standard deviation of the data, the numbers next to the error bars denote the quantity of experiments performed.

2.4 Discussion

2.4.1 Trajectory classification and spatial resolution model

In this chapter, we established that mouse macrophages can take up opsonized particles into a single joint or into two separate phagosomes, and that the probability for separate uptake increases with the attachment distance.

The experiments were categorized reliably into joint and separate uptake based on the distance between both particles. Separate uptake in this context included the uptake of only a single bead. For an experiment to be considered joint uptake, the particles had to stay closer than 800 nm surface-to-surface during at least 95% of the experiment. In most separate uptake experiments, the distance threshold of 800 nm was exceeded by multiple micrometers, as visible in the example in panel C of Figure 2.18. This means that as long as the distance threshold was chosen large enough to avoid misjudging joint uptake events as separate uptake, all experiments were classified correctly.

The exact distance of two particles can fluctuate even if both beads were taken up in a single phagosome. The main reason is that the membrane might only be wrapped loosely around the particles, allowing them to move relative to each other. The shape of the phagosome is determined by a balance between the energy required to curve the membrane around the target and the energy gained through membrane-target adhesion^[194]. Certain proteins, such as receptors or curved membrane proteins, can modify the contribution of these energy components by respectively augmenting adhesion or diminishing bending energy^[195]. The overall shape of a multi-bead-containing phagosome inherently encompasses a compromise between these factors. After uptake, the tension on the endomembrane can be modulated to facilitate membrane remodeling and trafficking events^[196], which might further alter how much the particles can move within the phagosome. Another conceivable reason for the separation between two particles within a single phagosome can be attributed to stretching of the phagosomal membrane. Direct stretching of this membrane is minimal because biological membranes strongly resist deformations that do not maintain their area^[197]. Nevertheless, the area of the phagosome is not constant because membrane can be added or removed during interaction with other organelles, for example by the temporary fusion with lysosomes^[198], as proposed in the kiss-and-run hypothesis^[77]. Additional minor influences on the inter-bead distance can be caused by disparities in particle sizes and uncertainties inherent in the particle tracking algorithm. Fortunately, the exact value of the distance threshold is of less importance, as in most experiments showing separate uptake the beads separated by multiple micrometers (see for example Figure 2.18). The threshold was determined to be 800 nm as this value is sufficiently large to accommodate all these considerations and avoids misclassifying joint uptake events.

Under certain conditions, bead pairs with identical center-to-center distances yet smaller diameters exhibited an elevated likelihood of separate uptake. For example, 1 μm -sized beads attached at a center-to-center distance of 1.5 – 2.0 μm were more likely to be taken up separate than 2 μm beads attached in direct contact. This phenomenon can be attributed to the fact that while the smaller beads generate a relatively weaker stimulus, this effect is confined to a smaller region, enhancing the discernibility between the beads.

Informed by our measurements with 2 μm -sized particles, we developed a model incorporating parameters such as the mean receptor distance d , the length scale L governing phagocytic signaling, and a geometric parameter a determining the contact region size between the

particle and the cell. This model effectively predicted the probabilities of separate uptake for both smaller (1 μm) and larger (3 μm) particles. Furthermore, the model's validity was underpinned through experiments on cells where the mean receptor distance had been altered via the reduction of Fc γ RI expression levels using RNA interference. In each instance, the experimentally determined probabilities of separation demonstrated strong agreement with the values anticipated by the model. For each particle size, the probability for separate uptake increased if the beads were attached to the cell membrane further apart from each other. Pairs of large particles with a diameter of 3 μm were scarcely taken up in a joint phagosome, even if they were attached while in direct contact with each other. After the uptake, phagosomes undergo transport towards the perinuclear region^[199]. The speed and duration of this phagosomal transport are notably influenced by the size of the target^[93,200], possibly leading to a potential underestimation of separation probabilities for larger beads. Larger particles exhibit more persistent intracellular transport, thereby increasing the likelihood of separate phagosomes being transported together coincidentally.

This phenomenon could explain why experimentally determined separation probabilities for the 3 μm particles tend to be lower than the theoretically predicted values (see Figure 2.24D). This effect was mitigated by the long observation period of 45 min. However, the observation period could not be extended indefinitely, since phagosomes are subject to phagosomal maturation^[10]. As part of the digestion process that degrades engulfed pathogens, phagosomes ultimately merge with lysosomes^[198]. Since it is unknown how many fusions and fission happen during the beads' trajectory, the information whether the beads were taken up in one single or two separate phagosomes might gradually become lost.

Additionally, it's important to acknowledge that multiple subtypes of Fc γ receptors are involved in the signaling during phagocytosis. Murine macrophages feature activating receptor types, namely Fc γ RI, Fc γ RIII, and Fc γ RIV^[106,72], along with the inhibitory receptor Fc γ R2b and the IgG-binding receptor FcRn, which doesn't directly induce or regulate cell activation^[72]. Moreover, different isotypes of IgG antibodies exist^[84], with each subtype exhibiting varying affinities for each Fc γ receptor type. All in all, this forms a complex regulatory system. However, Fc γ RI binds to IgG with substantially higher affinity compared to any other receptor^[201], which is why it was chosen as a target for RNA interference.

The receptor density value of $n = (13 \pm 7) \mu\text{m}^{-2}$ derived from the fitting procedure aligns well with existing experimental data. To compute the total number of receptors per cell, a value for the cell's total surface area is needed. The apparent surface area of a murine macrophage as observed under a light microscope is approximately twice the area that a cell occupies when spread out on a coverslip. However, it should be noted that during phagocytosis, J774 macrophages can expand their apparent membrane area by over fivefold^[202], utilizing various membrane reservoirs and flattening microscopic membrane wrinkles. In our experiments, the apparent surface area was estimated to be around $1 \cdot 10^3 \mu\text{m}^2$, which is consistent with literature values of a macrophage's size^[203]. Together with our value for the receptor density, the total number of receptors per cell can be estimated to be around $13 \cdot 10^3$. While prior measurements on human U937 monocytes suggested $7 \cdot 10^3$ receptors per cell^[204], data from murine monocytes indicated a greater antibody binding capacity of $1 \cdot 10^4$ Fc γ RI receptors^[205]. Both of these values match the order of magnitude of our result.

Studies have revealed that the initiation of phagocytosis requires targets to surpass a certain ligand density threshold^[206]. Furthermore, beads covered with a fixed quantity of IgG tend to exhibit a higher uptake probability if this IgG is closely clustered on the bead's

surface^[207]. These observations are matched by the model's predictions, as the model predicts that beads will only be internalized if the ligands are spaced tight enough to activate enough receptors within the contact region.

The model implies that the spatial arrangement of receptors can have a substantial impact on the cell's ability to distinguish two stimuli. To optimize resolution, maintaining a consistent distance between the limited pool of available receptors would be ideal. It has been observed that the mobility of proteins in the plasma membrane is lower than in artificial bilayers^[35]. The mobility is restricted by transmembrane pickets that connect to the cytoskeleton and the pericellular coat, hindering the free diffusion of membrane proteins such as receptors. Single-particle imaging of membrane proteins often reveals that their movement is confined to an area ranging from 40 nm to 300 nm in width^[38]. It can be hypothesized that this constraint on membrane protein mobility contributes to maintaining more evenly spaced receptors. In quantitative terms, the receptor spacing of $\delta = 0.30 \mu\text{m}$ determined by the experiments in this chapter suggests that each compartment should contain approximately one receptor.

The numerical value of the parameter α implies that the bead establishes contact with the membrane across a segment spanning an angle of $2 \cdot \arcsin(\alpha) = 86^\circ$ around the bead's center (see Figure 2.28). At a bead radius of $2 \mu\text{m}$, this means that the bead indents a flat membrane by a mere 150 nm. This is compatible with the observation that upon attachment, the beads initially remain on the cell's surface, as this slight indentation is imperceptible with brightfield microscopy. The exact depth of indentation a particle creates in the cell membrane upon contact depends on the adhesion energy between the membrane and the particle^[194].

Prior research indicated that, directly after touching the membrane, beads gradually bind to the membrane over a span of 1 – 2 min, primarily driven by unspecific adhesion and receptor-ligand interactions^[208,209]. After this adhesion phase, there is a period in which the beads remain fixed to the cell membrane until active phagocytosis begins. This temporal window is important for signaling, as the beads, being potential phagocytic targets, are already securely attached and the signaling cascades are initiated. However, at this point it is not yet evident if the beads will undergo joint or separate phagocytosis. Within this phase, mechanisms are triggered that ultimately decide the fate of the beads.

If different targets, such as multiple aggregated bacteria belonging to different species, undergo phagocytosis, a separate uptake of the individual species could potentially enhance subsequent phagosome transport and maturation. It has been observed that the many parameters of phagosomes depend on the properties of the particles inside. For instance,

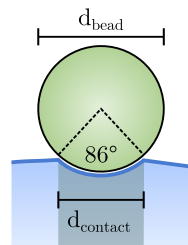


Figure 2.28: Schematic of contact area geometry. The contact angle of 86° corresponds to the geometric parameter $\alpha = d_{\text{contact}}/d_{\text{bead}} = 0.68 \pm 0.25$. In this case, the bead indents the membrane by 150 nm.

factors like particle size can impact the velocity of the phagosomal transport inside the cell^[93]. In this scenario, separate uptake would allow each phagosome to undergo processing at its own pace. Additionally, certain pathogens like mycobacteria or salmonella have evolved mechanisms to modify the phagosome subsequent to engulfment^[210,211], underscoring the potential necessity of separate uptake for effective degradation of these pathogens.

Moreover, macrophages play a role not only in pathogen elimination but also in presenting antigens from their targets to other components of the immune system. This process is regulated by the recognition of microbial-associated molecular patterns^[83], making it highly dependent on the precise composition of the target. Optimal antigen presentation might benefit from phagosomes containing only one category of target. In scenarios involving multiple similar targets, co-uptake of these targets within a single phagosome might demand fewer resources and coordination compared to uptake into multiple distinct phagosomes.

Our model suggests that a signal triggered by the activation of a single $Fc\gamma$ receptor expands to a width of $L = 530$ nm. This is the effective phagocytic signaling range for the part of the signaling cascade engaged during our dual bead experiments. According to the Sparrow criterion for resolution^[212], this implies that two identical targets could potentially be distinguished if they are separated by at least $L/\sqrt{2\ln 2} = 450$ nm. At this distance, the minimum between two Gaussian peaks with a full width at half maximum of L disappears. However, in practice, the finite number of receptors will increase the resolution limit. The value of L surpasses the average receptor distance δ derived from the model by about 1.7 times. The fact that there are slightly more receptors than the resolution limit ensures that enough receptors are available even in regions accommodating fewer receptors by chance. At the same time, the receptor density is low enough to avoid the expense of an excessive receptor count.

Notably, the effective range value L for phagocytic signaling matches the lower size limit for phagocytosis, which is often cited to be 500 nm^[76,213]. This lower limit originated from early observations indicating that polystyrene beads smaller than 500 nm are not phagocytized directly but instead accumulate on the cell surface, subsequently being internalized together in larger phagosomes^[78]. This observation led to the consensus that phagocytosis will not engage with very small beads, yet, the precise underlying cause has remained elusive. While our experiments weren't specifically designed to measure the lower size limit of phagocytosis, it seems plausible that the resolution limit of phagocytosis is similar to its lower size limit as achieving a higher resolution than the minimal target size would necessitate more receptors with only marginal benefits.

2.4.2 Actin dynamics and receptor mobility

In the experiments performed on LifeAct cells, direct indication of phagocytic uptake could be observed in some experiments. However, the number of experiments with localized actin polymerization around the beads was lower than expected. This may be a result of the bead drifting in and out of focus, which modulates the bead's appearance in the fluorescent image. This problem is further complicated as LifeAct staining usually provides less contrast compared to other stains such as phalloidin, as the LifeAct molecule can also bind to G-actin^[125]. Finally, phagocytosis is a relatively short process, usually lasting for about minute^[214,188]. This corresponds to only a few frames when imaging at 0.2 fps, making it easy to miss. All these factors made spotting the actin assembly during the phagocytic cup formation challenging. Despite these difficulties, in some experiments the uptake could

be observed directly and an example for joint uptake was provided.

It's worth noting that $\text{Fc}\gamma$ receptors exhibit clustering upon activation, which complicates the relationship between receptor count and distance. This clustering is a crucial element of the signaling process^[74]. Our model did not consider receptor diffusion, however in reality receptors can move on the cell membrane during the binding process, which might influence the outcome of the experiment. However, this effect is constrained by the limited mobility of the receptors due to membrane compartmentalization, as proposed by the picket-fence model^[215,37]. This restricted diffusion within the contact radius mitigates the impact of receptor mobility and clustering on the applicability of our model.

2.4.3 Phagocytic efficiency

By applying the logic of the model to a single bead with a single contact region, the probability for the uptake of a single bead can be calculated. This value is often referred to as the phagocytic efficiency in literature. In this case, the uptake probability is calculated by counting in how many cases the activation threshold of 0.5 is exceeded in the contact area of an individual bead. In Figure 2.29 this probability was calculated for different bead diameters using the values $\alpha = 0.68 \pm 0.25$, $\delta = (0.30 \pm 0.09) \mu\text{m}$ and $L = (0.53 \pm 0.11) \mu\text{m}$ obtained by the fit. For each datapoint, 10^6 different receptor patterns were evaluated.

Generally, the uptake probability predicted by the model rises with the bead diameter. This is in line with established experimental data, as discussed later. Looking at the plot, it is prominent that the red line does not follow a smooth curve, but shows several ridges

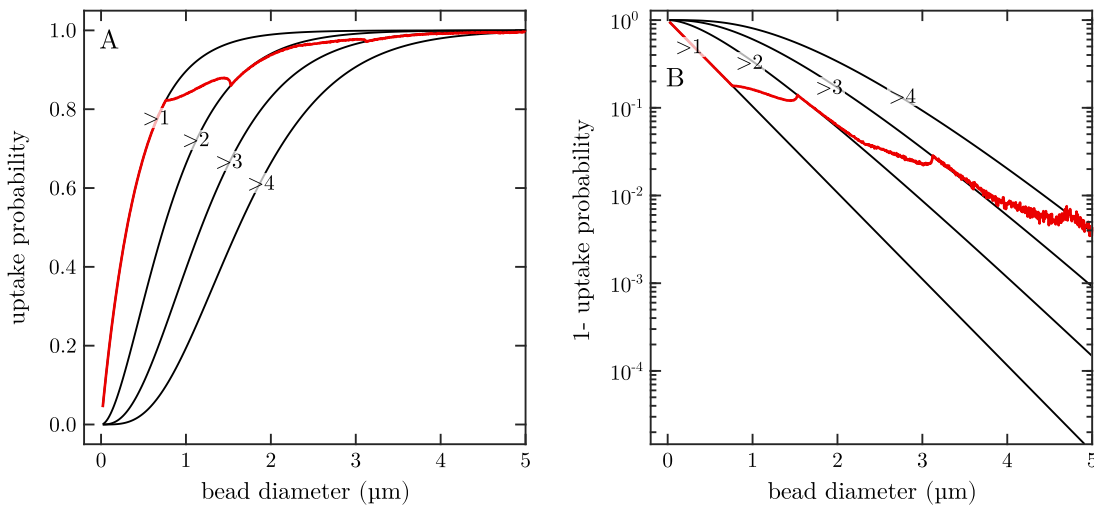


Figure 2.29: Phagocytic efficiency depending on particle size as predicted by the model. The red line shows the probability of a single beads of different diameters d to be taken up by the cell according to the model using the parameters $\alpha = 0.68 \pm 0.25$, $\delta = (0.30 \pm 0.09) \mu\text{m}$ and $L = (0.53 \pm 0.11) \mu\text{m}$. While panel A shows the uptake probability in a linear fashion, the panel B shows the probability that the bead is not taken up in a semi-logarithmic plot. As the contact region grows with the bead size, more and more active receptors are needed to reach the signaling threshold. The black lines represent the probability that at least N receptors fall into the contact region, this is denoted by the label “ $> N$ ” on each line. They are calculated by using the formula $P_i = 1 - \sum_{k=0}^{N-1} \lambda^k / k! \cdot e^{-\lambda}$ with $\lambda = \alpha \cdot d / \delta$.

and bumps. To understand this behavior, it helps to understand how the uptake behavior relates to the number of receptors in the contact area. For very small beads, a single receptor in the contact area is enough so that the activation level threshold is always exceeded. Below a certain bead diameter, the uptake probability is equal to the probability that the contact region contains at least one receptor. As the number of receptors inside the contact area follows a Poisson distribution, this probability can be calculated to $1 - e^{-\lambda}$, where $\lambda = \alpha \cdot d_{\text{bead}}/\delta$ is the expected average value for the number of receptors in the contact area. As the contact area gets larger, the finite width L of the activation peaks start to be more important. If the contact area is large enough, a single receptor will not be enough to push the average activation level in the contact region above the threshold, which partly counteracts the fact that the probability that more than one receptor is present in the contact region rises for larger contact regions.

A single receptor might not be sufficient to trigger uptake even earlier if that receptor is right at the edge of the contact region, because than a major part of the Gaussian peak falls outside of the contact region, reducing the average activation level inside the contact region. This causes the kink in the curve at $d_{\text{bead}} = 0.764 \mu\text{m}$. Eventually the contact region reaches a size where two receptors are needed to reach the activation threshold. This happens at $d_{\text{bead}} = 1.483 \mu\text{m}$. In the figure, multiple lines indicate the probabilities that more than N receptors are present. Those lines were calculated using the function $P_i = 1 - \sum_{k=0}^{N-1} \lambda^k/k! \cdot e^{-\lambda}$. As visible, the uptake probability follows each line for a bit, which means that in those regions, according to the model, the uptake is triggered if there are at least N receptors are present in the contact region.

These kinks in the uptake probability most likely an artifact of the model. Our model assumes that the receptor positions are static. In reality, receptors can diffuse on the cell membrane and move in or out of the contact region. As explained before, the receptor mobility even increases upon activation of the receptors^[74]. Also, the contact region size might vary between particles, depending on various parameters, such as the cell's stiffness or the distribution of IgG on the particle. This means that in reality, there is no hard limit on how many receptors are needed for phagocytosis of a specific particle to be triggered. Instead, we expect a more smooth transition of the experimental uptake probability, without the bends visible in Figure 2.29.

For bead diameters smaller than $0.5 \mu\text{m}$, the model predicts very low uptake probabilities, as it becomes unlikely that a receptor is present in the contact area. For the bead diameters $1 \mu\text{m}$, $2 \mu\text{m}$ and $3 \mu\text{m}$ used in this thesis, the model predicts uptake probabilities of 83.8%, 93.7% and 97.7%, respectively.

This numbers are high compared to experimental values reported previously. For example, K. Berghoff measured the uptake probability of $2 \mu\text{m}$ -sized beads via sedimentation experiments on the same cell-particle system and found an uptake probability of 34% when using a incubation period of 15 min and 45% for 30 min of incubation^[130]. In a study by A. Ramsperger using $3 \mu\text{m}$ -sized beads on macrophages, after a two hour incubation time, 65% to 69% of cell-particle interactions lead to internalization^[216]. This too is much less than the 98% reported by the model according to Figure 2.29. However, those experiments were designed totally different. While in Berghoff's and Ramsperger's experiments the beads were attached by chance, in the experiments performed in the scope of this chapter the beads were actively pushed onto the cell. Also, the fact that only cells with a high vitality (see Figure 2.13) were selected might increase the measured phagocytic efficiency.

For large bead sizes, the uptake probability rises and approaches 100% for beads larger

than $4 - 5 \mu\text{m}$. While in reality larger beads are in fact taken up more efficiently, this is only true to a point. For very large beads, the cell might initiate phagocytosis, but then struggle to complete the uptake process. For example, Champion et al. found that the chance for successful uptake drops drastically if the particle volume exceeds that of a bead with $15 \mu\text{m}$ diameter^[94]. Experimental data revealed that the total amount of beads engulfed per cell is highest for a bead diameter of around $2 - 3 \mu\text{m}$ ^[188,217] and then drops again for larger targets. Since our model only considers the initiation of phagocytosis, effects like the limited membrane reserve of macrophages are not considered and for larger particles, the uptake probabilities shown in Figure 2.29 does not match experimental probabilities for successful phagocytic uptake. Champion et al.,^[217] also found that the amount of beads attached per cell also drops for bead diameters larger than $3 \mu\text{m}$, indicating that the inability of cells to complete the uptake process cannot fully explain the discrepancy between our model and experiment data on the phagocytic efficiency. This means that while the model nicely explains the lower size limit of phagocytosis, it is not able to fully reproduce the upper size limit for phagocytosis.

2.5 Summary

This study focuses on understanding how the initial stimulus spreads within the cell during phagocytosis. By using IgG-coated microspheres as targets, we measured the probability for separate uptake based on the particles' distance and size when they attached to the cell. Our model for phagocytic signaling accurately predicted uptake probabilities for various bead sizes, distances, and reduced receptor numbers. These measurements provide a unique quantitative understanding on the spatial component of the phagocytic signaling. Combining measurements and our model, we determined the length scale of phagocytic signaling, a crucial step in quantitatively understanding this cellular process. This parameter aligns with the lower size limit of phagocytosis, a value previously measured experimentally, but unexplained.

3 Cell rheology using optical tweezers and mechanical aspects of phagocytosis

This chapter presents experiments designed to advance knowledge of the rheology of cells during phagocytosis. This was done using blinking optical tweezers, a method initially developed by K. Berghoff and thoroughly described in his PhD thesis^[130]. Later, a paper based on his work was published in a collaboration of K. Berghoff, W. Groß, me and H. Kress^[218]. Finally, W. Groß further developed the technique as described in his PhD thesis^[132]. Additional experiments were performed by J. Lix. In this work, this still young method was extended and refined for reliable application on a larger scale. While the acquisition technique was adapted from W. Groß, the evaluation protocol was reworked completely. The measurements recorded by J. Lix and W. Groß were reevaluated. Furthermore, the data pool was greatly extended by performing additional experiments.

3.1 Introduction

3.1.1 Mechanical aspects of phagocytosis

As described in chapter 1.3, phagocytosis can be structured into multiple steps, such as attachment, engulfment and the final cup closure. All of these steps are deeply mechanical processes. As soon as the cell and the target touch, more and more receptors like $\text{Fc}\gamma$ receptors, and other membrane proteins such as integrins bind to the target particle. This is especially important if the target is covered in opsonins such as IgG, which specifically bind to $\text{Fc}\gamma$ receptors. By this process, aided by membrane adhesion, the particle gradually becomes bound to the cell membrane with increasing firmness^[218]. After that, the membrane wraps around the particle, driven by active processes which overcome the bending stiffness of the membrane. This whole process is orchestrated by multiple different signaling cascades (see chapter 1.3.3), some of which react to IgG antibodies on the target particle and directly influence the mechanical properties of the membrane and the cytoskeleton. During this process, the membrane gradually engulfs the particle by forming the phagocytic cup, a membrane structure protruding from the cell and tightly enclosing the particle. When the target is completely covered by the cellular membrane and the membrane meets at one spot on the target, it is pinched off in a process related to the protein dynamin^[92] and a new vesicle containing the particle is formed inside the cell. This moment marks the end of the phagocytic engulfment process and the newly formed vesicle is called a phagosome. Especially for larger targets, macrophages need to undergo drastic changes in shape and size to engulf them which requires significant rearrangements of the cytoskeleton and the plasma membrane^[187].

Recently, advances in experimental techniques^[219] have made the mechanical aspects of phagocytosis more accessible. This has led to the acknowledgment that the mechanics of phagocytosis are crucial to the process itself and that mechanical properties of the target and the cell can influence the efficiency and the dynamics of phagocytosis. For example, Beningo

and Wang^[220] have observed that rigid polyacrylamid particles presented to macrophages have a higher probability of being taken up than softer particles of similar size, shape and chemical composition. Moreover, studies have shown that elongated, non-spherical particles are more likely to be engulfed by macrophages, if the portion of the shape presented to the cell has a high curvature^[94,214]. Even more, it seem that Dictyostelium cells can react to changes in the target's curvature occurring during the formation of the phagocytic cup and change their strategy depending on the target geometry^[221]. This suggests that mechanical processes may be an integral part of the signaling cascades involved in phagocytosis. In a study on neutrophils, elongated polystyrene particles have been more likely to be taken up^[222]. On the other hand, extremely elongated particles are rarely taken up by macrophages^[223]. This highlights that there still is little understanding on how physical particle parameters affect the particle-cell interaction and ultimately the course and the outcome of phagocytosis. This chapter aims to advance the knowledge on how the mechanical properties of the cell change before, during and after phagocytosis.

Through a variety of experiments, the knowledge on phagocytosis has expanded in recent years. It is quite established that the process of phagocytosis itself only takes a few minutes. For example, Paul et al.^[188] have analyzed brightfield image series of RAW 264.7 cells engulfing 1.85 μm silica beads and has found an average uptake time of 1.5 minutes. This matches the measurements reported by Richard et. al^[214], who have studied human neutrophils engulfing IgG-coated polystyrene particles and found average engulfment times of 37 – 90 s, depending on the bead size. However, both of these experiments solely rely on direct observation of the phagocytic uptake via brightfield microscopy, which can be unreliable for smaller particles.

Another important parameter of phagocytosis is the average time it takes for the uptake initiate after a target has been presented to the cell's surface. This time is currently mainly known via the measurement of the so-called phagocytic efficiency. In these measurements, beads are presented to cells for a certain amount of time, then the sample is fixed and the amount of engulfed beads is counted, sometimes using a fluorescent stain to mark all non-engulfed beads. Using this method, the number of engulfed beads per bead-cell interaction can be calculated as a function of the attachment time. For example, K. Berghoff has found that using an incubation time of 15 min, only 34% of particles attached to macrophages were taken up, after 30 min, 54% were engulfed^[130]. This ratio did not further increase when extending the incubation period to one hour, indicating that the engulfment can happen at any time in the first half hour after the attachment. While the latency period between attachment and uptake has been described before^[187], there is not much literature about what causes this delay in the uptake. This may be the case because many studies measuring uptake rates did not observe phagocytosis directly, but rather counted the formed phagosomes to draw conclusions. Single-cell experiments could provide valuable insight, as they allow to investigate the relationship between the duration of the latency period and other parameters like particle size or cell stiffness.

Measurements using colloidal force microscopy on human macrophages have reported a Young's modulus of 0.5 – 1.5 kPa for macrophages^[224], though the elastic modulus of macrophages decreases when presented pathogen-associated molecular patterns (PAMPs) like lipopolysaccharides^[225]. The softening of the macrophages comes with an increase in phagocytic activity^[225], underscoring how closely the initiation of phagocytosis is linked to mechanical stimuli. It has long been known that cells can mechanically interact with their surroundings. For example, immune cells detect cancer cells based on their higher stiffness compared to other tissue^[226]. It has been suggested that the cellular ability to sense stiffness

in their environment emerges from the impact the stiffness has on the remodeling of the actin cytoskeleton, as demonstrated by Gupta et al.^[227]. This illustrates how tightly intervened the mechanical properties and signaling cascades really are. The other way around, cells exert forces on their environment^[228]. For example, T-Cells have been measured to pull on particles with up to 0.8 nN of force^[229]. They usually achieve this by the use of myosin motors, which can create contractile forces inside the cell's actin cortex.

Actin also plays a major role during phagocytosis, as engulfing a large particle requires major rearrangements of the actin cytoskeleton^[13]. When using the actin-polymerization-inhibiting drug cytochalasin D, Tse et al.^[230] have found that the uptake of small particles with only 0.8 μm diameter was only be blocked partially. This was explained by suggesting that the uptake of small particles may be mediated by other, actin-independent processes such as clathrin-mediated endocytosis. To better distinguish phagocytosis from other uptake processes, it might be helpful to monitor the actin activity during live experiments. The process of phagocytosis also is influenced strongly by the target's shape and size^[188,220], highlighting how strongly the outcome of phagocytosis depends on mechanical aspects of the uptake process.

To recapitulate, despite the vast knowledge on the process of phagocytosis and the involved signaling cascades, a lot still remains in the dark. To shed light on the process of phagocytosis, it would be ideal to monitor the changes in the cytoskeleton of individual cells during the whole process of phagocytosis. The used method should also provide control over the attachment process and should be able to measure continuously from the moment of first contact, during the binding phase, the latency period, the phagocytic engulfment process and the phagosome maturation. While the actin cytoskeleton can be observed directly by observing the localization of filamentous actin using fluorescence microscopy, the mechanical properties of the cell can be accessed using the methods of microrheology. To accurately capture the moment of phagocytic uptake, both methods have to work simultaneously and require a high temporal resolution. Additionally, this would allow to observe the exact moment of phagocytosis, allowing to further investigate the purpose of the latency period before uptake. While many of the individual questions raised here have been addressed individually, this method could provide a more comprehensive picture on the process of phagocytosis and how the mechanics of phagocytosis are entangled with the signaling controlling the development of the phagocytic cup. The following section will survey established rheological methods before delving into the specifics of the blinking optical tweezers method.

3.1.2 Available microrheological methods

The knowledge on the mechanical properties of single cells is currently being extended by the use of microrheology. While this technique can be used on any soft matter, in biophysics it is used to study the mechanical properties of biological matter, including biological tissues and cells. The field of microrheology includes many different experimental methods, all of which use some kind of probing particle, like an opsonized polystyrene sphere (see chapter 2.2.3). This particle is attached to or submerged in the material of interest, which can be anything from a tissue sample, a single cell, or even only a single molecule whose unfolding force is to be measured^[231,232]. Then, a changing force or torque^[115,233] is applied to the particle and the reaction of the particle is recorded. The measured movement in response to a certain applied force contains information on the mechanical properties of the bead's surroundings. When compared with a rheological model, different parameters like the probed material's

stiffness or its viscosity can be calculated. The different methods of microrheology mainly differ in the means by which the external force is created. These are summarized in the next section.

In the simplest case of passive microrheology, no external force is applied at all. Instead, the thermal fluctuations of a particle are measured to determine the properties of the complex fluid surrounding it. By analyzing the time-dependent fluctuations in the particle's position, information about the local mechanical properties of the fluid can be extracted. This is often done by mean-squared displacement (MSD) analysis, which involves the calculation of the average squared displacement of the probe particle over different time intervals^[234]. From there, the diffusion coefficient D can be derived relating to the viscosity via the Stokes–Einstein relation^[235]:

$$D = \frac{k_B \cdot T}{6\pi \cdot \eta \cdot r} \quad (3.1)$$

Here, T is the temperature, k_B the Boltzmann constant, r the radius of the particle and η the dynamic viscosity of the fluid. For diffusion in a purely viscous material, the MSD increases linearly over time with a slope inversely proportional to the viscosity of the fluid. For viscoelastic materials, the behaviour of the particle gets sub-diffusive and the MSD grows slower the further time progresses^[236]. This can reveal information about the elasticity of the fluid^[237], but requires a long acquisition period, limiting temporal resolution. Opposing to this, our goal is to measure changes in mechanical properties during the highly dynamic process of phagocytosis, which requires a high temporal resolution. Furthermore passive microrheology is very sensitive to the experimental conditions, as non-diffusive forces on the probing particle create a movement superimposed on the Brownian motion. This active movement has to be estimated in order to correctly analyze the diffusive motion superimposed on it^[238]. However, it can be hard to distinguish components of the movement caused by diffusion and active movement caused by biological processes such as phagocytosis. In other words, the occurrence of biological processes within cells, such as phagocytosis, can introduce dynamic movements that may challenge the accuracy of passive microrheological measurements. This renders passive microrheology unfit for our needs.

In an article by M. Tassieri^[239], the author states that performing microrheology on living cells using optical tweezers may be problematic due to the long measurement time required for accurate results with a low signal-to-noise ratio. He argues that living cells are not in an equilibrium and active processes in action during acquisition, like actin-myosin interactions may substantially alter the viscoelastic response of the system before an accurate measurement can be finished.

Despite that, active microrheology is already being applied to living samples with great success^[240]. In active microrheology, an external force is applied to a sample, and the resulting response is measured. Because external forces are used, the method is invasive, also active microrheology requires more advanced instrumentation and sample preparation compared to passive microrheology. However, by actively pushing the system out of equilibrium, the viscoelastic response of the material can be measured fast by observing the reaction of the system to the changing force. The reduced acquisition time mitigates issues originating from the dynamic nature of the cell's structure or external drift. This makes active microrheology superior for investigating active processes like phagocytosis. However M. Tassieri makes a valid point that even in this case, the viscoelastic spectrum recorded from a single response

curve might suffer from a low signal-to-noise ratio.

Many different methods are viable to generate a controllable force for active microrheology. One option is to use ferro- or paramagnetic particles. By subjecting the sample to an inhomogeneous magnetic field, a pulling force can be created on the probing particle, which can be controlled by the strength of the field^[231,241,242]. This method is also known as magnetic tweezers, and has already been applied to study the rheology of macrophages by Bausch et al. in 1999^[243]. Alternatively, this approach can be adopted to measure rotational dynamics by using rotating magnetic fields to create a torque on the target microspheres^[244,115], a method called magnetic twisting cytometry. Also, microfluidics can be used to exert forces on microparticles. By pumping liquid through a microfluidic channel, a shear flow is created which creates a drag force on the particles in its way. However, this shear flow will also deform the whole cell, which makes this method better suited for measuring the deformability of the cell as a whole^[245,246]. Another way to exert external forces is to use atomic force microscopy (AFM)^[247]. An opsonized particle can be attached to the tip of an atomic force microscope and brought it in contact with a cell^[248]. Using this setup, the particle can be repeatedly pushed or pulled while being attached to the cell. The deformation of the sample is given from the vertical position of the tip and the force which the cantilever applies to the particle can be calculated from the deformation of the cantilever. This very direct approach provides very high temporal and spatial resolution, as the position of the cantilever can be measured with sub-Ångström precision and at a rate of 10 kHz^[249]. However, it cannot record the full process of phagocytosis, as full cup closure is impossible because the target particle has to remain attached to the cantilever. Finally, optical tweezers provide a reliable and minimally invasive method of applying forces to microparticles. This can be used to conduct microrheological studies^[250,251].

Each method of microrheology has its own benefits and disadvantages. For our experiments, we used optical tweezers, providing a highly controlled way to apply forces to individual beads. Using optical tweezers also gave us direct control over the attachment of the particle to the cell, which means that the rheological measurements could be started directly after the bead touches the cell membrane for the first time. Finally, the optical forces were switched rapidly by cycling the trap's power, which provided access to the high-frequency response of viscoelastic systems.

Regardless of the method to apply the force, the conventional way to do rheological measurements is to apply a sinusoidal stress to the system and observe the deformation caused by this stress. For different activation frequencies and amplitudes, the amplitude and the phase shift of the resulting movement can be measured. This provides detailed and precise data about the system's behavior over a wide range of time-scales, however it requires measuring each frequency individually and waiting for the system to reach equilibrium between measurements. Alternatively, the system can be pushed far out of equilibrium by suddenly activating the optical trap, allowing to record the relaxation of the bead into the trap. The recorded step-response of the system, i.e. its response to an instantaneous change in the applied force, contains all information of the full rheological spectrum, which can be recovered by a Fourier transformation^[252,253]. It should be noted that to reach a sufficient signal to noise ratio, averaging over multiple step-response events may be necessary^[239]. An insightful comparison of different rheological acquisition modes using optical tweezers was provided by Robertson-Anderson in 2018^[250].

The step-response method presents distinct advantages for our application. Notably, it quickly provides an overview of the global rheological properties. This facilitates measuring

the changes of rheological properties of a biological system over time, which is the main goal of our measurements.

3.1.3 Microrheology during phagocytosis using blinking optical tweezers

In this thesis, the rheological properties of the cell were investigated with the novel approach of blinking optical tweezers. To do that, the power of the trapping laser was rapidly switched on and off in a periodic manner, every time suddenly changing the force applied to the probing particle. The particle movement in response to the changing optical force was then analyzed and provided information on the mechanical properties of the cell.

The idea to cycle the laser power of optical traps is quite old and was already used in 1996 by Crocker and Grier to study colloidal suspensions^[254]. More recently it was demonstrated that by switching an optical trap between two positions in the sample using a SLM, an alternating force on a probing particle is created, which can be used to study rheological properties of complex fluids^[255]. While this paper provides a nice overview on the involved theory, the method was only demonstrated on beads suspended in water-based polyacrylamide solutions and not applied to biological samples.

In our experiments, the bead is attached to a cell, so a continuous trapping of the particle is not necessary. A schematic of the experimental setup is shown in Figure 3.1. In this setup, a force pulse on the bead is created by briefly redirecting the laser beam from position A to position B using a spatial light modulator. While the laser is active continuously, it only generates a significant force on the bead at position B. The viscoelastic movement of the bead during and shortly after the laser pulse can be used to obtain rheological data on the deformed cell. This method is able to measure the step-response of the system very quickly and in a direct manner, providing the temporal resolution needed for our application. Using optical traps also enabled arbitrary movement of the target particle, giving precise control on when and where the bead is attached to the cell. This made it possible to choose the cell and the cell region to which the bead is attached. This means that the beads could for example be attached directly to lamellopodia or, in contrast to that, very close to the cell nucleus, depending on the experimental goals. Furthermore, the method enables to continuously observe the cell morphology via brightfield and fluorescence microscopy simultaneously. In the experiments described in this chapter, this was used to observe the dynamics of the actin cortex by using LifeAct-GFP labeled macrophages.

Polystyrene beads covered with IgG antibodies were used as target particles in order to directly stimulate the biological machinery to initiate phagocytosis. To measure the cell stiffness using blinking optical tweezers, a bead was attached to the cell's surface and then repeatedly pulled on using an optical trap. The bead's reaction to the force pulse acting on it was observed. After the trap was disabled, the bead at least partially sprang back, due to the elastic component in the cells deformation, which was also recorded and can provide additional information on the cells elastic properties. However, because of the viscous component, the bead did not fully return to its original position.

Since the cell actively exerted forces on the bead, the bead moved even when the trap was switched off. This slow movement caused by the cell's force, and the incomplete elastic relaxation of the microscope stage accumulated over time and moved the bead by up to tens of micrometers relative to the coverslip. On top of that, the heating chamber of the microscope had been shut down to minimize vibrations caused by the fan, which led to the setup cooling down, potentially causing thermal stage drift. However, to effectively apply an

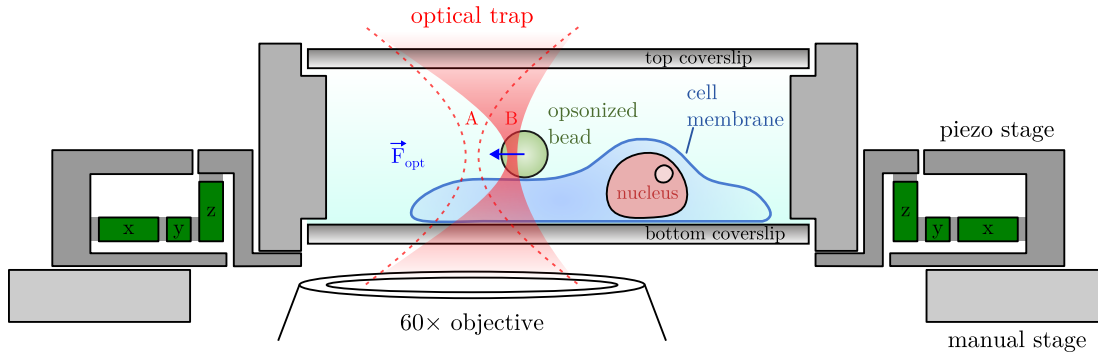


Figure 3.1: Concept of the blinking optical tweezer experiments. An opsonized bead is attached to a macrophage using optical tweezers. The optical trap was switched between the two positions A and B using a spatial light modulator. During attachment, the bead was trapped at the location B. After that, the automatic 3D feedback system used the piezo stage to keep the bead slightly off-center from the trap at location B. The optical trap was then switched to the position A where it created no relevant force on the bead, and was only switched back to position B for brief periods of time in order to repeatedly pull on the particle. The trajectory of the bead reveals information on the rheological properties of the region in which the cell is deformed by the optical force. At the same time, the actin dynamics were observed using fluorescence microscopy. The diagram is not to scale.

optical force to the bead, it needs to be placed slightly out of the trap's equilibrium position, ideally where the force acting on the bead reaches its maximum. It is also very important that the bead is exactly in the focal plane, as the calibration of the lateral optical forces is usually done with the bead in focus. Any axial shift between the bead and the trap will alter the magnitude of the optical force and its direction, rendering the calibration inapplicable. If the bead is moved further in or out of the trap, or slightly up or down relative to the trap, even only by $0.5\ \mu\text{m}$, the force acting on it will be severely reduced and can reach negligible values in a matter of minutes. While this still allows to study the adhesion dynamics of opsonized particles to cells^[218], the limited measurement time prevents any measurement long enough to also cover the process of phagocytosis and the following intracellular transport of the phagosome. This problem was solved by placing the sample on a computer-controlled piezo stage (see Figure 3.1). This stage is part of a feedback loop, which measures the bead's position between laser pulses and moves the sample to bring the bead back to its original position after each laser pulse.

Section 3.2.1 will explain how this feedback algorithm was implemented. Then, section 3.2.2 will elaborate how the calibration of the optical trap was carried out. The details of the acquisition sequence and the measurement process are explained in section 3.2.3, after which section 3.2.4 explains how viscoelastic materials like cells can be described by rheological models and applies this theory to the scenarios used during the experiments. Finally, section 3.3 lists all results, including observations on the actin dynamics during phagocytosis, the binding process and a detailed rheological analysis. Those results are elaborated further in section 3.4 and put into context. Finally, section 3.5 provides a short summary of the chapter.

3.2 Methods

3.2.1 Live tracking and feedback

3.2.1.1 Cross correlation tracker

To control the feedback loop, the bead was tracked in three dimensions during the data acquisition and a piezo stage (P-545.xR8S, Physik Instrumente, Karlsruhe, Germany) was used to move the bead back into the ideal position between blinking events. This ensures that the forces applied with the optical trap stay consistent. Since the piezostage also moves in the z -position to keep the bead in the focal plane, this feedback loop also acts as an auto-focus system. The application of the feedback loop is not limited to blinking experiments, but can also be used in other experiments to keep beads focused and at a fixed position in the field of view. This can be especially useful when using quantitative fluorescence microscopy to study phagocytosis, as it eliminates any influence of focusing on the fluorescence intensity around the bead and keeps the bead at a constant position in the image, making evaluation simpler and more reliable.

In this thesis, two different tracking algorithms were used. One of these trackers was the radial tracker already described in chapter 2.2.9. The other tracking algorithm is a cross-correlation based tracker developed by W. Groß^[132], which is based on the fast template matching algorithm published by Lewis in 1995^[256]. This cross-correlation tracker was used together with the modular acquisition software provided by W. Groß, performing the live tracking necessary for the blinking optical tweezers experiments described in chapter 3. At the time of the experiments, the radial tracking described in chapter 2.2.9 was not yet available. All functionality of the cross-correlation tracker is provided by the custom-written MATLAB class `CCTracker` written by W. Groß^[132].

The cross-correlation tracker is initialized by manually specifying the object positions in the first frame. The tracker then crops a reference region of a certain width around each tracked object. In every subsequent frame, the tracker uses the last known position of the bead to crop a scan region from the image. This scan region is then cross-correlated with the reference region, which yields a correlation matrix. If the scan region contains an object similar to the object captured in the reference region, the correlation matrix will show a distinct peak. A two dimensional Gaussian function is fitted to a small region around the maximum value in the correlation matrix to pinpoint the location of the maximum with sub-pixel accuracy. This location is then used to calculate the object's exact location inside the camera image. The tracker also calculates a value called similarity for each object. The similarity is one if the object found in the scan region exactly matches the reference image pixel by pixel and decreases the more the found object's appearance deviates. The tracker marks all particles whose similarity value falls below a certain threshold as lost and stops the tracking. Similarly, objects will be marked as lost if they move more than a certain threshold or reach the boundaries of the camera image. The tracking software by W. Groß also provides a fallback radial tracking mode which can be set up to engage once the similarity value falls below the minimum value. This radial symmetry fallback mode is fundamentally different from the radial tracking algorithm described in chapter 2.2.9. The fallback mode of the cross-correlation tracker uses a transformation described by Loy and Zelinsky^[257] to turn the whole image into a heat map highlighting centers of radial symmetry. In this heat map, a peak close to the last known position of the bead is selected. This position can then be used to crop a new reference image to newly initialize the cross-correlation tracker. It is

also possible to use the fallback radial tracker on its own by setting the tracking mode to “RadialOnly”. However, during the scope of this thesis this radial symmetry transformation tracking was only used as a fallback mode during the live tracking in the blinking optical tweezers experiments. In most cases, this fallback mode never engaged, because the feedback loop managed to keep the tracked bead in focus which caused the similarity value to stay high during the whole experiment.

However, the radial transform is still helpful, as it can be used to refine the manually specified starting positions for the cross-correlation tracker. This mitigates the disadvantage of the cross-correlation tracker that it can only track the manually specified starting position which might differ from the actual center of the tracked object. If the option `RefineStartPosWithRadial` is activated, the first frame will be processed by the radial symmetry transform and the manually specified starting points will be refined to match the local maximums in the generated radial symmetry heat map. This way, when tracking round objects, the tracker is always initialized in the exact center of the object, after which those will be tracked using only the cross-correlation tracking mode for as long as the similarity value is high. In the context of this thesis, the cross-correlation tracker was only used during the live-tracking experiments. For this use case, W. Groß provided the MATLAB class `CCTrackingModule`, which integrates this functionality into his modular acquisition software. All post-processing tracking was done using the radial symmetry tracker as described in chapter 2.2.9. I have since developed the MATLAB class `RadialTrackingModule`, allowing the integration of this advanced tracking algorithm into W. Groß’s acquisition software for future real-time tracking applications.

3.2.1.2 Performance comparison of radial and cross correlation tracker

To access the accuracy of the two trackers, a synthetic movie showing two beads was generated. To do so, the position of the beads was chosen so that one bead stays exactly in the center of the $161 \text{ px} \times 161 \text{ px}$ large image, while the other bead starts at a distance of 46 px to the right of the bead in the center and then moves around the central bead in a spiral pattern. The spiral pattern is visualized in Figure 3.2A, the moving bead does a total of 12 revolutions around the central bead while simultaneously reducing the distance to the central bead to only 4.6 px. All this was rendered as a constant movement in 10000 frames. The image intensity was calculated as the sum of two identical intensity functions, each depending on the distance to one of the beads:

$$I = I(\rho_1) + I(\rho_2) \quad (3.2)$$

For the intensity function $I(\rho)$, any function that drops to zero for $\rho \rightarrow \infty$ is suitable, it does however make sense to choose a function that closely recreates the appearance of beads in experimental images. Via trial and error it was determined that a radially symmetric pattern calculated by the function

$$I(\rho) = C \cdot \left(1 - \left(\frac{\rho}{\sigma}\right)^3\right) \cdot e^{-\frac{1}{2}(\rho/\sigma)^3} \quad \text{with } \sigma = 4.60 \text{ px} \quad (3.3)$$

closely resembles the experimental image of a $2 \mu\text{m}$ bead captured by the Luca-R camera. This function was solely chosen because the created intensity distribution matches the appearance of a $2 \mu\text{m}$ bead. Panel B nicely demonstrates this by comparing the experimental intensity

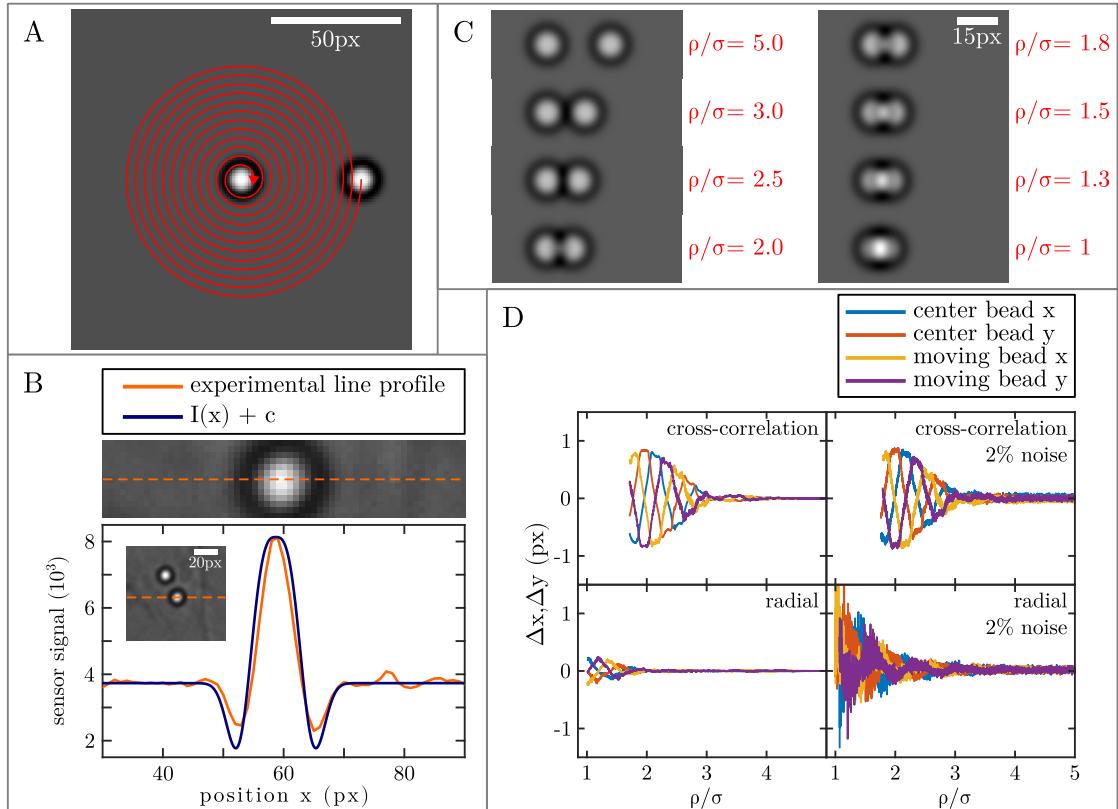


Figure 3.2: Comparison of the accuracy of the cross-correlation and the radial tracker. A synthetic movie shows two beads, whose intensity distribution was described by Equation 3.3. While one bead stays stationary in the center of the image, the other bead circles around the stationary bead, gradually moving towards the center (see panel A). Panel B shows how the function $I(\rho)$ in Equation 3.3 compares to an experimental intensity profile. In panel C, the appearance of a synthetic bead pair at different distances is shown. Panel D shows the tracking errors for the cross-correlation and the radial tracker for both coordinates of both beads and two different noise levels. The radial tracker shows less systematic error.

line profile of an experimental image with the analytical function. The function is related to the Ricker wavelet, which is sometimes also referred to as the mexican hat function due to its shape, however in Equation 3.3 the radial coordinate ρ is cubed instead of squared. Figure 3.2C shows a set of bead pairs at different distances ranging from $\rho = \sigma$ to $\rho = 5\sigma$. In the case of $\rho = 5\sigma$, both beads are far away from each other, while for $\rho = \sigma$, the image of both beads overlap strongly, making it successively harder for the trackers to correctly identify the beads' positions. For values $\rho/\sigma < 2$ the images become less realistic, as in reality the bead cannot overlap like this without also shifting vertically. Finally, the image intensities with and without noise were normalized to integers in the range of $0 \dots 255$ and saved as *.tif-Files.

To test the trackers' performance, the two beads in the two resulting image sequences were tracked with the two different trackers: Firstly, the image sequences were tracked using the cross-correlation tracker by W. Groß which was set to use a ROI width of 17 px, a scan width of 50 px, and a fit region radius of 2 px. The cross correlation tracker was initialized manually with the build-in automatic starting point refinement active. Then, the same movies were tracked using the radial tracker, set to use a active area radius of 12 px, with the masking radius set to the same value. The starting positions for the tracker were also specified manually. The tracking was stopped as soon as the unroundness value exceeded 0.4 or if a bead moved by more than 10 px in a single frame.

Figure 3.2D shows the deviations from the real trajectory in all mentioned cases. All trackers were able to accurately follow both beads at first, but then showed increasing errors as the beads moved closer to each other. Without noise, the radial tracker was able to track both beads accurately up to a very close distance of almost $\rho = \sigma$, while the cross-correlation tracker failed much sooner. The radial tracker also showed less systematic errors, which were below 0.3 px, while the cross-correlation tracker exhibited systematic errors of almost 1 px.

Additionally, a new set of test movies with artificial noise were generated. To do that, the calculated floating point image intensities for all pixels were then normalized to the range of zero to one. Then, a normally distributed noise with a standard deviation of 0.02 was added and the image intensities were normalized again to the 8 bit range of $\dots 255$. This level of noise is roughly comparable to the amount of noise encountered in our experimental applications. In the image with 2% noise, the radial tracker outperformed the cross-correlation tracker as well. However, the radial tracker seems to be sensitive to the noise, especially for very small bead distances, as the errors for those now easily exceeded 1 px. However, while the tracking error increased for $\rho < 2\sigma$, the radial tracker was still able to follow the objects, even if the objects overlapped very strongly, while the cross-correlation tracker failed much earlier. For the more relevant scenarios $\rho > 2\sigma$, the tracker was exceptionally accurate. The cross-correlation tracker is not affected much by the addition of the random noise, as the systematic errors for beads in close contact are larger than the uncertainty added by the noise.

All in all, the radial tracker is superior for the application needed in this thesis, as bead in close contact to each other need to be tracked. It also requires less computational time, increasing throughput. By using tapered active areas, as described in chapter 2.2.9, it might be possible to improve the reliability and accuracy of the radial tracker even further. Because of these benefits, it was the mainly used tracking algorithm for the rest of this thesis.

3.2.1.3 3D tracking

As mentioned before, the bead had to be kept in focus during the blinking optical tweezers experiments to keep the optical forces on the bead consistent. This was done by determining the z -position of the tracked bead and moving the piezo stage to counteract any focal drift between the blinking events.

To calculate how far the stage had to be moved, an algorithm which can determine the z -position of a bead relative to the focal plane was used. The live tracking software was set up to perform the two dimensional tracking as described before using the cross-correlation tracker. After that, a $15 \text{ px} \times 15 \text{ px}$ region of the captured image around the tracked particle was cropped and fed into the z tracking algorithm. Based on the appearance of the bead in this region, the algorithm determines the bead's axial position. To do that, a method developed by W. Groß^[132] was applied. This method is based on a convolutional neural network, which has been trained on reference data to correctly predict the z -position of observed beads.

The reference data was acquired by observing beads with a diameter of $2 \mu\text{m}$ on a coverslip using the pixelfly camera and 2×2 binning through the $60\times$ objective. Then, the sample was raised until all beads were completely out of focus. After that, a sequence of images was acquired, while lowering the sample by 100 nm using the piezo stage after each image. Multiple of those image stacks were taken, creating a pool of reference data containing a total of around 8250 beads^[132]. Then, the location of all beads in the training data was determined by calculating the maximum projection along the z -axis for each image stack and doing a cross-correlation with a reference image. This creates a heat map indicating the most likely bead positions, which then were obtained using a peak finder algorithm. From there, each bead was processed individually by cropping the stack to a region of $15 \text{ px} \times 15 \text{ px}$ around the bead's location. For each bead, the frame in which the central intensity of the bead's image reached its maximum was defined as the frame in which the bead is in focus. This individual frame was saved in a separate folder in which all in-focus images were collected. Similarly, the 15 frames before the in-focus frame and the 10 frames after the in-focus frame were collected in separate folders. This way, all images were categorized in 26 different categories corresponding to $z = -1.5 \mu\text{m}$ to $z = 1.0 \mu\text{m}$ with $0.1 \mu\text{m}$ steps. Based on this, the data was divided in training and validation data and the convolutional neural network was trained. For each input image, the neural network put out a set of 26 scores for each z -position. After correct training, the output score peaked at a distinct category, corresponding to a certain z -position. To increase the accuracy, a Gaussian function was fitted to small region around the maximum output score and the peak position of the Gaussian was used as the final estimate for the bead's z -position. A detailed description of this tracker can be found in chapter 3.4.1.2 of Groß's PhD. thesis^[132].

In this thesis, the z -tracker was used as provided by W. Groß. However, new training data with a smaller step size was recorded which can be used to retrain the network in the future. The newly acquired training data only uses 50 nm steps between two subsequent images, which will increase the neural net's resolution. Also, training data for different bead sizes was acquired which makes it possible to train a new neural net for other bead sizes. Additionally, images without 2×2 -binning were recorded, as disabling the binning will help increase accuracy, which might be important to reliably track $1 \mu\text{m}$ -sized particles. In Figure 3.3 beads of all three different sizes used in this thesis are shown when observed at different z -positions. For the figure, one bead of each size was chosen. The image was tightly cropped

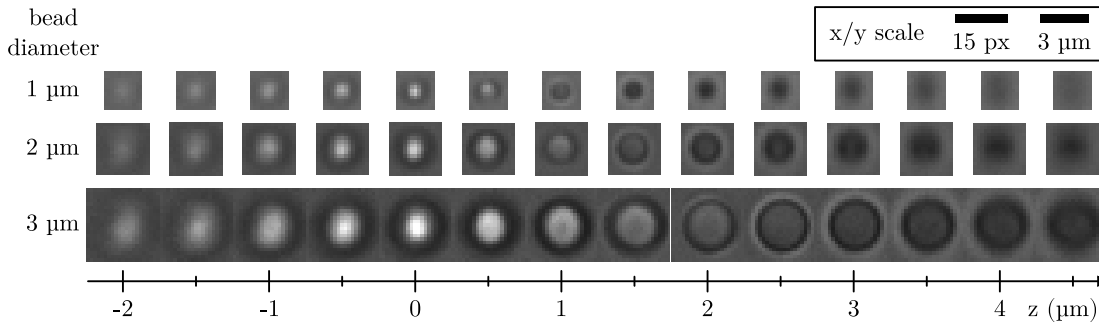


Figure 3.3: Images of beads at different focal positions. Beads of the sizes $1\ \mu\text{m}$, $2\ \mu\text{m}$ and $3\ \mu\text{m}$ were imaged in different positions relative to the focal plane. All images were recorded using the pco pixelfly camera using 2×2 binning. The images were cropped to $11\ \text{px} \times 11\ \text{px}$, $15\ \text{px} \times 15\ \text{px}$ and $21\ \text{px} \times 21\ \text{px}$ respectively. Images similar to those in this figure were used by W. Groß to train a neural network.

around the bead and the frame in which the central pixel of the bead showed the highest intensity was defined as $z = 0\ \mu\text{m}$. The figure was limited to showing only every tenth image in a small range around $z = 0\ \mu\text{m}$. The middle row in this figure shows images of $2\ \mu\text{m}$ -sized bead, recorded using the pixelfly camera with 2×2 binning and cropped to $15\ \text{px} \times 15\ \text{px}$. This is exactly the format of the images fed into the neural network to determine the z -position during live tracking.

3.2.1.4 Piezo stage testing

A control experiment was performed to confirm that the piezo stage moves exactly the same distance as specified in the software. To measure the actual movement of the piezo stage when directed to travel a specific distance in the software, we conducted an experiment using a single bead within the camera's field of view.

The bead, lying statically on the coverslip, served as an indicator to detect any movement of the coverslip. This bead was observed using three cameras simultaneously. By using the L80 setting on the microscope, 20% of the light was directed towards the pco pixelfly camera, while using the 50/50 beam splitter in the dual-camera port ensured that 40% of the total light hit each the IDT Nx4-S2 and the Andor iXon Ultra camera. This multi-camera setup was used to ensure the final result were not influenced by potential errors in the calibration of the apparent pixel sizes (see Table 2.2). The highspeed camera (IDT Nx4-S2) was set to use 4×4 binning, all other cameras used no binning. The piezo stage was set to a theoretical maximum moving speed of $5000\ \mu\text{m}/\text{s}$. The actual speeds reached during this tests and in real feedback experiments were much lower. The frame rate of the highspeed camera was set to its minimum value of 30 fps, both other cameras recorded at 2 fps.

Finally, a macro was used to move the piezo stage in a predetermined pattern. The stage was programmed to move one step in the $+x$ -direction, pause, and then back to its initial position. After that, a step is made towards the $-x$, the $+y$ and the $-y$ direction, each time returning to its starting position. This process, involving eight single steps, was repeated for nine different step sizes ranging from $0.5 - 30\ \mu\text{m}$. When counting all steps including those returning to the starting position, the stage moved a total of 72 times, each time pausing for at least one second between each step. This ensures that each camera captures at least one

image of the stationary bead between each step. The trajectories from movies acquired with the three cameras were all obtained by tracking the bead's movement with the radial tracker using an active radius of $1.5924\ \mu\text{m}$ (see chapter 2.2.9). In the next step, all the steps made by the piezo stage were identified in the trajectory and the distances by which the coverslip moved were determined from the trajectory. The distances measured in pixels were then transferred to a value in micrometer using the experimentally determined pixel sizes (see Table 2.2). The results of this control experiment will be presented in chapter 3.3.3.

3.2.2 Force calibration

For the experiments described in this chapter, it was necessary to know the exact force exerted on the bead by the optical trap. There are various methods for calibrating the forces generated by optical tweezers^[148]. All of these methods aim to find the relationship between the deflection of the trapped particle from its resting position and the force imposed on it by the trapping laser. To do this, the relative position of the particle to the trap and the optical force acting on it have to be measured accurately at the same time. The force acting on the trapped particles is easy to measure due to their low Reynolds number. Particles trapped in biological research usually have a diameter of $0.1 - 10\ \mu\text{m}$ and are suspended in liquid medium which has a viscosity similar to water. Even a large, $10\ \mu\text{m}$ -sized particle moving at the high speed of $1\ \text{mm/s}$ will only have a Reynolds number of 0.01 . Because of this low Reynolds number, any inertia can be neglected. This means that a particle moving in the force field of an optical trap in a homogeneous medium will always move back into its equilibrium position at a speed proportional to the force acting on it, as the flow of liquid around the particles is purely laminar. In this state, the drag force and the optical force will have the same magnitude and act in opposing directions. The drag force on the particle can be calculated from its velocity by utilizing Stokes' law:

$$F_{\text{Stokes}} = 6\pi\beta_0\eta r v \quad (3.4)$$

The factor β_0 is a correction factor which is one for particles in a homogeneous environment. However, if the particle is moving close to a hard boundary, as it is the case with trapped beads moving parallel to the coverslip just a few micrometer above the glass, the particle will react to the same force with a slower movement than it would be the case if it was surrounded by medium in all directions. In this case, the force on the particle can be calculated using Faxén's law, which states that the stokes force needed to move a sphere through a medium close to a boundary will be increased by a factor $\beta_0 > 1$ compared to it moving in homogeneous environment. The factor β_0 can be calculated from the radius r of the particle and the distance of the sphere's center to the boundary h ^[258,147]:

$$\beta_0 = \left(1 - \frac{9}{16}(r/h) + \frac{1}{8}(r/h)^3 - \frac{45}{256}(r/h)^4 - \frac{1}{16}(r/h)^5\right)^{-1} \quad (3.5)$$

A graphical representation of this increase can be seen in panel A of Figure 3.4. The correction factor β_0 starts from a value of $\beta_0 = 4.54$ for $h/r = 1$ and quickly drops to a value around one as soon as the distance of the bead to the boundary reaches a few bead radii.

The trap stiffness strongly depends on the bead size. The absolute restoring force on the trapped particles rises with the bead diameter^[259]. As described before in chapter 2.2.6.2, the trap stiffness increases proportional to the bead's volume for small particles and then grows

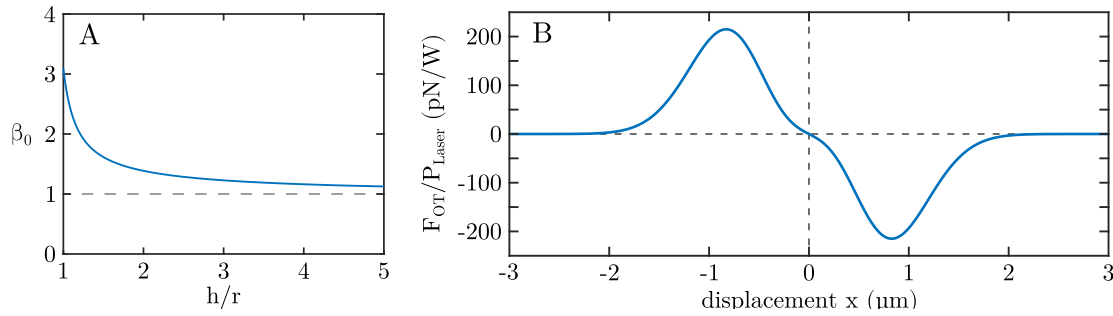


Figure 3.4: Force calibration of the optical tweezers. Panel A shows the correction factor β_0 for the drag force of a spherical object of radius r close to a flat boundary as predicted by Faxén’s law (Equation 3.4). The x -axis shows the ratio of h/r of the distance h from the particle’s center to the boundary’s surface to the particle’s radius. Panel B shows the used empirical force calibration curve. The optical force is plotted as a function of the displacement from the trap’s center in x direction. This analytical function was formulated by W. Groß^[132] and is backed up by experimental data. Because the force is proportional to the laser power, the vertical axis shows the force relative to the laser power measured before lens L1.

slower as soon as the particle size reaches the magnitude of the trapping beam’s wavelength. Meanwhile, the viscous drag on the particles only rises with the squared bead radius, as the cross-sectional area of the particle increases. Furthermore, for smaller particles, the trapping stiffness is more sensitive to imperfections in the beam’s shape^[173]. Combined, this means that potential problems with an unsatisfactory trapping stability will become much more prominent the smaller the trapped particles are. In our experiments, the 1 μm beads noticeably escaped the traps more often during our experiments. However, for a skilled operator, it was possible to perform experiments without any issues.

To calibrate the optical trap, the step-response of a trapped bead was measured. These calibration experiments were carried out by W. Groß and are described in more detail in section 3.4.1.4 of his PhD thesis^[132]. For the calibration, a polystyrene microparticle suspended in water was trapped at a distance of (7 ± 1) μm above the coverslip. Then, the system was pushed out of equilibrium and the relaxation of the bead into the trap was observed using the IDT Nx4-S2 highspeed camera. In theory, this could be done by switching the laser off, moving the stage 1 – 2 μm and activating the laser again. Unfortunately, the switching time of SLM is much slower than the time it takes for the bead to be pulled back into the trap. Also, the mechanical shutter cannot be used to switch the laser as it would introduce vibrations disturbing the sensitive measurement.

As a solution, the piezo stage was used to move the bead a fixed distance while keeping the laser active. This resulted in a sudden peak in drag force on the trapped bead which is shifted out of its equilibrium position by this force surge. By carefully tuning the speed of the piezo stage and the distance of the piezo stage’s movement, it was possible to create a situation in which the piezo stage has already stopped moving, but the bead has not yet reached its equilibrium position again. In this situation, the bead could freely relax into the trap. Since according to Equation 3.4, the velocity with which this relaxation happens is directly proportional to the optical force of the trap, the full force-displacement dependency could be measured without switching the laser power.

However, this method only works at low laser powers, which is why the calibration was

done using a laser power of only $P_{\text{Laser}} = 10 \text{ mW}$, measured after lens L1 (see Figure 2.6). At a laser power of 300 mW, as used in experiments, it is not feasible to push the bead out of equilibrium using the piezo stage, as the trap is too strong and the bead stays in place even if the stage moves at a high velocity. However, the force acting on the bead is generally proportional to the laser power, which means that the forces at higher laser powers can be calculated easily even from this calibration measurements.

W. Groß performed a total of 13 calibration experiments, all deflecting the bead in the $+x$ -direction. Furthermore, he measured the standard deviation of the trapped particle to be $\sigma = 61 \text{ nm}$, which using the equipartition theorem^[148] translates to a trapping stiffness of $k_x/P = k_B T / (P_{\text{Laser}} \cdot \sigma^2) = 107 \text{ pN}/\mu\text{m}^{-1}\text{W}^{-1}$. After evaluation, he came to the conclusion that the trap's force when using a hologram shifting the trap to the location $(x, y) = (-4, 4) \mu\text{m}$ can be described using the following equation (see Eq. 3.28 in his thesis^[132]):

$$F_{\text{OT}}(x) = P_{\text{Laser}} \cdot \exp\left(-\left(x/0.7 \mu\text{m}\right)^2\right) \cdot \left(-107 \text{ pN}\mu\text{m}^{-1} \cdot x + 9.9 \text{ pN}\mu\text{m}^{-2} \cdot x^2 - 1390 \text{ pN}\mu\text{m}^{-3} \cdot x^3\right) \quad (3.6)$$

A graphical representation of this calibration curve is shown in Figure 3.4B. While the curve was only measured in $+x$ direction, this formula can also be used to assume that the force profile of the trap is radially symmetric.

3.2.3 Experimental procedure

The setup was configured to allow the simultaneous imaging of the fluorescence and brightfield images as described in chapter 2.2.5.1 and illustrated in Figure 2.4. To achieve this, a filter limiting the brightfield illumination to long wavelengths was placed in the illumination light path. In the dual-camera port, the dichroic beam splitter was inserted to separate the fluorescent and the brightfield light before the cameras. Furthermore, the GFP filter cube was placed in the beam path. To prevent photodamage, multiple gray filters reduced the excitation light to only 1/512 of its maximum power. The excitation and brightfield shutters stayed open for the whole duration of the experiment to avoid any vibration interfering with the evaluation. The microscope was set to only output 80% of the light into the dual-camera port and 20% on the additional pixelfly camera, which was used for the live tracking. The live tracking of the bead enabled the correct function of the feedback system (see chapter 3.2.1). Both Nomarski prisms used for DIC imaging (see chapter 2.2.5.3) were removed from the beam path. All necessary electronic equipment was powered on and the heating chamber of the microscope was set to a temperature of 38.5 °C and allowed to warm up. This temperature is higher than the recommended incubation temperature of 37 °C for J774A.1 macrophages, however the heating had to be switched off during acquisition in order to avoid vibrations, causing the sample to cool down. Then, the laser was powered on and after a warm-up period the power meter's probe was temporally placed after lens L1 (see Figure 2.6). The laser power at this position was adjusted to 500 mW by turning the half-wave plate in front of the polarizing beam splitter. Early experiments were done with only 300 mW laser power, but the laser power was raised to create a stronger reaction of the bead in stiff environments, such as during the formation of the phagocytic cup.

All cell stiffness measurements were performed on LifeAct transfected cells using the 60× objective. After the sample was prepared as described in chapter 2.2.4, it was placed on the microscope and the cells were brought into focus. A hologram shifting the laser focus to

the position $(x, y) = (-4, 4) \mu\text{m}$ was generated and applied to the spatial light modulator. By switching the power of the SLM on and off, it was possible to switch the trap's position between the origin in the center of the field of view, where the bead is not affected, and the position $(x, y) = (-4, 4) \mu\text{m}$. At the start of the experiment, the SLM was activated and a $2 \mu\text{m}$ -sized, opsonized polystyrene bead was caught in the trap at the location $(x, y) = (-4, 4) \mu\text{m}$. Then, the sample was moved until a cell showing a strong LifeAct signal was found and the bead was positioned directly above this cell, with a few micrometers distance between the cell and the bead (see Figure 3.5, panel A). At this point, the heating chamber was shut down to prevent the vibrations of the fan to interfere with the measurements. After that, the image acquisition was started using all three cameras.

The image acquisition of the pixelfly camera, as well as the power of the SLM and the piezo stage were all controlled by a custom MATLAB software. This software has mainly been developed by W. Groß, building on code supplied by A. Sabri^[164] and K. Berghoff^[130], however I also provided some new code and contributed by rewriting the hologram generation algorithm. A detailed description of the software is provided in W. Groß's PhD thesis^[132]. The software was designed using the model-view-controller design pattern and apart from the image acquisition, all functions were encapsulated into separate software modules. This allowed easy maintenance and easy implementation of new functions. The core program directly controlled the pixelfly camera and was responsible for acquiring a brightfield overview image of the whole cell, including the probing bead. For the blinking experiments, three different modules were added to expand the functionality. The module `CCTrackingModule` adds cross-correlation tracking capability to the software. This was then used to track the position of the bead in real time using the 3D tracking algorithm as described in chapter 3.2.1.3 and in the PhD thesis by W. Groß^[132]. This positional information was then used by the module `PiezoFeedbackModule` to determine how much the sample had to be moved to return the bead to its target position in the image. This movement was then applied using the piezo stage. Finally, the software module `HOTModule` controls the power to the SLM and makes sure that the laser is switched at the correct times between the pixelfly camera image acquisitions.

The first camera to be started was always the pixelfly camera, which was set to use 2×2 binning to reduce the time the camera takes to acquire an image. As the bead's position in the camera's first image had to be specified manually to initialize the tracker, the other two cameras usually started with a delay of 5 – 20 s after the pixelfly camera, with only a short delay of less than 5 seconds between both cameras. The IDT-NX4 camera recorded high-speed brightfield image data of the bead at a speed of 500 fps. The highspeed camera was set to use 4×4 binning, as all images of the acquisition have to fit in the 5 GB internal memory of the highspeed camera. For the same reason, the field of view of the camera was tightly cropped around the bead. Both of these measures managed to increase the maximum recording time to about 23 minutes. The highspeed camera data was used to provide the high frame rate positional information needed for the rheological evaluation. Simultaneously, the Andor iXon camera was set to capture a fluorescent image of the whole cell every two seconds, providing information about the localization of filamentous actin inside the cell. The pixelfly camera images were relevant only during the acquisition process. They were used to obtain the bead's position, which is required for controlling the bead's position relative to the trap using the piezo stage.

The pixelfly camera started with a high frame rate to ensure that the software captures images as fast as possible the desired time between two frames was set to 0.3 s in the

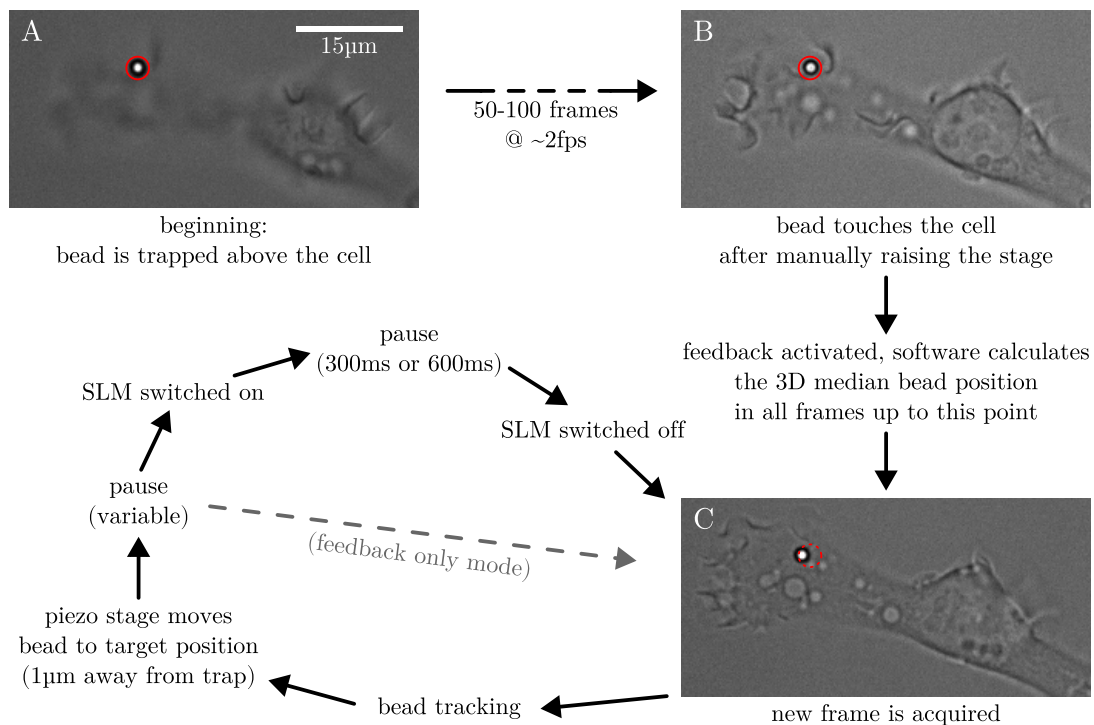


Figure 3.5: Diagram showing the sequence of events during blinking optical tweezers experiments. The acquisition software handled the image acquisition, particle tracking, piezo stage control and SLM switching. The measurements began with a 25 – 50 s period in which the bead hovered trapped above the cell and images were recorded at roughly 2 fps (panel A). Towards the end of this period, the stage was raised until the cell and the bead touched (panel B). At this point the feedback loop was activated. The software calculated the target position of the bead, captured a new frame, located the bead in the frame and moved the stage such that the bead was positioned at the target position 1 μm away from the optical trap (panel C, the red circle marks the trap position) so that the focal plane was kept constant relative to the particle (see chapter 3.2.1). Depending on whether the blinking had already been activated, which was done directly after activating the feedback, the SLM was switched on for a set amount of time right before the next frame was captured. The variable pause was chosen so that a new frame was captured every 2 s. The cycle was repeated 678 times (median over all experiments), after which the highspeed camera’s memory is exceeded and the rheological measurements are stopped. It was possible to continue the image acquisition in feedback-only mode.

software. However, the highest frame rate that the livetracking software is capable of in this configuration is around 2 fps. The frame rate was later dropped down to 0.5 fps in the moment the blinking is activated. This increase in frame rate was done for two major reasons: Firstly, before the feedback system can be activated, the trap's position in the image has to be determined. This is done by calculating the median position of the tracked bead in all images recorded before the feedback system is started. When using a high frame rate for the beginning of the experiment, more images can be captured until the feedback is started, which means that the trap's position can be calculated more accurately. Secondly, having a live, high-frame rate image of the cell as a reference makes the process of attaching the bead to the cell easier and more reliable.

Using the high frame rate, around 50 frames were captured without moving the microscope stage. This was done to ensure that no drag forces were acting on the bead and the x, y and z positions of the optical trap could be identified accurately in the field of view using the bead's trajectory. After that, the stage was gradually lifted until the cell touches the bead (see panel B in Figure 3.5). As soon as the bead was attached, the feedback loop was started. The software immediately calculated the median x, y and z position of the bead in all pixelfly images recorded up to that point. This 3D position represent the trap's position in the image. To calculate the target position at which the bead should be placed during the experiment, the position was shifted by a fixed amount into the $+x$ direction. This shift was set to $1\ \mu\text{m}$ in all experiments. At this value, the optical force acting on the bead is high, and stays relatively constant even if the bead is pulled towards the optical trap by a few $100\ \text{nm}$ (see Figure 3.4B). The target position was then saved and the software calculated the necessary stage movement to place the bead at the target position and sends a command to the piezo stage to execute this movement. This corrective movement was done each time after a frame was recorded by the pixelfly camera. This feedback loop is explained in more detail in chapter 3.2.1.

Around the same time as the feedback loop has been started, the blinking process was activated. After that, the SLM was switched off and was only powered on during the short laser pulses used to stimulate the cell. When the SLM was switched off, the trapping beam still passed the sample, but missed the bead by approximately $5 - 7\ \mu\text{m}$, which means that the optical force inflicted on the bead was negligible. Each time before an image was recorded by the pixelfly camera (panel C in 3.5), the power to the SLM was switched on for a set amount of time and then switched off again. After that, a waiting time was implemented to give the bead some time to relax. Following this waiting period with the SLM switched off, the pixelfly image was recorded and the 3D tracker engages to find the bead's position in the new image. The difference of the current bead position in the image and the target position was then calculated. The piezo stage was moved sequentially by this amount in x and y position. The stage was also moved in z -direction to keep the focus on the bead constant, however to increase the stability of the feedback loop, the stage was only moved by 30% of the distance between the current axial bead position and the target axial position.

After that, a short pause was implemented to ensure equal temporal spacing between the blinking events. This process was repeated for each frame until the end of the measurement. The duration of the pause was adjusted in a way that a full cycle of blinking, image acquisition and feedback happened every two seconds. After approximately 23 minutes, the IDT-NX4 high-speed camera stopped recording as soon as its memory was filled. When this happened, the heating chamber of the microscope was turned on again. At this point, the temperature inside had dropped to approximately $35\ ^\circ\text{C}$, which is the reason why the initial temperature

had been set a bit higher than the optimal 37°C. When the highspeed camera had stopped, rheological data was no longer acquired. However, in many experiments we chose to continue to record for another 20 minutes with the pixelfly and the iXon Ultra cameras, as those still provide information about the actin localization and potential uptake events can still be detected. Only in seven experiments the experiment ended before 23 minutes elapsed, which was caused by several sources of disturbance, such sudden vibrations or an extra bead within in the field of view, causing the initial bead to be lost.

3.2.4 Viscoelasticity and power-law rheology

As explained in chapter 3.1.2, the goal of microrheology is to measure and analyze how a material deforms under external forces. The stiffness of a material can be determined by measuring two physical parameters. The first parameter is the stress σ , which depends on the force and the geometry of the system. Generally, the stress is defined as the force acting on the system divided by a reference area. This reference area usually is the area on which the force acts, for example, in the case of a homogeneous rod being stretched, this area is the cross-section of the beam. The second parameter is the strain ϵ , which is a dimensionless value describing the deformation of the system relative to a reference state. In the case of the deformed rod, it is defined as its elongation divided by its length. For example, if the pulling force lengthens the rod by 1%, the strain is 0.01. Stress-strain relationships describe how a material deforms when a force is applied to it. This is not limited to axial deformations, as with a appropriate definition of the reference area, the same math can be used to describe systems deformed by shearing, torsion or even inhomogeneous deformations.

3.2.4.1 Constitutive models of viscoelasticity

In a purely elastic system, the deformation of a system only depends on the current stress applied to it. This is true for Hooke's law, which states that a linear relationship between strain and stress can be assumed. Most solids follow Hooke's law for smaller deformations, acting much like a simple spring. Materials which follow Hooke's law are called linear-elastic, or Hookean materials^[260].

Purely viscous systems behave totally different, as here the rate of the deformation depends on the force applied to it. This means that the strain at a constant stress is no longer constant, but increases linearly as the system continues to deform. The equivalent linear model for viscous systems is known as Stokes' law, which states that the velocity of a object moving in a viscous environment is proportional to the force applied to it. This model describes the behavior of ideal liquids, also known as Newtonian liquids^[260]. The behavior of viscous systems can be modeled by a dashpot, sometimes also called a Newton element, which moves at a rate proportional to the force applied to it. In reality many materials like polymers do not behave purely viscous or elastic, but their reaction to external forces combines attributes of both behaviors. When exposed to a fixed stress, their strain is time-dependent in a non-linear way. Viscoelastic models aim to describe this behavior and bridge the gap between Hooke's and Stokes' law by combining viscous and elastic properties. One way to do this, is to assume that the strain of a system can be calculated as a linear combination of multiple viscous and an elastic components. All of these linear rheological models can be visualized as a combination of springs and dashpots and vary only in the number and the arrangement of these elements, as shown in Figure 3.6. An example of such a constitutive rheological model

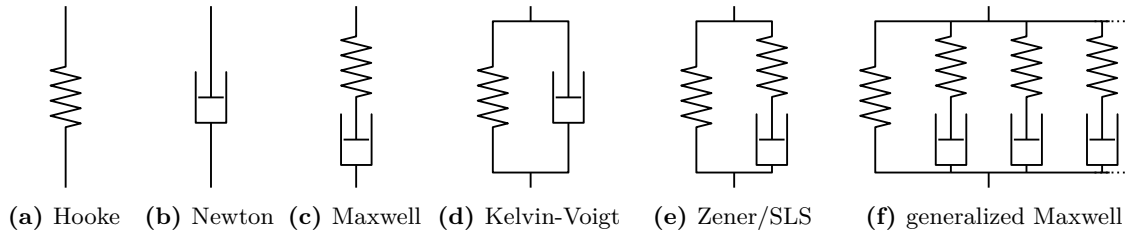


Figure 3.6: Dashpot and spring representation of commonly used linear rheological models.

is the Maxwell model, which assumes that the total strain of the system is the sum of an elastic and a viscous component (see Figure 3.6c). If a Maxwell material is suddenly deformed and then held at a constant strain, the stress in the material exponentially decreases with a specific timescale. This means that each Maxwell element has a specific relaxation time defined by the dashpot's resistance and the spring's stiffness. If we instead assume that the total stress required for a certain strain is the sum of a viscous and an elastic component, we get the Kelvin-Voigt model (see Figure 3.6d). Slightly more advanced is the standard linear solid (SLS) model, which adds a second spring (Figure 3.6e).

The Maxwell and the Kelvin-Voigt model are very simple and perform poorly when used to model the behavior of real viscoelastic materials. Meanwhile, the SLS model has been used to model the viscoelastic properties of cells^[261,262]. However, even the SLS model has its limitations and not all viscoelastic materials can be modeled. Simple models based on a linear combination of springs and dashpots like the SLS model will always be limited to describing viscoelastic behavior at specific timescales, defined by their relaxation times^[263]. For example, in a study by Li et al.^[264], the SLS model was unable to explain how intervertebral discs can resist prolonged loading but still are able to dissipate energy when subjected to low-frequency vibration. This has led to the idea of the generalized Maxwell model to find more usage^[265]. Here, the number of dashpots and springs is increased further (see Figure 3.6f) to account for the fact that the relaxation of viscoelastic materials does not occur at a single time, but at a set of times. However, since a generalized Maxwell model includes at least three springs and two dashpots, fitting the model to experimental data can become challenging. Even worse, the parameters of the individual springs and dashpots do not directly carry any physical meaning and useful physical properties have to be calculated from the fit results in a tedious process^[266]. In general, it seems that the viscoelastic spectrum of living cells lacks any distinct timescales, meaning that it cannot be modeled using a finite amount of discrete spring or dashpot elements^[263]. This means that the relaxation curve of a system subjected to a constant strain does not follow an exponential function with a specific time constant.

Because of that, any attempt to fit a multi-exponential function on the relaxation curve, as done when using a generalized Maxwell model, results in a set of parameters that strongly depend on the fitting interval and the number of exponentials used for the fit function. This way the fit results will be meaningless^[267]. Another consequence is that estimating fit parameters from the data is difficult, which makes accurate fitting challenging^[268]. To avoid all of these problems associated with rheological models composed of individual springs and dashpots, the evaluation of the blinking optical tweezer experiments in this thesis was done using power law rheology, which will be described in the next section.

3.2.4.2 The power law rheological model

Power law rheology is a simple, yet powerful model that does not rely on any linear combination of springs and dashpots. Instead, it states that the relaxation happens over a continuous range of timescales^[263]. It only features two fit parameters, which makes evaluation more straight-forward and reliable. In general, the function of a rheological model is to calculate the strain $\epsilon(t)$ of a system from the applied stress $\sigma(t)$.

As mentioned before, in viscoelastic systems the strain is not defined by the current strain alone, as the system shows hysteresis. Instead, the strain can be calculated by the following integral:

$$\epsilon(t) = \int_{-\infty}^t dt' J(t-t') \frac{d\sigma(t')}{dt'} \quad (3.7)$$

The function $J(t)$ is the tensile creep response^[269,270]. Each viscoelastic model can be described with a specific creep response function. The role of the creep response $J(t)$ is easier to understand when looking at the step response of a system described by Equation 3.7. If we assume that the strain on the system jumps from zero to the finite value σ_0 at the time $t' = 0$, the stress can be described using the Heaviside function $\theta(t)$:

$$\sigma(t') = \sigma_0 \cdot \theta(t') \quad (3.8)$$

When inserting this in the equation above, the derivative of the Heaviside function yields a delta distribution, which lets the total value of the integral come to:

$$\epsilon(t) = \begin{cases} 0 & \text{for } t \leq 0 \\ \sigma_0 \cdot J(t) & \text{for } t > 0 \end{cases} \quad (3.9)$$

In this form it is obvious that $J(t)$ describes the response to a suddenly applied constant stress. Basically, $J(t)$ is a time-dependent, inverse elastic modulus. Its value changes as a function of the time that has passed since the stress was applied. If $J(t)$ is constant, it describes a purely elastic system, and Equation 3.9 will turn into Hooke's law. For purely viscous systems, $J(t)$ is a linear function, and Equation 3.9 will represent Stoke's law.

For describing the behavior of cells, which are neither purely elastic nor purely viscous, we use a power law of the form

$$J(t) = j_0(t/\tau_0)^\beta \quad (3.10)$$

as suggested by Fabry et. al^[263,233] in 2001. τ_0 is a time normalization constant. It's value is arbitrary and was set to $\tau_0 = 1$ s to be consistent with prior research^[263]. This model has only two parameters. The first one is the tensile creep compliance j_0 , which has the unit m/N and describes how large the deformation in response to an external force will be. Secondly, the scalar exponent β can take values between 0 and 1. For $\beta = 0$, the creep compliance $J(t)$ becomes a constant and the described system becomes purely elastic. In this case, the creep compliance j_0 is the inverse elastic modulus of the system. For $\beta = 1$, the function $J(t)$ becomes a linear function and describes the creep compliance of a purely viscous system. Biological materials like cells usually exhibit values of β between zero and one.

3.2.4.3 Application to blinking optical tweezers

During the blinking experiments, the spatial light modulator (SLM) was powered off for most of the time. The force created by the optical trap is strongly dependent on the distance between the bead and the trap, as described Equation 3.6. When the SLM was off, the laser passed the sample roughly $5 - 7 \mu\text{m}$ away from the bead and the optical force on the bead is neglectable. Only during the moments in which the SLM was powered on, the laser got redirected into the proximity of the bead, creating an optical force pulling it into its focus.

Also, the force is proportional to the laser power of the trap. Since the nematic molecules cannot rotate instantly, the SLM has a finite reaction time. This means that the trap created at the bead's location does not reach its full power instantly, but with a time constant characteristic to the SLM. In the datasheet, the SLM's switching time is specified to be smaller than 16.7 ms. To verify this, a sample prepared as described in 2.2.4 was observed using the $60\times$ -objective. The microscope was focused on an empty region of the coverslip, the brightfield illumination was disabled and the infrared filter removed. This way the laser's reflection on the interface between the coverslip and the medium became visible to the camera. The IDT-Nx4-S2 highspeed camera was used to record the laser's reflection at a frame rate of 500 fps and using 4×4 binning. During the 98 seconds long acquisition, the SLM was set to a fixed hologram deflecting the laser from the origin to the position $(-4, 4)\mu\text{m}$ on the coverslip. The power of the SLM was off by default, which means that the laser mostly hit the origin. Only for brief pulses of 300 ms each, the SLM was activated. These pulses were repeated with a rate of 1.15 s^{-1} . In total, 111 pulses were recorded. To evaluate, the mean intensity in a $7 \times 7 \text{ px}^2$ (roughly $3 \times 3 \mu\text{m}^2$) region around the position $(-4, 4)\mu\text{m}$ was calculated. Each 300 ms pulse was isolated and fitted individually with the following exponential function using a least-square method:

$$I(t) = \begin{cases} I_0 + (I_1 - I_0) \cdot (1 - \exp(-(t-t_{\text{on}})/\tau_{\text{SLM,on}})) & \text{for } t \leq t_{\text{on}} \\ I_1 - (I_1 - I_0) \cdot (1 - \exp(-(t-t_{\text{off}})/\tau_{\text{SLM,off}})) & \text{for } t > t_{\text{off}} \end{cases} \quad (3.11)$$

Each of the 111 fits yielded two time constants, one for the power-on and one for the power-off switching time. In Figure 3.7A, the normalized intensities $(I(t) - I_0)/(I_1 - I_0)$ were plotted as a function of $t - t_{\text{on}}$. This creates a cluster of relaxation curves, highlighting the distribution of relaxation times. The bold, black line in the plots represents the function $I(t)$ using the median value for the switching time $\tau_{\text{SLM,on}}$ in all fits. In panel B, the same was done for the power-off switching process. The figure also includes histograms of the on and off switching times obtained by all 111 fits, shown in panels C and D. As seen in the figure, the exponential functions describe the changing laser power well. Only directly around the moment in which the SLM is switched on or off, the experimental data deviates from the exponential function, showing a more gradual change in laser power. Overall, the median switching time for the power-on events was 10.7 ms, with 68% of the data lying in the confidence interval (10.7 ± 1.0) ms. For the power-off events, the switching time was shorter, at only (9.0 ± 0.4) ms. The switching time for on and off events differs by a small, but significant amount. To simplify further evaluation, a value of $\tau_{\text{SLM}} = 10.0$ ms was used for both the power-on and power-off events in all following calculations. The switching time of the SLM was already measured by K. Berghoff. The plot in Figure 5.11 of his PhD thesis^[130] shows a switching time of (13.2 ± 1.9) ms for the deflected beam and (16.4 ± 2.1) ms for the beam hitting the origin. However, it remains unclear whether this times were measured

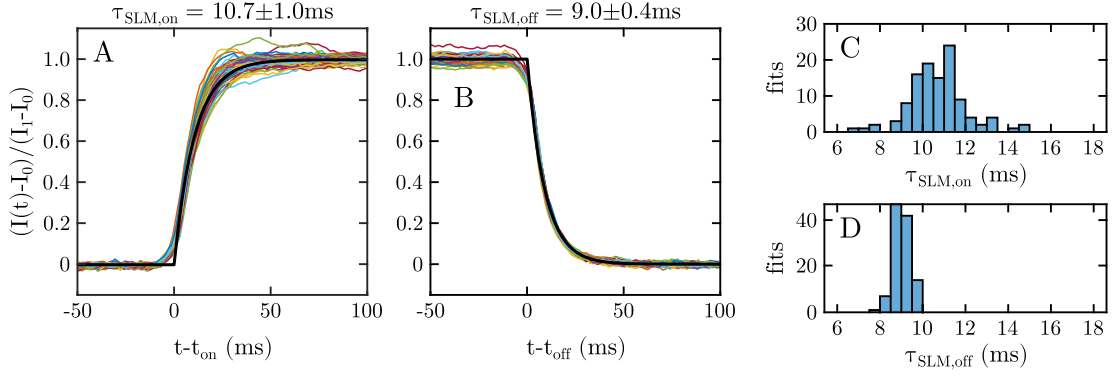


Figure 3.7: In panel A, the normalized intensity of the laser reflection during 111 power-on phases of the SLM is plotted. The bolt black line represents the function $I(t)$ (Equation 3.11) inserting the median time constant $\tau_{\text{SLM,on}}$ of 111 individual fits. In panel B, the same was done for the power-off phase of the SLM. On the right, panels C and D show the distributions of the relaxation times. Using those distributions, the confidence intervals of the switching time can be estimated.

when the SLM was switched on, off, or both. Berghoff states that both values match the manufacture’s claim of $\tau \leq 16.7$ ms and continues to use this value. However, since the particle is trapped in the deflected beam, only the smaller value of (13.2 ± 1.9) ms is relevant. While this still is longer than the value measured in this thesis, the difference is less significant. The remaining disparity is likely caused by differences in the trap geometry used or in the software used to drive the SLM. It is possible that K. Berghoff did not cycle the power to the SLM, but instead applied an empty hologram to disable the SLM. It is not known if this affected the switching time.

In our experiments, we switched the laser on for a duration of $T_{\text{on}} = 600$ ms with a laser power of 300 mW or for only $T_{\text{on}} = 300$ ms at 500 mW in later experiments. The total optical force acting on the bead during such an event can be calculated as the product of the optical trap force F_{OT} as defined by Equation 3.6 and the relative laser power applied.

$$F_{\text{HOT}} = F_{\text{OT}}(\rho(t)) \cdot \begin{cases} 0 & \text{for } t < T_{\text{on}} \\ 1 - e^{-(t-T_{\text{on}})/\tau_{\text{SLM}}} & \text{for } T_{\text{on}} \leq t < T_{\text{off}} \\ e^{-(t-T_{\text{off}})/\tau_{\text{SLM}}} & \text{for } T_{\text{off}} \leq t \end{cases} \quad (3.12)$$

The total force on the system is the sum of this optical force and the force which is applied to the bead by the cell itself. To obtain a stress, the total force has to be divided by the contact area A :

$$\sigma(t') = \frac{F_{\text{HOT}}(t') + F_{\text{Cell}}(t')}{A} \quad (3.13)$$

The contact area A is the area of the deformed material to which the force is applied. In reality, the amount of stretching created inside the cell when moving the bead is not homogeneous. Because of this, the contact area A in Equation 3.13 has to be seen as an effective contact area. In this case, it has been shown that the contact area increases after an opsonized bead touches a macrophage and then reaches a constant value after only two

minutes^[218]. By inserting the total force into Equation 3.7, we get:

$$\epsilon(t) = \int_{-\infty}^t dt' j_0 \frac{(t-t')^\beta}{\tau_0^\beta} \frac{d}{dt'} \left(\frac{F_{\text{HOT}}(t') + F_{\text{Cell}}(t')}{A(t')} \right) \quad (3.14)$$

In our experiments, we tracked the two-dimensional movement of the particle. It is easy to enhance the model to two dimensions by replacing the strain by a strain vector and using vectorial forces:

$$\vec{\epsilon}(t) = \int_{-\infty}^t dt' j_0 \frac{(t-t')^\beta}{\tau_0^\beta} \frac{d}{dt'} \left(\frac{\vec{F}_{\text{HOT}}(t') + \vec{F}_{\text{Cell}}(t')}{A(t')} \right) \quad (3.15)$$

To simplify this, we assume that the contact area and the cellular viscoelastic properties only change in a negligible manner during one blinking event. In this case, j_0 , A and β can be treated as constants:

$$\frac{dj_0}{dt'} = 0 \quad \frac{dA}{dt'} = 0 \quad \frac{d\beta}{dt'} = 0 \quad (3.16)$$

In reality, we cannot integrate starting from infinite negative time as this would require detailed knowledge about the history of the cell's force. At the moment the laser is switched on, the optical force has been zero and thus constant for 1.0 – 1.7 s. The viscoelastic response modeled by power law rheology does not feature a distinct relaxation time^[263], meaning that bead might still move slowly in response to previous laser pulses. Still, the viscoelastic relaxation speed in response to previous laser pulses will already have slowed down to a point where it is almost imperceptible during the brief acquisition window. This means that we can neglect the influence of the changing optical force from previous blinking events on the current strain. This leaves us with:

$$\vec{\epsilon}(t) = \frac{j_0}{A} \cdot \int_0^t dt' \frac{(t-t')^\beta}{\tau_0^\beta} \frac{d}{dt'} \vec{F}_{\text{HOT}}(t') + \frac{j_0}{A} \cdot \int_{-\infty}^t dt' \frac{(t-t')^\beta}{\tau_0^\beta} \frac{d}{dt'} \vec{F}_{\text{Cell}}(t') \quad (3.17)$$

In this equation, the first integral describes the direct reaction to the applied optical force, while the second integral contains the movement caused by the cell's force. Note that the first integral now starts at $t' = 0$. This means that when $\vec{F}_{\text{HOT}}(t')$ is known for $t' \geq 0$, the value of the integral can be calculated directly.

To address the second integral, we can assume that the cell's force only changes slowly. Specifically, we assume that the force of the cell is constant during the blinking event and has had this constant value for a time much longer than a single blinking event before. In this case the value of $(t-t')$ in the second integral is large for all values of t' at which the derivative $\frac{d}{dt'} F_{\text{Cell}}(t')$ is non-zero, as changes in the cell's force only happened a long time ago for $t' \ll 0$. This causes the second integral to change only slowly in time. In other words, since the cell's constant force has been applied for a long time, it causes a steady creep with a velocity that changes only very gradually. The creep velocity is not constant because the power law model lacks any distinct timescales, but the creep velocity will not change much during the short duration of the blinking event, as long as this duration is much smaller than the time since the last change in the cell's force. If the creep velocity caused by the cell is assumed to be constant during a single blinking event, the second integral can be approximated as a simple function linear in time. In conclusion, the constant force from the

cell causes the bead to drift with a velocity which does not change much over one blinking event. If we use this knowledge in our equation, we get:

$$\vec{\epsilon}(t) = \begin{pmatrix} m_x \\ m_y \end{pmatrix} \cdot t + \frac{j_0}{A} \int_0^t dt' \frac{(t-t')^\beta}{\tau_0^\beta} \frac{d\vec{F}_{\text{HOT}}(t')}{dt'} \quad (3.18)$$

Up to now, we only calculated the dimensionless strain value. The values m_x and m_y are the slopes of the drift created by the cell force. To obtain the distance the bead moves, we have to multiply the strain with a reference length, which is set to be the contact radius r . The trajectory of the bead can be calculated as follows:

$$\begin{pmatrix} x(t) \\ y(t) \end{pmatrix} = \begin{pmatrix} x_0 \\ y_0 \end{pmatrix} + r \cdot \vec{\epsilon}(t) \quad (3.19)$$

With this knowledge, we can finally write down the equation describing the 2D bead movement occurring in the time around the laser pulse:

$$\vec{\epsilon}(t) \cdot r = \begin{pmatrix} x(t) - x_0 \\ y(t) - y_0 \end{pmatrix} = \begin{pmatrix} v_{x,\text{Drift}} \\ v_{y,\text{Drift}} \end{pmatrix} \cdot t + \underbrace{\frac{r \cdot j_0}{A}}_{\alpha} \cdot \int_0^t dt' \frac{(t-t')^\beta}{\tau_0^\beta} \frac{d}{dt'} \vec{F}_{\text{HOT}}(x(t), y(t)) \quad (3.20)$$

In this equation, $\alpha = r \cdot j_0/A$ represents the amplitude of the response, combining the geometrical factor of the contact area and the elastic property of the creep compliance into one constant which is experimentally accessible. The origin of the coordinate system was chosen at the position of the optical trap. The values of x_0 and y_0 specify the position of the bead relative to the trap in the moment the laser is switched on. The constant drift velocity created by the cell force is now represented by the two components $v_{x,\text{Drift}} = r \cdot m_x$ and $v_{y,\text{Drift}} = r \cdot m_y$. Since the cell force is not necessarily parallel to the optical force, the drift velocity might have a different direction than the optical force on the bead. Equation 3.20 will later be used to create the fits to the experimental data. This way, the values of α and β can be extracted from experimental data.

3.2.4.4 Simulated blinking events

Before dealing with experimental data, Equation 3.20 was used to model the bead's expected movement during a blinking event, as seen in Figure 3.8. In the figure, a blinking event with a laser power of 500 mW for a duration 300 ms was simulated for different combinations of α and β . While Figure 3.8a shows the relative particle trajectory for a constant $\beta = 0.3$ and different values of α , Figure 3.8b shows the same trajectories for a constant $\alpha = 10 \text{ nm/pN}$ and changing values of β . In all cases, it was assumed that the bead starts $1 \mu\text{m}$ out of the trap's center and that the SLM is switched on at $t = 0.1 \text{ s}$. In the simulation, \vec{v}_{Drift} was set to zero. Furthermore, we choose $x_0 = 1 \mu\text{m}$ and $y_0 = 0$. Since the bead starts on the x -axis, the optical force will also be parallel to the x -axis. Because of that, the bead will only move on the x -axis, meaning $y(t) = 0$.

To determine the bead position, $x(t)$ was repeatedly calculated $100 \mu\text{s}$ after the last known position until the whole trajectory was found. This was done numerically by using Equation 3.20. The necessary values for the optical forces were calculated using Equations 3.6 and 3.12, and the bead's previous positions. These calculations also considered the finite switching

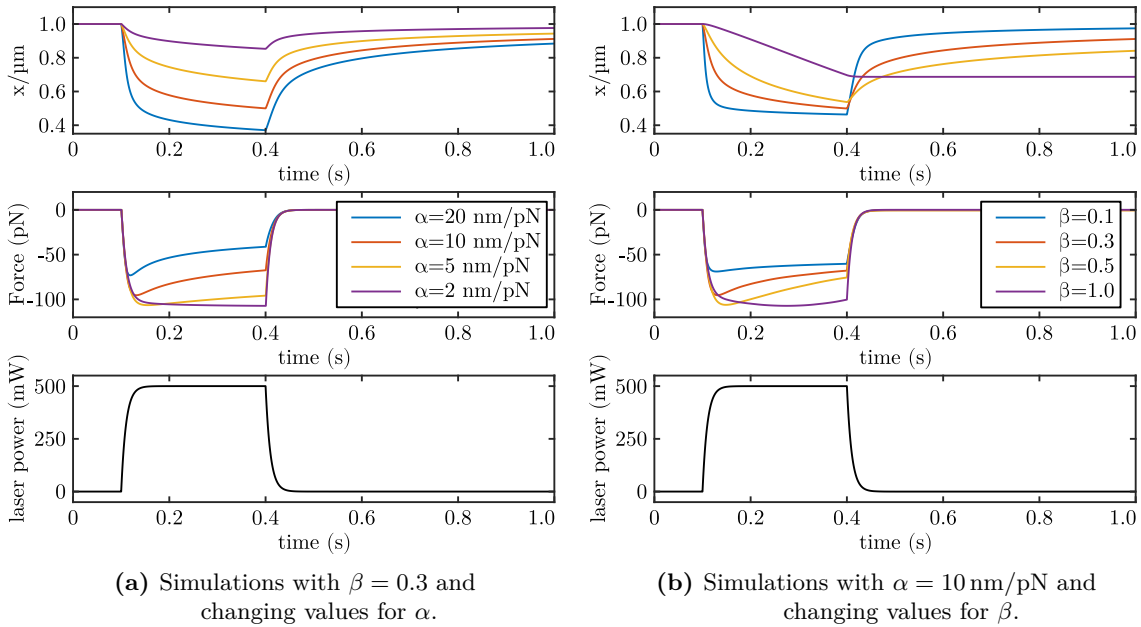


Figure 3.8: Simulation of the bead movement caused by blinking optical traps. By calculating the force acting on the particle using Equation 3.6 and utilizing the viscoelastic model, the bead's movement during a blinking event was modeled. Here, we simulated the movement of a bead attached to a cell reacting to an optical trap which was switched on for 300 ms using a laser power of 500 mW. At $t = 0$, a bead rested at the distance of $\rho = 1 \mu\text{m}$ from the trap's center. At $t = 0.1 \text{ s}$, the SLM was switched from its resting state to the hologram creating the trap, which led to the laser intensity of the trap to build up with a time constant of $\tau = 10 \text{ ms}$. Simultaneously, the force acting on the bead increased and the particle started to move towards the trap with a velocity depending on the viscoelastic parameters. Because the optical force is weaker at the trap's center, the force on the bead slightly decreased at that point. At $t = 0.4 \text{ s}$, the trap was switched off using the SLM which leads to a sudden decrease in the laser intensity and thus the force acting on the bead. Because part of the movement was elastic, the bead moved back towards its original position at $\rho = 1 \mu\text{m}$, however, for $\beta > 0$ it never fully returned, as there was a viscous contribution to the movement.

time $\tau_{\text{SLM}} = 10$ ms of the SLM. The result of this simulation for different values of α and β is shown in Figure 3.8.

As shown in the figure, as soon as the SLM was powered on, the laser power rose and the bead got pulled towards the trap, lowering the x -coordinate. While it was pulled towards the trap, the force on the particle decreased again. As soon as the SLM was switched off again, the particle relaxed. For small values of β , the particle behaved elastic and almost returns to its original position. Also, the shape of the relaxation curves when switching the laser on and off was very similar, as most of the deformation is elastic. If β was high, the particle behaved more viscous. For $\beta = 1$, the particle moved purely viscously, which meant that the particle did experience no spring-back at all after switching off the SLM. In other words, for higher values of β the differences in the shape of the relaxation curves between the on- and off-events increased. If the laser power could be switched on and off instantly, the initial velocity of the bead would be infinite, as in Equation 3.7, the term $d\sigma/dt$ would get infinity large. In the simulation, the maximum slope after switching on the SLM was limited by the SLM's reaction time of $\tau = 10$ ms.

To better understand the predictions of the model, this simulation was also used to find the maximum displacement reached when starting with a the bead at $x = 1 \mu\text{m}$ for different combinations of α and β . This was done for both the shorter (300 ms at 500 mW) and the longer (600 ms at 300 mW) laser pulses. This maximum displacement Δx is defined as the distance the bead travels from the moment the SLM is switched on to the moment right before the SLM is powered off again and the bead begins to move back. The value of Δx is easy to measure experimentally and still contains much information about the viscoelastic parameters. In our simulations, it was calculated by subtracting the minimal value of $x(t)$ which occurred during the simulation from the maximum value of $x(t)$, which in all cases was $x_0 = 1 \mu\text{m}$.

In Figure 3.9a and Figure 3.9b, the maximum bead displacement Δx is plotted as a function of α for different values of β . This is done for the shorter, powerful laser pulses as well as the longer, less powerful laser pulses. As expected, the maximum bead displacement always increased with larger amplitudes α . The effect of the exponent β on the maximum bead displacement is ambiguous: For the shorter pulses, smaller values of β lead to bigger maximum displacements, as the elastic component of the deformation is larger than the viscous contribution. For the longer, weak pulses, viscous effects contributed more to the total displacement and the influence of β on the maximum displacement is much smaller. Here, depending on the value of α , the maximum displacement can increase or decrease when altering the value of β . In Figure 3.9c, an illustration on how the maximum displacement Δx can be measured in experimental data is shown. This will be relevant later to estimate the parameter α from experimental data to prepare for fitting.

3.2.5 Rheological evaluation of experimental data

3.2.5.1 Radial tracking and calculation of the optical force

For the rheological evaluation, the image data recorded by the IDT-NX4 camera was used. A typical recording consisted of 689299 frames, which was the maximum number of frames the camera memory could hold. This recording was saved as an uncompressed, 8-bit *.avi file, which was fed into the portable radial tracking software described in chapter 2.2.9. The active radius was set to 4 px, corresponding to $1.7 \mu\text{m}$, since the camera used 4×4 binning

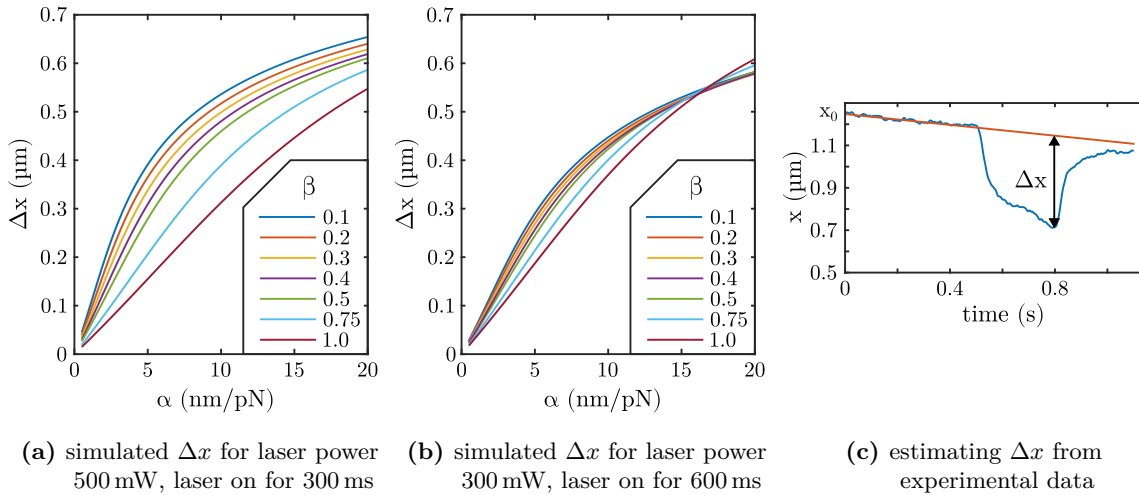


Figure 3.9: Dependence of $\Delta\rho$ on the viscoelastic parameters α and β . Multiple simulations of blinking events, similar to Figure 3.8, were done and the maximum displacement $\Delta\rho$ from the starting position $\rho = 1\ \mu\text{m}$ was determined. The blinking events all considered a switching time of $\tau = 10\ \text{ms}$ which is caused by the SLM. The simulations were done using two different sets of parameters. In panel (a), the laser was on for 300 ms with a power of 500 mW. In panel (b), the laser pulse took 600 ms at a power of only 300 mW. In both cases, the traveled distance $\Delta\rho$ depended on the viscoelastic parameters α and β . It monotonically increased with larger α , and usually decreased with higher exponents β , as the movement is dominated by the elastic component for short laser pulses. For very large α and longer laser pulses, the traveled distance was larger for more viscous environments, as seen in the right plot. The higher the exponent β , the stronger the impact of the pulse duration was, because of the higher viscous component. Panel (c) shows how Δx can be estimated from experimental data.

when recording. This was the same absolute value for the active radius as used when tracking the $2\ \mu\text{m}$ diameter beads in chapter 2. To prevent any spectral leakage caused by the hard selection the pixels used to calculate the bead's position, the internal scaling factor of the portable radial tracker was set to 10. This means that each frame was scaled up 10-fold by linear interpolation before being processed. This upscaling would not have been necessary if the active area tapering suggested in chapter 2.2.9, which continuously fades out the influence of pixels at the edge of the active area, would have been available at the time of evaluation.

The tracker was then started and determined the bead position from the individual frames by finding the local center of radial symmetry. Because of the upscaling, the computation time increased and depending on the hardware it took around 3 – 6 hours to track the image stack of a single blinking experiment, depending on the hardware. Combining all 93 experiments, $6.1 \cdot 10^7$ frames had to be tracked.

3.2.5.2 Camera synchronization

The trajectory of a each blinking experiment was loaded individually into a custom evaluation software. Upon loading, the distances in the saved trajectories were converted to micrometers using the pixel pitches listed in Table 2.2. The script also accessed the bead's trajectory in the image of the pco pixelfly recorded by the live-tracking as well as any metadata saved by the acquisition software. This included the time at which the blinking was activated

as well the movement of the piezo stage throughout the experiment. Since three cameras were used, it was necessary to determine when each frame has been acquired in a common time reference frame. Both the iXon Ultra camera used for the fluorescence images and the pixelfly camera used for the live tracking recorded with a variable frame rate, saving timestamps for each frame relative to the moment in which the corresponding camera was started. However, the highspeed camera used a constant frame rate of 500 fps. Therefore, the highspeed recording was used as a temporal reference and the beginning of the highspeed acquisition was defined as $t = 0$ during evaluation. The time each frame was taken by the IDT camera can be calculated by multiplying its frame number with 2 ms.

For the pixelfly camera, a timestamp was saved for each image, relative to the start of the pixelfly acquisition. Since the switching of the SLM happened a fixed time before the pixelfly image was recorded, these timestamps could be used to determine the fitting intervals. Unfortunately, over longer periods, the intervals between the image acquisition timestamps saved with the pixelfly acquisition did not match the observed time intervals between the blinking events in the highspeed trajectory exactly. Either the highspeed camera recorded slightly too slow, or the pixelfly camera slightly too fast. To handle this issue, the timestamps of the pixelfly camera were multiplied with a correction factor slightly above one. This correction factor was set individually for each experiment. Over all experiments, the median of the used time correction factors was 1.000016. While this is very close to one, the timestamp would be off by 16 ms after 1000 s of acquisition without it. This is significant when compared to the duration of a laser pulse, which in most experiments was only 300 ms long. Figure 3.10 shows how the alignment of the laser on and off events shifts during the experiment if the correction is not applied and how it is fixed using the correction factor. After applying the correction factor, the timestamps of the pixelfly acquisition were shifted back by a fixed amount to account for the fact that the pixelfly camera was started prior to the highspeed camera. This time shift was set manually for each experiment and had a median value of 10.6 s, but varied between experiments, since the acquisition of all cameras was triggered manually. In 89% of the experiments, the time offset was smaller than 20 s. The temporal offset between the fluorescence channel and the pixelfly channel was already determined during the evaluation of the LifeAct channel. With it, the timestamps recorded along the fluorescence images were converted to the same reference system relative to the start of the highspeed camera. Here, no correction factor was applied, as millisecond accuracy is not needed.

3.2.5.3 Calculation of the bead's position relative to the trap

To calculate the optical force acting on the bead, the exact x and y position of the bead had to be known relative to the equilibrium position. Since prior to attaching the bead to the cell it only moved in the optical trap driven by thermal fluctuations, the median bead position in this period could be used to calculate the position of the trap. To automatically determine the moment at which the bead came in contact to the cell, a first estimate for the trap's x -position was made by calculating the median bead position in the first 10 s of the highspeed trajectory. This process is illustrated in Figure 3.11, where the median is represented by a red line. Then, as shown in the figure, the first frame in which the bead was more than 400 nm away from this estimated trap x -position was searched. This frame marks the moment in which the bead was pushed out of the trap, which happened either because the cell pushed the bead out of the trap or, more likely, because the activation of the feedback loop which moved the bead 1 μm away from the trap to prepare for the first

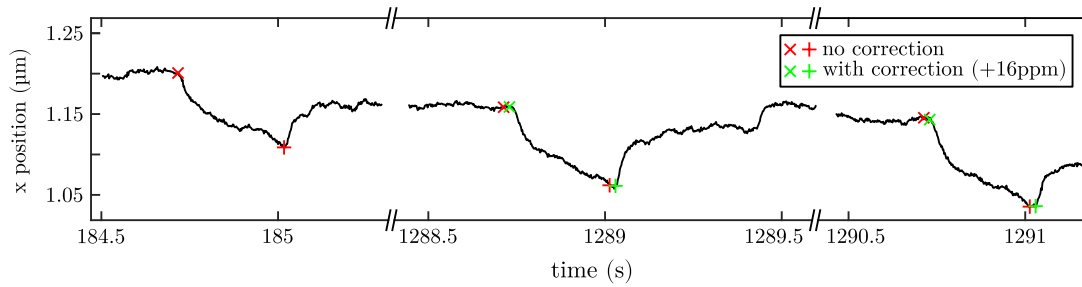


Figure 3.10: Misalignment of blinking events when not correcting for the different clock speeds of both cameras. In the figure, the x-trajectory of the bead as calculated from the highspeed image sequence is shown. The red \times -shaped markers indicate the moments in which the SLM has been switched on and were calculated by shifting the timestamps of the pixelfly images by a fixed offset. The green \times -shaped are calculated the same way, but the timestamps of the pixelfly camera were multiplied by the correction factor of 1.000016. While at $t = 185$ s, both markers align perfectly (only red markers shown), towards the end of the experiment at $t = 1290$ s, there is a significant offset. The $+$ -shaped markers highlight the moment the SLM was switched of and are set exactly 300 ms after the \times -shaped markers.

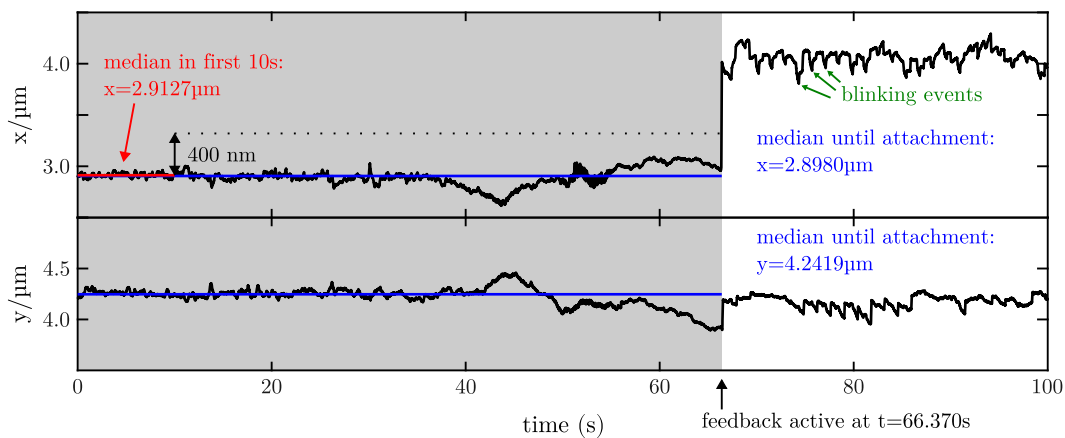


Figure 3.11: Determination of the trap position in the highspeed bead trajectory. As a first estimate, the median x position of the bead in the first 10 s of the experiment is calculated. In the example, this is $x = 2.9127 \mu\text{m}$, relative to the edge of the cameras field of view. After that, the moment in which the feedback was activated was found by searching for the moment at which the bead's x coordinate moves further than 400 nm away from this initial, coarse trap position. The final x and y coordinates of the trap's positions are calculated as the median bead position from the start of the experiment until the feedback loop is activated.

blinking experiments. The feedback loop was activated manually only a few seconds after the bead touched the cell, so the moments of attachment and start of the feedback were very close to each other and a distinction between those two events is not necessary. The blinking was activated manually after the activation of the feedback system, which means that the laser only started blinking a few seconds after the start of the feedback, when the piezo stage might already have moved one or two times.

The trap position in the image is calculated as the median bead position in all frames from the beginning to one frame prior to the activation of the feedback loop. These frames are highlighted by a gray background in the Figure 3.11, the median bead position in this period is shown as blue lines, both for the x and y position. Finally, these positions are subtracted from the bead's trajectory in the image to obtain the x and y coordinates of the bead relative to the trap. These relative coordinates will later be used to calculate the optical force acting on the bead during the phases in which the laser is active using Equation 3.6.

3.2.5.4 Example blinking measurement

In Figure 3.12, a short section of a blinking measurement is shown to visualize the evaluation process. The position of the bead relative to the trap is plotted in x - and y -direction in panels A and B. The sections in which the power to the SLM was active are highlighted with a gray background. In panel A, the x -position of the bead begins with a slow increase. As the laser was off during this moment, this drift was caused by the cell's force. Then, a sudden change in the x -position happened in the moment the SLM is powered on. The y -position as seen in panel B was always very close to zero and was almost not affected by the optical force. After the SLM was turned off again, the bead sprang back to a larger x -position. Soon after that, a sudden change in the x - and y -position could be observed. This change was caused by the movement of the piezo stage. After that, a pause phase happened which then was followed by the next blinking event, repeating the cycle. Shown in red, the figure also contains fits to the individual blinking events along with the fit parameters extracted from these fits. The process of fitting the individual blinking events will be discussed in chapter 3.2.5.6. In panels C and D, the optical force applied to the bead in x -, respectively y - direction is plotted. The absolute values of this forces were calculated from the bead position using Equation 3.12 and a laser power of $P_{\text{Laser}} = 500 \text{ mW}$, its direction is assumed to point straight to the trap in the origin. In the moments the laser was active, the a optical force pulled the bead in the $-x$ -direction. Since the bead is very close to the x -axis in this configuration, the forces in y -direction are negligible.

One thing that catches the eye is that the bead's x -position between blinking events stayed around $1.2 - 1.4 \mu\text{m}$, even though the feedback loop was set to move the bead back to $x = 1.0 \mu\text{m}$ after each blinking event. To illustrate the cause of this behavior, the bead positions obtained from the live-tracking of the pixelfly images were also included into the figure. Analog to chapter 3.2.5.3, the median bead position in the pixelfly images up to the last frame before the feedback was activated was calculated, corresponding to the location towards which the feedback loop steered the bead during acquisition. This position was than subtracted from the trajectory to obtain the bead's position relative to the trap in the pixelfly images. These positions are shown as cyan crosses in the figure, and lie much closer to $1 \mu\text{m}$. The reason for this mismatch was found in a timing error. It was intended that the pixelfly images should be captured after the laser was already switched off for at least $300 - 600 \text{ ms}$, the same amount of time as it was switched on. An error in the implementation caused the

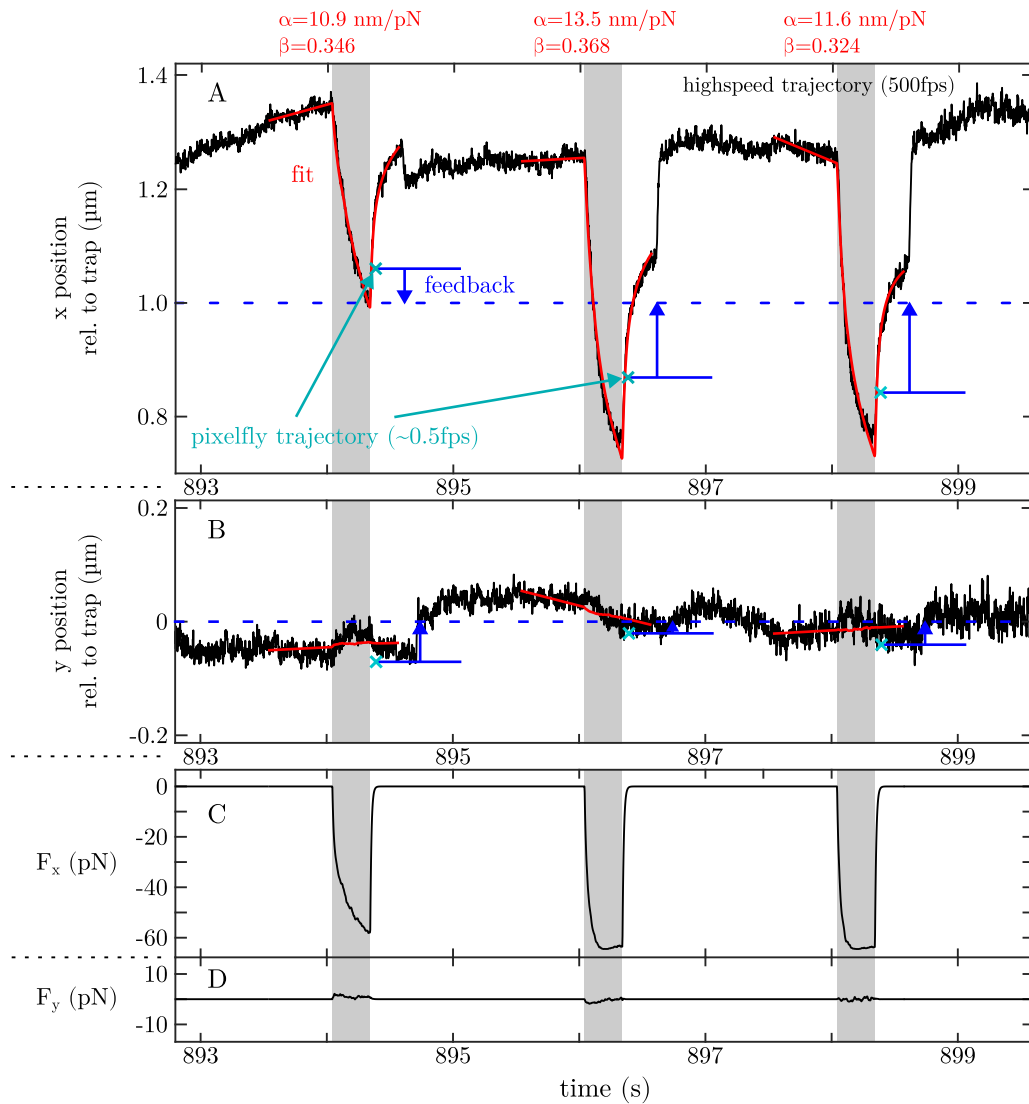


Figure 3.12: Adaptation of the fits to the experimental blinking trajectory. Panels A and B show the highspeed trajectory (black line) as well as the trajectory from the pco pixelfly (cyan crosses), both in the coordinate system relative to the trap position. Panels C and D show the optical force calculated from the bead's position. Because the bead is kept at the same y -position as the trap, the force F_y in this direction is almost zero. The red lines are fits by the viscoelastic model as described by Equation 3.20. The periods in which the SLM is powered on are highlighted by a gray background.

pixelfly images to be taken too soon. In the case of 300 ms laser pulses, the images were captured only around 60 ms after the laser was turned off. At this time, the bead has not had enough time to fully relax from the deformation created by the optical force. After the image is taken, the 3D tracking software takes 200 – 300 ms until the bead’s position is determined and the movement commands are sent to the piezo stage. During this time, the cell can fully relax, which means the full relaxation curve could still be observed by the highspeed camera. However, any relaxation that happens after the pixelfly image is recorded were not considered when calculating the necessary movement to bring the bead to its default position at $x = 1.0 \mu\text{m}$. This is why the bead ends up at x coordinates 200 – 400 nm larger than intended. In the figure, the way the applied feedback movements are calculated and applied is illustrated in blue.

3.2.5.5 Blinking event breakdown

Each blinking event can be broken down into multiple specific events during acquisition or evaluation. The sequence of operations during acquisition has already been illustrated in Figure 3.5. During evaluation, the first important time point marked the beginning of the fit interval. At this moment, the SLM had not been activated yet and there was no optical force on the bead. However, this time period before switching on the SLM was included in the fit interval because it was important for estimating the constant drift velocity caused by the cell’s force on the bead. The duration of this period was 500 ms or 600 ms, depending whether short or long laser pulses were used. In Figure 3.12, panel A and B, this is visible as the beginning of the red fit line. The second important time point is the moment in which the SLM was actually switched on. At this moment, the optical force started to rise as fast as the reaction time of the SLM allowed it. As the force on the bead increased quickly, and because the elastic component of the cellular response can adjust to changes in stress instantaneously, the bead moved towards the origin with an initial speed only limited by the switching time of the SLM. After that, the optical force changed less quickly, the bead’s speed reduced, and viscous effects gained a stronger impact on the bead’s movement. The optical force depended on the bead’s location and changed within a single blinking experiment. Because the bead’s displacement only changed a few hundred nanometers, the changes in the optical force were not huge, but they still needed to be considered. For example, because the first blinking event in Figure 3.12A started at higher displacement at $x > 1.3 \mu\text{m}$, the force on the bead was initially lower than in the following events where the bead was closer to the trap in the moment the SLM was powered on. According to Equation 3.12, the trap reaches its maximum force for $x = 0.83 \mu\text{m}$. Around this position, the influence of the bead position on the optical force is reduced, which is desirable. This effect can be seen for the second and third blinking event in Figure 3.12C: Because the bead was close to $x = 0.83 \mu\text{m}$, the force F_x was rather constant during the phase the SLM was powered on, even though the bead was still moving in the x -direction. After 300 ms or 600 ms, depending on the settings, the SLM was powered off again, marking the third time point. This led to a sudden drop in the optical force, which caused the bead to spring back to higher x coordinates.

Finally, the fourth time point marked the end of the fit interval. This time point was intended to be 300 ms after the SLM was shut off for the shorter laser pulses and 600 ms for the longer laser pulses. Initially, the pco pixelfly image should be recorded at this moment. Because of the error in the implementation as mentioned before, the pco pixelfly camera took the image about 240 ms too early and the software already started with the 3D tracking.

This by itself is no problem, as the recording of the image did not interfere with the bead's relaxation. However, as soon as the tracking was done, the software's feedback mechanism engaged the piezo stage to reposition the bead, much sooner than intended. Luckily, the first movement of the piezo stage usually happened slightly after the end of the fit interval. Unfortunately, the exact duration of the tracking process can vary, and this was not always the case. For some experiments, the fit interval had to be shortened slightly to exclude the feedback movement from the fit interval, especially when using 600 ms laser pulses. Here, most fits were done with the fit interval ending 575 ms after the SLM was shut off, shortening the intended off-period's duration by 25 ms. This ensured that no movement of the piezo stage happened during the fit interval.

Finally, the last events were the piezo stage's movements. The stage moved sequentially, first in the x -direction and about 110 ms later in the y -direction. After that, the movement of the piezo stage in z -direction happened, which brings the bead back into focus. This movement is not visible in Figure 3.12, as the highspeed trajectory was only tracked in two dimensions. It was followed by a pause phase used to space the blinking events equally, after which the next blinking event started and the cycle repeated.

3.2.5.6 Blinking event fitting

To obtain information on the mechanical properties of the cell, a function based on Equation 3.20 was fitted to the highspeed trajectory recorded during an specific fit interval. This interval started slightly before the SLM was activated and ended after the cell had some time to relax, just before the piezo stage moved. The optical force acting during this period was calculated based on the bead's position relative to the trap, taking into account the finite switching time of the SLM using Equation 3.12. The used fitting function has a high count of parameters. Most obvious are the amplitude α and the exponent β from the viscoelastic model. Furthermore, the linear drift function adds a total of four parameters: The drifting velocities $v_{x\text{Drift},x}$ and $v_{x\text{Drift},y}$ as well as the starting points x_0 and y_0 . Additionally, there is the temporal parameter T_{on} . In Equation 3.20, the time $t = 0$ marks the moment in which the fit is started. In Equation 3.12, there are the two values T_{on} and T_{off} which mark the moments in the fitting interval in which the SLM was switched on respectively off.

Because T_{on} was slightly inconsistent between blinking events, it was included into the fit. The way the fit interval was chosen, T_{on} was usually close to 500 ms or 600 ms, depending on whether 300 ms or 600 ms laser pulses were used. The initial value of T_{on} was estimated from the timestamps recorded during acquisition and should already be accurate within a few milliseconds. To allow the fit to account for small alignment errors, it was constrained to an interval 100 ms around the estimated value. The final value of T_{on} obtained by the fit does not contain information on the rheological properties of the cell. Unlike T_{on} , the value of T_{off} was not treated as a fit parameter. Instead, it was determined by adding 300 ms or 600 ms to T_{on} , depending on the duration of the laser pulse.

All in all this means that the fit had a total of seven different parameters. Luckily, the parameters x_0 and $v_{\text{Drift},x}$ only affect the x -dimension of the strain, while y_0 and $v_{\text{Drift},y}$ only affect the y -dimension. This means that they could be optimized independently. Additionally, the four parameters of the drift velocity and the starting point (x_0 , y_0 , $v_{\text{Drift},x}$ and $v_{\text{Drift},y}$) only affect the the fit function in a linear fashion. This makes it easier for any optimization algorithm to find the global minimum, as many entries of the Jacobian matrix will be zero or constant. In our case, the optimal parameters were found using least-square optimization,

which was done using the Levenberg–Marquardt algorithm implemented in MATLAB’s `nlinfit` function^[271]. Finally, the fit parameters were estimated from the dataset very easily to give the fit a starting point which is already close to optimal. This was done in the following way: As a first step, a linear fit was done to the x - and y -coordinates in the first 450 ms of the fitting interval. The slope of these fits gave a good estimate of the drift velocities ($v_{\text{Drift},x}$, $v_{\text{Drift},y}$) and the starting point (x_0 , y_0) was given by the starting points of the fits. For the x -coordinate, this is illustrated in Figure 3.9c.

Also, the two non-linear parameters α and β had to be estimated to give the fit a good starting point. For the exponent β , the constant initial value 0.3 was used for all fits, as we expected values of β in the range of 0.20 – 0.35^[218]. To get a good estimate for α , the maximum displacement Δx had to be measured first. For that, the already estimated parameters x_0 and $v_{\text{Drift},x}$ were used to calculate the linear drift function, which then was subtracted from the trajectory. Then, the 2%- and the 98%-quantile of the displacement after subtracting the linear drift were calculated. The difference Δx or Δy of those two quantiles shows the maximum deformation measured during the experiment. This process is illustrated in Figure 3.9c. This was also done for the y -dimension to obtain the displacement Δy , which was not strictly necessary as most of the time the value of Δy is very small, and Δy could simply have been assumed to be zero. However, implementing the fitting process in two dimensions allows more experimental flexibility for future experiments. These values were then used to estimate the value of α . A good estimator for α is the function $\alpha_{\text{estimate}} = \sqrt{\Delta x^2 + \Delta y^2} \cdot 0.03 \text{ pN}^{-1}$, which was used to provide a starting point for the fit. This function roughly approximates the nonlinear relationship between α and Δx plotted in Figure 3.9 as a single linear function, negating the influence of different values for β .

With these start parameters, the fit converged well to the measurement data using a least-square approach provided by MATLAB’s internal fitting toolbox. In Figure 3.12, the fit results are shown as the red lines, which fit the measured data well. The two dimensions were fitted simultaneously using Equation 3.20. Blinking events in which the fit did not match the measured trajectory well were excluded in the evaluation. This was quantified by calculating the coefficient of determination R^2 for each fit. Firstly, the sum of the squared differences between the measured data and the fit was calculated and divided by the number of datapoints, obtaining the mean squared residuum. This value was then divided by the variance of the experimental data. This yielded a value between 0 and 1 which finally was subtracted from one to get the final value for R^2 . All fits with a $R^2 < 0.85$ were excluded from the evaluation. This approach is commonly referred to as reduced chi-squared statistics, sometimes also simply as goodness of fit^[272].

3.3 Results

3.3.1 Overview of the performed experiments

In total, 93 experiments using blinking optical tweezers were performed, out of which 34 were performed by Johanna Lix or Wolfgang Groß. I reevaluated those 34 experiments and performed and evaluated additional 59 experiments.

Out of the 93 experiments, the data of 10 experiments had to be discarded. In four of those experiments, the reason to discard the data were methodical errors during acquisition, which were not recognized as such at the day of recording. For example, in one case the bead was not attached to the cell, but to the coverslip, where it stayed for almost the entire experiment. In another case, the blinking was never activated and the SLM stayed off during the whole acquisition. In two cases, the bead left the field of view of the highspeed camera, which indicates a failure in the feedback loop. Out of the remaining six discarded experiments, two were disturbed by external influences, specifically a second bead interfering with the measurement and debris falling on the observed cell, respectively. The final four experiments were discarded because the cell strongly contracted and clear signals of apoptosis were visible.

In all other 83 cases, a full evaluation was possible. This includes the stiffness data acquired by the blinking optical tweezers as well as the data on the actin dynamics during the experiments as captured by the Andor iXon camera during the experiment. In one of these 83 experiments, the laser pulse duration was wrongly set to 2s instead of 300 ms. This led to a significantly lower frame rate and a higher deflection of the beads position by the laser pulse. As evaluation was still possible when adapting the fit intervals, the experiment was kept in the dataset. In the following text, we will first summarize the observations made by fluorescence microscopy and only after that, we will report the results of the rheological data.

3.3.2 LifeAct flash analysis

Since we used LifeAct-GFP transfected J774A.1 macrophages, it was possible to monitor the concentration of filamentous actin in the area around the bead throughout the experiment. As mentioned in the previous chapter in section 2.3.2, in some experiments the formation of actin during phagocytosis can be observed as a visible increase in fluorescence intensity at the bead's location. These flashes could also be observed during the experiments described in this chapter. To enable a quantitative analysis of the flashes' intensities and durations, the exact location of the bead in the fluorescent image is necessary. Because the bead is kept at a constant position in the camera's field of view by the feedback loop, the evaluation is easy. As soon as the feedback is activated, the position of the bead in the fluorescent image does not change anymore. As a first step in the evaluation, this position in the fluorescence image had to be identified. Since the bead itself is not fluorescent and thus invisible in the GFP channel, this was done by using the brightfield image data recorded by the pixelfly camera as a reference. In the brightfield image stack, the average bead position after the feedback has been started was marked using a MATLAB tool custom-developed by me, as illustrated in Figure 3.13A. Both cameras recorded at 0.5 fps after the blinking was started. However, since the frame rate of the pixelfly camera was set to a higher value at the beginning of the experiments, and due to an oversight in how the acquisition control was implemented, it often took several minutes for the frame rate to adapt the newly set value. After that adaption period, the standard deviation of the inter-frame times was below 8 ms for both cameras,

3 Cell rheology using optical tweezers and mechanical aspects of phagocytosis

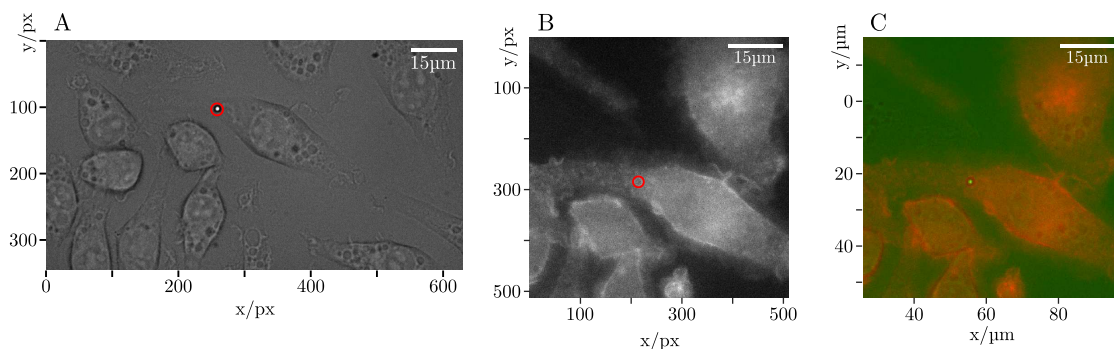


Figure 3.13: Alignment of the field of view between brightfield and fluorescence camera. As a first step, the position of the bead is marked in the brightfield image captured by the pixelfly camera (panel A). Because of the feedback loop, the bead will stay at this position during the whole experiments. Next, the rough location of the bead in the fluorescence image is marked (panel B). To verify the location of the bead in the fluorescence image, a colored overlay is created. For that, the fluorescence image is displayed on top of the brightfield image in a way that the bead's locations in both images align (panel C). If the bead's position was correctly marked in the fluorescence image, the cell boundary visible in the brightfield image should align well with the corresponding actin cortex in the fluorescence image. If not, the bead's position in the fluorescent image stack was iteratively adjusted, until the cells' locations in the overlay matched. This allows an accuracy around 300 nm. Only a single set of frames recorded directly after starting the feedback loop is shown here, but in the MATLAB tool the alignment can be checked for every timepoint in the image sequence. Finally, the position of the bead in the fluorescence image stack is known, which is essential for further evaluation.

and the average inter-frame time was very close to 2 s, only differing by about 0.002%. Still, the initially variable framerate of the pco pixelfly meant that the brightfield and fluorescent images could not be matched one by one. However, timestamps of each frame were saved for both cameras, and after manually specifying the delay between the timestamps of the pixelfly and the iXon Ultra camera, this could be used to find the best matching brightfield image for each fluorescence image. The temporal offset between the two cameras usually was typically around 10 s, sometimes a bit larger. This is equivalent to the time it took after the starting the pco pixelfly camera to manually start the iXon Ultra camera. In 90% of experiments, the time delay between the pixelfly channel and the fluorescent images was less than 16 s. This delay values will be important later to correctly align the rheological information with the fluorescence signal. Then, the approximate position of the bead in the fluorescence channel could be marked by eye (see Figure 3.13B).

The tool then provided an colored overlay of the brightfield and GFP channel (see Figure 3.13C) and a slider to scroll through the stack of fluorescence images. Since the two cameras had different apparent pixel sizes, the brightfield image was scaled according to Table 2.2 to match the fluorescence image before creating the overlay. This colored overlay proofed very helpful in fine-tuning the bead's location in the GFP channel and the temporal offset between the two cameras. Each time the bead position in the GFP channel was adjusted, the tool recalculated the overlay, which was repeated until the location of the fluorescent signal nicely matched the cell's location in all frames after the feedback was started. This way, the exact position at which the feedback keeps the bead in the GFP channel could be determined. Since the feedback loop kept the bead at a constant position throughout the

experiment, only one location had to be set for the whole image stack.

Now that the bead’s location in the fluorescent images is known, a qualitative evaluation was done by searching the experiments frame by frame for any visual indications of phagocytosis. These were found in 24 out of the 93 experiments. Depending on the observations, those 24 experiments were sorted into three categories. The first category includes all experiments in which a strong, ring shaped flash at the bead’s location was visible. This was the case in 17 experiments, as shown in Figure 3.14, where an image series of fluorescent signal around the time of the flash is shown for each experiment. The second category is similar and consists of three experiments with a visible peak in actin concentration. These cases were labeled “Flashes with Ruffling”, because in these cases, the actin structure already seemed to exist before the flash, suggesting that a membrane ruffle wrapped around the bead instead of the bead being engulfed by the formation of a phagocytic cup. Those events are shown in Figure 3.15. The distinction between the two cases was sometimes difficult, as clear criteria for distinction were missing. Finally, there were an additional four experiments that also showed a sudden increase in actin density at the bead’s location, but lacked the clear ring-shaped structure. These four experiments are also shown in Figure 3.15. All of these cases had in common, that a sudden, transient increase in the fluorescence intensity at the bead’s location was observed, indicating that actin polymerized around the particle, as it would be expected during the formation of the phagocytic cup. The flashes were constrained to a circular region with a diameter of $3\ \mu\text{m}$ (1.5 times the bead diameter) around the beads location and were usually visible for around $5 - 15\ \text{s}$. As the optical resolution using the $60\times$ -objective (numerical aperture 1.27) at green light is around $200\ \text{nm}$, the signal originating from the phagocytic cup around the $2\ \mu\text{m}$ -sized particle to area is expected to spread to a area around $2.5\ \mu\text{m}$, which matches this observation.

For a quantitative evaluation of the flashes’ durations, the average intensity $I_{\text{circle}}(t)$ of all pixels that lie in a circle with the radius $r_1 = 1.5\ \mu\text{m}$ around the bead’s location was calculated for all recorded images. This circle’s radius is 50% larger than the bead radius and it contains the whole region in which the actin flashes were observed. Additionally, to serve as a reference, the average intensity $I_{\text{ring}}(t)$ of all pixels in a ring around this circle was calculated. This ring included all pixels whose distance to the bead’s center is at least $r_1 = 1.5\ \mu\text{m}$ and not more than $r_2 = \sqrt{2} \cdot 1.5\ \mu\text{m} = 2.1213\ \mu\text{m}$. The value for the outer radius of the ring r_2 was chosen so that the area of the circle and the ring around the circle are identical. In Figure 3.14, the circle and ring areas are highlighted in red and green in the most top-left frame.

Figure 3.16A shows the average intensity in the circular area at the beads location as a function of the time relative to the observed flash. While the flash could be observed directly, as visible in the zoom-in provided in Figure 3.16B, the average intensity in the circle oscillated up and down and occasionally even exceeded the value reached during the phagocytic flash. The characteristics of these oscillations differed vastly from cell to cell, in some cases the intensity was rather constant while other cells showed quasi-periodic oscillations with a high amplitude.

flashes with ring shape

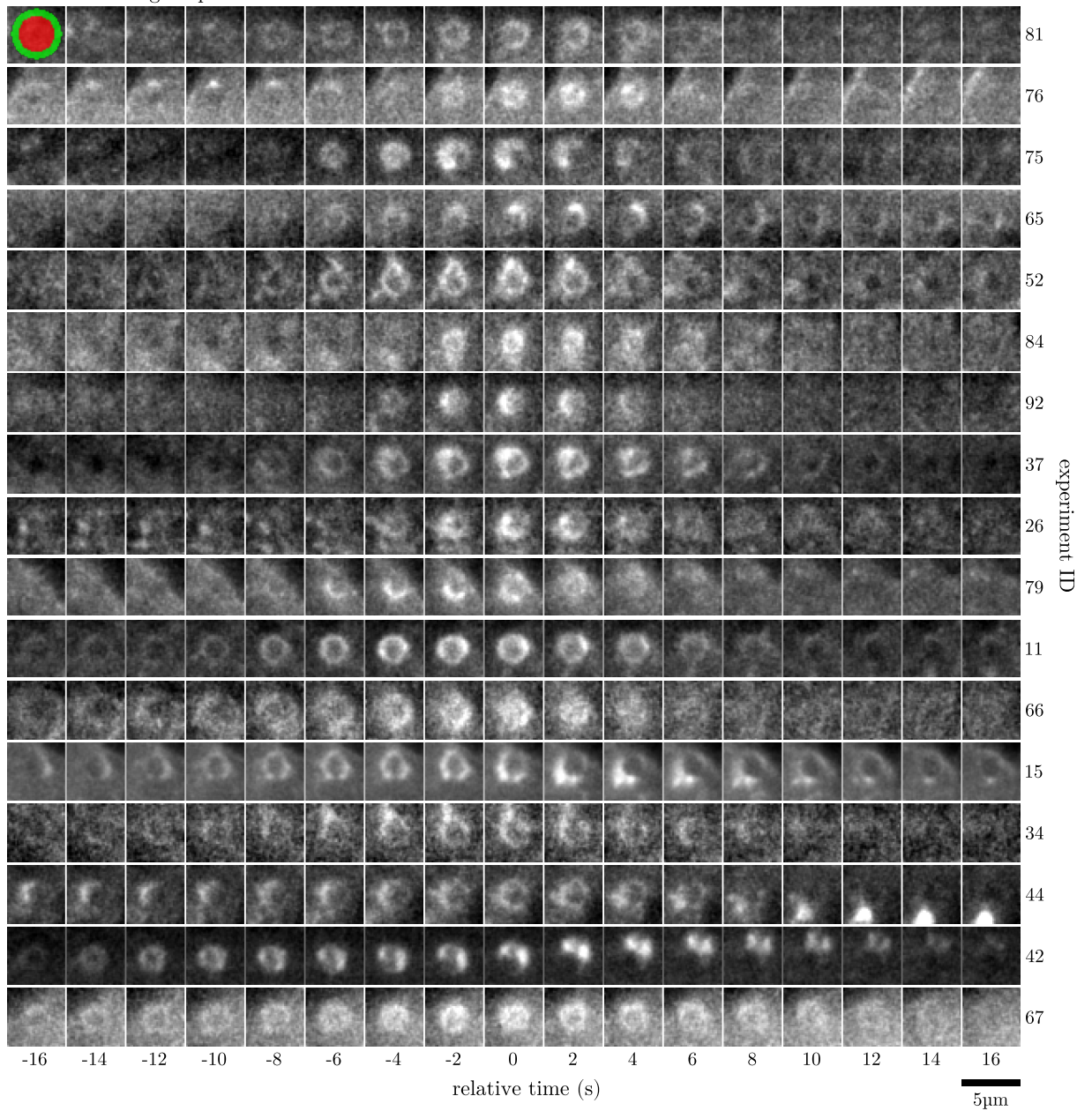


Figure 3.14: Ring-shaped actin flashes observed in blinking experiments. In 17 experiments, a visible, ring-shaped flash in the fluorescence channel was visible. This flash indicates the moment of phagocytosis. The figure shows the evolution of the actin network in a $35 \text{ px} \times 35 \text{ px}$ region around the target during this moment. As visible in the figure, the flashes are only visible for a few seconds. A very slight Gaussian blur ($\sigma = 0.1 \mu\text{m}$) was applied to the images to remove high-frequency noise. The experiments were roughly sorted by the flash’s duration, with the shortest signals at the top. The red and green areas in the upper left image show exemplarily the regions in which mean intensity values are calculated for the quantitative evaluation.

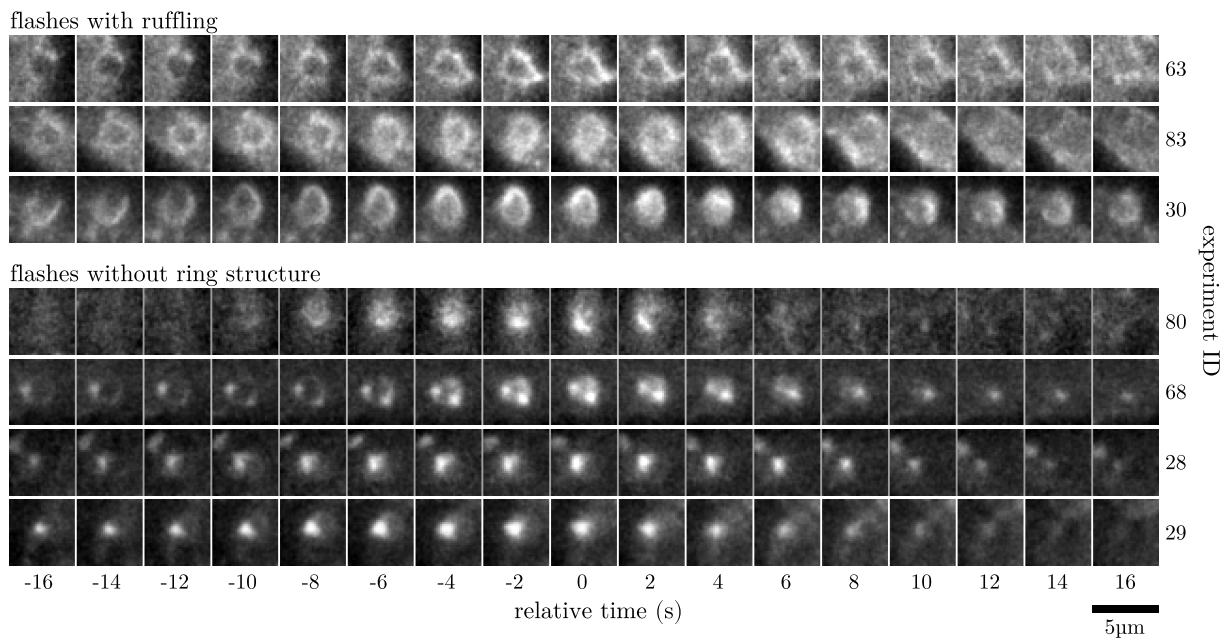


Figure 3.15: Additional seven flash events observed in blinking experiments. Beyond to the events shown in Figure 3.14, another seven events in which the fluorescence intensity around the bead showed a momentary increase were identified. In three experiments, a short rise in intensity was observed inside a ruffle-like dynamic structure, which exists on longer timescales. In another four experiments, a short intensity burst in the fluorescence signal around the bead was detected. These bursts are similar to the flashes in duration and intensity, but lack the clear ring-like structure of the flashes shown in Figure 3.14. A very slight Gaussian blur ($\sigma = 0.1 \mu\text{m}$) was applied to the images to remove high-frequency noise.

Meanwhile, the average intensity in the ring-shaped area around the bead followed the same oscillations, as seen in Figure 3.16C. However, the phagocytic flash did not influence the intensity in this area, which meant that the peak created by it is not present in this plot. This can be seen directly when comparing the zoom-in in panel B with panel D. To isolate the phagocytic flash, a new value called the recruitment ratio was defined. This value is the ratio of the average intensity in the circle and the ring:

$$R(t) = I_{\text{circle}}(t)/I_{\text{ring}}(t) \quad (3.21)$$

This ratio is shown in panels E and F of Figure 3.16. While the recruitment ratio stayed close to one for the whole duration of the experiment, its value could exceed values of 1.4 during the phagocytic uptake. This peak was a singular event, happening only once per experiment, which shows how powerful the recruitment ratio is as a metric to isolate the process of phagocytic phagocytosis for periodic actin oscillations.

In Figure 3.17A, the recruitment ratio is plotted again, this time with three different colors encoding the different flash categories. Along with the lines for the individual measurements, a solid black line indicates the average over all experiments. Due to the low number of experiments in some categories, all experiments were averaged together instead of calculating

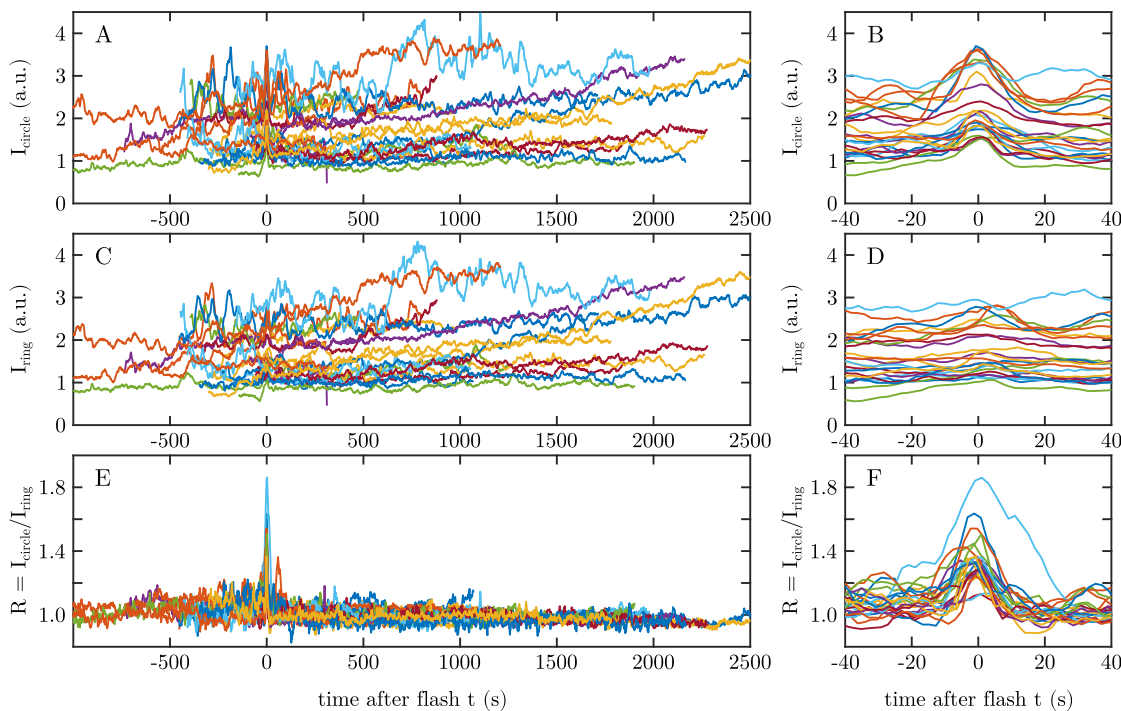


Figure 3.16: Calculation of the recruitment ratio R . Panel A and B show the mean fluorescence signal in a circular area with a radius of $1.5 \mu\text{m}$ around the bead's positions, plotted as a function of the time relative to the observed flash. All 24 experiments with visible actin flashes are shown. Panel C and D show the average intensity in a ring-shaped area around the circular area. While both signals show actin oscillations, only the signal inside the circle shows the characteristic increase cause by the actin flash. The ratio R between both intensities, as shown in panels E and F, highlights this difference, making it a suitable indicator for phagocytosis.

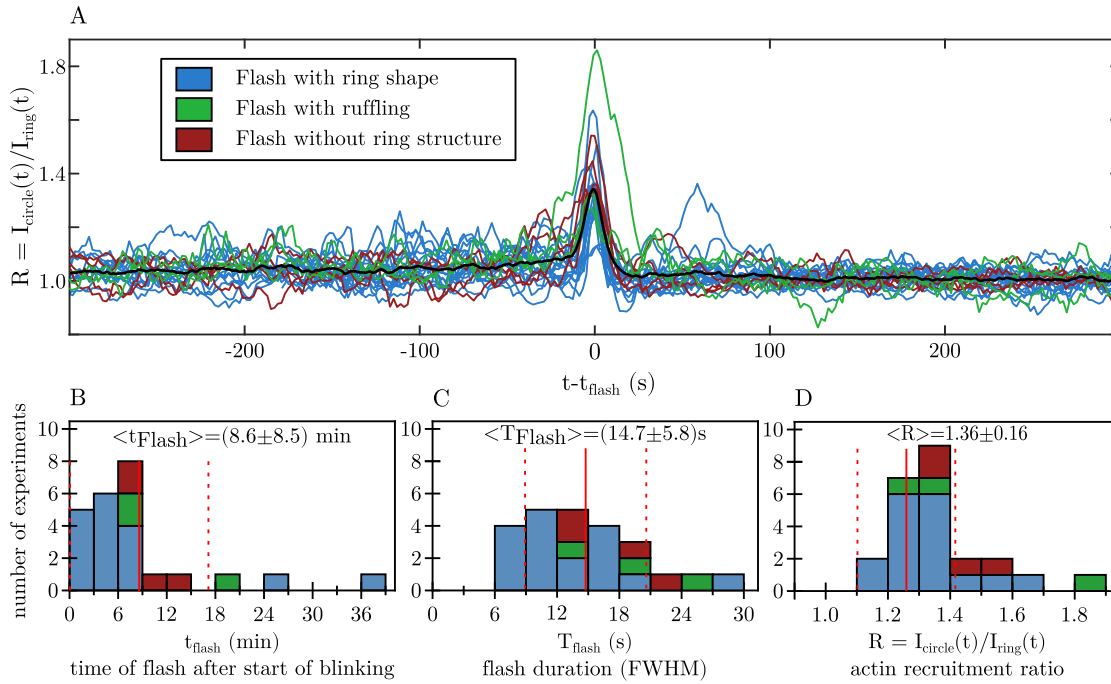


Figure 3.17: Evaluation of the actin flash timing and duration. Panel A shows the ratio R of the fluorescence intensity in a circular region (radius $1.5 \mu\text{m}$) around the bead's location relative to the intensity in a ring around it. The x -axis indicates the time relative to the flash's maximum intensity. The black line shows the averaged intensity of all experiments. The different colors indicate the different experiment categories. The FWHM of the averaged master curve (black) is $T_{\text{flash}} = 13.8$ s. Panel B shows at which time after starting the experiment, the uptake events happened. These uptake times t_{Flash} show a broad distribution, with an average of 8.6 min and a standard deviation of 8.5 min. By measuring the FWHM of the intensity peak in each individual experiment, a distribution of peak widths can be found as shown in panel C. The average FWHM flash duration in this distribution is $T_{\text{flash}} = (14.7 \pm 5.8)$ s. Finally, the maximum recruitment ratios observed during the peaks are listed in panel D. The average actin recruitment ratio was (1.36 ± 0.16) .

individual averages for each category. Except for the peak, the average recruitment value is astonishingly constant. This means that before or after the flashes, there was no consistent actin activity in the direct vicinity of the bead. During the phagocytic uptake, the average recruitment ratio reached a value of 1.342. It is also interesting that the recruitment ratio before the flash was higher than after the flash. The median value of the master curve from 200 s to 50 s prior of the flash is 1.046, while the median value for the experiment-average value of R in the time 50 s to 200 s after the flash is only 1.013.

The x -axis in Figure 3.17A shows the time relative to the moment in which a flash (as seen in Figure 3.14) occurred. In Figure 3.17B, a histogram shows the time at which the flashes occurred relative to the moment in which the blinking was started. As the blinking was started directly after attaching the bead to the cell, this is synonymous to the duration of the latency period which the beads stayed on the cell surface after attachment. Most flashes happened within the first ten minutes after the attachment, but in some experiments flashes were much later than that. As visible in the histogram, some beads were taken up almost

instantaneously while others took longer to be taken up. The average time it took from the attachment until a bead was taken up was:

$$\bar{t}_{\text{flash}} = (8.6 \pm 8.5) \text{ min} \quad (3.22)$$

The uncertainty here denotes the standard deviation of this time across all experiments.

To quantify the duration of the actin flashes, the full width at half maximum (FWHM) of the peaks was measured directly in all 24 experiments containing a flash event. To do this, the maximum value R_{max} measured during the flash was determined. Then, the time points t_1 and t_2 before and after the flash at which the value of $R(t)$ dropped below $(R_{\text{max}} - 1)/2 + 1$ were determined. The width of the flash $T_{\text{flash}} = t_1 - t_2$ was determined to be the amount of time that passed between these two points in time. Over all experiments, the mean result of this calculation was found to be:

$$\bar{T}_{\text{flash}} = (14.7 \pm 5.8) \text{ s} \quad (3.23)$$

The distribution of the flash durations is shown in Figure 3.17C, the error of 5.8 s is the standard deviation over all experiments. A direct measurement of the FWHM of the averaged curve in panel A returned a value of $T_{\text{flash, master}} = 13.8 \text{ s}$. This is slightly smaller than the average value of the individual experiments, which is caused by inhomogeneity of the peak shapes before the averaging.

Finally, the distribution of the recruitment ratios is shown in Figure 3.17D. The average was calculated to be:

$$\bar{R} = (1.36 \pm 0.16) \quad (3.24)$$

Again, 0.16 denotes the standard deviation. The color-coding for the different flash categories was also adopted into the histograms. Due of the small number of experiments, it is difficult to make a sound statement about the differences in the values of t_{flash} , T_{flash} and R between the individual categories.

3.3.3 Piezo stage overshoot

A hardware problem was later identified which caused that the piezo stage moved further than commanded. Because of this, the motion of the stage observed as steps in the highspeed trajectory was larger than the distance it should move according to the command that had been sent to it. This behavior is also visible Figure 3.12A, where on close inspection the observed stage movements are larger than the applied movements represented by the blue arrows.

Because of that, a calibration experiment was performed as described in chapter 3.2.1.4, where the stage was moved multiple times by different distances and the actual movement was observed using three cameras simultaneously to avoid any issues with the calibration. The ratio of the actually moved distance and the intended movement sent to the piezo stage was calculated for each movement event. This value will be called overshoot, as it is the factor by which the piezo stage overshoots its programmed movements. All 72 overshoot values for each camera are plotted in Figure 3.18. If the piezostage had complied with the movement distances commissioned by the software, we would expect the overshoot values to scatter around the factor 1. Instead, all values for the x -axis scattered around their average

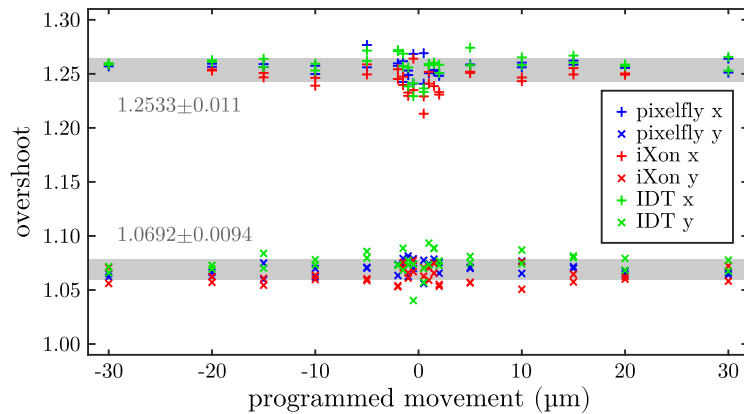


Figure 3.18: Measured overshoot values of the piezo stage for different step sizes, acquired using three cameras simultaneously. The overshoot value is defined as the real movement divided by the movement applied by the piezo stage. Since the value was consistently larger than one, the piezo stage reliably moves further than advised, with different factors in x - and y -direction. For small absolute movements, the tracking error has a larger influence on the overshoot values, which increases the uncertainty of the overshoot value around those values. The one standard deviation intervals around the average overshoot values for the x - and y -direction are depicted by the gray areas.

value of 1.2533 ± 0.0110 (standard deviation). The overshoot values for the y -axis were much lower, at only 1.0692 ± 0.0094 . The overshoot values for the z -axis were not measured. There was no significant difference between different cameras, which affirms that this overshoot cannot be chalked down to an error in the measurement of the pixel pitch. The unexpected mismatch of programmed and traveled movement suggest the conclusion that the internal calibration of the piezo stage is faulty.

3.3.4 Results of the rheological measurements

The trajectories around the moment in which the SLM was activated were fitted as described in chapter 3.2.5, providing time-resolved values for the viscoelastic parameters α and β . In 68% of the experiments, the number of fits performed was between 659 and 684. At a repetition rate of 0.5 s^{-1} , this perfectly corresponds to the 23 min acquisition time limit provided by the finite memory of the highspeed camera. Only 9 out of 83 valid experiments had less than 600 blinking events. Those were the experiments which were ended prematurely. In total, 97.7% of the fits showed valid results. This means that in 2.3% of all fits, the coefficient of determination R^2 was smaller than 0.85. This was especially the case for periods in which the cell was exceptionally stiff, as during those periods the reaction of the bead to the laser pulse became so small that the overlaying noise made fitting challenging.

3.3.4.1 Binding phase

We noticed that in a lot of experiments, the amplitude α quickly decreases within the first few minutes after the bead is attached to the cell. This binding phase can be studied even without the feedback system and was already observed and studied in great detail^[218]. In this previous research, we concluded that this decrease in the blinking amplitude α is not caused by a changing cell stiffness, but by the increasing contact area between the bead and

the cell which causes a larger volume of the cell to be deformed. Since in those previous studies the number of performed experiments was lower, it is worth re-investigating this phenomenon here. In the following paragraph, the new data will be analyzed and the results will be compared to previous results.

To quantify the binding dynamics, we plotted the rheological parameters α and β of the cell during the first 100 seconds after the blinking was started. To do this, the fit results from all valid 83 experiments were pooled. Fits which were marked as failed due to a high residuum value were excluded. The obtained values of α and β from all fits were subsequently organized into bins based on the time elapsed after activating the blinking, which was done immediately after attaching the bead to the cell. Each bin corresponded to a four-second interval. The results of this evaluation are shown in Figure 3.19A and 3.19B. Each bin contains between 162 and 224 individual fit results. It is clearly visible that the amplitude α drops quickly in the first minute after the bead is attached and then reaches a constant value. In contrast, the exponent β exhibits only a subtle modulation, likely lacking statistical significance. Averaging over all mean values for β in the 25 bins resulted in a value of $\beta = (0.263 \pm 0.012)$. The uncertainty here denotes the standard deviation of the bins' mean values. The standard deviation of all individual fits was 0.13, with 68% of fit reporting a value of β between 0.164 and 0.358.

It is plausible that the decrease in the blinking amplitude α does not originate from a change in the cells mechanical properties but rather from the bead gradually binding to the cell, as explained previously^[218]. Initially, the bead was only bound to the cell with a very small area, which means that only a small volume of the cell had to be deformed to move the bead. As the bead gradually binds to the cell, the contact area increased and more of the cell had to be deformed which requires a larger force for the same bead movement. This results in a lower amplitude during our blinking experiments.

As done before^[218], the contact radius $r(t)$ is assumed to rise during the attachment process, starting at zero and approaching the particle radius r_0 . A sigmoid curve can be used to describe its temporal evolution.

$$r(t) = \frac{r_0}{1 + \exp(-(t-\tau_{0,c})/\tau_b)} \quad (3.25)$$

Here, the particle radius $r_0 = 1 \mu\text{m}$ is a constant. Meanwhile, assuming the cell's viscoelastic properties do not change, the creep compliance j_0 remains constant duration the attachment. The amplitude α is defined as the ratio of the creep compliance j_0 and the bead contact circumference $r\pi$. The contact area is assumed to be circular, covering an area of $A = r^2\pi$ with the time-dependent contact radius r .

$$\alpha(t) = \frac{r(t) \cdot j_0}{A(t)} = \frac{j_0}{r(t) \cdot \pi} \quad (3.26)$$

Using the inverse squared standard errors of the mean for weighting, a direct fit to the data resulted in the values $j_0 = 13.7 \text{ (kPa)}^{-1}$, $\tau_{0,c} = 14.6 \text{ s}$ and $\tau_b = 12.7 \text{ s}$. To estimate the range of certainty for the three fit parameters, a simple bootstrapping approach was used. This means that the input data of the fit was substituted with randomly sampled data from the pool of measurements and the fit was done many times on different input datasets, each chosen randomly from the pool of all available measurements. This is useful, as it allows to estimate how much alterations on the input data influence the fit results.

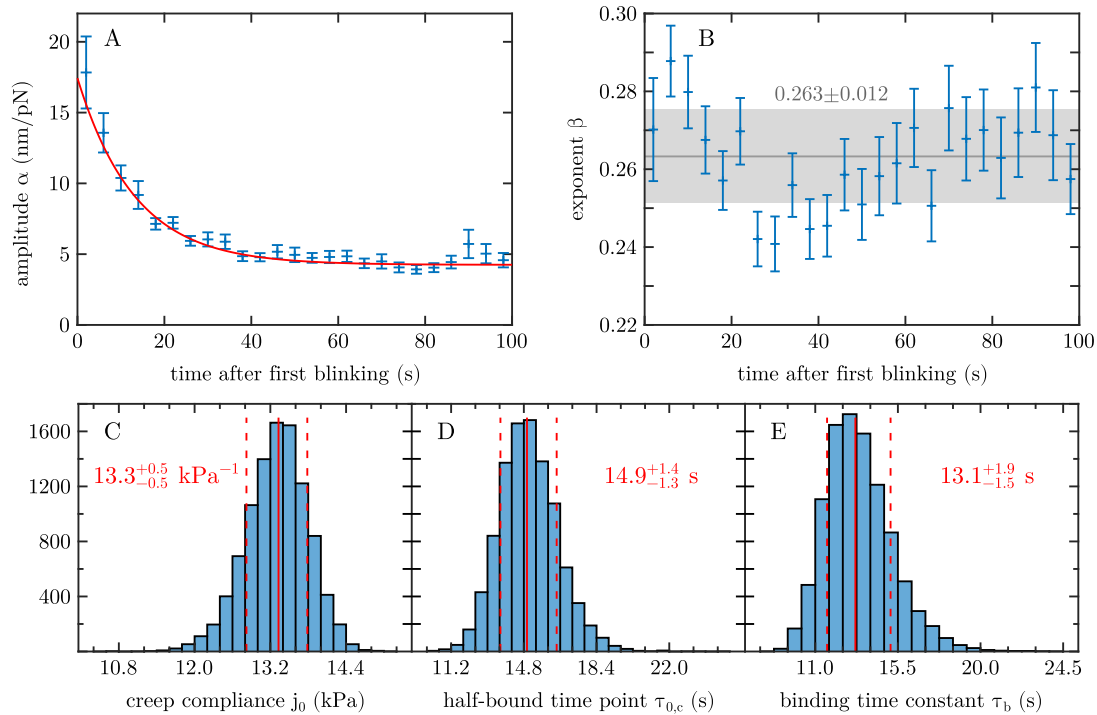


Figure 3.19: Evaluation of the viscoelastic parameters α and β after the attachment. To create the plots in panel A and B, the fit results of all 83 valid experiments were pooled and sorted into 4 s wide bins, depending on how long after the attachment they were recorded. The mean values for α and β in each bin are plotted in this figure, the error bars show the standard error of the mean. While the amplitude α quickly drops at the beginning of the experiment, the average exponent β within the bins only varies slightly around a value of 0.263 ± 0.012 (interval shown by gray area) during this time. Panels C, D and E show the distribution of the fit parameters j_0 , $\tau_{0,c}$ and τ_b , which resulted from fitting to 10^4 different simulated datasets, allowing to estimate the confidence intervals for each parameter. The solid red line in each panel marks the median value while the dashed lines represent the 15.85%- and the 84.14%-quantiles, marking the edge of the confidence interval. The red numbers represent the median parameter values and the corresponding confidence interval sizes.

For each datapoint in panel A, $N \approx 200$ individual values for α were measured. A new datapoint was created by selecting a random value out of this pool of N values N times. This creates a new set of values for α , that may include the same value multiple times, but exclude others. From this new set, the mean and the standard error of mean are calculated, and a new, simulated binned datapoint was created. This was done for all datapoints in panel A. After that, the fit was repeated as before, again using the standard error of mean of the simulated bins to calculate to weights for the least-square fit.

This was repeated 10000 times to obtain decent statistics. Figures 3.19C-E show the distribution of the individual fit parameters in the 10000 fit results. The final values for the fit parameters were obtained by calculating the median value for each fit parameter. The outer limits of the confidence interval are chosen as the 15.87%-quantile and the 84.14%-quantile of the distribution. With this definition, 68.27% of the data lie in the confidence interval, which means that for a Gaussian distribution the confidence interval spans one standard deviation

around the average value. The final values for the fit parameters obtained this way are:

$$\begin{aligned} j_0 &= 13.3_{-0.5}^{+0.5} (\text{kPa})^{-1} \\ \tau_{0,c} &= 14.9_{-1.3}^{+1.4} \text{ s} \\ \tau_b &= 13.1_{-1.5}^{+1.9} \text{ s} \end{aligned} \tag{3.27}$$

The median values and the edges of the confidence interval are shown in the figures 3.19C, 3.19D and 3.19E as dashed red lines.

3.3.4.2 Phagocytic uptake

While fits to the blinking events were done on all experiments, the results are especially interesting for the experiments containing a visible flash in the fluorescence channel. As described before, we found an indication of phagocytosis in the form of a brief rise in the LifeAct fluorescence intensity around the bead in 24 experiments, listed in Figure 3.14 and 3.15. Since these flashes indicate phagocytosis, the rheological evaluation of these experiments gives us access to the mechanical properties of the cells in the vicinity of the phagocytic cup before, during, and after phagocytosis. In two of those 24 experiments, the flash happened more than 23 min after the beginning of the experiment (see Figure 3.17B). In those two cases, no rheological data at the time of the flash is available, since the highspeed camera's memory did not allow any longer acquisition.

In most of the remaining experiments, a sudden increase in the blinking amplitude α can be observed at or slightly after the moment of the flash. An example of this can be seen in Figure 3.20. While panel A shows the average intensity in the circular and ring-shaped area around the bead, Figure 3.20B shows the particle trajectory during the experiment. Looking at the trajectory, it is directly visible that the optical trap created bigger movements of the bead in x -direction after the flash than before. This becomes even clearer when looking at panel C, where the maximum displacements, measured as shown in Fig. 3.9c, are plotted on a logarithmic y -axis. Based on this plot, qualitative assessments on the rheological behavior of

Figure 3.20: Full evaluation of a single blinking experiment. In the top, four pairs of brightfield and fluorescence images at different timepoints of the experiment are shown. In the first fluorescence image, two white circles are visible. In panel A, the mean intensity in the inner circle and in the ring between both circles is plotted throughout the experiment. It is clearly visible that there was a strong flash in the LifeAct intensity at $t = 210$ s that was much stronger than the background signal in the ring around the bead. In panel B, the bead position relative to the trap obtained from the highspeed recording is plotted in x - (blue) and y -direction (red). In panel C, the maximum displacements during the blinking (measured as shown in Figure 3.9c) are plotted. The displacement in x -direction showed a clear increase at the moment of the LifeAct flash. Next, the fit results are plotted. Both parameters α (amplitude, panel D) and β (exponent, panel E) suddenly increased around the time the particle is taken up. Furthermore, the binding phase is visible as a drop in α right after the attachment. Finally, the position of the piezo stage is plotted in panel F. At the time of phagocytosis, a small, sudden movement in z -direction could be observed, marked by an arrow. The values of α , β , Δx , Δy were smoothed by applying a 10 s moving average filter before plotting. The lighter colored lines in the background show the unfiltered data.

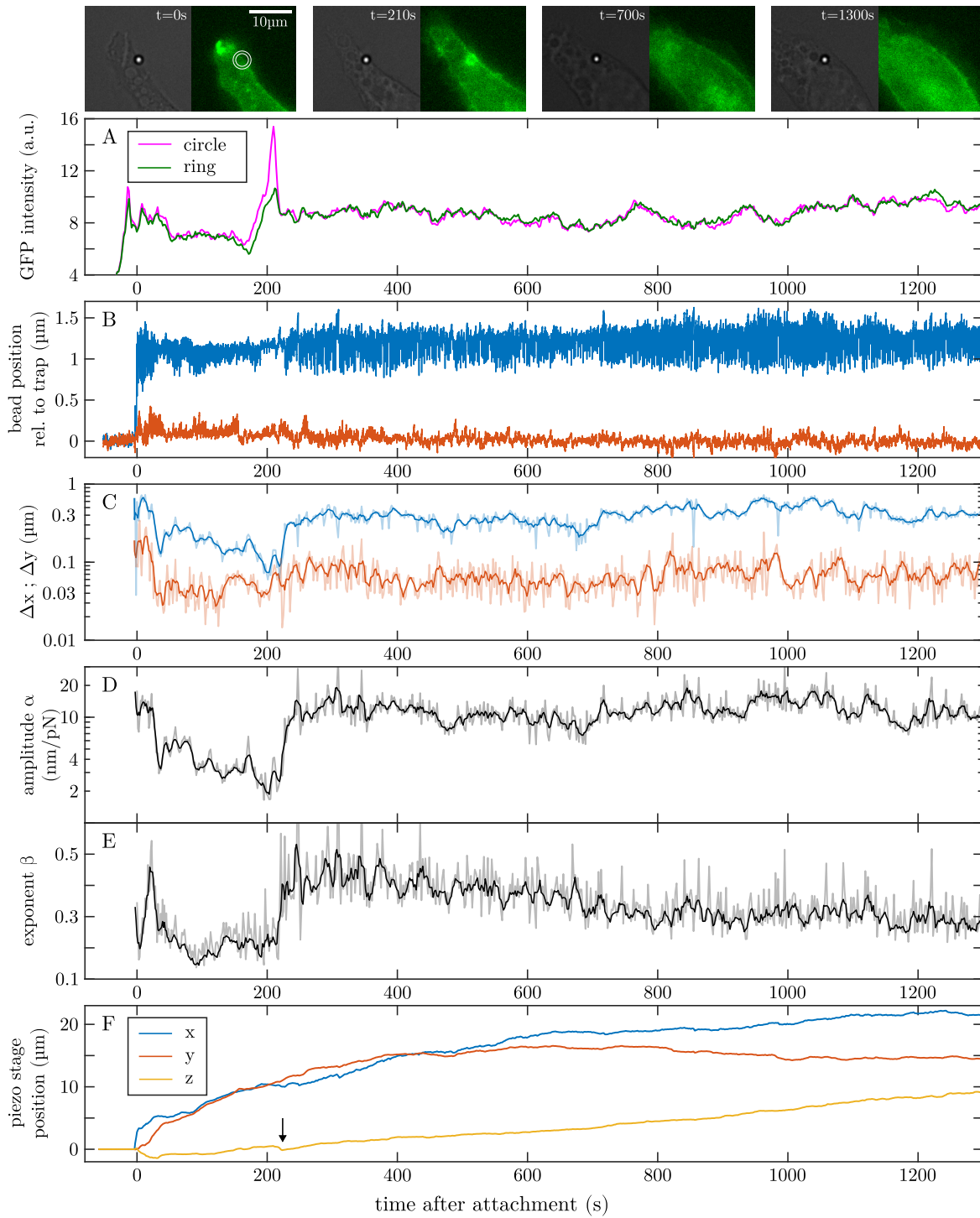


Figure 3.20: (Caption on previous page)

the cell during the experiment are possible without further analysis: For example, the binding phase is clearly visible, as the value of Δx dropped in the first minute of the experiment. In the moment of the actin flash, the amplitude of Δx was especially low, only to rise quickly and stay high afterwards.

This trend is reflected in the evaluation of the fit parameters: In panel D and E, it is obvious that both α and β rose in the moment the flash and stayed high for the rest of the experiment. In the example measurement, the value of α decreased continuously from the beginning of the experiment to the moment of the flash at $t = 200$ s, dropping all to approximately 2 nm/pN right in the moment of the flash. After the flash, the value was much larger, at roughly 10.6 nm/pN. This was a more than fivefold increase in the blinking amplitude within less than 30 seconds. However, in many other experiments with visible flashes, the initial decrease of α was not as steady. Often, the value of α only dropped in the first one or two minutes after attachment, then stayed at a low value until right before the flash. This was especially true if the flash was observed much later in the experiment. In some experiments a short, transient drop in the value of α was observed during the flash, however this was highly inconsistent between experiments. The increase in α after the flash was observed in almost all experiments. The pronounced increase of α , in combination with the actin flash can be seen as a clear indication of phagocytic uptake, as an increase in the density of filamentous actin during the phagocytic engulfment is expected. The value of α after the flash was similar to its initial value seconds after the attachment of the bead.

The value of β in panel E fluctuated a bit directly after the attachment and then quickly reached a value around 0.26. In the moment of the flash, it rose to values around 0.38, followed by a slow decrease over time for the rest of the experiment. At the end of the experiment, β reached a value of approximately 0.30. Finally, panel F shows the position of the piezo stage. The stage moved by tens of micrometers to keep the bead at a fixed position relative to the optical trap. The large movement in x -direction was facilitated by the optical force, which pulled the bead in $-x$ direction during the phases in which the SLM is active. An interesting detail in panel F is that the stage moved suddenly in z -direction in the moment the flash occurred. This is marked by a small arrow in the figure. This stage movement compensated for the bead being pulled down into the cell during the phagocytic uptake.

Similar trends are visible in the for the other experiments with visible actin flashes, although the increase in α and β was sometimes less pronounced. Figures 3.21A-C provide an overview of the actin recruitment ratio R and the average fit parameters α and β and in the time period 150 s before and after the flashes. Out of all 24 experiments with visible flashes, as listed in Figures 3.14 and 3.15, two experiments were omitted in Figure 3.21, as in these the flash happened after the end of the highspeed camera's acquisition. Any data recorded within two minutes after the bead was attached was excluded from this plot to avoid the influence of the binding process. In the background of the figure, the values of α and β determined by fits to individual blinking events are shown as small gray dots. This data was then sorted into 4 s wide bins based on the time relative to the flashes' maximum. Each bin is plotted as an errorbar indicating the average value in this bin and the standard deviation. To remove any influence from change of α during the beads' attachment periods, any value of α and β recorded in the first 2 min after the attachment was excluded from this plot.

It is easily visible that the average amplitude α increased drastically within about than 30 s after the actin flash. While the medium value of α in the period $[-150, -50]$ s was 2.47 nm/pN, it was 9.76 nm/pN for the period $[50, 150]$ s after the flash. To improve the visibility of small

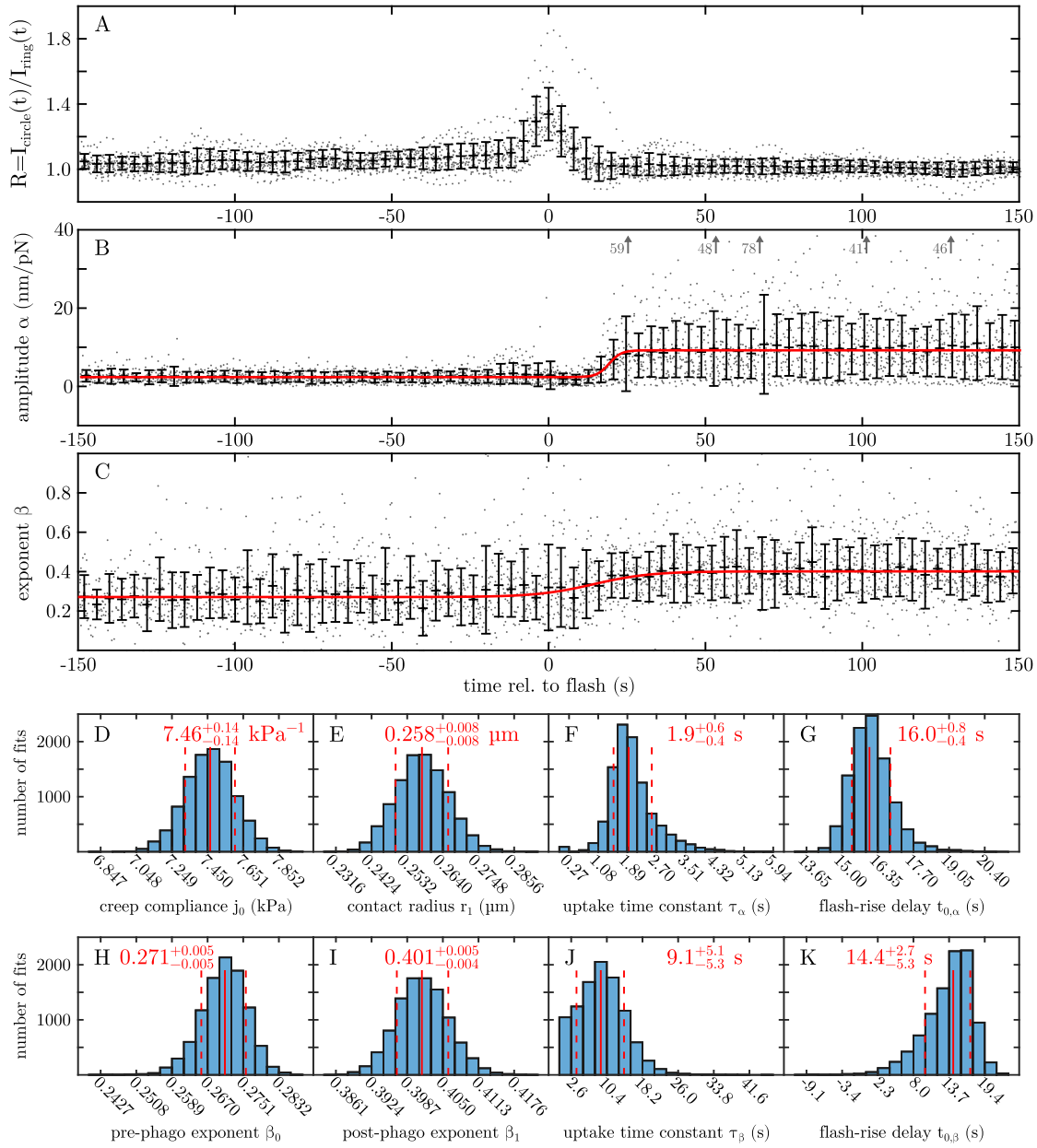


Figure 3.21: Evaluation of R , α and β during the visible actin flashes. The data of all experiments showing visible flashes was pooled into 4s wide bins. While panel A shows the recruitment ratio highlighting the flash, panels B and C reveal that the values of α and β rose after the flash has happened. The error bars indicate the standard deviation in each bin. Fits were done to panel B and C as described in the main text. Panels D to K show the distribution of the fit parameters as acquired by a bootstrapping approach, as well as their median values and confidence intervals. The red lines in panels B-F represent fits assuming a sigmoidal decrease in the contact radius, defined by equations 3.28 to 3.32.

effects on α and β in the vicinity of the flash, a zoom into Figure 3.21A-C is provided in Figure 3.22A-C. When looking at Figure 3.22B, it is visible that the increase in α did not happen exactly at the same time at which the actin flash is observed. Instead, α was constant right until the flash reaches its maximum. Then, for the duration 2 – 14 s after the flash, the average value of α was lower than ever before at an average of 2.1 nm/pN. Only after that, α began to rise.

Additionally, Figures 3.22D-F provide an overview on the evaluation of α and β over longer timescales up to beginning and the end of the experimentally accessible timeframe. As before, the first two minutes of all experiments were excluded from this plot to avoid the influence of the binding phase. In panel E, it is clearly visible that there was no continuous long-term decrease in α before the flash. Instead the values of α before and after the flash are both rather constant. As before, the viscoelastic exponent β was constant before the flash, and then increased suddenly around the time of the flash. However, after that, it began to drop slowly again for the rest of the experiment. In panel F of Figure 3.22, a purple line was fitted to the mean values of the bins for β measured more than 60 s after the flash's maximum, measuring the rate of slope of this decrease at -0.007 min^{-1} . This means that while the bead's environment became more viscous after the flash, this effect diminishes over time and the bead gradually sees itself in a more elastic environment again.

In the 54 experiments without visible flashes, there are no consistent trends of α and β except for decrease of α during the binding phase. In this experiments, the 16 s-averages of the fit parameters scattered around a $\alpha = (5.7 \pm 0.8) \text{ nm/pN}$ and $\beta = (0.294 \pm 0.014)$. The data is shown in the appendix of this thesis in Figure 5.1.

Following the logic applied during the evaluation of the binding process, the increase in $\alpha(t)$ after the flash can be explained by a change in the geometry of the deformation. It was assumed that the contact radius approached a constant value of $r_0 = 1 \mu\text{m}$ during the phase in which the particle bound to the cell.

If the bead is completely engulfed, more volume has to be deformed, but the cytoplasm is much softer than the actin cortex near the cell wall. After engulfment, the bead can slip under the actin cortex, moving more freely, leading to a larger value of α . This decoupling was modeled by a decrease in the contact radius of the bead to the stiff actin cortex. Meanwhile, the creep compliance j_0 of the cell is assumed to stay constant during the uptake process. It should be noted that this model cannot describe the temporary increase in the binding strength between phagosome and cytoskeleton as the bead passes the actin cortex. This detachment from the actin cortex was modeled by the following sigmoidal function, similar to Equation 3.26:

$$r(t) = r_0 + \frac{r_1 - r_0}{1 + \exp(-(t - t_{0,\alpha})/\tau_\alpha)} \quad (3.28)$$

Again, $r_0 = 1 \mu\text{m}$ is assumed to be the particle radius and thus constant. r_1 describes the contact radius after phagocytosis. Because the phagosome has mostly separated from the actin cortex at this point, the value of r_1 does not describe an actual contact area, but instead the hypothetical contact area that would provide the same amount of elasticity than the newly formed phagosome experiences inside the cytoplasm.

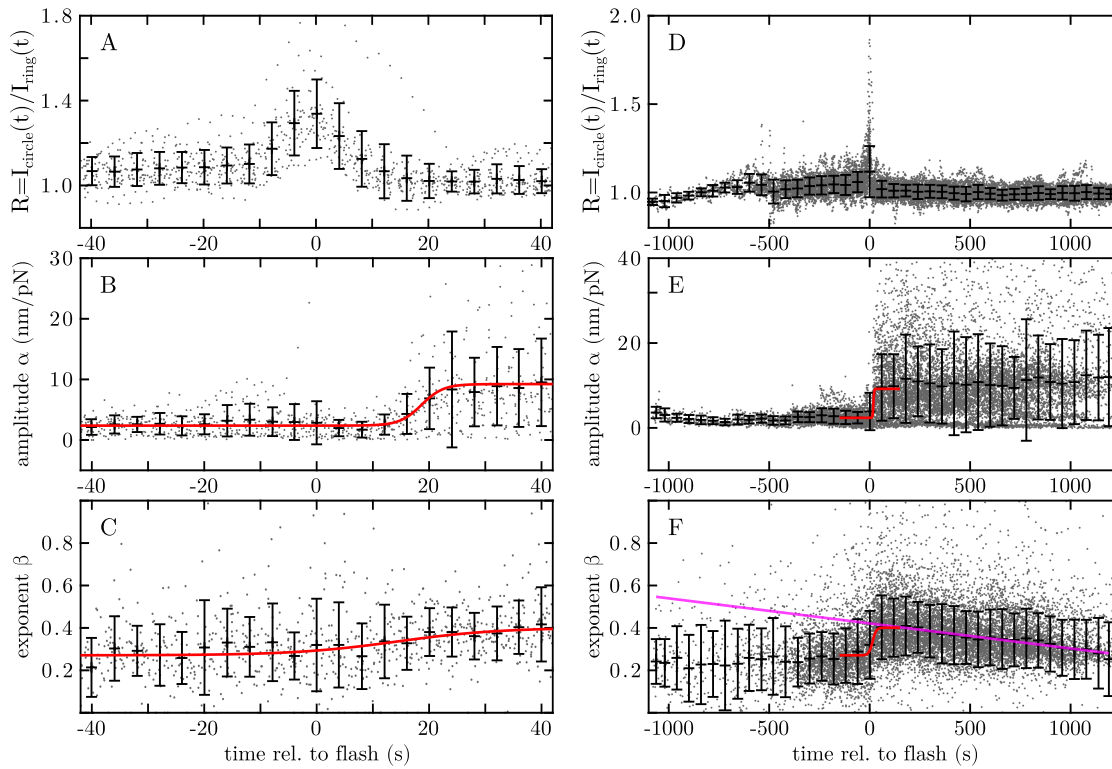


Figure 3.22: Evolution of the recruitment ratio and the rheological parameters around the flashes, alternative binning. Merely zooming in to Figure 3.21, panels A to C show the evaluation of the recruitment ratio R and the viscoelastic parameters α and β . It is visible that immediately after the flash, α drops slightly, only to increase directly afterwards. Panels D to F provide an overview over longer timescales, using 60 s-wide bins. It is visible that while the mean value of α stays constant after the flashes, β slowly drops at a rate of -0.007 min^{-1} , indicated by the pink line. The gray dots mark individual fit results omitting values that lie outside of the visible area. The red lines show same fits as before, defined by equations 3.28 to 3.32.

This means that the value of $\alpha(t)$ can be described by the following equation:

$$\alpha(t) = \frac{j_0}{r(t) \cdot \pi} \quad (3.29)$$

This function was fitted to the experimental data in Figure 3.21A. Similar to chapter 3.3.4.1, a bootstrapping approach was used to estimate the uncertainties of the fit results. For that, the average and standard deviation values of the individual bins in Figure 3.21B were replaced with newly calculated average and standard deviation values before fitting. Since each bin contained $N \approx 40$ data points, a random measurement value inside the bin was selected randomly N times. Then, the average and standard deviation of those N values were calculated. This was done for all bins to create a new full dataset. To this dataset, the function in Equation 3.29 was fitted using a least-square method weighted with the squared inverse standard error of mean of the new dataset. This was repeated 10^4 times. The resulting distributions of the four fit parameters are shown in panels D to G in Figure 3.21.

The bootstrapping returned the following values:

$$\begin{aligned}
 j_0 &= (7.46 \pm 0.14) \text{ kPa}^{-1} \\
 r_1 &= (0.258 \pm 0.008) \mu\text{m} \\
 \tau_\alpha &= 1.9_{-0.4}^{+0.6} \text{ s} \\
 t_{0,\alpha} &= 16.0_{-0.4}^{+0.8} \text{ s}
 \end{aligned}
 \tag{3.30}$$

The confidence intervals boundaries here correspond to the 15.85%- and 84.14%-quantiles of distributions shown in Figure 3.21, which are indicated in the histograms in panel D to G by red lines. Interestingly, the creep compliance j_0 is lower than the creep compliance estimated from the first 100 s after attachment at only 7.46 kPa^{-1} instead of the previous 13.3 kPa^{-1} . This means that the cell got stiffer since the initial attachment, which might be caused by the increased actin assembly during phagocytosis. The value of the contact radius dropped during phagocytosis, to a value of only $r_1 = 0.258 \mu\text{m}$ as the phagosome detached from the actin cortex. The small value of $\tau_\alpha = 1.9 \text{ s}$ indicates that this process was very fast. Interestingly, the rise of α happened with a slight delay of $t_{0,\alpha} = 16 \text{ s}$ after the LifeAct flashes. Parallel to this, the increase in the exponent β was fitted with the following sigmoidal function:

$$\beta(t) = \beta_1 + \frac{\beta_2 - \beta_1}{1 + \exp(-(t - t_{0,\beta})/\tau_\beta)}
 \tag{3.31}$$

The fit was done as before using the same bootstrapping method as before. The resulting distributions of the fit results are shown in panels H to K of Figure 3.21. The results were:

$$\begin{aligned}
 \beta_1 &= (0.271 \pm 0.005) \text{ kPa}^{-1} \\
 \beta_2 &= 0.401_{-0.004}^{+0.005} \mu\text{m} \\
 \tau_\beta &= 9.1_{-5.3}^{+5.1} \text{ s} \\
 t_{0,\beta} &= 14.4_{-5.3}^{+2.7} \text{ s}
 \end{aligned}
 \tag{3.32}$$

As visible, a significant increase in β from $\beta = 0.271$ to $\beta = 0.401$ was observed. The value $t_{0,\beta}$ describes the delay of this growth in β relative to the LifeAct flash. This delay is the same size as the delay observed for the parameter α , meaning α and β rise simultaneously, possibly because the changes have a common cause such as the fission of the phagosome from the cell membrane. Due to the large standard deviations in the values of β , and the relatively small change in the value of the exponent, the time constant τ_β describing how fast β is rising after the flash could only be determined with great uncertainty. While the median value of τ_β is much larger than τ_α , indicating that the rise of β takes longer, it still is very plausible that the rise of α and β happened at the same speed, which would be expected if both changes were caused by the same physiological process. Table 3.1 provides an overview over the values of α and β prior and after the flash as well as the values observed in the experiments without flashes. The values for α in this table were calculated from the fitted j_0 and r_1 values using Equation 3.26.

During this evaluation, the values of $v_{\text{Drift},x}$ obtained by the fits to the individual blinking events were also analyzed. These values contain information on the active force applied by the cell to the particle. Unfortunately, no consistent trends in this drift velocity related to

	α	β	r_0
pre-flash, $t = [-150, -50]$ s	(2.38 ± 0.05) nm/pN	(0.271 ± 0.005)	$1 \mu\text{m}$
post-flash, $t = [50, 150]$ s	(9.23 ± 0.23) nm/pN	(0.401 ± 0.005)	$(0.258 \pm 0.008) \mu\text{m}$
experiments without flash	(5.7 ± 0.8) nm/pN	(0.294 ± 0.014)	–

Table 3.1: Values of α and β pre- and post flash according to the fits shown in Fig. 3.21. The values of α were calculated individually using Equation 3.26 for each individual fit result in the bootstrapping, the uncertainties here denote the 15.85%- and 84.14%-quantiles of the results. The creep compliance has the same value of $j_0 = (7.46 \pm 0.14) \text{ kPa}^{-1}$ prior and after the flash.

the process of phagocytosis could be identified, as averaging the drift velocity over multiple experiments always resulted in values close to zero.

Since we now know that flashes are often accompanied by a sudden increase of α , we can search for such sudden increases in other experiments which did not contain a clear visual flash. If a sudden increase was found, the LifeAct signal at this moment could be investigated in great detail. This way, another four flashes could be revealed. Those flashes were only visible with very poor signal-to-noise ratio, but since they were accompanied by a sudden rise of α , it is very likely that these events also showed phagocytosis. These flashes are shown in Figure 3.23 as a image series. Giving how faint these flashes were, it is not surprising that these flashes have been missed by the first evaluation. With this new four experiments, a total of 28 out of 83 valid experiments showed clear indications of phagocytosis in the form of an actin flash and a rise in the rheological parameters α and β right after the flash occurred.

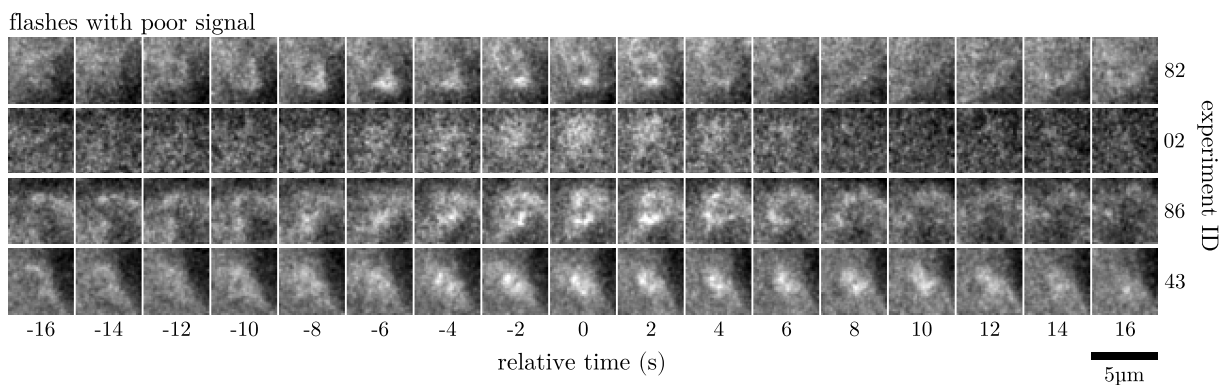


Figure 3.23: Flashes with poor signal-to-noise ratio observed during blinking experiments. In four experiments, a very weak flash was found after the exact time of the flash was revealed by the blinking data. In all these experiment, a sudden rise of the viscoelastic parameter α can be observed at the moment of the weak flash. As before, a slight Gaussian blur ($\sigma = 0.1 \mu\text{m}$) has been applied to the images to remove noise of high spatial frequency.

3.4 Discussion

Using the experimental technique described in this chapter, we were able to measure two aspects of phagocytosis at the same time. The simultaneous measurement of the concentration of filamentous actin around the bead and the rheological properties of the cell provides unique insight into the mechanical mechanisms that enable phagocytosis. The observation of actin flashes followed directly by an increase in the blinking amplitude α and the viscoelastic exponent β provides very strong evidence that we observed the moment of phagocytosis, as actin polymerization plays a fundamental role during phagocytosis^[13].

3.4.1 Uptake efficiency

In this chapter, 83 experiments were evaluated, providing data on the actin cortex through fluorescence microscopy and rheological data at the same time. When analyzing the results, we found strong evidence of phagocytic uptake in 28 of those experiments in the form of a transient, localized increase in actin density at the bead's location followed by a quick, significant change in the rheological properties.

It is likely that the increase in actin density is caused by the reorganization of actin that is associated with phagocytosis^[107]. Sometimes, the flashes was accompanied by a sudden movement of the particle in z -direction. This movement was not visible in the images, as any long-term movements would be compensated for by the feedback loop. However, a movement of the particle relative to the cell creates the need for a counteracting movement of the piezo stage to keep the bead in position, as for example visible in Figure 3.20. Since the bead usually rested on top of the cell prior to the flash, a subtle shift of the bead towards the coverslip was a especially clear indicator for phagocytic uptake. However, this shift was not consistent between experiments, which is why no quantitative evaluation of this effect was carried out.

The ratio of beads which are internalized thus is 28/83, or roughly one third. This value is often called the phagocytic efficiency, as it indicates how many beads which come into contact with the cells are taken up. K. Berghoff measured the phagocytic efficiency of the same particle-cell system via sedimentation experiments and obtained a value of 34% when using a incubation period of 15 min and 54% for an incubation time of 30 min^[130]. When considering that the most blinking experiments went on for around 23 min, a phagocytic efficiency of 1/3 is comparable to the results of K. Berghoff. Despite this, it should be noted that the sedimentation experiments differed substantially from our protocol. In Berghoff's experiments, the beads were added to the cells while those were chilled on ice to prevent premature phagocytosis during the sedimentation. After a time of 30 min, the incubation period was started at 37°C. At the end of the sedimentation phase the cells were chemically fixed and all beads outside the cells were stained using secondary antibody. Engulfed beads were not stained as they were covered by the cell membrane. After imaging, the phagocytic efficiency was calculated counting all cell-particle interactions and categorizing them into uptake and non-uptake. Still, the experimental uptake efficiency measured in this chapter aligns well with the established data.

3.4.2 LifeAct flashes

The 24 experiments initially recognized as uptake were sorted into different categories by visually inspecting the flashes. However, when looking at the times at which the flash occurred in the experiments, the durations of the flashes and the actin recruitment ratio, there does not seem to be a significant difference between the individual categories. In Figure 3.17, the categories were color-coded. When looking closely, for the flashes with ruffling and the flashes without a ring structure, the flash events seemed to happen slightly later into the experiments. Also, the duration of the flashes is slightly longer. However, due to the low number of experiments in those two categories and the only small differences, there is not enough evidence to attribute the different flash categories to different uptake mechanisms. Instead it is more likely that the visual categorization was not done independently of those values, and that all flashes were caused by the actin assembly during phagocytosis.

The flashes were observed at a time of $t_{\text{flash}} = (8.6 \pm 8.5)$ min after the attachment. This fits the observation of a latency period between the initial attachment of the target and the uptake, which was reported previously to last from only a few seconds up to 30 minutes^[186,187]. The flashes itself lasted for only $T_{\text{flash}} = (14.7 \pm 5.8)$ s (FWHM). Since our frame rate was only 0.5 fps, the flashes were only visible for a few frames. Nevertheless it is unlikely that flashes were missed because they were too short. The camera recording the fluorescence images maintained near-constant exposure, so light emitted by flashes will be captured. However, some experiments were initially missed due to their poor signal-to-noise ratio (see Figure 3.23). It is possible that certain experiments contain undetected flashes with a even worse signal.

The short duration of the flashes suggests that the process of phagocytic uptake does not happen within minutes but within seconds. This is in line with literature. For example, Richards et al. characterized phagocytosis by human neutrophils using micropipette aspiration^[214]. They measured engulfment durations of (37 ± 8) s for 4.6 μm -sized particles, with larger 6.2 μm -sized, beads taking (90 ± 12) s to be taken up. At a bead size of 2 μm , our value of $T_{\text{flash}} = (14.7 \pm 5.8)$ s seems compatible. Paul et al. measured an uptake time of (1.5 ± 0.9) min for 1.85 μm -sized silica particles and (3.2 ± 0.7) min for 2 μm -sized polystyrene particles on RAW 264.7 cells^[188]. This is significantly longer than the duration of the flashes observed in our experiments. However Paul's measurements suffered from a low temporal resolution, as image stacks were only taken every 30 – 60 s. It should be noted that it is not clear if the duration of the flash correlates with the duration of the physical uptake process. It is possible that the actin polymerization that is causing the flash is only happening during a specific part of the uptake process or, the other way around, that the actin structure may persist for some time after the phagosome is formed.

Overall, the flashes had a low signal-to-noise ratio. The actin recruitment ratio R , which was defined as the ratio of the fluorescence intensity in the bead's location to the intensity around it, reached an average value of 1.36, meaning that the flashes were on average only 36% brighter than the background. This is caused by the fact that the images were recorded using widefield microscopy, which results in images with a high background intensity due to out-of-focus fluorophores. Additionally, the LifeAct-GFP can also bind to globular actin, resulting in lower contrast compared to other stains such as phalloidin^[125].

3.4.3 Binding phase

Directly after attaching the beads to the cell, a binding phase with a decreasing blinking amplitude α could be measured. This decrease in α is most likely not caused by a change in the cell stiffness, which is measured by the creep compliance, but by an increase of the contact radius between the particle and the cell. As the particle binds to the cell, larger and larger regions of the cell have to be deformed, which results in a smaller displacement during the blinking experiments. Assuming the contact radius rises, following a sigmoidal function, from zero to $r_0 = 1 \mu\text{m}$ during the binding phase, a creep compliance of $j_0 = (13.3 \pm 0.5) \text{kPa}^{-1}$ was calculated, which is in the same order of magnitude as the number $j_0 = (20.0 \pm 0.6) \text{kPa}^{-1}$ reported by Berghoff et al. in 2021^[218].

However, the temporal parameters of the binding process reported by K. Berghoff et al. differed significantly from the values measured in this thesis^[218]. For example, the K. Berghoff measured $\tau_{0,c} = (39 \pm 5) \text{s}$, while the fit in Figure 3.19 reported a value of $\tau_{0,c} = 14.9_{-1.3}^{+1.4} \text{s}$.

The parameter $\tau_{0,c}$ represents the time after the attachment at which the contact radius reaches $0.5 \mu\text{m}$. This duration can be influenced strongly by how firmly the beads are attached to the cell by the experimentator. If the particles are attached to the bead with more force, the particle might already be bound to the cell more firmly at the beginning of the experiment. Most likely the beads were attached more firmly during the recent measurements, explaining the difference in $\tau_{0,c}$.

Figure 3.19 also reported the value $\tau_b = (28 \pm 3) \text{s}$ for the timescale of the binding process. This value is shorter than in previous experiments^[218] by a factor of two, since Berghoff measured $\tau_b = 13.1_{-1.5}^{+1.9} \text{s}$. It is unclear what caused this difference, as the speed of the binding process should not differ even if the beads were attached slightly more firmly. However, the experiments described in the article by Berghoff et. al were done many years ago. In the experiments performed for this thesis, a newer batch of particles was used, which might have slightly different properties even though the used beads were nominally identical. A.F.R.M. Ramsperger observed vast differences in the ζ -potential, the monomer content and the surface charge densities of supposedly identical beads^[96]. These properties have a direct impact on the interaction of those particles with cells. For example, particles with a lower ζ -potential showed an increased number of bead-cell interactions^[96]. It is not unlikely that small differences in the surface charge density can also speed up or slow down the cell-particle binding process.

The value for the creep compliance $j_0 = (13.3 \pm 0.5) (\text{kPa})^{-1}$ after the binding phase is a little higher than expected, as in previous experiments published in the Biophysical Journal, where cells showed a creep compliance of $2.8 - 9.5 (\text{kPa})^{-1}$ ^[218]. Only when treated with the actin-compromising drug CytoD the cells were reported to get softer and reach creep compliance values of up to $20 (\text{kPa})^{-1}$. These differences in j_0 are most likely a direct result of the improved calibration. Because previously the calibrations were carried out in glycerin, the optical forces on the beads might have been misjudged. Since then, a new calibration was done which removes this inaccuracy. However, the imprecise calibration used for the paper will only change the absolute values of the creep compliance and does not impair the impact of the paper.

The values of β after the attachment and before the uptake are in perfect agreement with the data published previously in the Biophysical Journal^[218], where it was established that β resides at values around $0.2 - 0.3$, with a slow decline around $-30 \cdot 10^{-3} \text{min}^{-1}$ to $-27 \cdot 10^{-3} \text{min}^{-1}$. This quick decline of β directly after the binding could not be found in

the newer data. It might be possible that this was an fitting artifact, or that it was caused by the missing feedback system, leading to a dropping optical force for later blinking events in the old data. However, we did find a slow decrease in β over longer timescales after the uptake, which will be discussed later. However, the overall value of the viscoelastic exponent is in line with observations of other research groups. For example, Laudadio et al. found the exponent for rat airway muscle cells to be around $0.2 - 0.3$ ^[273].

3.4.4 Actin oscillations

Actin oscillations are a known phenomenon^[274,275,276]. In previous blinking measurements, W. Groß reported a quasi-periodic actin remodeling on a timescale of about $30 - 40$ s^[132], superimposed on an oscillation with a much lower frequency. M. Kumar found similar periodicities in the actin signal, with characteristic times of (32 ± 17) s and (161 ± 61) s^[277]. It is speculated that these oscillations are fed by a positive feedback loop involving lipid-modifying enzymes which alter the properties of the cell membrane and assembly and disassembly of actin^[278]. As the signaling network controlling those actin oscillations and the one controlling phagocytosis partly overlap, it is likely that these oscillations might facilitate the phagocytic uptake. For example, the lipid-modifying enzyme PtdIns(4,5)P2 can also trigger actin polymerization by activating the N-WASP-Arp2/3 pathway^[88,279,280], directly influencing the actin polymerization in the phagocytic cup. Liebl and Griffiths^[281] also observed transient, but periodic bursts of actin-GFP 30 minutes after exposing multiple opsonized particles to a single macrophage. They describe a periodic oscillation of the actin-GFP intensity, which 2 minutes of actin assembly followed by 2 minutes of disassembly, which happens during the maturation of the phagosome. This implies that the bead had already been taken up by the cell at this point. This was also described by Poirier et al^[282], who observed that these flashes correlated with a mechanical deformation of the phagosome and suggested that these contractions may mechanically contribute to the enzymatic digestion of the phagocytic target.

In our measurements, some periodicity in the LifeAct-GFP signal could be found before and after the uptake, but nowhere as regular as in Liebl and Griffiths' research. This effect can be seen in Figure 3.16, where the absolute fluorescence intensities I_{circle} and I_{ring} fluctuate strongly, sometimes even exceeding the maximum intensity during the flash. However, the ratio $R = I_{\text{circle}}/I_{\text{ring}}$ only peaked once per experiment, suggesting that the LifeAct oscillations described are a phenomenon on a length scale larger than the actin flashes occurring during phagocytic uptake.

However, it can be speculated that fluctuations in the filamentous actin density induced by these oscillations could potentially trigger phagocytic uptake. In this case, the starting time of the phagocytic uptake process is somewhat random and with each actin wave there is a certain chance for the engulfment to be initiated. If this is true, the uptake times t_{flash} should follow a Poisson distribution. In fact, the average and the standard deviation for t_{flash} are identical, as expected for a Poisson distribution, underpinning the idea of the uptake process being initiated by chance. This means that the uptake probability per time unit is independent of the time the bead has already been attached to the cell.

3.4.5 Rheology around the moment of uptake

The rheological measurements provided two important values, the blinking amplitude α and the viscoelastic exponent β . As summarized in Table 3.1, the value of α settled in at $\alpha = 2.38 \text{ nm/pN}$ prior to the flash and then quadrupled to a value of 9.23 nm/pN after the flash. According to Equation 3.26, this change in α can originate from a changing creep compliance j_0 of the deformed material or a changing geometry, leading to more material being deformed. Regardless on what caused the changes in the blinking amplitude shortly after the flash, it is unlikely that they were caused directly by the formation of the phagocytic cup. According to the zipper model^[209], the phagocytic cup is thin, meaning it simply moves together with the bead without being deformed. Instead, all deformation is done to the surface of the cell, where the actin cortex provides most of the mechanical stability.

Meanwhile, experiments without any visible flashes showed an average blinking amplitude of $\alpha = (5.7 \pm 0.8) \text{ nm/pN}$, which is higher than for experiments in which phagocytosis happened later. The other way around, this implies that a strong bond of the bead to the cell, manifesting in a low value of α , might be required for phagocytosis to engage. This is plausible, as such a strong bond is facilitated by opsonins such as IgG, which at the same time bind to Fc γ -receptors, triggering phagocytosis^[74].

A short decrease in the value for the blinking amplitude α to a value of only 2.1 nm/pN was observed in the time window 2 – 14 s after the flash. It is plausible that in the moment the phagocytic cup is formed, more actin polymerized in the vicinity of the bead, which could have thickened or strengthened the actin cortex below the bead, leading to an decreasing blinking amplitude. However, the observed drop was not very pronounced. Adding to the complexity, the reliability of the fits is reduced during this periods because of the small blinking amplitude. For example, in Fig. 3.20, Δx dropped to 60 nm, and in some cases the value was even lower, causing the blinking to be less noticeable against the background noise. Shortly after this decrease, $t_{0,\alpha} = 16.0_{-0.4}^{+0.8} \text{ s}$ after the flash, the blinking amplitude rose again and reached a value of 9.23 nm/pN , rising quickly with a time constant of $\tau_\alpha = 1.9_{-0.4}^{+0.6} \text{ s}$. This is close to the temporal resolution, as data was recorded only once very two seconds and 4 s-wide bins were used during evaluation. This means that this increase could have been even faster in reality. The combination of a momentary dip in the blinking amplitude followed by a rapid increase during the act of phagocytosis is an exciting breakthrough that hasn't been documented until now. This was made possible by the unique combination of imaging the actin dynamics and simultaneously measuring the viscoelastic properties of the cell.

The blinking amplitude is largely influenced by how firmly the bead is connected to the actin cortex. The strength of this connection was represented through the contact radius $r(t)$. The increase of α by a factor of four can be explained by a decrease in the contact radius by the same factor from $r_0 = 1 \mu\text{m}$ before to $r_1 = 0.258 \mu\text{m}$ after the uptake. This decrease in r_0 represents the bead detaching from the actin cortex after being engulfed. However, this approximation disregards the fact that the actin cortex is not the only part of the cell being deformed after the phagosome has formed completely. Instead, a large part of the deformation now acts on the inside of the cell, pushing the bead through the cytoplasm. Still, the decoupling from the actin cortex, which is characterized by the creep compliance $j_0 = (7.46 \pm 0.14) \text{ kPa}^{-1}$ during the whole engulfment, can explain a majority of the increased blinking amplitude. This line of reasoning aligns with other measurements. For example, Van Citters et al. did atomic force microscopy and magnetic twisting cytometry on epithelial

cells^[283] and concluded that while F-actin plays a significant role in the mechanics of the cortical regions, its disruption has no effect on the rheology deep inside the cells.

Our value for the creep compliance j_0 of the cell's actin cortex during phagocytosis is lower than the value for j_0 measured during the binding process, which was $j_0 = (13.3 \pm 0.5) \text{ kPa}^{-1}$. This is expected, as the actin cortex might actually be reinforced by the increasing amount of filamentous actin around the bead. To match our values for j_0 with literature data, it is helpful to compare our values of j_0 with values obtained when modeling cells based on purely elastic behavior. In this case, β would be zero, and the value of j_0 is the inverse shear modulus G of the cell. Because for incompressible fluids, the shear modulus is three times the Young's modulus E , the value of E should roughly correspond to $E = 3/j_0$. We measured creep compliances in the range $j_0 = 7.46 - 13.3 \text{ nm/pN}$, which using this approximation corresponds to Young's moduli in the range of $0.23 - 0.40 \text{ kPa}$.

The Young's modulus of macrophages was measured by Leporatti et al., which reported values of $E = 0.29 - 0.83 \text{ kPa}$, with the smaller value corresponding to macrophages with were activated by adding lipopolysaccharides to the medium. These stiffness values match the values measured in our experiments.

At the same time, the value of viscoelastic exponent β rose from $\beta_0 = 0.271$ before the flash to $\beta_1 = 0.401$ after the flash. This means that the environment inside the cell is significantly less elastic and more viscous than the outer shell and the membrane of the cell. This makes sense, as the crowded environment of the cytoplasm is very viscous.

Interestingly, both the rise of α and β happen at the same time, both occurring around 15 s after the actin flash. This, together with the short decrease in α around 2 - 14 s after the flash, indicates that the flash happens slightly before the bead is separated from the actin cortex. As the process of phagocytosis is known to happen rather quickly, with durations of roughly one minute^[214,188], it is very likely that the observed actin flashes directly correspond to the phagocytic cup formation. Richards and Endres^[214] observed that while the complete engulfment takes around 30 s for beads of a similar size, it happens in two stages. According to them, the first, slow stage takes around three quarters of the time, however, only half of the bead is engulfed in this time. After that, the uptake accelerates and the second half of the bead is taken up in the remaining few seconds. This uptake mechanic closely matches the observations made in this thesis. It may very well be that the phase of low α happening 2 - 14 s after the flash corresponds to the first, slow phase of the uptake while the following sudden increase in α is caused by quick engulfment and phagosome scission during the second phase of the uptake process. It is plausible that this sharp increase in the beads motility marks the moment in which the phagosome is cut off the cell's plasma membrane, catalyzed by the enzyme dynamin^[92,284].

The speed of the increase in β could only be determined with poor precision, resulting in a time constant of $\tau_\beta = 9.1_{-0.5}^{+5.1} \text{ s}$. This large uncertainty was caused by the fact that increase in β is more subtle compared to the relatively large scattering in the values reported by the individual fits. Because of the large uncertainty, it cannot be ruled out that the rise of β followed the same dynamic as the increase in α , which happened with a time constant of $\tau_\alpha = 1.9_{-0.4}^{+0.8} \text{ s}$. However, even within the confidence intervals, the value of τ_β is much larger. Since both the change in α and β were caused by the same process, their dynamics should be aligned. It could however be possible that the cytosol and other components around the newly formed phagosome need some time to accommodate, which may alter the value of β even after the uptake is already completed. However, to the knowledge of the author there currently is no evidence supporting this claim and it might as well be possible that the effect

can be attributed completely the larger uncertainty in the determination of τ_β .

It would be nice to measure time constants τ_α and τ_β for individual experiments and search for correlations between the duration of the flash and the speed of the increase in α or β . However, because the values of α and β did fluctuate strongly in individual experiments, only values averaged over multiple experiments, as shown in Fig. 3.21 were used for evaluation, hindering the search for such correlations.

Another interesting observation was that the value of the viscoelastic exponent began to drop again right after the phagocytic uptake was finished. The value decreased with a rate of -0.007 min^{-1} , beginning from a value of $\beta_1 = 0.401$ right after the uptake often dipping below 0.3 at the end of the experiment. This effect could be caused by the phagosomal maturation^[10]. During phagosomal maturation, the phagosome is often transported from the cell periphery to the perinuclear region^[93]. It is plausible that the cell behaves more elastic and less viscous in this region, reducing the value of β . Furthermore, the binding of molecular motors such as kinesin or dynein links the phagosome to microtubules, which by nature are more elastic than viscous.

3.4.6 Piezo stage overshoot

As described in chapter 3.3.3, the piezo stage had a tendency to move further than commanded. Specifically, in the x -direction, it overshoot by 25% beyond the anticipated distance, while in the y -direction, it surpassed the expected position by 7%.

We can only speculate about the cause of this behavior. The piezo stage is rated for a maximum temperature of 40°C . During measurements, the highest temperature used is 38.5°C . This is close to the limit of the rated temperature range. To reach this temperature, the air entering the heating chamber has to be hotter and can easily exceed a temperature of 40°C . It is possible that the excessive thermal cycling caused some damage to the piezo stage. Another possible error source rises from the fact that the piezo stage is only rated to move a mass below 500 g. This low rating suggests that the stage is susceptible to mechanical stress, which could arise when mishandling the stage during installation and removal. Since it is not known to the author when this abnormal behavior started, the stage might have been miscalibrated from the factory. To acquire more detailed information, it would be possible to measure the voltage-position curve of the individual piezo axis by using the PIMicroMove software provided by the manufacturer. This software allows to directly specify the voltages applied to the piezo crystals. This way, it might be possible to gather more information on the problem and possibly recalibrate the stage.

The piezostage also shows another error pattern: Occasionally, the internal feedback loop of the piezo stage got saturated way before the stage reached any limit of its rated motion range of $0 - 200 \mu\text{m}$ in all directions. The manual of the piezo stage specifies that the zero point of the piezostage can shift when used in environments outside of its calibration temperature of $21 - 24^\circ\text{C}$. When using the piezo stage outside this temperature window, or when the stage has to deal with a large static force, it is recommended to perform an auto-zero procedure. However, the manual states that the zero-point should not be shifted by more than $10 \mu\text{m}$, otherwise the stage can hit physical limits and suffer damage. This suggests that the expected zero-point shift should be much smaller than that, which means that this thermal drift cannot fully explain the severely reduced range of motion observed. It is plausible that this problem is related to an inadequate calibration, which could cause the stage to hit its physical limits much sooner than expected.

Luckily, the behavior of the stage seems to be very reproducible. This means that the stage can still be used for scientific applications, without recalibration. In this case, all relative movement distances should be divided by the overshoot factor for this axis before sending the instructions to the piezo stage. It is also possible to reduce the moved distance even further than required to make the feedback loop more stable. In fact, this was already implemented for the z -direction. This was not yet done for during the scope of this thesis. Fortunately, the piezo stage was only used for the repositioning the bead during the rheological measurements in chapter 3. In this application, the exact distance traveled by the piezo stage is not important as long as the feedback loop is stable enough to hold the position of the bead constant. Though the faulty calibration might reduce the stability of the feedback loop, it functioned satisfactory during the experiments. As of the publication of this thesis, D. Gitschier has made promising efforts to recalibrate the piezo stage.

3.4.7 Thoughts on future methodical improvements

While the blinking optical tweezers method worked well, there are some optimizations to be made to the setup and the measurement process, which could further improve the capabilities of the method.

Initially, challenges arose with the image timing, as the pixelfly camera captured images approximately 240 ms too early. In this moment, the deformation of the cell was not fully relaxed yet, which caused a systematic error in the feedback system. Fixing this could improve the feedback algorithm's precision and stability, ensuring that each blinking event starts at the same position relative to the trap and making the optical force more consistent. Also, the acquisition software sometimes changed the rate in which the blinking events were repeated during acquisition. This happened due to a special behavior of the image timing using the CCTLLive software. This is less critical, because the software also saved timestamps for all images, which made it possible to identify the exact location of each blinking event. However, evaluation would have been much easier if all events were spaced uniformly.

Secondly, the SLM switching time of $\tau_{\text{SLM}} = 10$ ms is rather slow. This means that for a short time after each switching event the bead's velocity was limited by the slow change in the optical force, which hid any dynamics faster than a few milliseconds. We showed that it is viable to include the SLM's reaction time in the fit model, which allowed us to fit the viscoelastic model regardless of the slow reaction time. However, the system's response to a faster switch in the laser power would contain more information on the high-frequency response of the system, which would allow us to better validate our viscoelastic model. Additionally, the SLM could not be used to switch off the beam, but only to redirect it so that it misses the bead. The intense laser beam still passes the sample, even in the phases in which the SLM is powered off. It would be much better to use the AOM, which is part of the NoiseEater stabilization loop, to switch the laser power. The AOM would be able to completely switch on or off the trap in a matter of microseconds. The challenge is to include the AOM into the existing acquisition software. The easiest way to achieve this is to connect a programmable voltage supply to the setpoint modulation input of the AOM. This voltage supply should be controllable directly from MATLAB. This way, it is possible to integrate its functionality into the `HolographicOpticalTraps.m` class, which at the moment is responsible for supplying the SLM with the correct holograms and switching its power on and off.

In theory, if the blinking optical tweezers were implemented using an AOM for the power

switching and a quadrant photodiode (QPD) for measuring the bead's position, high-frequency blinking would be possible. An QPD can measure the bead position at a rate of tens of kHz^[285] or even MHz^[286]. Because of this and the fast switching time of the AOM, the laser could be switched on and off at a high rate, for example 10 s^{-1} , and it would be possible to measure detailed rheological data with a high temporal resolution. This should make it possible to measure the rheological properties during the short process of phagocytosis with more detail. For example, the rise of the blinking amplitude α , which happens with a time constant of only $\tau_\alpha = 1.9\text{ s}$ could be resolved better, which is barely possible with the current frame rate of only 0.5 s^{-1} . It might also be possible to better resolve the moment in which the phagosome passes the actin cortex, which causes the short drop in the value of α in the moment shortly after the flash.

In this case, a high laser power of multiple Watts might be necessary to create measurable bead displacements within the short laser pulses. Even then, phototoxicity is significantly reduced by using the AOM, because the trapping laser no longer passes the sample during inactive periods. However, when choosing the right laser power, it should be taken into account that at a higher repetition rate the cell has less time to relax between blinking events, which could challenge the assumption that the optical force from previous blinking events does not influence the strain during the current blinking event. Implementing the position feedback system would be possible by pausing the blinking every few seconds to accurately measure the bead's position. While it is not feasible to implement a QPD to our holographic optical tweezers setup, as measuring the beads' position with a QPD does not work when using the holographic functionality of the setup, using the AOM to switch the laser power provides many benefits. The higher temporal resolution can also mitigate any concerns regarding the hypothesis that biological processes might alter the rheological properties of the cell within a single measurement, as raised by M. Tassieri^[239]. The AOM might also be very useful when calibrating optical traps in water with the step-response method, as it avoids having to compensate for the influence of the slowly rising laser power on a bead's velocity into the trap caused by the switching time of the SLM.

Measuring the viscoelasticity of cells using pulsed forces can also be done with magnetic tweezers. This method is not new, as Bausch et. al already described magnetic bead microrheology in 1999^[243]. The main advantage here is that since the magnetic force is active over a longer distance, no positional feedback system is necessary, which reduces the complexity of the acquisition immensely. When using magnetic tweezers, the power to the magnet can be cycled with a fixed frequency throughout the whole experiment without any disruptions by the moving stage. Also, multiplexing is possible, as the magnetic force can act on multiple beads at once. Disadvantages are the fact that the attachment process cannot be controlled directly, that the force can only be applied in one direction, and that the coil's inductive properties mean that the magnetic field will take a certain time to be switched on or off. At typical coil values ($L \approx 10\text{ mH}$, $R \approx 3\ \Omega$), the time constant is a few milliseconds. This is in the same order of magnitude as when using a SLM, but much slower than possible with an AOM.

One aspect to consider is that the optical force always pointed in the $-x$ -direction, which on average created a net force on the particle. It is unclear how this force influenced the process of phagocytosis. However, it is possible to configure the piezo stage to alternate between $-x$ and $+x$ directions relative to the trap when setting the bead up. By doing so the net forces would, on average, cancel each other out, which might reduce the impact on the force on physiological processes. Another suboptimal property of the used optical setup is the

long path length the laser travels until hitting the sample. The distance from the beam has to travel from exiting the fiber to the SLM has a length of approximately 4.1 m, the distance from the SLM to the microscope objective's backplane is adjusted to exactly 2.5 m. Because of that, thermal drifts and or other disturbances such as vibrations have a stronger impact on the alignment of the laser than if the beam path was shorter. However, because there are many required optical components in the beam path, shortening it is challenging. An old measurement of the laser's pointing stability done by K. Berghoff revealed fluctuations around $1.1 \cdot 10^{-5}$ rad. This means that when the laser hits the SLM, it's center already fluctuates by $4.1 \text{ m} \cdot 1.1 \cdot 10^{-5} \text{ rad} = 45 \text{ nm}$. According to Equation 2.10 and when using the 60 \times -objective, a change in the beam exit angle from the SLM by $1.1 \cdot 10^{-5}$ rad corresponds to a change in the trap position of $2.253 \text{ mm} \cdot 1.1 \cdot 10^{-5} \text{ rad} = 25 \text{ nm}$. Adding both of these numbers, the long-term stability of the laser is limited to around 70 nm. Fortunately, this is not a huge problem, as most blinking events were done at bead positions close to the force maximum at $x = 0.83 \mu\text{m}$. Around this position the optical force is pretty constant, and moving the trap by a few tens of nanometers will not alter the optical force significantly.

3.5 Conclusion

All in all, the measurement in this chapter provided a strong demonstration of what is possible using the method of blinking optical tweezers. Together with a big pool of data, we were able to measure the phagocytic efficiency of the used opsonized beads by directly observing each phagocytic event. We established that after touching the cell for the first time, the target binds to the cell within the first two minutes. This is then followed by a passive phase in which the bead stays attached to the surface of the cell, but is not yet engulfed. The engulfment itself happens quickly within roughly one minute and can happen anywhere from zero to more than 30 minutes after the initial bead-cell contact. However, more than half the uptakes happen in the first 10 minutes after the attachment. After the uptake, the bead experiences a more viscous, less elastic environment.

During all those steps, rheological data, information on the actin density, the drift velocity caused by the cell and data on the bead's overall transport velocity were gathered. This provides insights in to the steps of phagocytosis with a very high temporal resolution, which are have never been seen before. A graphical summary of all numerical results is provided in Figure 3.24 We showed that the changes in the observed blinking amplitude α can be explained mostly by the changing contact geometry, which is modeled by the contact radius $r(t)$. Meanwhile the creep compliance j_0 , modeling the viscoelastic stiffness of the actin cortex, only changed very little, dropping from $(13.3 \pm 0.5) \text{ kPa}^{-1}$ at binding to $(7.46 \pm 0.14) \text{ kPa}^{-1}$ at the moment of phagocytosis.

During the uptake, we observed an approximately 10s long period of reduced blinking amplitude, indicated as a dashed line in the Figure. The transient drop in the blinking amplitude α might caused by an stronger bond to the actin cortex in the moment the phagosome passes the actin cortex. This binding could be modeled by a temporal increase in $r(t)$, as indicated by the dashed lines in Figure 3.24.

The new method of blinking optical tweezers also provides much potential for future research. Apart from methodical improvements, as discussed above, it would be possible to investigate more advanced biological questions. For example, beads could be coated with fibronectin to investigate the influence of integrins during phagocytosis. Additionally to observing actin, other stains could be used to observe the localization of other proteins during phagocytosis, such as IgG, Fc γ R, or other signaling molecules involved in phagocytosis. This will be incredibly useful to study the role of those proteins for the process of phagocytosis. Measurements could be done on cells treated with different drugs inhibiting certain parts of the signaling. All in all, blinking optical tweezers are an incredibly powerful tool. Together with the synchronous imaging of the actin density in the cell, the method provides a plethora of data all from a single experiment.

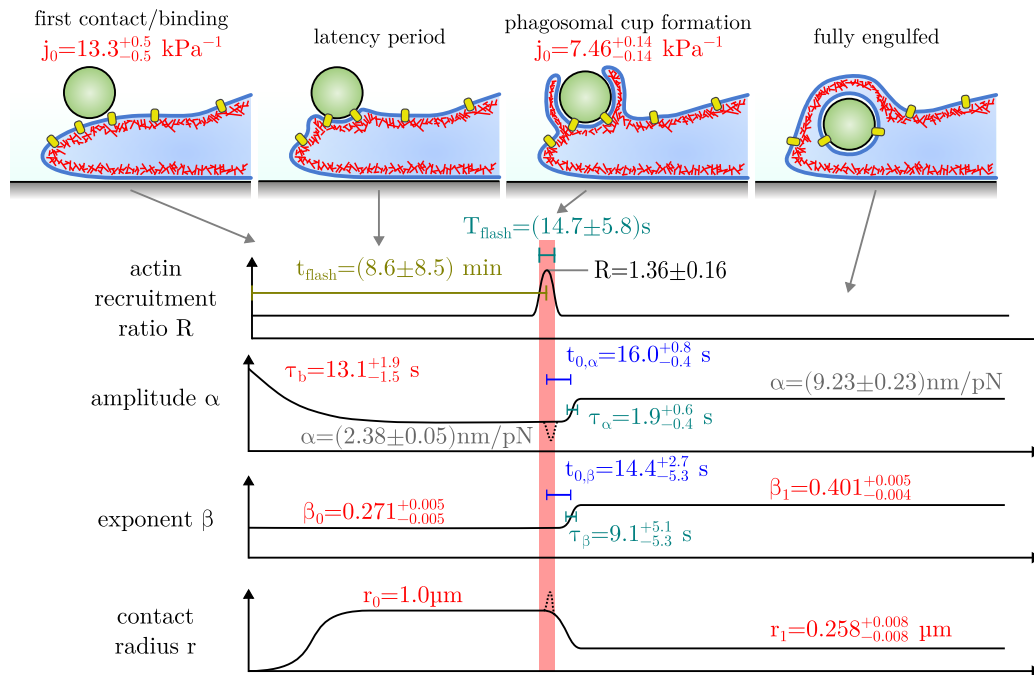


Figure 3.24: Graphical summary of the numerical results of the blinking experiments. The three parameters R , α and β were measured directly. To model the changing contact geometry of the bead, we modeled the development of the contact radius r . This explains most of the dynamics of α . The creep compliance of the cell was only measured by fitting a sigmoidal function to the experimental data of α at two times, once during the binding process and another time during the sudden increase of α right after the flash. The dashed lines in the plots for α and r indicate the transient decrease of α shortly after the maximum of the actin flashes, which can be explained by the phagosome passing through the actin cortex.

4 Synopsis

In the pursuit of understanding the intricate dance of cellular processes governing phagocytosis, new techniques were introduced in this thesis, shedding light on the initiation of phagocytosis as well as the process of the phagocytic engulfment itself and the mechanical aspects involved in this fundamental biological phenomenon.

While chapter 2 focused on the initiation of phagocytosis and the signaling involved, chapter 3 complemented this by shedding light on the mechanical side of phagocytosis and on the role of actin dynamics. In chapter 2, blinking holographic optical tweezers were employed to investigate the resolution limit of signaling cascades controlling phagocytosis. Two precisely attached beads on the cell's surface served as probes to measure the propagation of a single stimulus, thus revealing to which extend the initial phagocytic trigger spreads inside the cell. This method offers an unprecedented glimpse into the complex dynamics of signal transmission during phagocytosis. Furthermore, blinking optical tweezers were introduced in chapter 3 and used to investigate the mechanical aspects of phagocytosis. By measuring the viscoelastic response of the cell and the dynamics from the first contact of the target to its engulfment, this technique unveiled the rheological parameters of the cell before, during and after the phagocytic cup formation. This provided novel results on the dynamics of the phagocytic uptake. Together, these revelations provide an excellent overview on when and how the individual steps involved in phagocytosis are carried out and on the mechanics of the whole process.

The contributions of this thesis extend far beyond the immediate findings. The methods and insights presented in both chapters offer a versatile toolkit for future research endeavors. New insights gained from these experiments could include understanding how phagocytosis is influenced by mechanical properties of the target or the environment of the cell.

5 Appendix

On the double page, some supplementary information is provided. Table 5.1 provides a list of probabilities for different uptake scenarios as predicted by the phagocytic signaling model introduced in section 2.3.3. All probabilities in this list were calculated using the fit parameters $\delta = 0.53 \mu\text{m}$, $\alpha = 0.68$ and $\Delta = 0.3 \mu\text{m}$ as reported in Equation 2.27. The data in this table is consistent with the plot in Figure 2.24B, where the combined probability for uptake into two separate phagosomes and the uptake of only a single particle is plotted as a function of attachment distance for different bead sizes.

Figure 5.1 is similar to Figure 3.21, but presented for all 54 experiments without an observable actin flash at the bead location. As seen in Figure 5.1, except for the decrease of α during the binding process, the values of α and β did not significantly change during those experiments. The medium fit parameters observed during the experiments without flashes were $\alpha = 3.1 \text{ nm/pN}$ and $\beta = 0.28$, which are very similar to the fit parameters prior to the uptake in experiments with observed flashes, however the value of α is slightly larger than observed prior to the flashes. At a contact radius of $1 \mu\text{m}$, this corresponds to a creep compliance of $9.8 (\text{kPa})^{-1}$ (see Equation 3.29).

d (μm)	0.5 μm beads				1 μm beads				2 μm beads				3 μm beads				4 μm beads				5 μm beads				10 μm beads							
	Two	Join	No	Sing	Two	Join	No	Sing	Two	Join	No	Sing	Two	Join	No	Sing	Two	Join	No	Sing	Two	Join	No	Sing	Two	Join	No	Sing	Two	Join	No	Sing
1.0	16.0	30.0	10.4	43.7	14.7	57.6	2.5	25.2																								
1.2	25.3	20.6	10.4	43.7	26.1	44.4	2.6	26.8																								
1.4	33.2	12.9	10.3	43.6	38.8	31.5	2.6	27.2	9.2	81.3	0.4	9.1																				
1.6	38.5	7.4	10.3	43.7	49.4	20.7	2.6	27.2	17.9	70.2	0.4	11.5																				
1.8	42.0	4.0	10.4	43.6	57.7	12.6	2.6	27.1	30.8	57.0	0.4	11.8																				
2.0	44.0	2.1	10.3	43.7	63.0	7.2	2.6	27.2	47.0	40.8	0.4	11.8																				
2.2	45.0	1.0	10.4	43.7	66.4	3.8	2.6	27.1	60.5	27.3	0.4	11.8	17.1	79.1	0.0	3.7																
2.4	45.4	0.5	10.4	43.7	68.3	2.0	2.6	27.1	71.1	16.8	0.4	11.7	29.5	66.1	0.1	4.3																
2.6	45.8	0.2	10.3	43.7	69.3	1.0	2.6	27.2	78.2	9.7	0.4	11.8	46.5	49.0	0.1	4.5	14.1	84.6	0.0	1.3												
2.8	45.8	0.1	10.4	43.7	69.8	0.4	2.6	27.2	82.6	5.2	0.4	11.8	62.0	33.5	0.1	4.5	25.2	73.3	1.5	1.6												
3.0	46.1	0.0	10.4	43.5	70.0	0.2	2.6	27.2	85.2	2.7	0.4	11.8	74.4	21.0	0.1	4.5	41.1	57.3	1.6	1.6												
3.2	45.9		10.4	43.7	70.2	0.1	2.6	27.1	86.5	1.3	0.4	11.8	83.1	12.3	0.1	4.5	58.4	40.0	1.6	1.6												
3.4	46.0		10.4	43.7	70.2	0.0	2.6	27.1	87.2	0.6	0.4	11.7	88.6	6.9	0.1	4.5	72.4	26.0	1.6	1.6	20.5	78.8	0.0	0.8								
3.6	46.0		10.3	43.7	70.2		2.6	27.2	87.5	0.3	0.4	11.8	91.9	3.6	0.1	4.5	82.8	15.6	1.6	1.6	34.4	64.8	0.8	0.8								
3.8	46.0		10.4	43.6	70.2		2.6	27.1	87.8	0.1	0.4	11.7	93.7	1.8	0.1	4.5	89.6	8.8	1.6	1.6	52.5	46.7	0.8	0.8								
4.0	46.0		10.4	43.6	70.3		2.6	27.1	87.8	0.1	0.4	11.8	94.6	0.8	0.1	4.5	93.7	4.7	1.6	1.6	67.8	31.4	0.8	0.8								
4.2	45.9		10.4	43.7	70.3		2.6	27.1	87.8	0.0	0.4	11.8	95.1	0.4	0.1	4.5	96.0	2.4	1.6	1.6	79.9	19.3	0.8	0.8								
4.4	45.9		10.4	43.7	70.1		2.6	27.2	87.8		0.4	11.8	95.3	0.2	0.1	4.5	97.2	1.1	1.6	1.6	88.0	11.2	0.8	0.8								
4.6	45.9		10.4	43.8	70.4		2.6	27.0	87.8		0.4	11.8	95.4	0.1	0.1	4.5	97.8	0.5	1.6	1.6	93.2	6.1	0.8	0.8								
4.8	45.9		10.4	43.7	70.2		2.6	27.2	87.8		0.4	11.8	95.4	0.0	0.1	4.5	98.1	0.2	1.6	1.6	96.1	3.1	0.8	0.8								
5.0	45.9		10.4	43.7	70.3		2.6	27.1	87.9		0.4	11.7	95.4	0.1	0.1	4.5	98.3	0.1	1.6	1.6	97.6	1.6	0.8	0.8								
5.2	46.0		10.4	43.6	70.3		2.6	27.1	87.9		0.4	11.7	95.4	0.1	0.1	4.5	98.3	0.0	1.6	1.6	98.5	0.7	0.8	0.8								
5.4	46.1		10.3	43.6	70.3		2.6	27.1	87.9		0.4	11.8	95.5	0.1	0.1	4.5	98.4	0.0	1.6	1.6	98.9	0.3	0.8	0.8								
5.6	45.8		10.4	43.8	70.2		2.6	27.2	87.9		0.4	11.7	95.5	0.1	0.1	4.5	98.4	0.0	1.6	1.6	99.1	0.1	0.8	0.8								
5.8	45.9		10.4	43.7	70.3		2.6	27.1	87.8		0.4	11.8	95.4	0.1	0.1	4.5	98.4	0.0	1.6	1.6	99.1	0.1	0.8	0.8								
6.0	46.0		10.4	43.7	70.3		2.6	27.1	87.8		0.4	11.8	95.4	0.1	0.1	4.5	98.4	0.0	1.6	1.6	99.1	0.1	0.8	0.8								
6.2	46.0		10.4	43.6	70.3		2.6	27.1	87.9		0.4	11.8	95.4	0.1	0.1	4.5	98.4	0.0	1.6	1.6	99.2	0.0	0.8	0.8								
6.4	45.9		10.4	43.7	70.3		2.6	27.1	87.9		0.4	11.7	95.4	0.1	0.1	4.5	98.4	0.0	1.6	1.6	99.2	0.0	0.8	0.8								
6.6	46.0		10.4	43.6	70.3		2.6	27.1	87.8		0.4	11.8	95.5	0.0	0.0	4.5	98.4	0.0	1.6	1.6	99.2	0.0	0.8	0.8								
6.8	45.9		10.4	43.7	70.3		2.6	27.1	87.8		0.4	11.8	95.4	0.1	0.1	4.5	98.4	0.0	1.6	1.6	99.2	0.0	0.8	0.8								
7.0	46.0		10.4	43.6	70.3		2.6	27.0	87.8		0.4	11.8	95.5	0.1	0.1	4.5	98.4	0.0	1.6	1.6	99.2	0.0	0.8	0.8								
7.2	46.0		10.4	43.6	70.3		2.6	27.1	87.9		0.4	11.7	95.4	0.1	0.1	4.5	98.4	0.0	1.6	1.6	99.2	0.0	0.8	0.8								
7.4	45.9		10.4	43.7	70.3		2.6	27.1	87.8		0.4	11.8	95.5	0.1	0.1	4.5	98.4	0.0	1.6	1.6	99.2	0.0	0.8	0.8								
7.6	46.1		10.4	43.6	70.3		2.6	27.1	87.8		0.4	11.8	95.5	0.1	0.1	4.5	98.4	0.0	1.6	1.6	99.2	0.0	0.8	0.8								
7.8	45.9		10.4	43.7	70.3		2.6	27.1	87.8		0.4	11.8	95.5	0.1	0.1	4.5	98.4	0.0	1.6	1.6	99.2	0.0	0.8	0.8								
8.0	45.9		10.4	43.7	70.2		2.6	27.2	87.8		0.4	11.8	95.5	0.1	0.1	4.5	98.4	0.0	1.6	1.6	99.2	0.0	0.8	0.8								

Table 5.1: Probabilities predicted by the separate uptake model for different bead sizes and distances. All probabilities are listed as percentages. For each combination of bead size and distance, there are four possible outcomes: Separate uptake into two phagosomes (Two), uptake into one joint phagosome (Join), no uptake at all (No) and the uptake of only a single bead (Sing). The distances are measured from bead center to center. The model uses the values $\delta = 0.53 \mu\text{m}$, $\alpha = 0.68$ and $\Delta = 0.3 \mu\text{m}$, as listed in Equation 2.27. For each scenario, 10^6 different receptor distributions were considered to calculate the probabilities. Values which are exactly zero were omitted for clarity. Note that the model also returns

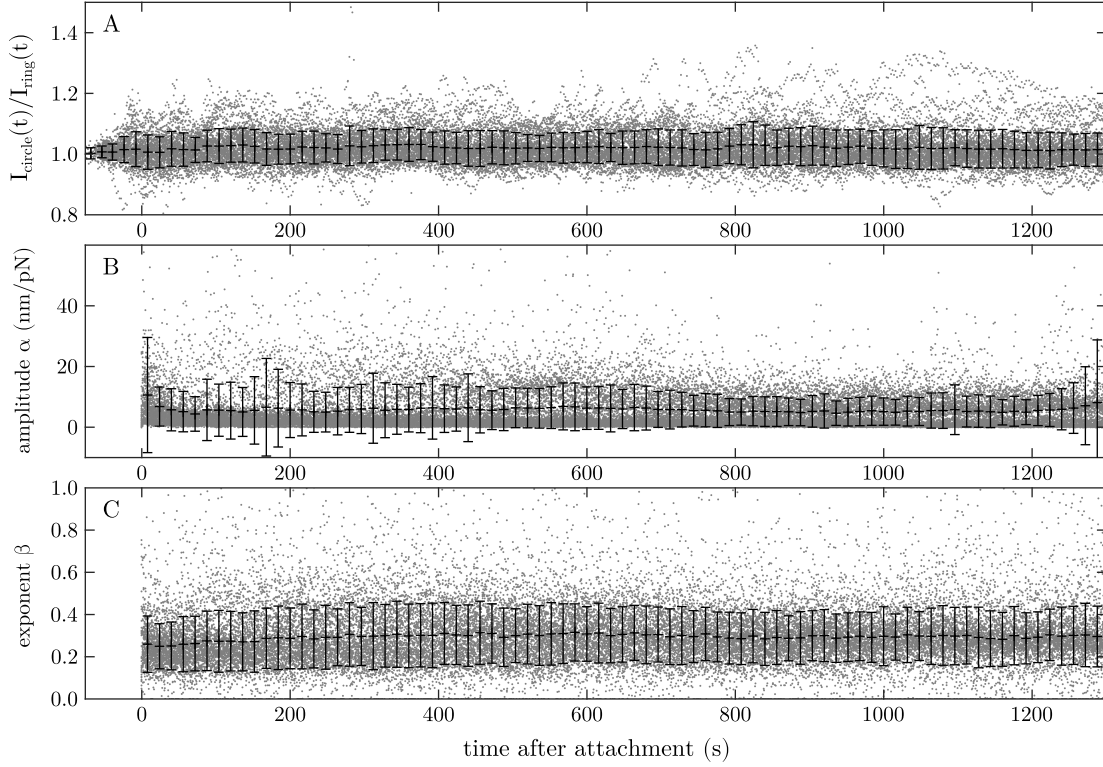


Figure 5.1: Evaluation of the actin recruitment ratio R (panel A) and the rheological parameters α and β (panels B and C) in all experiments without an observed actin flash. The data was plotted as a function of time after the first blinking event. While the gray dots represent individual blinking events, the data was also sorted into 16 s wide bins, represented as error bars. The size of the error bars matches the standard deviation in each bin. As visible, except for a significant decrease of α right after the attachment, all three parameters remained constant during the whole experiment. Averaging over the mean parameter values for each bin resulted in $\alpha = (5.7 \pm 0.8) \text{ nm/pN}$, $\beta = (0.294 \pm 0.014)$ and $R = (1.020 \pm 0.006)$. The uncertainties here denote the standard deviation of the bin averages. However, the individual fit values scattered across a wide range, with the median and the 15.85%- and 84.14%-quantiles stretching over a range of $\alpha = 3.1^{+7.5}_{-2.1} \text{ nm/pN}$, $\beta = 0.28^{+0.13}_{-0.10}$ and $R = 1.01^{+0.06}_{-0.04}$.

6 Bibliography

- [1] **R. Sender, S. Fuchs, R. Milo.** Revised Estimates for the Number of Human and Bacteria Cells in the Body. *PLoS Biol.*, 14(8):e1002533, 2016. doi:[10.1371/journal.pbio.1002533](https://doi.org/10.1371/journal.pbio.1002533).
- [2] **S. Arandjelovic, K. S. Ravichandran.** Phagocytosis of apoptotic cells in homeostasis. *Nat. Immunol.*, 16(9):907–917, 2015. doi:[10.1038/ni.3253](https://doi.org/10.1038/ni.3253).
- [3] **W. B. Herring.** Blood and the Hematopoietic System. In **R. Taylor**, editor, *Fam. Med.*, pages 1262–1296. Springer, New York, 1983. doi:[10.1007/978-1-4757-4002-8_79](https://doi.org/10.1007/978-1-4757-4002-8_79).
- [4] **T. R. L. Klei, S. M. Meinders, T. K. van den Berg, R. van Bruggen.** From the Cradle to the Grave: The Role of Macrophages in Erythropoiesis and Erythrophagocytosis. *Front. Immunol.*, 8:73, 2017. doi:[10.3389/fimmu.2017.00073](https://doi.org/10.3389/fimmu.2017.00073).
- [5] **R. Green, H. F. Noller.** Ribosomes and translation. *Annu. Rev. Biochem.*, 66:679–716, 1997. doi:[10.1146/annurev.biochem.66.1.679](https://doi.org/10.1146/annurev.biochem.66.1.679).
- [6] **P. Fagone, S. Jackowski.** Membrane phospholipid synthesis and endoplasmic reticulum function. *J. Lipid Res.*, 50(SUPPL.):S311–S316, 2009. doi:[10.1194/jlr.R800049-JLR200](https://doi.org/10.1194/jlr.R800049-JLR200).
- [7] **M. Lowe.** Structural organization of the Golgi apparatus. *Curr. Opin. Cell Biol.*, 23(1):85–93, 2011. doi:[10.1016/j.ceb.2010.10.004](https://doi.org/10.1016/j.ceb.2010.10.004).
- [8] **T. Stephan, C. Brüser, M. Deckers, A. M. Steyer, F. Balzarotti, M. Barbot, T. S. Behr, G. Heim, W. Hübner, P. Ilgen, F. Lange, D. Pacheu-Grau, J. K. Pape, S. Stoldt, T. Huser, S. W. Hell, W. Möbius, P. Rehling, D. Riedel, S. Jakobs.** MICOS assembly controls mitochondrial inner membrane remodeling and crista junction redistribution to mediate cristae formation. *EMBO J.*, 39(14):1–24, 2020. doi:[10.15252/emboj.2019104105](https://doi.org/10.15252/emboj.2019104105).
- [9] **P. T. Conduit, A. Wainman, J. W. Raff.** Centrosome function and assembly in animal cells. *Nat. Rev. Mol. Cell Biol.*, 16(10):611–624, 2015. doi:[10.1038/nrm4062](https://doi.org/10.1038/nrm4062).
- [10] **O. V. Viera, R. J. Botelho, S. Grinstein.** Phagosome maturation: aging gracefully. *Biochem. J.*, 366(3):689–704, 2002. doi:[10.1042/bj20020691](https://doi.org/10.1042/bj20020691).
- [11] **K. A. Bohnert, A. E. Johnson.** Branching Off: New Insight Into Lysosomes as Tubular Organelles. *Front. Cell Dev. Biol.*, 10(May):1–8, 2022. doi:[10.3389/fcell.2022.863922](https://doi.org/10.3389/fcell.2022.863922).
- [12] **V. Shepherd.** The Cytomatrix as a Cooperative System of Macromolecular and Water Networks. *Curr. Top. Dev. Biol.*, 75(06):171–223, 2006. doi:[10.1016/S0070-2153\(06\)75006-2](https://doi.org/10.1016/S0070-2153(06)75006-2).
- [13] **R. C. May, L. M. Machesky.** Phagocytosis and the actin cytoskeleton. *J. Cell Sci.*, 114(6):1061–1077, 2001. doi:[10.1242/jcs.114.6.1061](https://doi.org/10.1242/jcs.114.6.1061).
- [14] **M. S. Almén, K. J. Nordström, R. Fredriksson, H. B. Schiöth.** Mapping the human membrane proteome: a majority of the human membrane proteins can be classified according to function and evolutionary origin. *BMC Biol.*, 7(1):50, 2009. doi:[10.1186/1741-7007-7-50](https://doi.org/10.1186/1741-7007-7-50).
- [15] **M. Llanses Martinez, E. Rainero.** Membrane dynamics in cell migration. *Essays Biochem.*, 63(5):469–482, 2019. doi:[10.1042/EBC20190014](https://doi.org/10.1042/EBC20190014).

- [16] **K. Burridge, G. Nuckolls, C. Otey, F. Pavalko, K. Simon, C. Turner.** Actin-membrane interaction in focal adhesions. *Cell Differ. Dev.*, 32(3):337–342, 1990. doi:[10.1016/0922-3371\(90\)90048-2](https://doi.org/10.1016/0922-3371(90)90048-2).
- [17] **E. Armingol, A. Officer, O. Harismendy, N. E. Lewis.** Deciphering cell-cell interactions and communication from gene expression. *Nat. Rev. Genet.*, 22, 2021. doi:[10.1038/s41576-020-00292-x](https://doi.org/10.1038/s41576-020-00292-x).
- [18] **K. Keren.** Cell motility: The integrating role of the plasma membrane. *Eur. Biophys. J.*, 40(9):1013–1027, 2011. doi:[10.1007/s00249-011-0741-0](https://doi.org/10.1007/s00249-011-0741-0).
- [19] **R. S. Gracià, N. Bezlyepkina, R. L. Knorr, R. Lipowsky, R. Dimova.** Effect of cholesterol on the rigidity of saturated and unsaturated membranes: Fluctuation and electrodeformation analysis of giant vesicles. *Soft Matter*, 6(7):1472–1482, 2010. doi:[10.1039/b920629a](https://doi.org/10.1039/b920629a).
- [20] **G. B. Nash, W. B. Gratzer.** Structural determinants of the rigidity of the red cell membrane. *Biorheology*, 30(5-6):397–407, 1993. doi:[10.3233/BIR-1993-305-611](https://doi.org/10.3233/BIR-1993-305-611).
- [21] **G. Meacci, H. Wolfenson, S. Liu, M. R. Stachowiak, T. Iskratsch, A. Mathur, S. Ghassemi, N. Gauthier, E. Tabdanov, J. Lohner, A. Gondarenko, A. C. Chander, P. Roca-Cusachs, B. O’Shaughnessy, J. Hone, M. P. Sheetz.** α -Actinin links extracellular matrix rigidity-sensing contractile units with periodic cell-edge retractions. *Mol. Biol. Cell*, 27(22):3471–3479, 2016. doi:[10.1091/mbc.E16-02-0107](https://doi.org/10.1091/mbc.E16-02-0107).
- [22] **M. Edidin.** Lipids on the frontier: a century of cell-membrane bilayers. *Nat. Rev. Mol. Cell Biol.*, 4(5):414–418, 2003. doi:[10.1038/nrm1102](https://doi.org/10.1038/nrm1102).
- [23] **E. Gorter, F. Grendel.** On bimolecular layers of lipoids on the chromocytes of the blood. *J. Exp. Med.*, 41(4):439–444, 1925. doi:[10.1084/jem.41.4.439](https://doi.org/10.1084/jem.41.4.439).
- [24] **J. F. Danielli, H. Davson.** A contribution to the theory of permeability of thin films. *J. Cell. Comp. Physiol.*, 5(4):495–508, 1935. doi:[10.1002/jcp.1030050409](https://doi.org/10.1002/jcp.1030050409).
- [25] **S. J. Singer, G. L. Nicolson.** The Fluid Mosaic Model of the Structure of Cell Membranes. *Science*, 175(4023):720–731, 1972. doi:[10.1126/science.175.4023.720](https://doi.org/10.1126/science.175.4023.720).
- [26] **G. L. Nicolson.** The Fluid - Mosaic Model of Membrane Structure: Still relevant to understanding the structure, function and dynamics of biological membranes after more than 40 years. *Biochim. Biophys. Acta - Biomembr.*, 1838(6):1451–1466, 2014. doi:[10.1016/j.bbamem.2013.10.019](https://doi.org/10.1016/j.bbamem.2013.10.019).
- [27] **K. Simons, E. Ikonen.** Functional rafts in cell membranes. *Nature*, 387(6633):569–572, 1997. doi:[10.1038/42408](https://doi.org/10.1038/42408).
- [28] **D. A. Brown, E. London.** Structure and origin of ordered lipid domains in biological membranes. *J. Membr. Biol.*, 164(2):103–114, 1998. doi:[10.1007/s002329900397](https://doi.org/10.1007/s002329900397).
- [29] **S. Thomas, A. Preda-Pais, S. Casares, T.-D. Brumeanu.** Analysis of lipid rafts in T cells. *Mol. Immunol.*, 41(4):399–409, 2004. doi:[10.1016/j.molimm.2004.03.022](https://doi.org/10.1016/j.molimm.2004.03.022).
- [30] **T. T. Mills, S. Tristram-Nagle, F. A. Heberle, N. F. Morales, J. Zhao, J. Wu, G. E. Toombes, J. F. Nagle, G. W. Feigenson.** Liquid-liquid domains in bilayers detected by wide angle x-ray scattering. *Biophys. J.*, 95(2):682–690, 2008. doi:[10.1529/biophysj.107.127910](https://doi.org/10.1529/biophysj.107.127910).
- [31] **K. Simons, D. Toomre.** Lipid rafts and signal transduction. *Nat. Rev. Mol. Cell Biol.*, 1(1): 31–39, 2000. doi:[10.1038/35036052](https://doi.org/10.1038/35036052).

- [32] **J. B. Helms, C. Zurzolo.** Lipids as targeting signals: Lipid rafts and intracellular trafficking. *Traffic*, 5(4):247–254, 2004. doi:[10.1111/j.1600-0854.2004.0181.x](https://doi.org/10.1111/j.1600-0854.2004.0181.x).
- [33] **I. Levental, K. R. Levental, F. A. Heberle.** Lipid Rafts: Controversies Resolved, Mysteries Remain. *Trends Cell Biol.*, 30(5):341–353, 2020. doi:[10.1016/j.tcb.2020.01.009](https://doi.org/10.1016/j.tcb.2020.01.009).
- [34] **S. Munro.** Lipid Rafts. *Cell*, 115(4):377–388, 2003. doi:[10.1016/s0092-8674\(03\)00882-1](https://doi.org/10.1016/s0092-8674(03)00882-1).
- [35] **T. Fujiwara, K. Ritchie, H. Murakoshi, K. Jacobson, A. Kusumi.** Phospholipids undergo hop diffusion in compartmentalized cell membrane. *J. Cell Biol.*, 157(6):1071–1081, 2002. doi:[10.1083/jcb.200202050](https://doi.org/10.1083/jcb.200202050).
- [36] **D. Krapf.** Compartmentalization of the plasma membrane. *Curr. Opin. Cell Biol.*, 53:15–21, 2018. doi:[10.1016/j.ceb.2018.04.002](https://doi.org/10.1016/j.ceb.2018.04.002).
- [37] **A. Kusumi, C. Nakada, K. Ritchie, K. Murase, K. Suzuki, H. Murakoshi, R. S. Kasai, J. Kondo, T. Fujiwara.** Paradigm shift of the plasma membrane concept from the two-dimensional continuum fluid to the partitioned fluid: High-speed single-molecule tracking of membrane molecules. *Annu. Rev. Biophys. Biomol. Struct.*, 34(1):351–378, 2005. doi:[10.1146/annurev.biophys.34.040204.144637](https://doi.org/10.1146/annurev.biophys.34.040204.144637).
- [38] **S. M. Mylvaganam, S. Grinstein, S. A. Freeman.** Picket-fences in the plasma membrane: functions in immune cells and phagocytosis. *Semin. Immunopathol.*, 40(6):605–615, 2018. doi:[10.1007/s00281-018-0705-x](https://doi.org/10.1007/s00281-018-0705-x).
- [39] **A. Lambrechts, M. Van Troys, C. Ampe.** The actin cytoskeleton in normal and pathological cell motility. *Int. J. Biochem. Cell Biol.*, 36(10):1890–1909, 2004. doi:[10.1016/j.biocel.2004.01.024](https://doi.org/10.1016/j.biocel.2004.01.024).
- [40] **E. Grazi.** What is the diameter of the actin filament? *FEBS Lett.*, 405(3):249–252, 1997. doi:[10.1016/S0014-5793\(97\)00214-7](https://doi.org/10.1016/S0014-5793(97)00214-7).
- [41] **G. Salbreux, G. Charras, E. Paluch.** Actin cortex mechanics and cellular morphogenesis. *Trends Cell Biol.*, 22(10):536–545, 2012. doi:[10.1016/j.tcb.2012.07.001](https://doi.org/10.1016/j.tcb.2012.07.001).
- [42] **N. Morone, T. Fujiwara, K. Murase, R. S. Kasai, H. Ike, S. Yuasa, J. Usukura, A. Kusumi.** Three-dimensional reconstruction of the membrane skeleton at the plasma membrane interface by electron tomography. *J. Cell Biol.*, 174(6):851–862, 2006. doi:[10.1083/jcb.200606007](https://doi.org/10.1083/jcb.200606007).
- [43] **B. Wehrle-Haller.** Structure and function of focal adhesions. *Curr. Opin. Cell Biol.*, 24(1):116–124, 2012. doi:[10.1016/j.ceb.2011.11.001](https://doi.org/10.1016/j.ceb.2011.11.001).
- [44] **S. R. Cunha, P. J. Mohler.** Ankyrin protein networks in membrane formation and stabilization. *J. Cell. Mol. Med.*, 13(11-12):4364–4376, 2009. doi:[10.1111/j.1582-4934.2009.00943.x](https://doi.org/10.1111/j.1582-4934.2009.00943.x).
- [45] **E. S. Chhabra, H. N. Higgs.** The many faces of actin: matching assembly factors with cellular structures. *Nat. Cell Biol.*, 9(10):1110–1121, 2007. doi:[10.1038/ncb1007-1110](https://doi.org/10.1038/ncb1007-1110).
- [46] **M. F. Carrier.** Control of actin dynamics. *Curr. Opin. Cell Biol.*, 10(1):45–51, 1998. doi:[10.1016/S0955-0674\(98\)80085-9](https://doi.org/10.1016/S0955-0674(98)80085-9).
- [47] **T. D. Pollard.** Regulation of actin filament assembly by Arp2/3 complex and formins. *Annu. Rev. Biophys. Biomol. Struct.*, 36:451–477, 2007. doi:[10.1146/annurev.biophys.35.040405.101936](https://doi.org/10.1146/annurev.biophys.35.040405.101936).
- [48] **A. Y. Pollitt, R. H. Insall.** WASP and SCAR/WAVE proteins: the drivers of actin assembly. *J. Cell Sci.*, 122(15):2575–2578, 2009. doi:[10.1242/jcs.023879](https://doi.org/10.1242/jcs.023879).

- [49] **H. Miki, S. Suetsugu, T. Takenawa.** WAVE, a novel WASP-family protein involved in actin reorganization induced by Rac. *EMBO J.*, 17(23):6932–6941, 1998. doi:[10.1093/emboj/17.23.6932](https://doi.org/10.1093/emboj/17.23.6932).
- [50] **J. E. Bear, J. F. Rawls, C. L. Saxe.** SCAR, a WASP-related protein, isolated as a suppressor of receptor defects in late Dictyostelium development. *J. Cell Biol.*, 142(5):1325–1335, 1998. doi:[10.1083/jcb.142.5.1325](https://doi.org/10.1083/jcb.142.5.1325).
- [51] **Z. Chen, D. Borek, S. B. Padrick, T. S. Gomez, Z. Metlagel, A. M. Ismail, J. Umetani, D. D. Billadeau, Z. Otwinowski, M. K. Rosen.** Structure and control of the actin regulatory WAVE complex. *Nature*, 468(7323):533–538, 2010. doi:[10.1038/nature09623](https://doi.org/10.1038/nature09623).
- [52] **K. Rottner, T. E. Stradal, B. Chen.** WAVE regulatory complex. *Curr. Biol.*, 31(10):R512–R517, 2021. doi:[10.1016/j.cub.2021.01.086](https://doi.org/10.1016/j.cub.2021.01.086).
- [53] **E. D. Goley, M. D. Welch.** The ARP2/3 complex: An actin nucleator comes of age. *Nat. Rev. Mol. Cell Biol.*, 7(10):713–726, 2006. doi:[10.1038/nrm2026](https://doi.org/10.1038/nrm2026).
- [54] **B. L. Goode, M. J. Eck.** Mechanism and function of formins in the control of actin assembly. *Annu. Rev. Biochem.*, 76:593–627, 2007. doi:[10.1146/annurev.biochem.75.103004.142647](https://doi.org/10.1146/annurev.biochem.75.103004.142647).
- [55] **C. D. Nobes, A. Hall.** Rho, Rac, and Cdc42 GTPases regulate the assembly of multimolecular focal complexes associated with actin stress fibers, lamellipodia, and filopodia. *Cell*, 81(1):53–62, 1995. doi:[10.1016/0092-8674\(95\)90370-4](https://doi.org/10.1016/0092-8674(95)90370-4).
- [56] **R. Kozma, S. Ahmed, A. Best, L. Lim.** The Ras-Related Protein Cdc42Hs and Bradykinin Promote Formation of Peripheral Actin Microspikes and Filopodia in Swiss 3T3 Fibroblasts. *Mol. Cell. Biol.*, 15(4):1942–1952, 1995. doi:[10.1128/mcb.15.4.1942](https://doi.org/10.1128/mcb.15.4.1942).
- [57] **J. V. Small, T. Stradal, E. Vignal, K. Rottner.** The lamellipodium: Where motility begins. *Trends Cell Biol.*, 12(3):112–120, 2002. doi:[10.1016/S0962-8924\(01\)02237-1](https://doi.org/10.1016/S0962-8924(01)02237-1).
- [58] **M. Krause, A. Gautreau.** Steering cell migration: Lamellipodium dynamics and the regulation of directional persistence. *Nat. Rev. Mol. Cell Biol.*, 15(9):577–590, 2014. doi:[10.1038/nrm3861](https://doi.org/10.1038/nrm3861).
- [59] **P. K. Mattila, P. Lappalainen.** Filopodia: Molecular architecture and cellular functions. *Nat. Rev. Mol. Cell Biol.*, 9(6):446–454, 2008. doi:[10.1038/nrm2406](https://doi.org/10.1038/nrm2406).
- [60] **D. Vignjevic, S. I. Kojima, Y. Aratyn, O. Danciu, T. Svitkina, G. G. Borisy.** Role of fascin in filopodial protrusion. *J. Cell Biol.*, 174(6):863–875, 2006. doi:[10.1083/jcb.200603013](https://doi.org/10.1083/jcb.200603013).
- [61] **R. Michiels, N. Gensch, B. Erhard, A. Rohrbach.** Pulling, failing, and adaptive mechanotransduction of macrophage filopodia. *Biophys. J.*, 121(17):3224–3241, 2022. doi:[10.1016/j.bpj.2022.07.028](https://doi.org/10.1016/j.bpj.2022.07.028).
- [62] **H. Kress, E. H. Stelzer, D. Holzer, F. Buss, G. Griffiths, A. Rohrbach.** Filopodia act as phagocytic tentacles and pull with discrete steps and a load-dependent velocity. *Proc. Natl. Acad. Sci. U. S. A.*, 104(28):11633–11638, 2007. doi:[10.1073/pnas.0702449104](https://doi.org/10.1073/pnas.0702449104).
- [63] **S. R. Barger, N. C. Gauthier, M. Krendel.** Squeezing in a Meal: Myosin Functions in Phagocytosis. *Trends Cell Biol.*, 30(2):157–167, 2020. doi:[10.1016/j.tcb.2019.11.002](https://doi.org/10.1016/j.tcb.2019.11.002).
- [64] **S. M. Ferguson, P. De Camilli.** Dynamin, a membrane-remodelling GTPase. *Nat. Rev. Mol. Cell Biol.*, 13(2):75–88, 2012. doi:[10.1038/nrm3266](https://doi.org/10.1038/nrm3266).
- [65] **B. M. Gumbiner.** Cell Adhesion: The Molecular Basis of Tissue Architecture and Morphogenesis. *Cell*, 84(3):345–357, 1996. doi:[10.1016/S0092-8674\(00\)81279-9](https://doi.org/10.1016/S0092-8674(00)81279-9).
- [66] **R. O. Hynes.** Integrins. *Cell*, 110(6):673–687, 2002. doi:[10.1016/S0092-8674\(02\)00971-6](https://doi.org/10.1016/S0092-8674(02)00971-6).

- [67] **B. M. Gumbiner.** Regulation of cadherin-mediated adhesion in morphogenesis. *Nat. Rev. Mol. Cell Biol.*, 6(8):622–634, 2005. doi:[10.1038/nrm1699](https://doi.org/10.1038/nrm1699).
- [68] **H. Uchiyama, K. C. Anderson.** Cellular Adhesion Molecules. *Transfus. Med. Rev.*, 8(2): 84–95, 1994. doi:[10.1016/S0887-7963\(94\)70101-2](https://doi.org/10.1016/S0887-7963(94)70101-2).
- [69] **F. C. Chien, C. W. Kuo, Z. H. Yang, D. Y. Chueh, P. Chen.** Exploring the formation of focal adhesions on patterned surfaces using super-resolution imaging. *Small*, 7(20):2906–2913, 2011. doi:[10.1002/smll.201100753](https://doi.org/10.1002/smll.201100753).
- [70] **A. Johnson, B. Alberts.** *Molecular Biology of the Cell: A Problems Approach*. Taylor & Francis, 2014.
- [71] **V. Sourjik.** Receptor clustering and signal processing in E. coli chemotaxis. *Trends Microbiol.*, 12(12):569–576, 2004. doi:[10.1016/j.tim.2004.10.003](https://doi.org/10.1016/j.tim.2004.10.003).
- [72] **P. Bruhns.** Properties of mouse and human IgG receptors and their contribution to disease models. *Blood*, 119(24):5640–5649, 2012. doi:[10.1182/blood-2012-01-380121](https://doi.org/10.1182/blood-2012-01-380121).
- [73] **C. E. Hargreaves, M. J. Rose-Zerilli, L. R. Machado, C. Iriyama, E. J. Hollox, M. S. Cragg, J. C. Strefford.** Fc γ receptors: Genetic variation, function, and disease. *Immunol. Rev.*, 268(1):6–24, 2015. doi:[10.1111/imr.12341](https://doi.org/10.1111/imr.12341).
- [74] **J. A. Swanson, A. D. Hoppe.** The coordination of signaling during Fc receptor-mediated phagocytosis. *J. Leukoc. Biol.*, 76(6):1093–1103, 2004. doi:[10.1189/jlb.0804439](https://doi.org/10.1189/jlb.0804439).
- [75] **A. Aderem, D. M. Underhill.** Mechanisms of phagocytosis in macrophages. *Annu. Rev. Immunol.*, 17(1):593–623, 1999. doi:[10.1146/annurev.immunol.17.1.593](https://doi.org/10.1146/annurev.immunol.17.1.593).
- [76] **L. A. H. Allen, A. Aderem.** Mechanisms of phagocytosis. *Curr. Opin. Immunol.*, 8(1):36–40, 1996. doi:[10.1016/S0952-7915\(96\)80102-6](https://doi.org/10.1016/S0952-7915(96)80102-6).
- [77] **M. Desjardins.** Biogenesis of phagolysosomes: The “kiss and run” hypothesis. *Trends Cell Biol.*, 5(5):183–186, 1995. doi:[10.1016/s0962-8924\(00\)88989-8](https://doi.org/10.1016/s0962-8924(00)88989-8).
- [78] **R. A. Weisman, E. D. Korn.** Phagocytosis of Latex Beads by Acanthamoeba. I. Biochemical Properties. *Biochemistry*, 6(2):485–497, 1967. doi:[10.1021/bi00854a017](https://doi.org/10.1021/bi00854a017).
- [79] **H. Kumar, T. Kawai, S. Akira.** Pathogen recognition by the innate immune system. *Int. Rev. Immunol.*, 30(1):16–34, 2011. doi:[10.3109/08830185.2010.529976](https://doi.org/10.3109/08830185.2010.529976).
- [80] **M. Desjardins, M. Houde, E. Gagnon.** Phagocytosis: The convoluted way from nutrition to adaptive immunity. *Immunol. Rev.*, 207(1):158–165, 2005. doi:[10.1111/j.0105-2896.2005.00319.x](https://doi.org/10.1111/j.0105-2896.2005.00319.x).
- [81] **S. Greenberg, S. Grinstein.** Phagocytosis and innate immunity. *Curr. Opin. Immunol.*, 14(1):136–145, 2002. doi:[10.1016/S0952-7915\(01\)00309-0](https://doi.org/10.1016/S0952-7915(01)00309-0).
- [82] **F. Nimmerjahn, J. V. Ravetch.** Fc γ receptors as regulators of immune responses. *Nat. Rev. Immunol.*, 8(1):34–47, 2008. doi:[10.1038/nri2206](https://doi.org/10.1038/nri2206).
- [83] **A. R. Mantegazza, J. G. Magalhaes, S. Amigorena, M. S. Marks.** Presentation of Phagocytosed Antigens by MHC Class I and II. *Traffic*, 14(2):135–152, 2013. doi:[10.1111/tra.12026](https://doi.org/10.1111/tra.12026).
- [84] **G. Vidarsson, G. Dekkers, T. Rispens.** IgG Subclasses and Allotypes: From Structure to Effector Functions. *Front. Immunol.*, 5:520, 2014. doi:[10.3389/fimmu.2014.00520](https://doi.org/10.3389/fimmu.2014.00520).
- [85] **J. V. Ravetch, S. Bolland.** IgG Fc Receptors. *Annu. Rev. Immunol.*, 19(1):275–290, 2001. doi:[10.1146/annurev.immunol.19.1.275](https://doi.org/10.1146/annurev.immunol.19.1.275).

- [86] **T. D. Troutman, J. F. Bazan, C. Pasare.** Toll-like receptors, signaling adapters and regulation of the pro-inflammatory response by PI3K. *Cell Cycle*, 11(19):3559–3567, 2012. doi:[10.4161/cc.21572](https://doi.org/10.4161/cc.21572).
- [87] **R. S. Flannagan, V. Jaumouillé, S. Grinstein.** The cell biology of phagocytosis. *Annu. Rev. Pathol. Mech. Dis.*, 7(1):61–98, 2012. doi:[10.1146/annurev-pathol-011811-132445](https://doi.org/10.1146/annurev-pathol-011811-132445).
- [88] **R. Rohatgi, H.-y. H. Ho, M. W. Kirschner.** Mechanism of N-Wasp Activation by Cdc42 and Phosphatidylinositol 4,5-Bisphosphate. *J. Cell Biol.*, 150(6):1299–1310, 2000. doi:[10.1083/jcb.150.6.1299](https://doi.org/10.1083/jcb.150.6.1299).
- [89] **D. M. Underhill, A. Ozinsky.** Phagocytosis of microbes: Complexity in action. *Annu. Rev. Immunol.*, 20(2):825–852, 2002. doi:[10.1146/annurev.immunol.20.103001.114744](https://doi.org/10.1146/annurev.immunol.20.103001.114744).
- [90] **J. A. Swanson, S. C. Baer.** Phagocytosis by zippers and triggers. *Trends Cell Biol.*, 5(3):89–93, 1995. doi:[10.1016/S0962-8924\(00\)88956-4](https://doi.org/10.1016/S0962-8924(00)88956-4).
- [91] **D. Vorselen, S. R. Barger, Y. Wang, W. Cai, J. A. Theriot, N. C. Gauthier, M. Krendel.** Phagocytic ‘teeth’ and myosin-II ‘jaw’ power target constriction during phagocytosis. *Elife*, 10, 2021. doi:[10.7554/eLife.68627](https://doi.org/10.7554/eLife.68627).
- [92] **B. Antony, C. Burd, P. De Camilli, E. Chen, O. Daumke, K. Faelber, M. Ford, V. A. Frolov, A. Frost, J. E. Hinshaw, T. Kirchhausen, M. M. Kozlov, M. Lenz, H. H. Low, H. McMahon, C. Merrifield, T. D. Pollard, P. J. Robinson, A. Roux, S. Schmid.** Membrane fission by dynamin: what we know and what we need to know. *EMBO J.*, 35(21):2270–2284, 2016. doi:[10.15252/embj.201694613](https://doi.org/10.15252/embj.201694613).
- [93] **S. Keller, K. Berghoff, H. Kress.** Phagosomal transport depends strongly on phagosome size. *Sci. Rep.*, 7(1), 2017. doi:[10.1038/s41598-017-17183-7](https://doi.org/10.1038/s41598-017-17183-7).
- [94] **J. A. Champion, S. Mitragotri.** Role of target geometry in phagocytosis. *Proc. Natl. Acad. Sci. U. S. A.*, 103(13):4930–4934, 2006. doi:[10.1073/pnas.0600997103](https://doi.org/10.1073/pnas.0600997103).
- [95] **N. Doshi, S. Mitragotri.** Macrophages recognize size and shape of their targets. *PLoS One*, 5(4):1–6, 2010. doi:[10.1371/journal.pone.0010051](https://doi.org/10.1371/journal.pone.0010051).
- [96] **A. F. R. M. Ramsperger, J. Jasinski, M. Völkl, T. Witzmann, M. Meinhart, V. Jérôme, W. P. Kretschmer, R. Freitag, J. Senker, A. Fery, H. Kress, T. Scheibel, C. Laforsch.** Supposedly identical microplastic particles substantially differ in their material properties influencing particle-cell interactions and cellular responses. *J. Hazard. Mater.*, 425:127961, 2022. doi:[10.1016/J.JHAZMAT.2021.127961](https://doi.org/10.1016/J.JHAZMAT.2021.127961).
- [97] **M. Eisentraut, A. Sabri, H. Kress.** The spatial resolution limit of phagocytosis. *Biophys. J.*, 122(5):868–879, 2023. doi:[10.1016/j.bpj.2023.01.030](https://doi.org/10.1016/j.bpj.2023.01.030).
- [98] **J. Gould.** Superpowered skin. *Nature*, 563(7732):S84–S85, 2018. doi:[10.1038/d41586-018-07429-3](https://doi.org/10.1038/d41586-018-07429-3).
- [99] **E. A. Lumpkin, M. J. Caterina.** Mechanisms of sensory transduction in the skin. *Nature*, 445(7130):858–865, 2007. doi:[10.1038/nature05662](https://doi.org/10.1038/nature05662).
- [100] **D. Shooter.** Use of two-point discrimination as a nerve repair assessment tool: preliminary report. *ANZ J. Surg.*, 75(10):866–868, 2005. doi:[10.1111/j.1445-2197.2005.03557.x](https://doi.org/10.1111/j.1445-2197.2005.03557.x).
- [101] **J. Tong, O. Mao, D. Goldreich.** Two-point orientation discrimination versus the traditional two-point test for tactile spatial acuity assessment. *Front. Hum. Neurosci.*, 7(SEP), 2013. doi:[10.3389/fnhum.2013.00579](https://doi.org/10.3389/fnhum.2013.00579).

- [102] **C. M. Chuong, B. J. Nickoloff, M. Elias, L. A. Goldsmith, E. Macher, P. A. Maderson, J. P. Sundberg, H. Tagami, P. M. Plonka, K. Thestrup-Pedersen, B. A. Bernard, J. M. Schröder, P. Dotto, C. H. Chang, M. L. Williams, K. R. Feingold, L. E. King, A. M. Kligman, J. L. Rees, E. Christophers.** What is the 'true' function of skin? *Exp. Dermatol.*, 11(2):159–87, 2002. doi:[10.1034/j.1600-0625.2002.00112.x](https://doi.org/10.1034/j.1600-0625.2002.00112.x).
- [103] **Y. Shi, E. Sezgin, W. Chen.** Editorial: The Role of Biomembranes and Biophysics in Immune Cell Signaling. *Front. Immunol.*, 12, 2021. doi:[10.3389/fimmu.2021.740373](https://doi.org/10.3389/fimmu.2021.740373).
- [104] **A. N. Barclay.** Membrane proteins with immunoglobulin-like domains - A master superfamily of interaction molecules. *Semin. Immunol.*, 15(4):215–223, 2003. doi:[10.1016/S1044-5323\(03\)00047-2](https://doi.org/10.1016/S1044-5323(03)00047-2).
- [105] **L. C. Davies, S. J. Jenkins, J. E. Allen, P. R. Taylor.** Tissue-resident macrophages. *Nat. Immunol.*, 14(10):986–995, 2013. doi:[10.1038/ni.2705](https://doi.org/10.1038/ni.2705).
- [106] **F. Junker, J. Gordon, O. Qureshi.** Fc Gamma Receptors and Their Role in Antigen Uptake, Presentation, and T Cell Activation. *Front. Immunol.*, 11:1393, 2020. doi:[10.3389/fimmu.2020.01393](https://doi.org/10.3389/fimmu.2020.01393).
- [107] **V. Jaumouillé, Y. Farkash, K. Jaqaman, R. Das, C. A. Lowell, S. Grinstein.** Actin cytoskeleton reorganization by syk regulates fc γ receptor responsiveness by increasing its lateral mobility and clustering. *Dev. Cell*, 29(5):534–546, 2014. doi:[10.1016/j.devcel.2014.04.031](https://doi.org/10.1016/j.devcel.2014.04.031).
- [108] **F. Kiefer, J. Brumell, N. Al-Alawi, S. Latour, A. Cheng, A. Veillette, S. Grinstein, T. Pawson.** The Syk Protein Tyrosine Kinase Is Essential for Fc γ Receptor Signaling in Macrophages and Neutrophils. *Mol. Cell. Biol.*, 18(7):4209–4220, 1998. doi:[10.1128/mcb.18.7.4209](https://doi.org/10.1128/mcb.18.7.4209).
- [109] **A. Sobota, A. Strzelecka-Kiliszek, E. Gładkowska, K. Yoshida, K. Mrozińska, K. Kwiatkowska.** Binding of IgG-Opsonized Particles to Fc γ R Is an Active Stage of Phagocytosis That Involves Receptor Clustering and Phosphorylation. *J. Immunol.*, 175(7):4450–4457, 2005. doi:[10.4049/jimmunol.175.7.4450](https://doi.org/10.4049/jimmunol.175.7.4450).
- [110] **A. Mócsai, J. Ruland, V. L. Tybulewicz.** The SYK tyrosine kinase: A crucial player in diverse biological functions. *Nat. Rev. Immunol.*, 10(6):387–402, 2010. doi:[10.1038/nri2765](https://doi.org/10.1038/nri2765).
- [111] **E. García-García, C. Rosales.** Signal transduction during Fc receptor-mediated phagocytosis. *J. Leukoc. Biol.*, 72(6):1092–108, 2002. doi:[10.1189/jlb.72.6.1092](https://doi.org/10.1189/jlb.72.6.1092).
- [112] **L. A. Kamen, J. Levinsohn, J. A. Swanson.** Differential Association of Phosphatidylinositol 3-Kinase, SHIP-1, and PTEN with Forming Phagosomes. *Mol. Biol. Cell*, 18(7):2463–2472, 2007. doi:[10.1091/mbc.e07-01-0061](https://doi.org/10.1091/mbc.e07-01-0061).
- [113] **S. Greenberg.** Signal transduction of phagocytosis. *Trends Cell Biol.*, 5(3):93–99, 1995. doi:[10.1016/S0962-8924\(00\)88957-6](https://doi.org/10.1016/S0962-8924(00)88957-6).
- [114] **D. M. Underhill, H. S. Goodridge.** Information processing during phagocytosis. *Nat. Rev. Immunol.*, 12(7):492–502, 2012. doi:[10.1038/nri3244](https://doi.org/10.1038/nri3244).
- [115] **M. Irmischer, A. M. De Jong, H. Kress, M. W. Prins.** A method for time-resolved measurements of the mechanics of phagocytic cups. *J. R. Soc. Interface*, 10(82):20121048, 2013. doi:[10.1098/rsif.2012.1048](https://doi.org/10.1098/rsif.2012.1048).
- [116] **J. A. Swanson.** Shaping cups into phagosomes and macropinosomes. *Nat. Rev. Mol. Cell Biol.*, 9(8):639–649, 2008. doi:[10.1038/nrm2447](https://doi.org/10.1038/nrm2447).

- [117] **S. A. Freeman, S. Grinstein.** Phagocytosis: receptors, signal integration, and the cytoskeleton. *Immunol. Rev.*, 262(1):193–215, 2014. doi:[10.1111/imr.12212](https://doi.org/10.1111/imr.12212).
- [118] **E. R. Dufresne, G. C. Spalding, M. T. Dearing, S. A. Sheets, D. G. Grier.** Computer-generated holographic optical tweezer arrays. *Rev. Sci. Instrum.*, 72(3):1810–1816, 2001. doi:[10.1063/1.1344176](https://doi.org/10.1063/1.1344176).
- [119] **R. L. Eriksen, V. R. Daria, J. Glückstad.** Fully dynamic multiple-beam optical tweezers. *Opt. Express*, 10(14):597, 2002. doi:[10.1364/oe.10.000597](https://doi.org/10.1364/oe.10.000597).
- [120] **H. Kress, J.-G. Park, C. O. Mejean, J. D. Forster, J. Park, S. S. Walse, Y. Zhang, D. Wu, O. D. Weiner, T. M. Fahmy, E. R. Dufresne.** Cell stimulation with optically manipulated microspheres. *Nat. Methods*, 6(12):905–909, 2009. doi:[10.1038/nmeth.1400](https://doi.org/10.1038/nmeth.1400).
- [121] **P. Ralph, J. Prichard, M. Cohn.** Reticulum cell sarcoma: an effector cell in antibody-dependent cell-mediated immunity. *J. Immunol.*, 114(2 pt 2):898–905, 1975.
- [122] **ATCC.** J774A.1 Datasheet, see <https://www.atcc.org/api/pdf/product-sheet?id=TIB-67>, 2021.
- [123] **A. B. Kashekodi, T. Meinert, R. Michiels, A. Rohrbach.** Miniature scanning light-sheet illumination implemented in a conventional microscope. *Biomed. Opt. Express*, 9(9):4263, 2018. doi:[10.1364/boe.9.004263](https://doi.org/10.1364/boe.9.004263).
- [124] **J. Riedl, A. H. Crevenna, K. Kessenbrock, J. H. Yu, D. Neukirchen, M. Bista, F. Bradke, D. Jenne, T. A. Holak, Z. Werb, M. Sixt, R. Wedlich-Soldner.** Lifeact: a versatile marker to visualize F-actin. *Nat. Methods*, 5(7):605–607, 2008. doi:[10.1038/nmeth.1220](https://doi.org/10.1038/nmeth.1220).
- [125] **M. Melak, M. Plessner, R. Grosse.** Actin visualization at a glance. *J. Cell Sci.*, 130(3):525–530, 2017. doi:[10.1242/jcs.189068](https://doi.org/10.1242/jcs.189068).
- [126] **H. Cerutti, J. A. Casas-Mollano.** On the origin and functions of RNA-mediated silencing: From protists to man. *Curr. Genet.*, 50(2):81–99, 2006. doi:[10.1007/s00294-006-0078-x](https://doi.org/10.1007/s00294-006-0078-x).
- [127] **K. Okamura, E. C. Lai.** Endogenous small interfering RNAs in animals. *Nat. Rev. Mol. Cell Biol.*, 9(9):673–678, 2008. doi:[10.1038/nrm2479](https://doi.org/10.1038/nrm2479).
- [128] **M. M. Zhang, R. Bahal, T. P. Rasmussen, J. E. Manautou, X. bo Zhong.** The growth of siRNA-based therapeutics: Updated clinical studies. *Biochem. Pharmacol.*, 189(January), 2021. doi:[10.1016/j.bcp.2021.114432](https://doi.org/10.1016/j.bcp.2021.114432).
- [129] **D. Karlsson, G. Zacchi, A. Axelsson.** Electronic Speckle Pattern Interferometry: A Tool for Determining Diffusion and Partition Coefficients for Proteins in Gels. *Biotechnol. Prog.*, 18(6):1423–1430, 2002. doi:[10.1021/bp0255659](https://doi.org/10.1021/bp0255659).
- [130] **K. Berghoff.** *Entwicklung einer Arbeitsstation zur optischen Mikromanipulation und Charakterisierung des Einflusses von Aktin auf die Zellmechanik der Phagozytose.* PhD thesis, University of Bayreuth, 2018.
- [131] **S. Keller.** *Abhängigkeit des phagosomalen Transportes von der Größe des Phagosomes.* PhD thesis, University of Bayreuth, 2019.
- [132] **Wolfgang Groß.** *Development of Optical and Mechanical Techniques to Investigate Rheology and Adhesion in Biological and Biomimetic Systems.* PhD thesis, University of Bayreuth, 2022.
- [133] **A. Köhler.** Ein neues Beleuchtungsverfahren für mikrophotographische Zwecke. *Zeitschrift für wissenschaftliche Mikroskopie und für Mikroskopische Tech.*, 10(4):433–440, 1893.

- [134] **H. Balasubramanian, C. M. Hobson, T. L. Chew, J. S. Aaron.** Imagining the future of optical microscopy: everything, everywhere, all at once. *Commun. Biol.*, 6(1):1–12, 2023. doi:[10.1038/s42003-023-05468-9](https://doi.org/10.1038/s42003-023-05468-9).
- [135] **F. Zernike.** How I discovered phase contrast. *Science*, 121(3141):345–349, 1955. doi:[10.1126/science.121.3141.345](https://doi.org/10.1126/science.121.3141.345).
- [136] **C. R. Burch, J. P. P. Stock.** Phase-Contrast Microscopy. *J. Sci. Instrum.*, 19(5):71–75, 1942. doi:[10.1088/0950-7671/19/5/302](https://doi.org/10.1088/0950-7671/19/5/302).
- [137] **M. G. Nomarski.** Interferential polarizing device for study of phase objects, US Pat. No. 2924142, 1960.
- [138] **M. Eisentraut.** *Entwicklung und Implementierung eines Bildverarbeitungsalgorithmus zur automatisierten Erkennung von aktiven Zellen in differentialinterferenzkontrastmikroskopischen Bildserien.* Bachelor thesis, University of Bayreuth, 2014.
- [139] **H. E. Rosenberger.** Differential Interference Contrast Microscopy. In *Interpret. Tech. Microstruct. Anal.*, pages 79–104. Springer US, Boston, MA, 1977. doi:[10.1007/978-1-4684-2370-9_5](https://doi.org/10.1007/978-1-4684-2370-9_5).
- [140] **J. Kapuscinski.** DAPI: a DNA-Specific Fluorescent Probe. *Biotech. Histochem.*, 70(5):220–233, 1995. doi:[10.3109/10520299509108199](https://doi.org/10.3109/10520299509108199).
- [141] **O. Shimomura, F. H. Johnson, Y. Saiga.** Extraction, Purification and Properties of Aequorin, a Bioluminescent Protein from the Luminous Hydromedusan, Aequorea. *J. Cell. Comp. Physiol.*, 59(3):223–239, 1962. doi:[10.1002/jcp.1030590302](https://doi.org/10.1002/jcp.1030590302).
- [142] **D. C. Prasher, V. K. Eckenrode, W. W. Ward, F. G. Prendergast, M. J. Cormier.** Primary structure of the Aequorea victoria green-fluorescent protein. *Gene*, 111(2):229–233, 1992. doi:[https://doi.org/10.1016/0378-1119\(92\)90691-H](https://doi.org/10.1016/0378-1119(92)90691-H).
- [143] **S. Sudhakar, M. Kazem, A. Tobias, J. Jachowski, M. Bugiel, A. Jannasch, E. Schäffer.** Germanium nanospheres for ultraresolution picotensiometry of kinesin motors. *Science*, 371(6530):eabd9944, 2021. doi:[10.1126/science.abd9944](https://doi.org/10.1126/science.abd9944).
- [144] **A. Jannasch, A. F. Demirörs, P. D. Van Oostrum, A. Van Blaaderen, E. Schäffer.** Nanonewton optical force trap employing anti-reflection coated, high-refractive-index titania microspheres. *Nat. Photonics*, 6(7):469–476, 2012. doi:[10.1038/nphoton.2012.140](https://doi.org/10.1038/nphoton.2012.140).
- [145] **A. Ashkin.** Acceleration and Trapping of Particles by Radiation Pressure. *Phys. Rev. Lett.*, 24(4):156–159, 1970. doi:[10.1103/PhysRevLett.24.156](https://doi.org/10.1103/PhysRevLett.24.156).
- [146] **A. Ashkin, J. M. Dziedzic, J. E. Bjorkholm, S. Chu.** Observation of a single-beam gradient force optical trap for dielectric particles. *Opt. Lett.*, 11(5):288, 1986. doi:[10.1364/OL.11.000288](https://doi.org/10.1364/OL.11.000288).
- [147] **K. Svoboda, S. M. Block.** Biological Applications of Optical Forces. *Annu. Rev. Biophys. Biomol. Struct.*, 23(1):247–285, 1994. doi:[10.1146/annurev.biophys.23.1.247](https://doi.org/10.1146/annurev.biophys.23.1.247).
- [148] **K. C. Neuman, S. M. Block.** Optical trapping. *Rev. Sci. Instrum.*, 75(9):2787–2809, 2004. doi:[10.1063/1.1785844](https://doi.org/10.1063/1.1785844).
- [149] **D. McGloin, J. Reid.** Forty Years of Optical Manipulation. *Opt. Photonics News*, 21(3):20, 2010. doi:[10.1364/OPN.21.3.000020](https://doi.org/10.1364/OPN.21.3.000020).
- [150] **M. D. Wang, H. Yin, R. Landick, J. Gelles, S. M. Block.** Stretching DNA with optical tweezers. *Biophys. J.*, 72(3):1335–1346, 1997. doi:[10.1016/S0006-3495\(97\)78780-0](https://doi.org/10.1016/S0006-3495(97)78780-0).

- [151] **A. Gennerich, A. P. Carter, S. L. Reck-Peterson, R. D. Vale.** Force-Induced Bidirectional Stepping of Cytoplasmic Dynein. *Cell*, 131(5):952–965, 2007. doi:[10.1016/j.cell.2007.10.016](https://doi.org/10.1016/j.cell.2007.10.016).
- [152] **A. E. Clemen, M. Vilfan, J. Jaud, J. Zhang, M. Bärmann, M. Rief.** Force-dependent stepping kinetics of myosin-V. *Biophys. J.*, 88(6):4402–4410, 2005. doi:[10.1529/biophysj.104.053504](https://doi.org/10.1529/biophysj.104.053504).
- [153] **M. J. Schnitzer, S. M. Block.** Kinesin hydrolyses one ATP per 8-nm step. *Nature*, 388(6640):386–390, 1997. doi:[10.1038/41111](https://doi.org/10.1038/41111).
- [154] **A. Ashkin.** Forces of a single-beam gradient laser trap on a dielectric sphere in the ray optics regime. *Biophys. J.*, 61(2):569–582, 1992. doi:[10.1016/S0006-3495\(92\)81860-X](https://doi.org/10.1016/S0006-3495(92)81860-X).
- [155] **A. Callegari, M. Mijalkov, A. B. Gököz, G. Volpe.** Computational toolbox for optical tweezers in geometrical optics. *J. Opt. Soc. Am. B*, 32(5), 2015. doi:[10.1364/JOSAB.32.000B11](https://doi.org/10.1364/JOSAB.32.000B11).
- [156] **T. A. Nieminen, N. du Preez-Wilkinson, A. B. Stilgoe, V. L. Loke, A. A. Bui, H. Rubinsztein-Dunlop.** Optical tweezers: Theory and modelling. *J. Quant. Spectrosc. Radiat. Transf.*, 146(May 2019):59–80, 2014. doi:[10.1016/j.jqsrt.2014.04.003](https://doi.org/10.1016/j.jqsrt.2014.04.003).
- [157] **A. B. Stilgoe, T. A. Nieminen, G. Knöener, N. R. Heckenberg, H. Rubinsztein-Dunlop.** The effect of Mie resonances on trapping in optical tweezers. *Opt. Express*, 16(19):15039, 2008. doi:[10.1364/OE.16.015039](https://doi.org/10.1364/OE.16.015039).
- [158] **Y. Harada, T. Asakura.** Radiation forces on a dielectric sphere in the Rayleigh scattering regime. *Opt. Commun.*, 124(5-6):529–541, 1996. doi:[10.1016/0030-4018\(95\)00753-9](https://doi.org/10.1016/0030-4018(95)00753-9).
- [159] **M. S. Rocha.** Optical tweezers for undergraduates: Theoretical analysis and experiments. *Am. J. Phys.*, 77(8):704–712, 2009. doi:[10.1119/1.3138698](https://doi.org/10.1119/1.3138698).
- [160] **M. Kerker.** *The scattering of light and other electromagnetic radiation.* Academic Press, 1969. ISBN 9781483191744. doi:[10.1021/j150340a005](https://doi.org/10.1021/j150340a005).
- [161] **J. A. Lock.** Calculation of the radiation trapping force for laser tweezers by use of generalized Lorenz-Mie theory. I. Localized model description of an on-axis tightly focused laser beam with spherical aberration. *Appl. Opt.*, 43(12):2532–2544, 2004. doi:[10.1364/AO.43.002532](https://doi.org/10.1364/AO.43.002532).
- [162] **K. Visscher, S. P. Gross, S. M. Block.** Construction of multiple-beam optical traps with nanometer-resolution position sensing. *IEEE J. Sel. Top. Quantum Electron.*, 2(4):1066–1076, 1996. doi:[10.1109/2944.577338](https://doi.org/10.1109/2944.577338).
- [163] **E. R. Dufresne, D. G. Grier.** Optical tweezer arrays and optical substrates created with diffractive optics. *Rev. Sci. Instrum.*, 69(5):1974–1977, 1998. doi:[10.1063/1.1148883](https://doi.org/10.1063/1.1148883).
- [164] **A. Sabri.** *Cellular decision making during phagocytosis.* PhD thesis, Biological Physics Group University of Bayreuth, 2015.
- [165] **AA Opto-Electronic.** Datasheet MT110 AO Modulator/Shifter, 2010.
- [166] **N. Uchida, Y. Ohmachi.** Elastic and photoelastic properties of TeO₂ single crystal. *J. Appl. Phys.*, 40(12):4692–4695, 1969. doi:[10.1063/1.1657275](https://doi.org/10.1063/1.1657275).
- [167] **M. A. Seldowitz, J. P. Allebach, D. W. Sweeney.** Synthesis of digital holograms by direct binary search. *Appl. Opt.*, 26(14):2788, 1987. doi:[10.1364/ao.26.002788](https://doi.org/10.1364/ao.26.002788).
- [168] **R. W. Gerchberg, W. O. Saxton.** A Practical Algorithm for the Determination of Phase from Image and Diffraction Plane Pictures. *Optik (Stuttg.)*, 35(2):237–246, 1972.

- [169] **J. Liesener, M. Reicherter, T. Haist, H. J. Tiziani.** Multi-functional optical tweezers using computer-generated holograms. *Opt. Commun.*, 185(1-3):77–82, 2000. doi:[10.1016/S0030-4018\(00\)00990-1](https://doi.org/10.1016/S0030-4018(00)00990-1).
- [170] **J. E. Curtis, B. A. Koss, D. G. Grier.** Dynamic holographic optical tweezers. *Opt. Commun.*, 207(1-6):169–175, 2002. doi:[10.1016/S0030-4018\(02\)01524-9](https://doi.org/10.1016/S0030-4018(02)01524-9).
- [171] **K. Chaitavon, S. Sumriddetchkajorn, J. Nukeaw.** Highly sensitive refractive index measurement with a sandwiched single-flow-channel microfluidic chip. *RSC Adv.*, 3(19):6981–6984, 2013. doi:[10.1039/c3ra23119d](https://doi.org/10.1039/c3ra23119d).
- [172] **M. Montes-Usategui, E. Pleguezuelos, J. Andilla, E. Martín-Badosa.** Fast generation of holographic optical tweezers by random mask encoding of Fourier components. *Opt. Express*, 14(6):2101, 2006. doi:[10.1364/oe.14.002101](https://doi.org/10.1364/oe.14.002101).
- [173] **K. D. Wulff, D. G. Cole, R. L. Clark, R. DiLeonardo, J. Leach, J. Cooper, G. Gibson, M. J. Padgett.** Aberration correction in holographic optical tweezers. *Opt. Express*, 14(9):4169, 2006. doi:[10.1364/oe.14.004169](https://doi.org/10.1364/oe.14.004169).
- [174] **G. Sinclair, J. Leach, P. Jordan, G. Gibson, E. Yao, Z. J. Laczik, M. J. Padgett, J. Courtial.** Interactive application in holographic optical tweezers of a multi-plane Gerchberg-Saxton algorithm for three-dimensional light shaping. *Opt. Express*, 12(8):1665, 2004. doi:[10.1364/opex.12.001665](https://doi.org/10.1364/opex.12.001665).
- [175] **G. Whyte, J. Courtial.** Experimental demonstration of holographic three-dimensional light shaping using a Gerchberg-Saxton algorithm. *New J. Phys.*, 7:117, 2005. doi:[10.1088/1367-2630/7/1/117](https://doi.org/10.1088/1367-2630/7/1/117).
- [176] **Leibniz Institute DSMZ.** J774A.1 cell line web page, see <https://www.dsmz.de/collection/catalogue/details/culture/ACC-170>, 2024.
- [177] **C. D. Bortner, J. A. Cidlowski.** Apoptotic volume decrease and the incredible shrinking cell. *Cell Death Differ.*, 9(12):1307–1310, 2002. doi:[10.1038/sj.cdd.4401126](https://doi.org/10.1038/sj.cdd.4401126).
- [178] **S. Elmore.** Apoptosis: A Review of Programmed Cell Death. *Toxicol. Pathol.*, 35(4):495–516, 2007. doi:[10.1080/01926230701320337](https://doi.org/10.1080/01926230701320337).
- [179] **K. Miura.** Tracking Movement in Cell Biology. In *Adv. Biochem. Eng. Biotechnol.*, pages 267–295. Springer-Verlag, Berlin, Heidelberg, 2005. doi:[10.1007/b102218](https://doi.org/10.1007/b102218).
- [180] **C. D. Saunter.** Quantifying subpixel accuracy: An experimental method for measuring accuracy in image-correlation-based, single-particle tracking. *Biophys. J.*, 98(8):1566–1570, 2010. doi:[10.1016/j.bpj.2009.12.4297](https://doi.org/10.1016/j.bpj.2009.12.4297).
- [181] **R. Parthasarathy.** Rapid, accurate particle tracking by calculation of radial symmetry centers. *Nat. Methods*, 9(7):724–726, 2012. doi:[10.1038/nmeth.2071](https://doi.org/10.1038/nmeth.2071).
- [182] **H. Ma, F. Long, S. Zeng, Z.-L. Huang.** Fast and precise algorithm based on maximum radial symmetry for single molecule localization. *Opt. Lett.*, 37(13):2481, 2012. doi:[10.1364/ol.37.002481](https://doi.org/10.1364/ol.37.002481).
- [183] **H. Yücel, N. T. Okumuşoğlu.** A new tracking algorithm for multiple colloidal particles close to contact. *J. Phys. Condens. Matter*, 29(46):465101, 2017. doi:[10.1088/1361-648X/aa908e](https://doi.org/10.1088/1361-648X/aa908e).
- [184] **L. W. Tu.** Bump Functions and Partitions of Unity. In **K. R. S. Axler**, editor, *An Introd. to Manifolds*, pages 127–134. Springer, New York, 2007. ISBN 0387480986. doi:[10.1007/978-0-387-48101-2_13](https://doi.org/10.1007/978-0-387-48101-2_13).

- [185] **A. Nuttall**. Some windows with very good sidelobe behavior. *IEEE Trans. Acoust.*, 29(1): 84–91, 1981. doi:[10.1109/TASSP.1981.1163506](https://doi.org/10.1109/TASSP.1981.1163506).
- [186] **K. Berghoff, S. Keller, W. Gross, L. Gebhardt, H. Kress**. Application of optical tweezers for biochemical and thermal cell stimulation. In *Light Robot. Nanobiophotonics*, pages 385–410. Elsevier, 2017. ISBN 9780081022481. doi:[10.1016/B978-0-7020-7096-9.00013-6](https://doi.org/10.1016/B978-0-7020-7096-9.00013-6).
- [187] **M. Herant, V. Heinrich, M. Dembo**. Mechanics of neurophil phagocytosis: Experiments and quantitative models. *J. Cell Sci.*, 119(9):1903–1913, 2006. doi:[10.1242/jcs.02876](https://doi.org/10.1242/jcs.02876).
- [188] **D. Paul, S. Achouri, Y. Z. Yoon, J. Herre, C. E. Bryant, P. Cicuti**. Phagocytosis dynamics depends on target shape. *Biophys. J.*, 105(5):1143–1150, 2013. doi:[10.1016/j.bpj.2013.07.036](https://doi.org/10.1016/j.bpj.2013.07.036).
- [189] **S. Greenberg, J. el Khoury, F. di Virgilio, E. M. Kaplan, S. C. Silverstein**. Ca²⁺-independent F-actin assembly and disassembly during Fc receptor-mediated phagocytosis in mouse macrophages. *J. Cell Biol.*, 113(4):757–767, 1991. doi:[10.1083/jcb.113.4.757](https://doi.org/10.1083/jcb.113.4.757).
- [190] **J. S. Van Zon, G. Tzircotis, E. Caron, M. Howard**. A mechanical bottleneck explains the variation in cup growth during Fc γ R phagocytosis. *Mol. Syst. Biol.*, 5(298), 2009. doi:[10.1038/msb.2009.59](https://doi.org/10.1038/msb.2009.59).
- [191] **E. A. Francis, V. Heinrich**. Integrative experimental/computational approach establishes active cellular protrusion as the primary driving force of phagocytic spreading by immune cells. *PLOS Comput. Biol.*, 18(8):1–26, 2022. doi:[10.1371/journal.pcbi.1009937](https://doi.org/10.1371/journal.pcbi.1009937).
- [192] **D. M. Richards, R. G. Endres**. Target shape dependence in a simple model of receptor-mediated endocytosis and phagocytosis. *Proc. Natl. Acad. Sci. U. S. A.*, 113(22):6113–6118, 2016. doi:[10.1073/pnas.1521974113](https://doi.org/10.1073/pnas.1521974113).
- [193] **W. Gross, H. Kress**. Simultaneous measurement of the Young’s modulus and the Poisson ratio of thin elastic layers. *Soft Matter*, 13(5):1048–1055, 2017. doi:[10.1039/c6sm02470j](https://doi.org/10.1039/c6sm02470j).
- [194] **H. T. Spanke, R. W. Style, C. François-Martin, M. Feofilova, M. Eisentraut, H. Kress, J. Agudo-Canalejo, E. R. Dufresne**. Wrapping of Microparticles by Floppy Lipid Vesicles. *Phys. Rev. Lett.*, 125(19):198102, 2020. doi:[10.1103/PhysRevLett.125.198102](https://doi.org/10.1103/PhysRevLett.125.198102).
- [195] **R. K. Sadhu, S. R. Barger, S. Penič, A. Iglič, M. Krendel, N. C. Gauthier, N. S. Gov**. Theoretical model of efficient phagocytosis driven by curved membrane proteins and active cytoskeleton forces. *bioRxiv*, page 2022.01.04.474893, 2022. doi:[10.48550/arXiv.2201.01133](https://doi.org/10.48550/arXiv.2201.01133).
- [196] **A. Saric, S. A. Freeman**. Endomembrane Tension and Trafficking. *Front. Cell Dev. Biol.*, 8: 611326, 2021. doi:[10.3389/fcell.2020.611326](https://doi.org/10.3389/fcell.2020.611326).
- [197] **R. Skalak, A. Tozeren, R. P. Zarda, S. Chien**. Strain Energy Function of Red Blood Cell Membranes. *Biophys. J.*, 13(3):245–264, 1973. doi:[10.1016/S0006-3495\(73\)85983-1](https://doi.org/10.1016/S0006-3495(73)85983-1).
- [198] **J. P. Luzio, P. R. Pryor, N. A. Bright**. Lysosomes: Fusion and function. *Nat. Rev. Mol. Cell Biol.*, 8(8):622–632, 2007. doi:[10.1038/nrm2217](https://doi.org/10.1038/nrm2217).
- [199] **A. Blocker, F. F. Severin, J. K. Burkhardt, J. B. Bingham, H. Yu, J.-C. C. Olivo, T. A. Schroer, A. A. Hyman, G. Griffiths**. Molecular Requirements for Bi-directional Movement of Phagosomes Along Microtubules. *J. Cell Biol.*, 137(1):113–129, 1997. doi:[10.1083/jcb.137.1.113](https://doi.org/10.1083/jcb.137.1.113).
- [200] **B. Kasmapour, A. Gronow, C. K. Bleck, W. Hong, M. G. Gutierrez**. Size-dependent mechanism of cargo sorting during lysosome-phagosome fusion is controlled by Rab34. *Proc. Natl. Acad. Sci. U. S. A.*, 109(50):20485–20490, 2012. doi:[10.1073/pnas.1206811109](https://doi.org/10.1073/pnas.1206811109).

- [201] **C. E. van der Poel, R. M. Spaapen, J. G. J. van de Winkel, J. H. W. Leusen.** Functional Characteristics of the High Affinity IgG Receptor, Fc γ RI. *J. Immunol.*, 186(5): 2699–2704, 2011. doi:[10.4049/jimmunol.1003526](https://doi.org/10.4049/jimmunol.1003526).
- [202] **J. Lam, M. Herant, M. Dembo, V. Heinrich.** Baseline mechanical characterization of J774 macrophages. *Biophys. J.*, 96(1):248–254, 2009. doi:[10.1529/biophysj.108.139154](https://doi.org/10.1529/biophysj.108.139154).
- [203] **F. Krombach, S. Münzing, A. M. Allmeling, J. T. Gerlach, J. Behr, M. Dörger.** Cell size of alveolar macrophages: an interspecies comparison. *Environ. Health Perspect.*, 105(suppl 5):1261–1263, 1997. doi:[10.1289/ehp.97105s51261](https://doi.org/10.1289/ehp.97105s51261).
- [204] **H. B. Fleit, S. D. Wright, J. C. Unkeless.** Human neutrophil Fc(γ) receptor distribution and structure. *Proc. Natl. Acad. Sci. U. S. A.*, 79(10 I):3275–3279, 1982. doi:[10.1073/pnas.79.10.3275](https://doi.org/10.1073/pnas.79.10.3275).
- [205] **C. Kerntke, F. Nimmerjahn, M. Biburger.** There Is (Scientific) Strength in Numbers: A Comprehensive Quantitation of Fc Gamma Receptor Numbers on Human and Murine Peripheral Blood Leukocytes. *Front. Immunol.*, 11:118, 2020. doi:[10.3389/fimmu.2020.00118](https://doi.org/10.3389/fimmu.2020.00118).
- [206] **Y. Zhang, A. D. Hoppe, J. A. Swanson.** Coordination of Fc receptor signaling regulates cellular commitment to phagocytosis. *Proc. Natl. Acad. Sci.*, 107(45):19332–19337, 2010. doi:[10.1073/pnas.1008248107](https://doi.org/10.1073/pnas.1008248107).
- [207] **N. Kern, R. Dong, S. M. Douglas, R. D. Vale, M. A. Morrissey.** Tight nanoscale clustering of Fc γ receptors using DNA origami promotes phagocytosis. *Elife*, 10:e68311, 2021. doi:[10.7554/eLife.68311](https://doi.org/10.7554/eLife.68311).
- [208] **A. Rohrbach, T. Meyer, E. H. Stelzer, H. Kress.** Measuring Stepwise Binding of Thermally Fluctuating Particles to Cell Membranes without Fluorescence. *Biophys. J.*, 118(8):1850–1860, 2020. doi:[10.1016/j.bpj.2020.03.005](https://doi.org/10.1016/j.bpj.2020.03.005).
- [209] **S. Tollis, A. E. Dart, G. Tzircotis, R. G. Endres.** The zipper mechanism in phagocytosis: Energetic requirements and variability in phagocytic cup shape. *BMC Syst. Biol.*, 4(1):149, 2010. doi:[10.1186/1752-0509-4-149](https://doi.org/10.1186/1752-0509-4-149).
- [210] **F. Porte, J.-P. Liautard, S. Köhler.** Early Acidification of Phagosomes Containing *Brucella suis* Is Essential for Intracellular Survival in Murine Macrophages. *Infect. Immun.*, 67(8): 4041–4047, 1999. doi:[10.1128/IAI.67.8.4041-4047.1999](https://doi.org/10.1128/IAI.67.8.4041-4047.1999).
- [211] **C. C. Scott, R. J. Botelho, S. Grinstein.** Phagosome Maturation: A Few Bugs in the System. *J. Membr. Biol.*, 193(3):137–152, 2003. doi:[10.1007/s00232-002-2008-2](https://doi.org/10.1007/s00232-002-2008-2).
- [212] **A. W. Jones, J. Bland-Hawthorn, P. L. Shopbell.** Towards a General Definition for Spectroscopic Resolution. In **R. A. Shaw, H. E. Payne, J. J. E. Hayes**, editors, *Astron. Data Anal. Softw. Syst. IV*, volume 77 of *Astronomical Society of the Pacific Conference Series*, page 503, Epping, Australia, 1995.
- [213] **M. Desjardins, G. Griffiths.** Phagocytosis: latex leads the way. *Curr. Opin. Cell Biol.*, 15 (4):498–503, 2003. doi:[10.1016/S0955-0674\(03\)00083-8](https://doi.org/10.1016/S0955-0674(03)00083-8).
- [214] **D. M. Richards, R. G. Endres.** The mechanism of phagocytosis: Two stages of engulfment. *Biophys. J.*, 107(7):1542–1553, 2014. doi:[10.1016/j.bpj.2014.07.070](https://doi.org/10.1016/j.bpj.2014.07.070).
- [215] **V. Jaumouillé, S. Grinstein.** Receptor mobility, the cytoskeleton, and particle binding during phagocytosis. *Curr. Opin. Cell Biol.*, 23(1):22–29, 2011. doi:[10.1016/j.ceb.2010.10.006](https://doi.org/10.1016/j.ceb.2010.10.006).

- [216] **A. F. R. M. Ramsperger, V. K. B. Narayana, W. Gross, J. Mohanraj, M. Thelakkat, A. Greiner, H. Schmalz, H. Kress, C. Laforsch.** Environmental exposure enhances the internalization of microplastic particles into cells. *Sci. Adv.*, 6(50):1–10, 2020. doi:[10.1126/sciadv.abd1211](https://doi.org/10.1126/sciadv.abd1211).
- [217] **J. A. Champion, A. Walker, S. Mitragotri.** Role of particle size in phagocytosis of polymeric microspheres. *Pharm. Res.*, 25(8):1815–1821, 2008. doi:[10.1007/s11095-008-9562-y](https://doi.org/10.1007/s11095-008-9562-y).
- [218] **K. Berghoff, W. Gross, M. Eisentraut, H. Kress.** Using blinking optical tweezers to study cell rheology during initial cell-particle contact. *Biophys. J.*, 120(16):3527–3537, 2021. doi:[10.1016/J.BPJ.2021.04.034](https://doi.org/10.1016/J.BPJ.2021.04.034).
- [219] **D. Vorselen, R. L. D. Labitigan, J. A. Theriot.** A mechanical perspective on phagocytic cup formation. *Curr. Opin. Cell Biol.*, 66:112–122, 2020. doi:[10.1016/j.ccb.2020.05.011](https://doi.org/10.1016/j.ccb.2020.05.011).
- [220] **K. A. Beningo, Y.-I. Wang.** Fc-receptor-mediated phagocytosis is regulated by mechanical properties of the target. *J. Cell Sci.*, 115(4):849–856, 2002.
- [221] **M. Clarke, U. Engel, J. Giorgione, A. Müller-Taubenberger, J. Prassler, D. Veltman, G. Gerisch.** Curvature recognition and force generation in phagocytosis. *BMC Biol.*, 8(1):154, 2010. doi:[10.1186/1741-7007-8-154](https://doi.org/10.1186/1741-7007-8-154).
- [222] **H. Safari, W. J. Kelley, E. Saito, N. Kaczorowski, L. Carethers, L. D. Shea, O. Eniola-Adefeso, O. Eniola-Adefeso.** Neutrophils preferentially phagocytose elongated particles—An opportunity for selective targeting in acute inflammatory diseases. *Sci. Adv.*, 6(24), 2020. doi:[10.1126/sciadv.aba1474](https://doi.org/10.1126/sciadv.aba1474).
- [223] **J. A. Champion, S. Mitragotri.** Shape Induced Inhibition of Phagocytosis of Polymer Particles. *Pharm. Res.*, 26(1):244–249, 2009. doi:[10.1007/s11095-008-9626-z](https://doi.org/10.1007/s11095-008-9626-z).
- [224] **S. Leporatti, A. Gerth, G. Köhler, B. Kohlstrunk, S. Hauschildt, E. Donath.** Elasticity and adhesion of resting and lipopolysaccharide-stimulated macrophages. *FEBS Lett.*, 580(2): 450–454, 2006. doi:[10.1016/j.febslet.2005.12.037](https://doi.org/10.1016/j.febslet.2005.12.037).
- [225] **N. R. Patel, M. Bole, C. Chen, C. C. Hardin, A. T. Kho, J. Mih, L. Deng, J. Butler, D. Tschumperlin, J. J. Fredberg, R. Krishnan, H. Koziel.** Cell Elasticity Determines Macrophage Function. *PLoS One*, 7(9):1–10, 2012. doi:[10.1371/journal.pone.0041024](https://doi.org/10.1371/journal.pone.0041024).
- [226] **J. O. Abaricia, N. Farzad, T. J. Heath, J. Simmons, L. Morandini, R. Olivares-Navarrete.** Control of innate immune response by biomaterial surface topography, energy, and stiffness. *Acta Biomater.*, 133:58–73, 2021. doi:[10.1016/j.actbio.2021.04.021](https://doi.org/10.1016/j.actbio.2021.04.021).
- [227] **M. Gupta, B. R. Sarangi, J. Deschamps, Y. Nematbakhsh, A. Callan-Jones, F. Margadant, R.-M. Mège, C. T. Lim, R. Voituriez, B. Ladoux.** Adaptive rheology and ordering of cell cytoskeleton govern matrix rigidity sensing. *Nat. Commun.*, 6(1):7525, 2015. doi:[10.1038/ncomms8525](https://doi.org/10.1038/ncomms8525).
- [228] **P. Roca-Cusachs, V. Conte, X. Trepast.** Quantifying forces in cell biology. *Nat. Cell Biol.*, 19(7):742–751, 2017. doi:[10.1038/ncb3564](https://doi.org/10.1038/ncb3564).
- [229] **A. Sawicka, A. Babataheri, S. Dogniaux, A. I. Barakat, D. Gonzalez-Rodriguez, C. Hivroz, J. Husson.** Micropipette force probe to quantify single-cell force generation: application to T-cell activation. *Mol. Biol. Cell*, 28(23):3229–3239, 2017. doi:[10.1091/mbc.e17-06-0385](https://doi.org/10.1091/mbc.e17-06-0385).

- [230] **S. M. Tse, W. Furuya, E. Gold, A. D. Schreiber, K. Sandvig, R. D. Inman, S. Grinstein.** Differential Role of Actin, Clathrin, and Dynamin in Fc γ Receptor-mediated Endocytosis and Phagocytosis. *J. Biol. Chem.*, 278(5):3331–3338, 2003. doi:[10.1074/jbc.M207966200](https://doi.org/10.1074/jbc.M207966200).
- [231] **K. C. Neuman, A. Nagy.** Single-molecule force spectroscopy: Optical tweezers, magnetic tweezers and atomic force microscopy. *Nat. Methods*, 5(6):491–505, 2008. doi:[10.1038/nmeth.1218](https://doi.org/10.1038/nmeth.1218).
- [232] **R. Rounsevell, J. R. Forman, J. Clarke.** Atomic force microscopy: mechanical unfolding of proteins. *Methods*, 34:100–111, 2004. doi:[10.1016/j.ymeth.2004.03.007](https://doi.org/10.1016/j.ymeth.2004.03.007).
- [233] **B. Fabry, G. N. Maksym, J. P. Butler, M. Glogauer, D. Navajas, J. J. Fredberg.** Scaling the Microrheology of Living Cells. *Phys. Rev. Lett.*, 87(14):148102, 2001. doi:[10.1103/PhysRevLett.87.148102](https://doi.org/10.1103/PhysRevLett.87.148102).
- [234] **N. Gal, D. Lechtman-Goldstein, D. Weihs.** Particle tracking in living cells: A review of the mean square displacement method and beyond. *Rheol. Acta*, 52(5):425–443, 2013. doi:[10.1007/s00397-013-0694-6](https://doi.org/10.1007/s00397-013-0694-6).
- [235] **J. T. Edward.** Molecular volumes and the Stokes-Einstein equation. *J. Chem. Educ.*, 47(4):261, 1970. doi:[10.1021/ed047p261](https://doi.org/10.1021/ed047p261).
- [236] **Y. Meroz, I. M. Sokolov.** A toolbox for determining subdiffusive mechanisms. *Phys. Rep.*, 573:1–29, 2015. doi:[10.1016/j.physrep.2015.01.002](https://doi.org/10.1016/j.physrep.2015.01.002).
- [237] **L. J. Bonales, A. Maestro, R. Rubio, F. Ortega.** Microrheology of Complex Fluids. In *Hydrodyn. - Adv. Top.* InTech, 2011. doi:[10.5772/28362](https://doi.org/10.5772/28362).
- [238] **J. W. R. Mellnik, M. Lysy, P. A. Vasquez, N. S. Pillai, D. B. Hill, J. Cribb, S. A. McKinley, M. G. Forest.** Maximum likelihood estimation for single particle, passive microrheology data with drift. *J. Rheol.*, 60(3):379–392, 2016. doi:[10.1122/1.4943988](https://doi.org/10.1122/1.4943988).
- [239] **M. Tassieri.** Linear microrheology with optical tweezers of living cells ‘ is not an option ’! *Soft Matter*, 11(29):5792–5798, 2015. doi:[10.1039/C5SM01133G](https://doi.org/10.1039/C5SM01133G).
- [240] **D. Wirtz.** Particle-tracking microrheology of living cells: Principles and applications. *Annu. Rev. Biophys.*, 38(1):301–326, 2009. doi:[10.1146/annurev.biophys.050708.133724](https://doi.org/10.1146/annurev.biophys.050708.133724).
- [241] **M. Tanase, N. Biais, M. Sheetz.** Magnetic Tweezers in Cell Biology. In *Methods Cell Biol.*, pages 473–493. Elsevier, 2007. doi:[10.1016/S0091-679X\(07\)83020-2](https://doi.org/10.1016/S0091-679X(07)83020-2).
- [242] **I. De Vlaminck, C. Dekker.** Recent advances in magnetic tweezers. *Annu. Rev. Biophys.*, 41(1):453–472, 2012. doi:[10.1146/annurev-biophys-122311-100544](https://doi.org/10.1146/annurev-biophys-122311-100544).
- [243] **A. R. Bausch, W. Möller, E. Sackmann.** Measurement of local viscoelasticity and forces in living cells by magnetic tweezers. *Biophys. J.*, 76(1 I):573–579, 1999. doi:[10.1016/S0006-3495\(99\)77225-5](https://doi.org/10.1016/S0006-3495(99)77225-5).
- [244] **N. Wang, J. P. Butler, D. E. Ingber.** Mechanotransduction Across the Cell Surface and Through the Cytoskeleton. *Science*, 260(5111):1124–1127, 1993. doi:[10.1126/science.7684161](https://doi.org/10.1126/science.7684161).
- [245] **G. M. Whitesides.** The origins and the future of microfluidics. *Nature*, 442(7101):368–373, 2006. doi:[10.1038/nature05058](https://doi.org/10.1038/nature05058).
- [246] **F. J. Armistead, J. Gala De Pablo, H. Gadêlha, S. A. Peyman, S. D. Evans.** Cells Under Stress: An Inertial-Shear Microfluidic Determination of Cell Behavior. *Biophys. J.*, 116(6):1127–1135, 2019. doi:[10.1016/j.bpj.2019.01.034](https://doi.org/10.1016/j.bpj.2019.01.034).

- [247] **D. J. Müller, Y. F. Dufrêne.** Atomic force microscopy as a multifunctional molecular toolbox in nanobiotechnology. *Nanosci. Technol. A Collect. Rev. from Nat. Journals*, pages 269–277, 2009. doi:[10.1142/9789814287005_0028](https://doi.org/10.1142/9789814287005_0028).
- [248] **E. Nelsen, C. M. Hobson, M. E. Kern, J. P. Hsiao, E. T. O'Brien, T. Watanabe, B. M. Condon, M. Boyce, S. Grinstein, K. M. Hahn, M. R. Falvo, R. Superfine.** Combined Atomic Force Microscope and Volumetric Light Sheet System for Correlative Force and Fluorescence Mechanobiology Studies. *Sci. Rep.*, 10(1), 2020. doi:[10.1038/s41598-020-65205-8](https://doi.org/10.1038/s41598-020-65205-8).
- [249] **H. J. Butt, B. Cappella, M. Kappl.** Force measurements with the atomic force microscope: Technique, interpretation and applications. *Surf. Sci. Rep.*, 59(1-6):1–152, 2005. doi:[10.1016/j.surfrep.2005.08.003](https://doi.org/10.1016/j.surfrep.2005.08.003).
- [250] **R. M. Robertson-Anderson.** Optical Tweezers Microrheology: From the Basics to Advanced Techniques and Applications. *ACS Macro Lett.*, 7(8):968–975, 2018. doi:[10.1021/acsmacrolett.8b00498](https://doi.org/10.1021/acsmacrolett.8b00498).
- [251] **Y. A. Ayala, B. Pontes, D. S. Ether, L. B. Pires, G. R. Araujo, S. Frases, L. F. Romão, M. Farina, V. Moura-Neto, N. B. Viana, H. M. Nussenzveig.** Rheological properties of cells measured by optical tweezers. *BMC Biophys.*, 9(1):5, 2016. doi:[10.1186/s13628-016-0031-4](https://doi.org/10.1186/s13628-016-0031-4).
- [252] **B. Fabry, G. N. Maksym, J. P. Butler, M. Glogauer, D. Navajas, N. A. Taback, E. J. Millet, J. J. Fredberg.** Time scale and other invariants of integrative mechanical behavior in living cells. *Phys. Rev. E - Stat. Physics, Plasmas, Fluids, Relat. Interdiscip. Top.*, 68(4):1–18, 2003. doi:[10.1103/PhysRevE.68.041914](https://doi.org/10.1103/PhysRevE.68.041914).
- [253] **G. Lenormand, E. Millet, B. Fabry, J. P. Butler, J. J. Fredberg.** Linearity and time-scale invariance of the creep function in living cells. *J. R. Soc. Interface*, 1(1):91–97, 2004. doi:[10.1098/rsif.2004.0010](https://doi.org/10.1098/rsif.2004.0010).
- [254] **J. C. Crocker, D. G. Grier.** Methods of digital video microscopy for colloidal studies. *J. Colloid Interface Sci.*, 179(1):298–310, 1996. doi:[10.1006/jcis.1996.0217](https://doi.org/10.1006/jcis.1996.0217).
- [255] **D. Preece, R. Warren, R. M. L. Evans, G. M. Gibson, M. J. Padgett, J. M. Cooper, M. Tassieri.** Optical tweezers: wideband microrheology. *J. Opt.*, 13(4):044022, 2011. doi:[10.1088/2040-8978/13/4/044022](https://doi.org/10.1088/2040-8978/13/4/044022).
- [256] **J. Lewis.** Fast Template Matching. *Vis. Interface*, 95:120–123, 1995.
- [257] **G. Loy, A. Zelinsky.** Fast radial symmetry for detecting points of interest. *IEEE Trans. Pattern Anal. Mach. Intell.*, 25(8):959–973, 2003. doi:[10.1109/TPAMI.2003.1217601](https://doi.org/10.1109/TPAMI.2003.1217601).
- [258] **H. Faxén.** Der Widerstand gegen die Bewegung einer starren Kugel in einer zähen Flüssigkeit, die zwischen zwei parallelen ebenen Wänden eingeschlossen ist. *Ann. Phys.*, 373(10):89–119, 1922. doi:[10.1002/andp.19223731003](https://doi.org/10.1002/andp.19223731003).
- [259] **N. Malagnino, G. Pesce, A. Sasso, E. Arimondo.** Measurements of trapping efficiency and stiffness in optical tweezers. *Opt. Commun.*, 214(1-6):15–24, 2002. doi:[10.1016/S0030-4018\(02\)02119-3](https://doi.org/10.1016/S0030-4018(02)02119-3).
- [260] **H. Markovitz.** The emergence of rheology. *Phys. Today*, 21(4):23–30, 1968. doi:[10.1063/1.3034918](https://doi.org/10.1063/1.3034918).
- [261] **E. J. Koay, A. C. Shieh, K. A. Athanasiou.** Creep indentation of single cells. *J. Biomech. Eng.*, 125(3):334–341, 2003. doi:[10.1115/1.1572517](https://doi.org/10.1115/1.1572517).

- [262] **L. A. MacQueen, M. D. Buschmann, M. R. Wertheimer.** Mechanical properties of mammalian cells in suspension measured by electro-deformation. *J. Micromechanics Microengineering*, 20(6), 2010. doi:[10.1088/0960-1317/20/6/065007](https://doi.org/10.1088/0960-1317/20/6/065007).
- [263] **P. Kollmannsberger, B. Fabry.** Linear and nonlinear rheology of living cells. *Annu. Rev. Mater. Res.*, 41(1):75–97, 2011. doi:[10.1146/annurev-matsci-062910-100351](https://doi.org/10.1146/annurev-matsci-062910-100351).
- [264] **S. Li, A. G. Patwardhan, F. M. Amirouche, R. Havey, K. P. Meade.** Limitations of the standard linear solid model of intervertebral discs subject to prolonged loading and low-frequency vibration in axial compression. *J. Biomech.*, 28(7):779–790, 1995. doi:[10.1016/0021-9290\(94\)00140-Y](https://doi.org/10.1016/0021-9290(94)00140-Y).
- [265] **D. Borin, L. Puzzi, V. Martinelli, M. Cibinel, R. Lapasin, O. Sbaizero.** An engineering insight into the relationship of selective cytoskeletal impairment and biomechanics of HeLa cells. *Micron*, 102:88–96, 2017. doi:[10.1016/j.micron.2017.09.002](https://doi.org/10.1016/j.micron.2017.09.002).
- [266] **D. Jalocha, A. Constantinescu, R. Neviere.** Revisiting the identification of generalized Maxwell models from experimental results. *Int. J. Solids Struct.*, 67-68:169–181, 2015. doi:[10.1016/j.ijsolstr.2015.04.018](https://doi.org/10.1016/j.ijsolstr.2015.04.018).
- [267] **T. A. Wilson.** Time constants may be meaningless in exponentials fit to pressure relaxation data. *J. Appl. Physiol.*, 77(3):1570–1571, 1994. doi:[10.1152/jappl.1994.77.3.1570](https://doi.org/10.1152/jappl.1994.77.3.1570).
- [268] **R. Lewandowski, B. Chorążyczewski.** Identification of the parameters of the Kelvin–Voigt and the Maxwell fractional models, used to modeling of viscoelastic dampers. *Comput. Struct.*, 88(1-2):1–17, 2010. doi:[10.1016/j.compstruc.2009.09.001](https://doi.org/10.1016/j.compstruc.2009.09.001).
- [269] **F. M. Hecht, J. Rheinlaender, N. Schierbaum, W. H. Goldmann, B. Fabry, T. E. Schäffer.** Imaging viscoelastic properties of live cells by AFM: Power-law rheology on the nanoscale. *Soft Matter*, 11(23):4584–4591, 2015. doi:[10.1039/c4sm02718c](https://doi.org/10.1039/c4sm02718c).
- [270] **D. A. Flormann, C. Anton, M. O. Pohland, Y. Bautz, K. Kaub, E. Terriac, T. E. Schäffer, J. Rheinlaender, A. Janshoff, A. Ott, F. Lautenschläger.** Oscillatory Microrheology, Creep Compliance and Stress Relaxation of Biological Cells Reveal Strong Correlations as Probed by Atomic Force Microscopy. *Front. Phys.*, 9(August):1–12, 2021. doi:[10.3389/fphy.2021.711860](https://doi.org/10.3389/fphy.2021.711860).
- [271] **G. A. F. Seber, C. J. Wild.** *Nonlinear Regression*. John Wiley & Sons, Inc., Auckland, New Zealand, 2003. ISBN 978-0-471-47135-6.
- [272] **J. P. Barrett.** The coefficient of determination—some limitations. *Am. Stat.*, 28(1):19–20, 1974. doi:[10.1080/00031305.1974.10479056](https://doi.org/10.1080/00031305.1974.10479056).
- [273] **R. E. Laudadio, E. J. Millet, B. Fabry, S. S. An, J. P. Butler, J. J. Fredberg.** Rat airway smooth muscle cell during actin modulation: Rheology and glassy dynamics. *Am. J. Physiol. - Cell Physiol.*, 289(6 58-6), 2005. doi:[10.1152/ajpcell.00060.2005](https://doi.org/10.1152/ajpcell.00060.2005).
- [274] **T. A. Masters, M. P. Sheetz, N. C. Gauthier.** F-actin waves, actin cortex disassembly and focal exocytosis driven by actin-phosphoinositide positive feedback. *Cytoskeleton*, 73(4):180–196, 2016. doi:[10.1002/cm.21287](https://doi.org/10.1002/cm.21287).
- [275] **G. Gerisch, T. Bretschneider, A. Müller-Taubenberger, E. Simmeth, M. Ecke, S. Diez, K. Anderson.** Mobile actin clusters and traveling waves in cells recovering from actin depolymerization. *Biophys. J.*, 87(5):3493–3503, 2004. doi:[10.1529/biophysj.104.047589](https://doi.org/10.1529/biophysj.104.047589).
- [276] **O. D. Weiner, W. A. Marganski, L. F. Wu, S. J. Altschuler, M. W. Kirschner.** An Actin-Based Wave Generator Organizes Cell Motility. *PLoS Biol.*, 5(9):e221, 2007. doi:[10.1371/journal.pbio.0050221](https://doi.org/10.1371/journal.pbio.0050221).

- [277] **M. A. Kumar.** *Untersuchung von f-Aktin-Oszillationen während der Phagozytose.* PhD thesis, University of Bayreuth, 2023.
- [278] **S. Buracco, S. Claydon, R. Insall.** Control of actin dynamics during cell motility. *F1000Research*, 8:1977, 2019. doi:[10.12688/f1000research.18669.1](https://doi.org/10.12688/f1000research.18669.1).
- [279] **R. Rohatgi, P. Nollau, H.-Y. H. Ho, M. W. Kirschner, B. J. Mayer.** Nck and Phosphatidylinositol 4,5-Bisphosphate Synergistically Activate Actin Polymerization through the N-WASP-Arp2/3 Pathway. *J. Biol. Chem.*, 276(28):26448–26452, 2001. doi:[10.1074/jbc.M103856200](https://doi.org/10.1074/jbc.M103856200).
- [280] **T. D. Pollard, G. G. Borisy.** Cellular Motility Driven by Assembly and Disassembly of Actin Filaments. *Cell*, 112(4):453–465, 2003. doi:[10.1016/S0092-8674\(03\)00120-X](https://doi.org/10.1016/S0092-8674(03)00120-X).
- [281] **D. Liebl, G. Griffiths.** Transient assembly of F-actin by phagosomes delays phagosome fusion with lysosomes in cargo-overloaded macrophages. *J. Cell Sci.*, 122(16):2935–2945, 2009. doi:[10.1242/jcs.048355](https://doi.org/10.1242/jcs.048355).
- [282] **M. B. Poirier, C. Fiorino, T. K. Rajasekar, R. E. Harrison.** F-actin flashes on phagosomes mechanically deform contents for efficient digestion in macrophages. *J. Cell Sci.*, 133(12), 2020. doi:[10.1242/jcs.239384](https://doi.org/10.1242/jcs.239384).
- [283] **K. M. Van Citters, B. D. Hoffman, G. Massiera, J. C. Crocker.** The Role of F-Actin and Myosin in Epithelial Cell Rheology. *Biophys. J.*, 91(10):3946–3956, 2006. doi:[10.1529/biophysj.106.091264](https://doi.org/10.1529/biophysj.106.091264).
- [284] **A. C. Sundborger, J. E. Hinshaw.** Regulating dynamin dynamics during endocytosis. *F1000Prime Rep.*, 6, 2014. doi:[10.12703/p6-85](https://doi.org/10.12703/p6-85).
- [285] **S. Keen, J. Leach, G. Gibson, M. J. Padgett.** Comparison of a high-speed camera and a quadrant detector for measuring displacements in optical tweezers. *J. Opt. A Pure Appl. Opt.*, 9(8), 2007. doi:[10.1088/1464-4258/9/8/S21](https://doi.org/10.1088/1464-4258/9/8/S21).
- [286] **R. Huang, I. Chavez, K. M. Taute, B. Lukić, S. Jeney, M. G. Raizen, E. L. Florin.** Direct observation of the full transition from ballistic to diffusive Brownian motion in a liquid. *Nat. Phys.*, 7(7):576–580, 2011. doi:[10.1038/nphys1953](https://doi.org/10.1038/nphys1953).

7 List of Figures

1.1	Schematic of a section through an eukaryotic animal cell.	3
1.2	Steps during the phagocytic cup formation	9
2.1	Schematic of the phagocytic signaling process and the involved key proteins	15
2.2	Different uptake scenarios after attachment of a bead pair	15
2.3	Phase contrast image of adherent J774A.1 mouse macrophages	23
2.4	Illustration of the light paths for different wavelengths and the filters used in the microscope.	25
2.5	Forces created by individual rays of a focused laser beam through a fully transparent dielectric sphere	29
2.6	Lightpath of the trapping laser in the holographic optical tweezers setup	33
2.7	Trapping laser propagation after the SLM, as calculated by the ray transfer matrices	35
2.8	Schematic showing the operating principle of the spatial light modulator	37
2.9	Relationship of curvature and focal length of a curved mirror	40
2.10	Laser deflection and intensity created by different holograms	42
2.11	Comparison of different methods to combine multiple holograms	45
2.12	Experimental demonstration of the Gerchberg-Saxton algorithm	47
2.13	DIC image of different cell phenotypes and possible attachment points	49
2.14	Attachment of a bead pair to a cell	51
2.15	Example of the radial tracker's operation	52
2.16	Active area shapes depending on the masking radius and the particle distance	54
2.17	Examples for perfectly radially symmetric and perfectly radially anti-symmetric patterns	56
2.18	Joint and separate uptake trajectory classification examples	59
2.19	Graphical representation of the particle distances for dual-bead experiments performed using 2 μm particles without adding siRNA	60
2.20	Graphical representation of the particle distances for dual-bead experiments performed on 1 μm and 3 μm -sized particles	62
2.21	Graphical representation of the particle distances for dual-bead experiments performed on cells treated with siRNA	63
2.22	Phagocytic cup formation during joint uptake observed by fluorescence microscopy	67
2.23	Illustration of different receptor placements in the context of the spatial resolution model	68
2.24	Predicted and experimental separate uptake probabilities for differently-sized beads	71
2.25	Area occupied by a single receptor in a hexagonal grid	72
2.26	Wester Blot of CD64 and tubulin on siRNA-treated cells	75
2.27	Experimental and predicted separate uptake probabilities for dimers on different cell treatments	76
2.28	Schematic of contact area geometry	79
2.29	Phagocytic efficiency depending on particle size as predicted by the model	81
3.1	Concept of the blinking optical tweezer experiments.	91
3.2	Comparison of the accuracy of the cross-correlation and the radial tracker	94
3.3	Images of beads at different focal positions	97
3.4	Force calibration of the optical tweezers	99
3.5	Diagram showing the sequence of events during blinking optical tweezers experiments	102
3.6	Representation of commonly used linear rheological models	105
3.7	Measurement of the SLM's switching time.	108

7 List of Figures

3.8	Simulation of the bead movement caused by blinking optical traps	111
3.9	Dependence of $\Delta\rho$ on the viscoelastic parameters α and β	113
3.10	Misalignment of blinking events when not correcting for the different clock speeds of both cameras	115
3.11	Determination of the trap position in the highspeed bead trajectory	115
3.12	Adaption of the the fits to the experimental blinking trajectory	117
3.13	Alignment of the field of view between brightfield and fluorescence camera	122
3.14	Ring-shaped actin flashes observed in blinking experiments	124
3.15	Additional seven flash events observed in blinking experiments	125
3.16	Calculation of the recruitment ratio R	126
3.17	Evaluation of the actin flash timing and duration	127
3.18	Measured overshoot values of the piezo stage for different step sizes	129
3.19	Evaluation of the viscoelastic parameters α and β after the attachment.	131
3.20	Full evaluation of a single blinking experiment	132
3.21	Evolution of the recruitment ratio and the rheological parameters around the flashes .	135
3.22	Evolution of the recruitment ratio and the rheological parameters around the flashes, alternative binning	137
3.23	Flashes with poor signal-to-noise ratio observed during blinking experiments	139
3.24	Graphical summary of the numerical results of the blinking experiments	151
5.1	Evolution of the recruitment ratio and the rheological parameters in experiments without visible flash	157

8 List of Tables

2.1	Physical parameters and model numbers of available objectives	25
2.2	Pixel sizes in images acquired by different cameras	27
2.3	Acquisition modes of dual-bead experiments for different bead sizes and cell treatments	48
2.4	Number of separate uptake events for different bead sizes and attachment distances .	65
2.5	Number of separate uptake events observed on siRNA-treated cells	75
3.1	Values of α and β pre- and post flash	139
5.1	Probabilities predicted by the separate uptake model for different bead sizes and distances	156

9 Acknowledgments

I extend my gratitude to the University of Bayreuth Graduate School for their generous funding, enabling me to present my research at significant events such as the 2019 meeting of the German Physical Society in Regensburg and the 2022 annual meeting of the Biophysical Society in San Francisco.

Special recognition is due to Alexander Rohrbach and Rebecca Michiels from the University of Freiburg, Germany, for their contribution in providing Lifeact-GFP-transfected J774A.1 macrophages. I would also like to thank Jana Ritschar for helping me with the Western Blots.

Recognition is extended to H. Spanke for our fruitful collaboration, and appreciation is conveyed to all other co-authors of my publications. Heartfelt appreciation is directed to the technical assistants of our lab. I also want to thank K. Berghoff for developing the optical setup, as his efforts were instrumental in the realization of this thesis. Furthermore, I want to thank A. Sabri for the insight provided in his master thesis. A special note of gratitude is reserved for my doctoral advisor, Holger Kress, whose unwavering support and confidence have been a guiding force throughout my academic journey.

Wolfgang Gross deserves heartfelt acknowledgment for his substantial contributions to the success of my PhD, marked by numerous professional discussions and constructive feedback, enhancing the quality of my research.

Simon Wieland's exceptional support during the late phase of my thesis, coupled with the provision of accommodations in Bayreuth, played a pivotal role in the completion of my work. I express sincere thanks to Marius R. for generously offering a place to stay in Bayreuth on numerous occasions. Deepest thanks go to my parents, family, and my beloved wife for their unwavering encouragement and understanding.

I am profoundly grateful for the support and collaboration of these individuals and institutions, without which this thesis would not have been possible.

10 List of Publications

Publications

- **K. Berghoff¹, W. Gross¹, M. Eisentraut, H. Kress.** Using Blinking Optical Tweezers to Study Cell Rheology During Initial Cell-Particle Contact. *Biophysical Journal*, 120(16), 3527-3537, 2021, [doi:10.1016/J.BPJ.2021.04.034](https://doi.org/10.1016/J.BPJ.2021.04.034)
- **H.T. Spanke, R.W. Style, C. François-Martin, M. Feofilova, M. Eisentraut, H. Kress, J. Agudo-Canalejo, E. R. Dufresne.** Wrapping of Microparticles by Floppy Lipid Vesicles. *Physical Review Letters*, 125(19), 198102, 2020, [doi:10.1103/PhysRevLett.125.198102](https://doi.org/10.1103/PhysRevLett.125.198102)
- **M. Eisentraut, A. Sabri, H. Kress.** The spatial resolution limit of phagocytosis. *Biophysical Journal*, 122(5), 868-879, 2023, [doi:10.1016/j.bpj.2023.01.030](https://doi.org/10.1016/j.bpj.2023.01.030)

¹joint first author

Conference contributions

- **Regensburg, 2019:** Frühjahrstagung Deutsche Physikalische Gesellschaft, “Probing cellular resolution limits during phagocytosis”
- **San Francisco, 2022:** Biophysical Society Annual Meeting, Platform Talk “Sensing the spatial resolution limit of phagocytosis”, [doi:10.1016/j.bpj.2021.11.1975](https://doi.org/10.1016/j.bpj.2021.11.1975)

11 Eidesstattliche Versicherung

Hiermit versichere ich an Eides statt, dass ich die vorliegende Arbeit selbstständig verfasst und keine anderen als die von mir angegebenen Quellen und Hilfsmittel verwendet habe. Weiterhin erkläre ich, dass ich die Hilfe von gewerblichen Promotionsberatern bzw. -vermittlern oder ähnlichen Dienstleistern weder bisher in Anspruch genommen habe, noch künftig in Anspruch nehmen werde. Zusätzlich erkläre ich hiermit, dass ich keinerlei frühere Promotionsversuche unternommen habe.

Bayreuth, 29.04.2024

.....

(Manuel Eisentraut)